

Next-to-Leading Order Corrections to $W\gamma + \text{jet}$ and $WZ + \text{jet}$ Production at Hadron Colliders

Zur Erlangung des akademischen Grades eines

DOKTORS DER NATURWISSENSCHAFTEN

von der Fakultät für Physik des

Karlsruher Institutes für Technologie (KIT)

genehmigte

DISSERTATION

von

Dipl.-Phys. Christoph Englert

aus Hardheim

Tag der mündlichen Prüfung: 23. April 2010

Referent: Prof. Dr. Dieter Zeppenfeld

Korreferent: Prof. Dr. Ulrich Nierste

Abstract

Electroweak boson pair production in association with jets represents important signal and background processes to searches of Standard Model physics and beyond at present and future collider experiments. The full next-to-leading order corrections from Quantum chromodynamics to $W\gamma + \text{jet}$ and $WZ + \text{jet}$ production at hadron colliders have been computed and implemented into a fully-flexible Monte Carlo program. Leptonic decays of the W and Z are included throughout.

The total corrections at the Large Hadron Collider (LHC) are highly phase space-dependent and sizable, enlarging the cross sections by 30-50% compared to the leading order approximation. The corrections are mainly characterized by unsuppressed extra jet radiation, which also accounts for the only mild reduction of the cross sections' scale dependencies. At the Tevatron, we find an increase of the total cross section by around 30%. The corrections' impact is less sizable compared to the LHC findings.

An important application of the calculation is the search for anomalous $WW\gamma$ couplings in $W\gamma$ production, where significance-improving strategies rely on vetoing additional jet activity. Providing improved precision for $W\gamma + \text{jet}$ production, we add higher accuracy to the veto performance, but also address a crucial theoretical part towards more inclusive measurements. To this end, the effect of anomalous $WW\gamma$ couplings on $W\gamma + \text{jet}$ production is included and discussed.

Zusammenfassung

Jet-assoziierte Produktion elektroschwacher Eichbosonen ist ein wichtiger Signal- und Untergrundprozess bei der Suche nach bekannter Physik und Phänomenen jenseits des Standardmodells an heutigen und zukünftigen Beschleuniger-Experimenten. Die vollen nächst-führenden Quantenchromodynamik (QCD)-Korrekturen zur $W\gamma + \text{jet}$ und $WZ + \text{jet}$ Produktion an Hadron-Beschleunigern, inklusive leptonischer Zerfälle von W und Z , wurden berechnet und in einem voll-flexiblen Monte Carlo Programm implementiert.

Die Korrekturen am Large Hadron Collider (LHC) sind stark phasenraumabhängig. Mit einer Vergrößerung des totalen Wirkungsquerschnitts um 30-50% im Vergleich zur führenden Ordnung sind diese gleichzeitig nicht vernachlässigbar. Charakteristisch ist dabei die nur schwach unterdrückte zusätzliche Jet-Emission, die ihrerseits auch für die nur geringe Reduktion der Skalenabhängigkeit der Wirkungsquerschnitte verantwortlich ist. Für die Bedingungen am Tevatron ergibt sich eine Vergrößerung des Wirkungsquerschnitts um 30%. Die relativen Korrekturen sind weniger stark phasenraumabhängig als am LHC.

Eine wichtige Anwendung findet die Rechnung bei der Suche nach anomalen $WW\gamma$ Kopplungen, bei der signifikanzverbessernde Strategien Jet-Vetos implementieren. Indem wir die QCD Korrekturen zur $W\gamma + \text{jet}$ Produktion bereitstellen, ermöglichen wir die Berücksichtigung höherer Ordnung QCD bei der Veto-Effizienz und behandeln einen theoretisch wichtigen Beitrag für inklusivere Mess-Strategien. Für diesen Zweck werden auch die Effekte anomaler $WW\gamma$ Kopplungen auf die $W\gamma + \text{jet}$ Produktion in nächst-führender Ordnung QCD berechnet und diskutiert.

Contents

1	Introduction	1
2	Foundations	3
2.1	Axiomatic QFT and Gauge Theories	3
2.1.1	The Standard Model	5
2.1.2	The Standard Model as a low-energy effective theory	10
2.2	QCD-improved Hadron Collider Calculations	11
2.2.1	IR safety	11
2.2.2	Soft and collinear singularities and dipole subtraction	13
2.2.3	Dipole subtraction	14
2.2.4	Virtual corrections	17
2.2.5	Event generation using Monte-Carlo methods	23
2.2.6	Constructing the phase space	24
3	Elements of the calculation	29
3.1	Leading order contributions	29
3.1.1	Numerical implementation, speed and comparisons	31
3.1.2	Anomalous $WW\gamma$ couplings	33
3.2	Real emission contributions	35
3.2.1	Real emission matrix elements	35
3.2.2	Numerical implementation, speed and di-jet comparisons	37
3.2.3	Dipole subtraction	38
3.3	Virtual contributions	45
3.3.1	'Boxline' corrections	46
3.3.2	'Pentline' corrections	51
3.3.3	Fermionic loop corrections to WZj production	53
3.3.4	Cancellation of IR divergencies and finite remainders	54
3.3.5	Numerical implementation and gauge checks	55
3.4	Finite collinear remainders	57
3.5	Test and Comparisons	59
4	$W^\pm\gamma j$ production at hadron colliders	61
4.1	General Monte-Carlo input parameters	61
4.2	Scale dependence of production cross sections	61
4.3	Photon isolation and differential distributions	65
4.4	Impact of non-standard $WW\gamma$ couplings	80

5	$W^\pm Zj$ production at hadron colliders	89
5.1	General Monte-Carlo input parameters	89
5.2	Scale dependence of production cross sections	90
5.3	Differential distributions	92
6	Summary and Outlook	99
A	Pentline building block	101
A.1	Abelian pentline	101
A.2	Non-abelian pentline	103
B	Catani Seymour Dipole Formulae	105
B.1	The \mathbf{I} operator	105
B.2	Finite Collinear Terms	105
B.2.1	Finite collinear terms related to $\mathcal{M}^{\bar{q}Q \rightarrow g}$	107
B.2.2	Finite collinear terms related to $\mathcal{M}^{gQ \rightarrow q}$	109
B.2.3	Finite collinear terms related to $\mathcal{M}^{\bar{q}g \rightarrow \bar{Q}}$	110
B.2.4	Compact Expressions	112
B.2.5	Integral Formulae	113
	Bibliography	114
	List of figures	124
	List of tables	131
	Acknowledgements	133

Chapter 1

Introduction

*Revolution, Evolution, obwohl wir alle aufrecht gehn,
werden wir uns ewig fragen, warum sich die Dinge drehn.*

— Die Fantastischen Vier in Neues Land
Die 4. Dimension (1993)

The Standard Model of particle physics (e.g. [1] for pedagogical introductions), equally blessed with experimental success and afflicted with theoretical caveats, remains one of the most predictive and precise theories ever developed hitherto. Joint efforts of experimentalists and theorists have provided agreement of theory and measurement, that has to be met by theories, which intend to formulate particle physics at the desired, more fundamental level. Despite its success in all fields of modern-day particle phenomenology, the Standard Model is, of course, subject to continuous testing. In this sense the upcoming era of the Large Hadron Collider (LHC) at CERN marks the next milestone of experiments, that is going to sharpen the understanding of particle interactions, which has been formed and consolidated by measurements at the Fermilab Tevatron and the CERN Large Electron Positron Collider (LEP).

A crucial part of *quantitative* understanding of LHC data is undoubtedly experimental *and* theoretical precision of measurement and simulation. Perturbative analysis, while only providing limited insights* into Quantum Field Theories (QFTs) such as the Standard Model, still remain by-now state-of-the-art methods to get a numerical handle on diverse models in a realistic collider setting. Naturally, perturbative approaches thereby miss characteristics of a QFT if limited to the semiclassical limit, i.e. to the leading order of perturbative series expansion. In general, and in particular at hadron colliders such as the LHC, radiative corrections from Quantum chromodynamics (QCD) are likely to turn out sizable. A theoretically deeper understanding of electroweak physics, which is one of LHC's primary goals, might thus be obscured by unknown higher-order QCD effects.

Reliable simulations of signal and background processes, within every consistent model in terms of fully-flexible Monte Carlo programs, therefore require at least next-to-leading order (NLO) QCD precision of cross sections and differential distributions to be taken into account when analyzing experimental data. The necessity of improved

*Non-local classical solutions such as instantons or sphalerons, while playing fundamental roles in many areas of particle physics, e.g. Leptogenesis or axionic solutions to the strong \mathcal{CP} problem, are not governed by perturbative approaches.

QCD-accuracy for electroweak production processes has thus been agreed on as common goal of precision phenomenology and was summarized in the so-called “Les Houches wish-list” of LHC processes [2]. Over the past few years, considerable improvement in completing this task has been accomplished, cf. [3–10] for recent results.

This thesis covers the NLO QCD corrections to $W^\pm\gamma + \text{jet}$ [9] and $W^\pm Z + \text{jet}$ production [10] at the CERN LHC, but we also revise these processes for the Tevatron. Special care is devoted to the development of a fully-flexible, highly cross-checked and numerically stable parton-level Monte Carlo implementation of these processes, based on the VBFNLO-framework [11]. Throughout, leptonic decays of the massive vector bosons to leptons are considered, taking into account all off-shell and finite width effects. We also include non-standard $WW\gamma$ couplings to the $W^\pm\gamma + \text{jet}$ production channels.

The $W^\pm\gamma j$ production is not only an important background searches for anomalous $WW\gamma$ couplings at the LHC [12], but also comprises all scales of the electroweak and strong sector of the SM. Improved QCD precision therefore also asses uncertainties of proper photon-jet isolation criteria at hadron colliders.

$W^\pm Z j$ production generalizes the $W^\pm\gamma j$ calculation to a fully leptonic final state. SM multi-lepton signals are irreducible backgrounds to any new electroweak physics model, e.g. to decay chains of supersymmetric particles, or to strongly interacting models with additional massive W and Z bosons [13].

The layout of this work is the following: Chapter 2 sets the stage for relativistic QFTs, introduces the model-building ingredients of the SM, and gives necessary details on parton-level NLO QCD calculations at hadron colliders, in order to make this thesis self-consistent. Special emphasis is put on infrared safety of (differential) cross sections, discussing the anatomy soft and collinear singularities encountered in QCD loop calculations; the infrared subtraction algorithm is introduced and infrared-safe photon isolation criteria in jet cross sections at NLO QCD are discussed. The chapter closes with an outline of the Monte-Carlo methods used for the purpose of this thesis.

Chapter 3 gives details on the calculation, as well as details on the numerical Monte-Carlo implementation thereof. The infrared subtraction algorithm is performed explicitly and the analytic and numerical structure of the loop corrections is outlined. A discussion of the implementations’ numerical quality and the performed numerical checks is appended.

Chapters 4 and 5 are devoted to the numerical results of NLO QCD $W\gamma j$ and WZj production at the LHC and the Tevatron. As already mentioned, leptonic decays are taken into account throughout this thesis, but we will refer to the processes as $W\gamma j$ and WZj production for convenience. Scale uncertainties, total and differential cross sections alongside total and differential correction factors are given, discussing the impact of the QCD corrections on the processes at the LHC and the Tevatron experiments. Chapter 4 also compares different photon isolation criteria, and discusses the influence of anomalous $WW\gamma$ couplings on $W\gamma j$ production at NLO QCD.

Chapter 6 closes with a summary of this thesis.

Chapter 2

Foundations

2.1 Axiomatic QFT and Gauge Theories

The interpretation of classical Electromagnetism and gravity as relativistic gauge theories had been well-established long before the gauge principle found application to the other two known fundamental forces. Understanding the weak and strong interactions in terms of non-abelian gauge theories turned out to be more involved, as characteristic properties are hidden by spontaneous symmetry breaking and confinement, respectively. The Standard Model (Tab. 2.1) combines the strong, the weak and the electromagnetic interactions in the simplest consistent way to form a chiral gauge theory based on the group $SU(3)_C \times SU(2)_L \times U(1)_Y$. Summarizing theoretical progress of decades, it can be considered as today's paradigm of a renormalizable relativistic and realistic QFT [14]. The requirement of renormalizability in the context of gauge theories is mathematically equivalent to the (effective) Lagrangian containing only local lorentz-invariant interaction terms of the quantum fields, dictated by the inner symmetries, up to mass dimension four. Quantum fields thereby mean (complex) irreducible representations of the universal enveloping group of the proper orthochronous subgroup of the Lorentz group $SO(1, 3)$,

$$SO(1, 3)_+^\uparrow \simeq SL(2, \mathbb{C})/\mathbb{Z}_2, \quad (2.1)$$

where $SL(2, \mathbb{C})$ should be understood as a real Lie group in this context. There is an isomorphism of the complexified Lie algebra

$$\mathbb{C} \times \mathfrak{sl}(2, \mathbb{C}) \simeq \mathfrak{su}(2, \mathbb{C}) \oplus \mathfrak{su}(2, \mathbb{C}) \quad (2.2)$$

and we may label all irreducible representations of the Lorentz group by two isospins (i, j) , with $i, j \neq 0$ for the two non-equivalent spinor modules, which correspond to the two non-equivalent Weyl-representations of $SL(2, \mathbb{C})$ in the Infeld–van der Waerden formalism. Commonly these are distinguished by dotted and undotted indices. In the more general approach to construct representations of (pseudo-)orthogonal Spin groups, i.e. by embedding the algebra $\mathfrak{so}(n, m)$ into a complex Clifford algebra $\mathcal{C}(n + m)$, the Weyl spinor-representations refer to the transformation properties under the even subalgebra*, which gives rise to reducibility of the Clifford algebra's representation in even dimensions. The familiar Dirac spinor, i.e. the complex irreducible representation

*The Clifford algebra comes with a \mathbb{Z}_2 -gradation, so that it can be decomposed into an 'even' and 'odd' part.

of the Clifford algebra, thus decomposes into two Weyl spinors

$$\Psi = \begin{pmatrix} \psi_\alpha \\ \bar{\chi}^{\dot{\alpha}} \end{pmatrix}, \quad \bar{\chi}^{\dot{\alpha}} = i(\sigma^2)^{\dot{\alpha}\alpha} \chi_\alpha^*, \quad (2.3)$$

under the action of the Lorentz group. These spinors are also called left- and right-handed spinors in physicists' language as the chirality operators

$$\mathbb{P}_{L,R} = \frac{1}{2} (\mathbb{1} \pm \gamma_5) := \frac{1}{2} (\mathbb{1} \pm i\gamma^0\gamma^1\gamma^2\gamma^3) \quad (2.4)$$

in the Weyl basis

$$\gamma^\mu = \begin{pmatrix} 0 & \sigma^\mu \\ \bar{\sigma}^\mu & 0 \end{pmatrix} \quad (2.5)$$

covariantly project out the upper and lower entries of (2.3). In (2.5) the σ^μ are the Pauli matrices σ^i extended by $\sigma^0 = \mathbb{1}$, and $\bar{\sigma}^{\dot{\alpha}\alpha} = \varepsilon^{\alpha\beta}\varepsilon^{\dot{\alpha}\dot{\beta}}\sigma_{\beta\dot{\beta}}$. Comparing (2.3) and (2.4), we see $\psi_R \sim \psi_L^c$.

All irreducible representations of the Lorentz group can be constructed from these spinorial representation by standard methods. The vectorial representation, e.g., is given by $(\frac{1}{2}, \frac{1}{2})$. This way we govern the representations of the Lorentz group that cover the ‘‘outer symmetry’’ of the field theory. Applying the Coleman-Mandula theorem [15], which states that the representation of a non-trivial quantum field theory (with the addition of some reasonable arguments) is given by a direct product representation of outer and inner symmetries, we still have to fix the quantum fields transformation properties under the internal gauge group, which is done in sec. 2.1.1.

After second quantization [16], i.e. promoting the fields to operators acting on an axiomatically introduced Fock space, the quantum fields are mathematically to be understood as operator-valued tempered distributions [17]. A standard textbook method of quantization is the generalization of the Feynman path integral formalism to functional integrals. The path integral's measure, however, is not meaningful in its mathematical sense, and neither is the naive generalization to the functional measure. Yet, the path integral formulation is the particle physicists' preferred concept due to apparent realizations of symmetries. It also allows straightforward application of perturbation theory via Feynman rules (see sec. 2.1.1).

In the language of Constructive Quantum field theory second quantization amounts to a functional generalization of the Feynman-Kac [18] formula, which gives a mathematically reasonable adoption of the Feynman path integral. At an even more axiomatic level, a rigorous QFT's fundamental mathematical ingredients are summarized in the Wightman Axioms [19]. These also give the notion of functional integration and renormalization a mathematically rigorous formulation in dimensions $d < 4$. Their validity, however, in the context of interacting four dimensional Yang-Mills theories [20] is yet undelivered. Nonetheless the concept of gauge invariance solved with perturbative means has turned out extremely successful. The astonishing agreement of theory and experiment is subject to a whole book of tables [21]. Even though the very mathematical concept of QFTs in $d = 4$ remains presently vague to unclear, their textbook-application is experimentally well justified.

2.1.1 The Standard Model

The inner gauge invariance realized in Yang-Mills theories consistently accounts for massless vectors, such as the photon and the gluon, to all orders of perturbation theory. Starting point of an interacting $SU(n)$ gauge theory is the gauge action

$$S = -\frac{1}{4} \int d^4x F_{\mu\nu}^a F^{a\mu\nu}, \quad (2.6)$$

where the field strength two-form is

$$F_{\mu\nu}^a = \partial_\mu A_\nu^a - \partial_\nu A_\mu^a + ig f^{abc} A_\mu^b A_\nu^c, \quad (2.7)$$

with A_μ^a , the corresponding gauge vector field (connection) in direction of the Lie-algebra generator $t^a \in \mathfrak{su}(n)$, satisfying

$$[t^a, t^b] = i f^{abc} t^c. \quad (2.8)$$

In (2.7), g denotes the coupling constant of the theory. QCD and the electroweak interactions are constructed from a $SU(3)_C \times SU(2)_L \times U(1)_Y$ gauge theory, with the fermions $\psi_i \in \text{Mod}\{SU(3)_C \times SU(2)_L \times U(1)_Y\}$ of Tab. 2.1 added,

$$S_f = \int d^4x \psi_i^\dagger i \bar{\sigma}^\mu (D_\mu^{(\alpha)})_{ij} \psi_j, \quad \alpha = C, L, Y, \quad (2.9)$$

Table 2.1: Particle content of the minimal Standard Model. i denotes the generation index, i.e. $u^i = (u, c, t)$ and $d^i = (d, s, b)$. The table lists eigenstates of the Lagrangian, and the mass eigenstates after symmetry breaking. The bar denotes the complex conjugate module on which the complex conjugate representation operates.

\mathcal{L} -state	$SU(3)_C \times SU(2)_L \times U(1)_Y$	$U(1)_{\text{QED}}$	m -state	$SL(2, \mathbb{C})$
$(u^i, d^i)_L$	$(3, 2, \frac{1}{6})$	$(\frac{2}{3}, -\frac{1}{3})$	$(u^i, d^i)_L$	$(\frac{1}{2}, 0)$
$(u^i)_L^c$	$(\bar{3}, 1, -\frac{2}{3})$	$-\frac{2}{3}$	$(u^i)_L^c$	$(0, \frac{1}{2})$
$(d^i)_L^c$	$(\bar{3}, 1, \frac{1}{3})$	$\frac{1}{3}$	$(d^i)_L^c$	$(0, \frac{1}{2})$
$(\nu_e^i, e^i)_L$	$(1, 2, -\frac{1}{2})$	$(0, -1)$	$(\nu_e^i, e^i)_L$	$(\frac{1}{2}, 0)$
$(e^i)_L^c$	$(1, 1, 1)$	1	$(e^i)_L^c$	$(0, \frac{1}{2})$
$g_\mu^{1,\dots,8}$	$(8, 1, 0)$	1	$g_\mu^{1,\dots,8}$	$(\frac{1}{2}, \frac{1}{2})$
$W_\mu^{1,2,3}$	$(1, 3, 0)$	± 1	W_μ^\pm	$(\frac{1}{2}, \frac{1}{2})$
B_μ	$(1, 1, 0)$	0	Z_μ^0, γ_μ	$(\frac{1}{2}, \frac{1}{2})$
$\Phi = (\phi_1, \phi_2)$	$(1, 2, x)$	± 1 0	ϕ^\pm h, ϕ^0	$(0, 0)$
spontaneously breaks $SU(2)_L \times U(1)_Y \rightarrow U(1)_{\text{QED}}$				
LOCAL INNER SYMMETRIES			LORENTZ GROUP	

where

$$(D_\mu^{(\alpha)})_{ij} = \partial_\mu + ig^{(\alpha)} A_\mu^{a,(\alpha)} t_{ij}^{a,(\alpha)} \quad (2.10)$$

is the gauge-covariant derivative.

When quantizing the theory, using e.g. the path-integral approach, it turns out necessary to “fix the gauge” of QCD (and QED): The operator bilinear in the gauge fields that follows from (2.7) in momentum space

$$-\frac{1}{4} F_{\mu\nu}^a F^{a\mu\nu} = -\frac{1}{2} A_\mu^a(k) (k^2 g_{\mu\nu} - k^\mu k^\nu) A_\mu^a(k) + \dots \quad (2.11)$$

exhibits a non-trivial kernel, so that its inverse does not exist and we can not construct the free theory to apply perturbation theory. In the path integral this shows up as an integration over gauge-equivalent field configurations of the classical action, leading to a “divergent” path integral along these trajectories in group space; the path integral can not be given a meaning in terms of functional Gaussian integration. A way to avoid this problem is the Faddeev-Popov-DeWitt method [23], that selects a specific section in the gauge orbit to split-off the integration over gauge-equivalent configurations. Doing so,

$$S + S_{\text{fix}} = S - \int d^4x \frac{1}{2\xi} (\partial_\mu A^{a\mu})^2, \quad (2.12)$$

can be understood as the theory’s new classical action of the generating functional, which now allows to define a gauge boson propagator. Calculating Green’s functions, the additional integration over the gauge group cancels against the respective contribution to the normalization.

Additionally, for non-abelian gauge theories, the Faddeev-Popov-de Witt approach introduces a new set of fermions with bosonic statistics, the so-called ghost fields,

$$S_{\text{ghost}} = - \int d^4x \bar{u}_g^a (\partial^2 + gf^{abc} \partial^\mu A_\mu^b) u_g^c. \quad (2.13)$$

These fields do not give rise to physical states but serve as negative degrees of freedom for the gauge-vector fields, and e.g. keep polarization functions transverse. Besides, they play a fundamental role in retaining non-abelian gauge invariance, which is manifestly broken by the fixing (2.12) at the classical level. At the quantum level, there is a (supersymmetric) extension to the gauge transformation of the ghosts, the Becchi-Rouet-Stora-Tuyin (BRST) transformation [24], that guarantees the invariance of physical results under gauge fixing, and therefore restores all consequences of classical gauge invariance. The Slavnov-Taylor identities [14, 25], i.e. the Ward identities [26] of non-abelian gauge theories, that follow from global BRST symmetry play a fundamental role in the proof of renormalizability, as well as provide stringent checks of gauge invariance for actual calculations (see sec. 3.3.5).

Symmetry breaking of the electroweak group $SU(2)_L \times U(1)_Y$ to Quantum electrodynamics in the SM is triggered by adding a scalar[†] Higgs field [27] to the theory, that

[†]This scalar representation is the only one compatible with unbroken four dimensional Lorentz symmetry.

transforms under the fundamental complex representation of $SU(2)_L$,

$$S_H = \int d^4x \left((D_\mu^{(L)}\Phi)^\dagger D^{(L),\mu}\Phi - V(\Phi) \right). \quad (2.14)$$

The Higgs-potential

$$V(\Phi) = \mu^2 \Phi^\dagger \Phi + \lambda (\Phi^\dagger \Phi)^2 \quad (2.15)$$

is chosen to select a vacuum $\langle \Phi_0 \rangle$ which breaks $SU(2)_L \times U(1)_Y$. This is done by assigning a tachyonic mass to Φ , $\mu^2 < 0$. The symmetry is said to be broken “spontaneously”, as there is still a symmetry that connects the degenerate non-trivial vacua, which is, however, not manifest by expanding around a fixed (but arbitrary) direction $\langle \Phi_0 \rangle$. In unitary Fujikawa-Lee-Sanda R_ξ -gauge (see below and [28]), the would-be-Goldstone bosons of the $SU(2)_L \times U(1)_Y$ -breaking become the longitudinal degrees of freedom of the appropriately defined linear combinations of $SU(2)_L \times U(1)_Y$ gauge fields,

$$\begin{aligned} Z_\mu^0 &= \frac{1}{\sqrt{g^2 + g'^2}} (gW_\mu^3 - g'B_\mu), \\ A_\mu^0 &= \frac{1}{\sqrt{g^2 + g'^2}} (g'W_\mu^3 + gB_\mu), \\ W_\mu^\pm &= \frac{1}{\sqrt{2}} (W^1 \mp iW^2). \end{aligned} \quad (2.16)$$

These gauge bosons acquire masses

$$m_{W^\pm}^2 = \frac{g_L^2 v^2}{4}, \quad m_{Z^0}^2 = \frac{m_{W^\pm}^2}{\cos^2 \theta_w}, \quad m_{A^0}^2 = 0 \quad (2.17)$$

where $v \approx 246$ GeV denotes the Higgs’ vacuum expectation value. The only apparent gauge symmetries after the expanding around the new vacuum are QCD and $U(1)_{QED}$. The (classical) mass relation of (2.17) is experimentally well-established, and is a direct consequence from $SU(2)_L \simeq Sp(2)$, i.e. $SU(2)$ is a symplectic group:

$$\Phi \sim i\sigma^2 \Phi^* = \Phi^c, \quad (2.18)$$

where “ \sim ” means unitary equivalent. This means that the Higgs sector actually exhibits a global symmetry $SU(2)_L \times SU(2)_R$, into which the $SU(2)_L \times U(1)_Y$ -subgroup is weakly gauged. The Higgs’ vacuum expectation value breaks $SU(2)_L \times SU(2)_R \rightarrow SU(2)_{R+L}$ under which the massive $SU(2)_L$ gauge bosons form a triplet, i.e. are degenerate in mass. Assigning $U(1)_Y$ quantum numbers to the Higgs rotates the quantum fields by $\cos \theta_w$, and the mass eigenvalues by $\cos^{-1} \theta_w$, consequently.

The property (2.18) is also used to assign masses to up- and down-type quarks via the vacuum expectation value of the same Higgs field[‡] (2.14) and Yukawa-interactions:

$$-S_{\text{Yuk}} = \int d^4x \left(Y_{ij}^{(u)} \bar{\psi}_i \Phi u_j^c + Y_{ij}^{(d)} \bar{\psi}_i \Phi^c d_j^c + \text{h.c.} \right), \quad (2.19)$$

[‡]Because of this minimal choice the Standard Model is often referred to as the Minimal Standard Model. Assigning different Higgs fields to up- and down type quarks have been discussed in the literature in the context of two-Higgs-doublet scenarios.

where $\psi_i = (u_i, d_i)_L$ denotes the three weak quark doublets. The Yukawa sector can be diagonalized with bi-unitary transformations $L_u Y^{(u)} R_u^\dagger$, $L_d Y^{(d)} R_d^\dagger$, which rotate the up- and down fields of right- and left handedness, respectively, to the mass eigenstates in flavor space. The neutral electroweak currents in (2.9) remain unaffected due to unitarity, but there is a relic dependence in the charged weak current, which is expressed in terms of the unitary Cabibbo-Kobayashi-Maskawa (CKM) matrix [29],

$$V = L_u^\dagger L_d = \begin{pmatrix} V_{ud} & V_{us} & V_{ub} \\ V_{cd} & V_{cs} & V_{cb} \\ V_{td} & V_{ts} & V_{tb} \end{pmatrix}. \quad (2.20a)$$

The absolute values of the entries of the CKM matrix read [21]

$$|V| = \begin{pmatrix} 0.97419 \pm 0.00022 & 0.2257 \pm 0.0010 & 0.00359 \pm 0.00016 \\ 0.2256 \pm 0.0010 & 0.97334 \pm 0.00023 & 0.0415_{-0.0011}^{+0.0010} \\ 0.00874_{-0.00037}^{+0.00026} & 0.0407 \pm 0.0010 & 0.999133_{-0.000043}^{+0.000044} \end{pmatrix}. \quad (2.20b)$$

In the SM, with 3 generations of quarks, the 3-by-3 CKM matrix is characterized by three angles and one complex phase, which is the only acceptable source of \mathcal{CP} -violation in the SM[§].

Selected Standard Model Feynman rules

From the SM Lagrangian one can straightforwardly deduce the Feynman rules [1] relevant for this thesis. The gluon-, ghost-, electroweak boson- and fermion propagators are, respectively,

$$\begin{array}{c} \xrightarrow{\hspace{1cm}} \\ \text{-----} \\ g_\mu^a(k) \quad g_\nu^b(k) \end{array} = \frac{-ig_{\mu\nu}\delta^{ab}}{k^2}, \quad (2.21a)$$

$$\begin{array}{c} \xrightarrow{\hspace{1cm}} \\ \text{-----} \\ u_g^a(k) \quad u_g^b(k) \end{array} = \frac{i\delta_{ab}}{k^2}, \quad (2.21b)$$

$$\begin{array}{c} \xrightarrow{\hspace{1cm}} \\ \text{-----} \\ V_\mu(k) \quad V_\nu(k) \end{array} = \frac{-i}{k^2 - m_V^2 + im_V\Gamma_V} \left(g_{\mu\nu} - \frac{k_\mu k_\nu}{k^2 - m_V^2 + im_V\Gamma_V} \right), \quad (2.21c)$$

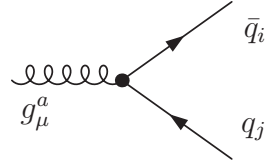
$$\begin{array}{c} \xrightarrow{\hspace{1cm}} \\ \text{-----} \\ f_i(k) \quad f_j(k) \end{array} = \frac{i\delta^{ij}k_\mu\gamma^\mu}{k^2} = \frac{i\delta^{ij}\not{k}}{k^2}, \quad (2.21d)$$

with the particle width Γ_V to take the finite lifetime of the massive electroweak bosons into account via the Breit-Wigner propagator (2.21c). For the photon we obviously

[§]An additional source of \mathcal{CP} -violation is given by including the dimension four $SU(3)_C$ operator $\tilde{F}F$, with the hodge dual field strength $\tilde{F} = *F$. This term is *not* forbidden by gauge invariance, and arises from finite-energy QCD-instanton configurations. However, it leads to an unacceptably large dipole moment of the neutron. We are forced to tune the overall quark phase of the CKM matrix, to cancel this large contribution [22]. This is known as the strong \mathcal{CP} -problem.

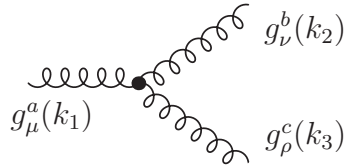
set $m_V = 0$. Note that we choose unitary gauge for the electroweak sector and Feynman gauge for QCD and the Kronecker symbol in the fermion propagator represents all quantum numbers carried by the particle. The small arrows in (2.21) denote the momentum flow which can be different from the charge flow, yielding an additional minus sign for fermions. In the following we also specify the charge flow of the W^\pm by an additional arrowed line.

The gauge boson-fermion couplings are given by the covariant derivative (2.9). The Feynman rule for quark-gluon interactions reads



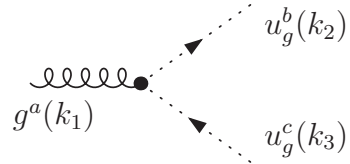
$$= ig_s t_{ij}^a \gamma^\mu, \quad (2.22)$$

where t^a are the Gell-Mann matrices of $\mathfrak{su}(3)$. The trilinear gluon coupling that arises from the non-abelian structure of $\mathfrak{su}(3)$, (2.7), is given by



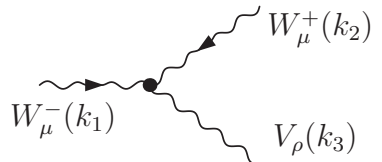
$$= g_s f^{abc} [g_{\mu\nu}(k_1 - k_2)_\rho + g_{\nu\rho}(k_2 - k_3)_\mu + g_{\rho\mu}(k_3 - k_1)_\nu], \quad (2.23)$$

and the gluon-gluon-ghost vertex from (2.12) is



$$= g_s f^{abc} k_2^\mu. \quad (2.24)$$

The trilinear interaction of the electroweak gauge bosons in mass eigenbasis reads



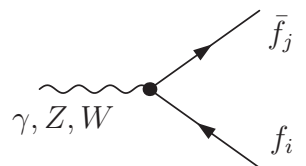
$$= ieC [g_{\mu\nu}(k_1 - k_2)_\rho + g_{\nu\rho}(k_2 - k_3)_\mu + g_{\rho\mu}(k_3 - k_1)_\nu], \quad (2.25a)$$

with

$$C = \begin{cases} 1 & V = \gamma \\ -\cot \theta_w & V = Z \end{cases}. \quad (2.25b)$$

In (2.23)–(2.25) all momenta are chosen to be incoming.

The interaction of quarks and leptons with the electroweak gauge boson mass eigenstates is



$$= ie\gamma_\mu (C_L \mathbb{P}_L + C_R \mathbb{P}_R) \quad (2.26a)$$

	$\gamma f_i f_j$	$Z f_i f_j$	$W^+ \bar{u}_i d_j$	$W^- d_i u_j$	$W^+ \bar{\nu}_i \ell_j$	$W^- \ell_i \nu_j$	
C_L	$-Q_f \delta_{ij}$	$g_f^- \delta_{ij}$	$\frac{1}{\sqrt{2s_w}} V_{ij}$	$\frac{1}{\sqrt{2s_w}} (V_{ij})^\dagger$	$\frac{1}{\sqrt{2s_w}} \delta_{ij}$	$\frac{1}{\sqrt{2s_w}} \delta_{ij}$	(2.26b)
C_R	$-Q_f \delta_{ij}$	$g_f^+ \delta_{ij}$	0	0	0	0	

where the electric charge of the fermions Q_f follows from tab. 2.1, $s_w = \sin \theta_w$, and we have introduced

$$g_f^+ = -\tan \theta_w Q_f, \quad g_f^- = \frac{I_{w,f}^3 - \sin^2 \theta_w Q_f}{\sin \theta_w \cos \theta_w}, \quad (2.26c)$$

and $I_{w,f}^3 = \sigma^3/2$ is the weak isospin of the fermions (cf. tab. 2.1).

2.1.2 The Standard Model as a low-energy effective theory

From its very construction, the Standard Model is fully renormalizable [14]. Upon fixing its 19 parameters, the SM remains, in principle, predictive up to arbitrary energy scales in terms of an asymptotic expansion in the gauge couplings. There are, however reasonable drawbacks and caveats, some of which were already mentioned in sec. 2.1.1. The absence of a sufficient source of \mathcal{CP} violation is in contrast to the Sakharov conditions [30] to reproduce the observed baryon– anti-baryon asymmetry. There is neither a viable cold dark-matter candidate nor a right handed neutrino, strongly suggested from neutrino oscillations. Why there are, to present knowledge, exactly three generations of quarks and leptons, is unknown, and there is no SM-mechanism, which explains their observed mass-hierarchical structure.

These are just several of a variety of questions, which are either unsolved or un-addressed by fixing the respective parameters in the SM Lagrangian “by hand” and constantly fuel TeV-scale model-building. A flaw of the SM, which has become most seminal to most model-builders[¶] is the so-called Hierarchy Problem, which arises by the scalar Higgs triggering electroweak symmetry breaking while, at the same time being the only candidate to provide masses to the fundamental fermions. This multi-cast character of the Higgs is not buffered by an additional (global, approximate) symmetry, so that the smallness of the electroweak scale conflicts with ’t Hooft’s naturalness criterion, and is solely fixed by fine-tuning the classical parameters to get the quantum theory right.

The Hierarchy Problem has led to a plethora of more or less consistent alternatives to the SM at scales around a TeV. Common to all of the BSM scenarios is that they approach the experimentally well-established SM predictions in the low energy limit. A model-independent view on this top-bottom approach is the extension of the SM with additional SM-gauge invariant higher-dimensional and thus non-renormalizable

[¶]This is due to the fact that precision measurements suggest that the evident breakdown of presently known accidental symmetries of the SM, such as baryon-minus-lepton number, requires test at scales of several thousands of TeV. This is way beyond any present and near future experimental reach.

operators[¶]

$$\mathcal{L}^{\text{eff}} = \mathcal{L}_{\text{SM}} + \frac{1}{\Lambda} \mathcal{L}^{(5)} + \frac{1}{\Lambda^2} \mathcal{L}^{(6)} + \dots, \quad (2.27)$$

i.e. working bottom-up by fitting \mathcal{L}^{eff} . Studying the effect of these higher-dimensional and non-SM operators on distributions eventually allows to formulate general exclusion bounds on new physics given experimental data. The specific BSM model is however unspecified, except for the fact that the additional degrees of freedom participate in SM gauge interactions. This is generally signaled by breakdown of unitarity at scales above Λ , a defect which is to be mended by the full BSM theory but is present in the intermediate energy scale-description of the effective Lagrangian notion.

2.2 QCD-improved Hadron Collider Calculations

2.2.1 IR safety

At the desired LHC center-of-mass energy of $\sqrt{s} = 14$ TeV, the effect of finite quark masses, although needed to avoid overall theoretical pathologies [32,33], play a subdominant role. Calculations in the chiral limit $m_q = 0$ for the light flavors sufficiently govern GeV-scale dynamics and greatly simplify by using helicity methods [34]. Generic to theories with massless particles such as the gluons, infrared (IR), i.e. soft and collinear, divergencies show up in quantum corrections, that are only mended according to the Kinoshita-Lee-Naunberg (KLN) theorem [33,35], when dealing with sufficiently inclusive observables**, cf. sec. 2.2.2.

Technically this causes some difficulties for the Monte-Carlo (MC) implementation of processes, as the KLN-cancellation happens among integrated phase spaces of different parton multiplicities. In fact, this numerical issue has been subject of continuous research over past decades [36]. The by-now standard “algorithm” to keep track and deal with IR divergencies in a MC setting is the Catani-Seymour dipole formalism [37], which is explained in sec. 2.2.2 in more detail.

Hadronic jet cross sections in the parton model [38] are given by

$$\sigma^{\text{had}}(p(k_1)p(k_2) \rightarrow \tilde{X}) = \sum_{a,b} \int \int_0^1 dx_a dx_b f_{a/P}(x_a) f_{b/P}(x_b) \sigma(a(x_a k_1) b(x_b k_2) \rightarrow X) \Theta(\mathcal{C}(\tilde{X})) \mathcal{F}(X, \tilde{X}) \quad (2.28)$$

[¶]This kind of extension implicitly assumes that no other low-energy degrees of freedom exist beyond the SM. There are examples in the literature, where this assumption does not apply. In these models the SM-sector is coupled to another (SM-like) sector at very high scales, leaving a “hidden valley” of low-energy degrees of freedom. These states can have significant phenomenological impact [31].

**In principle these singularities are already present at the leading order level, depending on the process. A familiar example is the t -channel photon singularity in Rutherford scattering in Electrodynamics. The leading order IR singularities are effectively cut away by applying finite experimental detection bounds, but can also be consistently resummed into Sudakov factors [1].

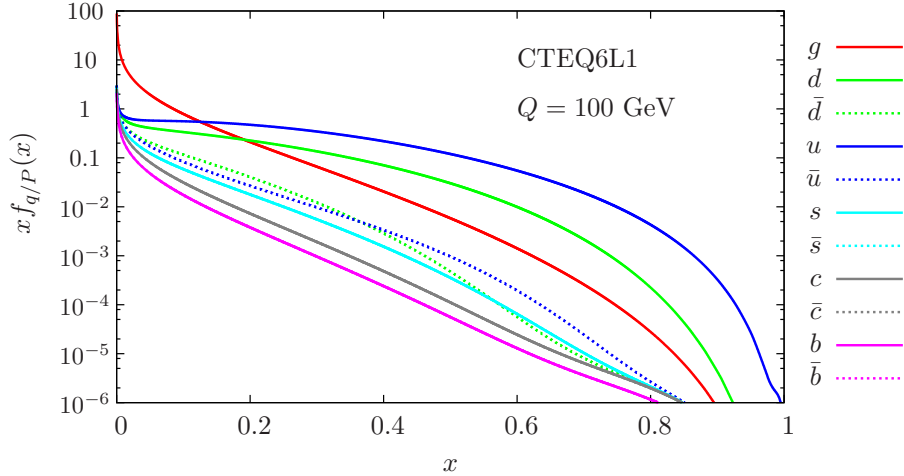


Figure 2.1: Parton distribution functions CTEQ6L1 [39] used for leading order cross section calculations in this thesis. Shown are distributions with factorization scale $Q = 241$ GeV. The anti-quark and quark distributions of the non-valence flavors of the proton lie on top of each other. At the Tevatron, quark- and anti-quark distribution get interchanged for the anti-proton beam.

where $f_{a/p}$, the parton distribution function (pdf) of parton a , denotes the probability of finding a parton a with momentum fraction x_a inside the proton p with momentum k_1 (fig. 2.1). In (2.28) $\Theta(\mathcal{C})$ summarizes the processes' selection criteria (“cuts”) we wish or need to impose. \mathcal{F} is a function, that determines how the partons of the final state X with momenta $p_f^{(j)}$ are combined to a final state jet observable \tilde{X} in an IR-safe fashion:

$$\mathcal{F}\left(p_f^{(1)}, \dots, p_f^{(i-1)}, p_f^{(i)}, p_f^{(i+1)}, \dots\right) \longrightarrow \mathcal{F}\left(p_f^{(1)}, \dots, p_f^{(i-1)}, p_f^{(i+1)}, \dots\right) \\ \text{if } p_f^{(i)} \cdot p_f^{(j)} \rightarrow 0 \text{ for all } j \text{ with } i \text{ fixed but arbitrary,} \quad (2.29)$$

i.e. the jet-definition is not sensitive to collinear or soft radiation. The partonic cross sections are determined by the QFT we want to analyze. Requiring “occurrence of scattering” by factorizing out identical initial and final states of the QFT’s S -matrix,

$$(2\pi)^4 \delta(p_i - p_f) T = \mathbb{1} - S, \quad (2.30)$$

where p_i, p_f denote the sum of initial and final state momenta, respectively, the partonic cross section is proportional to the phase space-integrated squared modulus of the T matrix elements

$$\sigma(a(x_a k_1) b(x_b k_2) \rightarrow X) = \frac{1}{\Phi} \int d\text{LIPS}(X) |\langle a(x_a k_1) b(x_b k_2) | T | X \rangle|^2. \quad (2.31)$$

In the above equation Φ denotes the flux-factor, which is a homogeneous function of first degree for massless initial state momenta,

$$\Phi(\eta p_a \cdot p_b) = \eta \Phi(p_a \cdot p_b) = \eta [4\sqrt{p_a \cdot p_b}], \quad (2.32)$$

whith $p_{a,b} = x_{a,b}k_{1,2}$. In perturbation theory, the matrix elements of the T operator have the well-know diagrammatic representation in terms of Feynman graphs.

Even if \tilde{X} denotes an IR-safe final state observable by construction (2.29), the initial state in (2.28) is fully determined which spoils the KNL-cancellations. The IR-singularities associated with initial state collinear radiation remain in (2.31), e.g. a photon can tell the difference between a quark and a collinear quark-gluon pair in deep inelastic scattering. Factorization of these singularities is universal [40], so that the collinear singularities can be absorbed into a process-independent renormalization of the pdfs at the price of introducing a relic and unphysical factorization scale in the partonic cross section and the pdfs. This scale, in physical factorization schemes, tells us the collinear mass scale, at which we define the pdfs in (2.28).

In principle, μ_F^2 is arbitrary and the hadronic cross section should not depend on a specific scale choice as we only dial finite contributions among two operands. In practice, however, we cannot calculate absolute values of the pdfs by perturbative means, but have to extract them from a single experiment via fits to fixed-order perturbative predictions. Thus, a residual dependence on μ_F remains. The dynamical evolution that results from integrating out collinear emissions by shifting about $d\mu_F$ are yet again governed by perturbation theory, yielding a special set of renormalization group equations [41] (RGEs), the integro-differential Dokshitzer-Gribov-Lipatov-Altarelli-Parisi (DGLAP) equations [42]. Solving this system to determine $f_{a/P}(x_a, \mu_F^2)$ for a given initial distribution $f_{a/P}(x_a, \mu_F^2)$ amounts to resummation of the leading logarithms $\alpha_s^n \log^n(\mu_F^2/\mu_F^2)$ to all orders of perturbation theory which arise from multiple strongly-ordered emissions in virtuality. These logarithms show up as part of the NLO calculation, and can be sizable if the factorization scale is considerably different from a processes' characteristic scale $\mu_F' = Q$ (if such a scale is to exist at all). In fact, the RGEs (see also sec. 2.2.4), rearrange the coefficients of the perturbative series expansion such that the μ_F dependence decreases by going to a higher order in perturbative theory as is further explained in sec. 2.2.4. Studying the influence of variations of μ_F (and μ_R , see below) on fixed-order cross sections is therefore commonly utilized to asses the cross sections' theoretical uncertainty from higher order corrections. This is yet to be taken caution as the RGE is only a statement of invariance, independent of kinematics and the process itself, so that one should consider the determined uncertainties as lower limits.

2.2.2 Soft and collinear singularities and dipole subtraction

A general loop integral in dimensional regularization, fig. 2.2, can be cast into a form

$$\mathcal{T}_n^{\mu_1 \dots \mu_m} = \frac{(2\pi\mu)^{4-d}}{i\pi^2} \int d^d k \frac{k^{\mu_1} \dots k^{\mu_m}}{d_1 d_2 \dots d_n} \quad \text{with } d_i = (q + k_i)^2 + i0 \quad (2.33)$$

for massless propagators. μ denotes the so-called 't Hooft mass, which introduces an arbitrary mass scale to engineer the canonical scaling dimension of the integral and the gauge coupling. The classification of singularities of infrared origin ("mass singularities") is due to Kinoshita [35] (see also [43, 44]):

- *Soft singularities* arise from a massless particle-exchange between two on-shell particles, fig. 2.3 (a). The logarithmic singularity results from the soft momentum

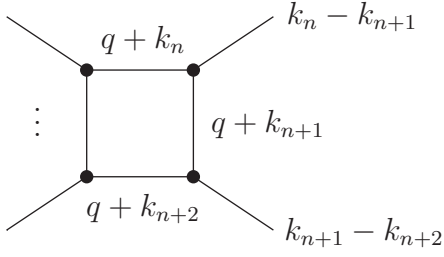


Figure 2.2: Generic one-loop Feynman diagram. The external lines are on-shell, i.e. $(k_{j+1} - k_j)^2 = m_j^2 \equiv 0$.

in the massless propagator, i.e.

$$q \rightarrow -k_n \quad \Longrightarrow \quad d_n \rightarrow 0 \quad (2.34)$$

in fig. 2.2. The momentum transfer of the propagator tends to zero according to (2.33).

- *Collinear mass singularities* arise when a massless on-shell particle is attached to two massless propagators, fig. 2.3 (b). The logarithmic singularity results from the propagators' loop momentum becoming collinear to the external particle, i.e.

$$q \rightarrow -k_{n+1} + x_n(k_n - k_{n+1}) \quad \Longrightarrow \quad d_n \rightarrow (1 + x_n)^2(k_n - k_{n+1})^2 = 0. \quad (2.35)$$

As already mentioned in the beginning of this section, the cancellation of the divergencies against contributions from soft and collinear radiation, respectively [33, 35] is deeply buried in the concept of unitary QFTs. A heuristic argument can be derived from noting that a different Cutkosky-cut [45] applied to a squared real emission graph corresponds to a one-loop interference diagram, so that unitarity relates these two contributions.

2.2.3 Dipole subtraction

The Catani-Seymour dipole subtraction [37] is a method that introduces bookkeeping of IR singularities to one-loop QCD calculations in a process-independent and systematic manner. Therefore, keeping track of the cancellations described in the above section heavily simplifies. In a nutshell, the divergent piece, which is due to factorization proportional to the Born-level matrix element, is subtracted from and re-added to the NLO cross section in dimensional regularization $d = 4 - 2\varepsilon$,

$$\sigma_m^{\text{NLO}} = \sigma_m^{\text{B}} + [\sigma_m^{\text{V}} + \sigma_{m+1}^{\text{A}}] + [\sigma_{m+1}^{\text{R}} - \sigma_{m+1}^{\text{A}}] + \sigma_m^{\text{C}}. \quad (2.36)$$

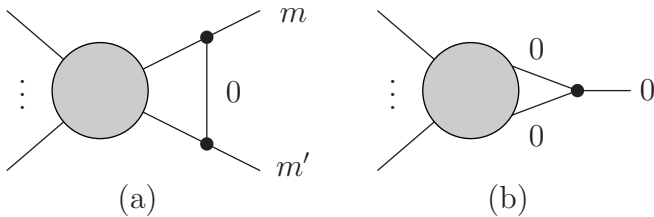


Figure 2.3: Feynman graph topologies that give rise to soft singularities (a), and collinear divergencies (b) at the one loop level.

At the one-loop level the divergencies show up as isolated poles proportional to ε^{-2} and ε^{-1} in the amplitudes' Laurent series expansion (see also sec. 2.2.4). m denotes in (2.36) and in the following the number of partons of the leading order expansion. σ_m^C is the collinear counter terms that renormalize the pdfs in the $\overline{\text{MS}}$ subtraction scheme at one-loop:

$$\begin{aligned} d\sigma_{ab}^C(p_a, p_b; \mu_F^2) &= -\frac{\alpha_s}{2\pi} \frac{1}{\Gamma(1-\varepsilon)} \sum_{cd} \int_0^1 \int_0^1 dz_a dz_b d\sigma_{cd}^B(z_a p_a, z_b p_b) \\ &\quad \times \left\{ \delta_{bd} \delta(1-z_b) \left[-\frac{1}{\varepsilon} \left(\frac{4\pi\mu^2}{\mu_F^2} \right)^\varepsilon P^{ac}(z_a) \right] \right. \\ &\quad \left. + \delta_{ac} \delta(1-z_a) \left[-\frac{1}{\varepsilon} \left(\frac{4\pi\mu^2}{\mu_F^2} \right)^\varepsilon P^{bd}(z_b) \right] \right\}, \quad (2.37) \end{aligned}$$

with P^{ab} the Altarelli-Parisi probabilities for collinear parton splittings $a(p_a) \rightarrow b(z_a p_a)$.

σ^A can be fully constructed on the real-emission phase space from color dipoles, i.e. from a pair of soft or collinear partons (the *emitter*) that recoils against a third parton (the *spectator*). Schematically, the subtraction terms can be written as

$$\int_{m+1} d\sigma^A = \int_{m+1} \left(\sum_{\text{dipoles}} d\sigma^B \otimes dV_{\text{dipole}} \right), \quad (2.38)$$

where the dipoles will involve different Born-level kinematics and phase space factors, indicated in (2.38). Having subtracted the divergent piece from the last bracket of (2.36), the entire cancellation takes place among σ_{m+1}^A and σ_m^V . With the appropriate choice of dipoles given in [37], σ_{m+1}^A can be integrated analytically over a one-parton phase space, so that

$$\int_{m+1} d\sigma^A + \int_m \sigma_m^C = \int_m [d\sigma^B \otimes \mathbf{I}] + \int_0^1 dx \int_m [d\sigma^B \otimes (\mathbf{P}(x, \mu_F^2) + \mathbf{K}(x))]. \quad (2.39)$$

The \mathbf{I} operator contains all singular poles multiplying the Born-level matrix element, and the operators $\mathbf{P} + \mathbf{K}$ gives rise to a finite collinear remainder. The IR poles can be cancelled against the poles from the virtual one-loop contribution, yielding a NLO cross section with, in the limit $\varepsilon \rightarrow 0$, separately finite integrals over the m and $m+1$ parton configurations by construction. Hence,

$$\begin{aligned} \sigma^{\text{NLO}} &= \sigma^B + \int_{m+1} \left[(d\sigma^R)_{\varepsilon=0} - \left(\sum_{\text{dipoles}} d\sigma^B \otimes dV_{\text{dipole}} \right)_{\varepsilon=0} \right] \\ &\quad + \int_m [d\sigma^V + d\sigma^B \otimes \mathbf{I}]_{\varepsilon=0} + \int_0^1 dx \int_m [d\sigma^B \otimes (\mathbf{P}(x, \mu_F^2) + \mathbf{K}(x))] \end{aligned} \quad (2.40)$$

can be integrated by means of Monte Carlo methods (see sec. 2.2.5).

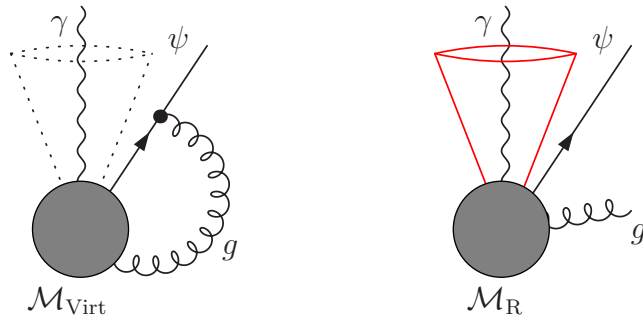


Figure 2.4: A naive photon isolation criterion limits the phase space of the soft gluon and hence spoils the KLN-cancellation.

Photon isolation

Considering no decay of the photon introduces further subtleties. A collinear photon-quark configuration gives rise to a QED-final state singularity, which is mended by including non-perturbative jet fragmentation functions. In order to avoid this additional source of theoretical uncertainty, one is tempted to introduce an isolation criterion such as a minimum separation of any parton (or jet) from the photon in the pseudorapidity–azimuthal angle–plane (cf. sec. 2.2.6),

$$R_{j\gamma} = \sqrt{[\Delta\phi(j\gamma)]^2 + [\Delta\eta(j\gamma)]^2} \geq R_{\min} = \text{const.} \quad (2.41)$$

This clearly removes any dependence on fragmentation, but limits also the phase space of soft gluon radiation at NLO QCD: In fig. 2.4 the quark emission is outside a cone around the photon of size δ_0 . Yet, the soft-gluon-emission that cancels the IR singularity of the virtual correction to this configuration is required to be integrated over the full solid angle around the quark. Expelling the soft gluon from the cone around the photon thus spoils the cancellation of IR divergencies.

To maintain the IR safety while minimizing the contribution of fragmentation, we have to allow soft radiation inside the photon cone, while vetoing collinear configurations to largest extend. Already in [12], but in more detail described in [46], an all-order IR-safe prescription was spelled out: soft QCD emission into the photon isolation cone is allowed, if

$$\sum_{i, R_{i\gamma} < R} p_T^{\text{parton}, i} \leq \Xi(\mathcal{E}, R) = \frac{1 - \cos R}{1 - \cos \delta_0} \mathcal{E} \quad \forall R \leq \delta_0, \quad (2.42a)$$

where the index i runs over all partons, found in a cone around the photon of size R . The QCD-IR-safe cone size around the photon is given by δ_0 , and \mathcal{E} denotes an energy scale of the event, which determines the penetrability of the photon cone by parton radiation. The precise form of (2.42a) is motivated from the soft phase space integral over the photon cone; IR-safety, however, leaves no restrictions on Ξ but

$$\lim_{R \rightarrow 0} \Xi(\mathcal{E}, R) = 0, \quad (2.42b)$$

i.e. collinear emission has to become increasingly soft to vanishing when approaching the photon in the azimuthal-angle–pseudorapidity plane. For the purpose of this thesis we use the functional form of (2.42a). (2.42b) obviously allows a broad range different isolation schemes, which determine experimentally distinct observables. Fixing the photon isolation according to (2.42a), we analyze the systematic effect of different choices of the event's \mathcal{E} in sec. 4.3.

2.2.4 Virtual corrections

We write the virtual amplitude in d dimensions

$$\mathcal{M}_d = \mathcal{M}_B + \mathcal{M}_d^{\text{1loop}}. \quad (2.43)$$

The UV divergencies can be consistently absorbed into redefinitions of the classical Lagrangian's parameters by adding UV counter terms when dealing with renormalizable field theories [14]. Schematically, the unrenormalized one loop contribution can be expressed as

$$\mathcal{M}_d^{\text{1loop}} = \sum_{i(k)} \mathcal{D}_i \otimes \mathcal{T}_i \quad (2.44)$$

where $\mathcal{T}_i, \mathcal{D}_i$ stand for the tensorial Lorentz- and Dirac algebra parts of the amplitude, that follow from summing the k contributing one-loop Feynman diagrams in d dimensions and subsequent algebraic manipulations. The tensor integrals can be reduced to a basis of scalar integrals by standard methods [47, 48].

Eventually, we are interested in the limit $d \rightarrow 4$; we thus split up

$$\mathcal{M}_d^{\text{1loop}} = \sum_{i(k)} (\mathcal{D}_i^4 \oplus \mathcal{D}_i^{d-4}) \otimes (\mathcal{T}_i^{\text{UV,div}} \oplus \mathcal{T}_i^{\text{IR,div}} \oplus \tilde{\mathcal{T}}_i). \quad (2.45)$$

Here \mathcal{D}_i^4 denotes the four-dimensional part of the \mathcal{D}_i and $\tilde{\mathcal{T}}_i$ is the finite parts of the tensor integrals in the limit $d \rightarrow 4$. Note that, due to specific form of Dirac algebra in d dimensions, the leading contribution of \mathcal{D}_i^{d-4} is $\mathcal{O}(d-4)$. The specific representation of $\mathcal{T}^{\text{UV,div}}$, and $\mathcal{T}^{\text{IR,div}}$, of which the latter can be solely deconstructed to triangle coefficients, have been given in the literature [43, 49, 50]. Expanding (2.44) yields

$$\mathcal{M}_d^{\text{1loop}} = \sum_{i(k)} \left\{ \underbrace{(\mathcal{D}_i^4 \otimes \tilde{\mathcal{T}}_i)}_{\text{(I)}} \oplus \underbrace{(\mathcal{D}_i^{d-4} \otimes \tilde{\mathcal{T}}_i)}_{\text{(II)}} \oplus \underbrace{(\mathcal{D}_i^4 \otimes \mathcal{T}_i^{\text{IR,div}})}_{\text{(III)}} \right. \\ \left. \oplus \underbrace{(\mathcal{D}_i^4 \otimes \mathcal{T}_i^{\text{UV,div}})}_{\text{(IV)}} \oplus \underbrace{(\mathcal{D}_i^{d-4} \otimes \mathcal{T}_i^{\text{IR,div}})}_{\text{(V)}} \oplus \underbrace{(\mathcal{D}_i^{d-4} \otimes \mathcal{T}_i^{\text{UV,div}})}_{\text{(VI)}} \right\}. \quad (2.46)$$

The contributions (V) and (VI) give rise to so-called rational terms, i.e. finite contributions from the interplay of numerator and denominator algebra for $d \rightarrow 4$. The UV pole structure of the tensor coefficient, which is vanishing for pentagon graphs and

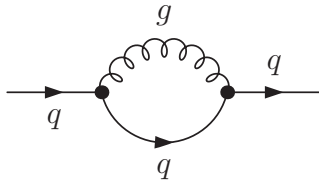


Figure 2.5: Quark self-energy correction at $\mathcal{O}(\alpha_s)$ contributing to the quark renormalization.

beyond, is largely independent of the masses that appear as arguments of the coefficients. All rational terms of UV origin can be deduced from a small set of pole residues given in [49]. This is not the case for rational terms that arise from the non-universal IR singularities, which consequently caused the bulk of the algebra in performing the one-loop calculation. Yet, only very recently, it is shown in [44], that the entire unrenormalized amplitude is manifestly free of rational terms of IR-origin, even though they might arise in intermediate steps of the calculation. This allowed the authors of [44] to prepare a general roadmap to construct the rational terms of one-loop QCD amplitudes on a graph-by-graph basis, by omitting all IR-rational terms *a priori*. Meanwhile, the absence of (V) in the unrenormalized one-loop amplitude gives a strong algebraic check of the consistency of the performed algebra.

LSZ, renormalization and renormalization constants

In the context of QFTs, the two-point correlation function can be written in terms of a spectral density function, which is determined by the underlying theory. For a fermion field ψ with mass λ , we have

$$\langle \Omega | \mathcal{T} \bar{\psi}(x) \psi(0) | \Omega \rangle = \int_0^\infty dm^2 \rho(m^2) D_F(x, m^2), \quad (2.47)$$

with

$$\rho(m^2) = \delta(m^2 - m_\lambda^2) |\langle \Omega | \psi(0) | \lambda \rangle|^2 + \text{multi-particle states} \quad (2.48)$$

and the usual Feynman propagator D_F . Eq. (2.47) has become renowned as Källén-Lehmann representation [51], which contains the field strength renormalization $Z_\psi = |\langle \Omega | \psi(0) | i \rangle|^2$, i.e. the probability to pull a fermionic one-particle state λ off the (interacting) vacuum. The renormalization constants can be written as perturbative expansion and are needed to extract the S matrix elements from the joint pole residues of the connected, amputated QFT's Green's functions according to the Lehmann-Symanzik-Zimmermann (LSZ) reduction [52].

The field strength renormalization changes the pole residue of the particles' propagators (2.47). This can be rectified by field redefinitions in the classical Lagrangian^{††},

^{††}In (2.49) we limit ourselves to the relevant relevant renormalization constants for the purpose of this thesis.

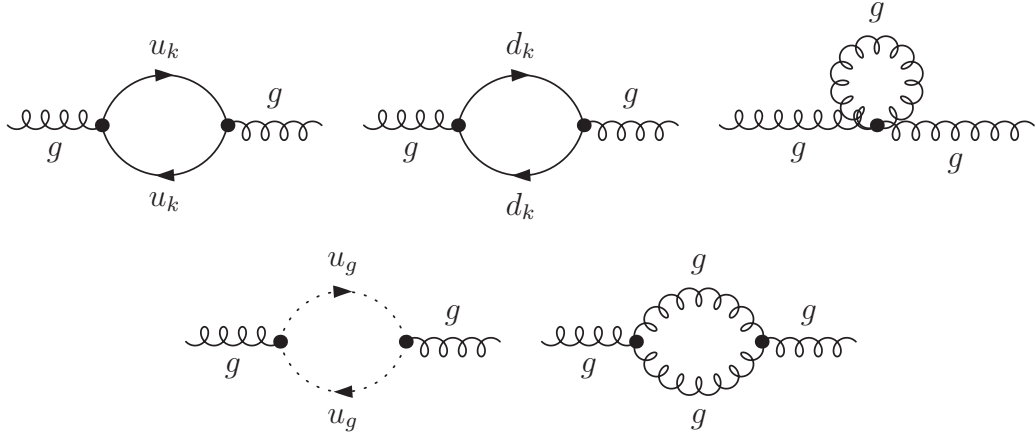


Figure 2.6: Gluon self-energy at $\mathcal{O}(\alpha_s)$ contributing to the gluon renormalization. k denotes the generation index, e.g. $d_k = (d, s, b)$.

$$\psi^0 = \sqrt{Z_\psi} \psi^r, \quad A_\mu^0 = \sqrt{Z_A} A_\mu^r, \quad g_s^0 = \frac{Z_1}{Z_\psi \sqrt{Z_A}} g_s^r \equiv Z_{g_s} g_s^r, \quad (2.49)$$

which yield propagator residues of one, i.e. we apply on-shell renormalization. The “bare” (non-interacting) fields in (2.49) denoted by the zero-exponent are altered with respect to the renormalized quantities by quantum corrections. Gauge invariance, constructed at the *classical* level in sec. 2.1.1 translates into relations among amplitudes with different external particle multiplicity and relations among the renormalization constants in the quantized theory (sec. 3.3.5). Thereby, gauge invariance is the key ingredient to maintain perturbative unitarity in the interacting theory.

From (2.49) we can construct the QCD-counter term Lagrangian by introducing additional interactions, which result from writing

$$Z_\psi = 1 + \delta_\psi, \quad Z_A = 1 + \delta_A, \quad Z_1 = 1 + \delta_1, \quad (2.50)$$

so that

$$g_s^0 = (1 + \delta_{g_s}) g_s^r = (1 + \delta_1 - \delta_\psi - \frac{1}{2}\delta_A) g_s^r. \quad (2.51)$$

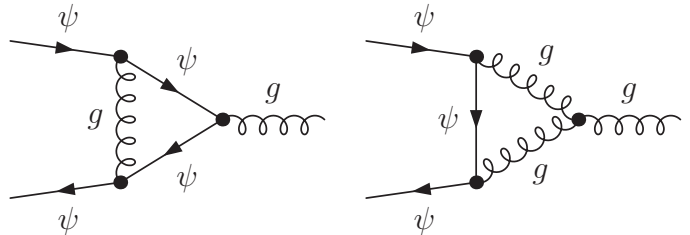


Figure 2.7: Vertex correction at $\mathcal{O}(\alpha_s)$, giving rise to the renormalization constant δ_1 .

The Feynman rules that follow from (2.49), (2.50) are

$$\begin{array}{c} \text{wavy line} \\ g_\mu^a \end{array} \begin{array}{c} \text{cross} \\ \times \end{array} \begin{array}{c} \text{arrow} \\ \bar{q}_i \\ \text{arrow} \\ q_j \end{array} = i\delta_1 t_{ij}^a \gamma^\mu, \quad (2.52)$$

$$\begin{array}{c} \text{wavy line} \\ g_\mu^a(k) \end{array} \begin{array}{c} \text{cross} \\ \times \end{array} \begin{array}{c} \text{wavy line} \\ g_\nu^b(k) \end{array} = i\delta_A(k^2 g_{\mu\nu} - k^\mu k^\nu) \delta^{ab}, \quad \begin{array}{c} \text{arrow} \\ f_i(k) \end{array} \begin{array}{c} \text{cross} \\ \times \end{array} \begin{array}{c} \text{arrow} \\ f_j(k) \end{array} = i\delta^{ij} \delta_\psi \not{k}.$$

The renormalization constants in dimensional regularization $d = 4 - 2\varepsilon$ can be derived from the one loop correction to the propagators in figs. 2.5, 2.6,

$$\tilde{\Sigma}(\not{p}) = \not{p} \Sigma(p^2), \quad (2.53a)$$

$$\Pi^{\mu\nu}(p^2) = \left(g^{\mu\nu} - \frac{p^\mu p^\nu}{p^2} \right) \Pi(p^2), \quad (2.53b)$$

with vacuum polarization functions (cf. (2.33))

$$\Sigma(p^2) = \frac{\alpha_s}{4\pi} (1 - \varepsilon) C_F B_0(p^2, 0, 0), \quad (2.54a)$$

$$\Pi(p^2)^{m=0} = \frac{\alpha_s}{4\pi} \left(\frac{4N_F T_r}{3} - \frac{5C_A}{3} + \mathcal{O}(\varepsilon) \right) p^2 B_0(p^2, 0, 0), \quad (2.54b)$$

where $C_A = t_{\text{adj}}^a t_{\text{adj}}^a$ is the Casimir of the Lie algebras adjoint representation, $C_F = t^a t^a$ is the Casimir of the fundamental representation with Dynkin index T_r , under which the N_F massless fermions transform. $B_0(p^2, 0, 0)$ denotes the massless scalar two-point function

$$B_0(p^2, 0, 0) = \frac{(2\pi\mu)^{2\varepsilon}}{i\pi^2} \int d^{4-2\varepsilon} k \frac{1}{k^2(k-p)^2} = \left(\frac{4\pi\mu^2}{-p^2} \right)^\varepsilon \Gamma(1 + \varepsilon) \left(\frac{1}{\varepsilon} + 2 \right). \quad (2.55)$$

with the $+i0$ propagator prescription understood. The contribution to the gluon self-energy from the massive top quark is

$$\begin{aligned} \Pi(p^2)^{m_t} = \frac{\alpha_s}{3\pi} T_r \left[2m_t^2 (B_0(p^2, m_t^2, m_t^2) - B_0(0, m_t^2, m_t^2)) \right. \\ \left. + p^2 B_0(p^2, m_t^2, m_t^2) - 2m_t^2 + \mathcal{O}(\varepsilon^0) \right]. \end{aligned} \quad (2.56)$$

We are only interested in renormalization, so that the additional terms $\mathcal{O}(\varepsilon)$ in (2.54) and $\mathcal{O}(\varepsilon^0)$ can be neglected. In the limit $m_t \rightarrow 0$ we recover the contribution of a single massless flavor in (2.54b).

To write down the on-shell counter terms and field strength renormalization constants we have to approach $m^2 \rightarrow 0$ in (2.54b), which amounts to a scale-less loop integral. From the axioms of d -dimensional integration [53], such integrals vanish identically. Upon expanding the right-hand side of (2.55) in ε , we encounter a logarithmic

singularity for $p^2 \rightarrow 0$, which is exactly the collinear mass singularity of sec. 2.2.2. This limit becomes apparent on the right-hand side of (2.55) by analytical continuation^{‡‡} $d > 4, \varepsilon < 0$:

$$\begin{aligned} 0 &= \lim_{p^2 \rightarrow 0} \left[\left(\frac{-p^2}{4\pi\mu^2} \right)^{|\varepsilon|} \right] \Gamma(1 - |\varepsilon|) \left(-\frac{1}{|\varepsilon|} + 2 \right) \\ &= \lim_{p^2 \rightarrow 0} \left[-\frac{\Gamma(1 - |\varepsilon|)}{|\varepsilon|} + \left(2 + \log \left(\frac{4\pi\mu^2}{-p^2} \right) \right) + \mathcal{O}(|\varepsilon|) \right]. \end{aligned} \quad (2.57)$$

We can use analyticity in d of (2.55) to perform $\varepsilon \rightarrow 0$ uniformly. Thus, the finite part of the massless two-point function exactly reproduces the ε -pole for $p^2 \rightarrow 0$. In fact, this requires the identification of ultraviolet and single infrared poles,

$$B_0(0, 0, 0) = \bar{\mathcal{S}}^{\text{UV}}(\tilde{\mu}) - \bar{\mathcal{S}}^{\text{IR},1}(\tilde{\mu}) = 0, \quad (2.58)$$

with the definition of the $\varepsilon \rightarrow 0$ singular factors

$$\bar{\mathcal{S}}^{\text{UV}}(\tilde{\mu}) = \bar{\mathcal{S}}^{\text{IR},1}(\tilde{\mu}) = \left(\frac{4\pi\mu^2}{\tilde{\mu}^2} \right)^\varepsilon \frac{\Gamma(1 + \varepsilon)}{\varepsilon} \quad (2.59)$$

and $\tilde{\mu}$ an arbitrary reference scale. Using on-shell renormalization for quarks and gluons, the counter term coefficients can be read off (2.54). The transversality of the gluon propagator is articulated differently in the self-energy (2.54b) and the counter term (2.52). The renormalization condition for the propagator-pole residue to be equal to one, is therefore

$$\begin{aligned} \delta_A^{m_t} &= -\frac{\partial \Pi(p^2)}{\partial p^2} \Big|_{p^2=0} = -\frac{\alpha_s}{3\pi} T_r \left[2m_t^2 \frac{\partial B_0(p^2, m_t^2, m_t^2)}{\partial p^2} \Big|_{p^2=0} + B_0(0, m_t^2, m_t^2) + \mathcal{O}(\varepsilon^0) \right] \\ &= -\frac{\alpha_s}{3\pi} T_r \left(\frac{4\pi\mu^2}{m_t^2} \right)^\varepsilon \frac{\Gamma(1 + \varepsilon)}{\varepsilon} + \mathcal{O}(\varepsilon^0) \end{aligned} \quad (2.60)$$

for the massive top quark, from which also follows $\delta_A^{m=0} \sim B_0(0, 0, 0)$ (the derivative of the B function contains no poles in ε). We summarize the quark- and gluon renormalization constants (cf. [55]):

$$\begin{aligned} \delta_\psi &= -\frac{\alpha_s}{4\pi} C_F (\bar{\mathcal{S}}^{\text{UV}}(\tilde{\mu}) - \bar{\mathcal{S}}^{\text{IR},1}(\tilde{\mu})) , \\ \delta_A &= -\frac{\alpha_s}{4\pi} \left[\left(\frac{4N_f T_r}{3} - \frac{5C_A}{3} \right) (\bar{\mathcal{S}}^{\text{UV}}(\tilde{\mu}) - \bar{\mathcal{S}}^{\text{IR},1}(\tilde{\mu})) + \frac{4T_r}{3} \bar{\mathcal{S}}^{\text{UV}}(m_t) \right], \end{aligned} \quad (2.61)$$

The complete vertex correction fig. 2.7 yields a more involved expression. Its UV-divergent part, however, simplifies considerably,

$$\Gamma^\mu = \frac{\alpha_s}{4\pi} (C_F + C_A) \bar{\mathcal{S}}^{\text{UV}}(\tilde{\mu}) \gamma^\mu + \mathcal{O}(\varepsilon_{\text{UV}}^0), \quad (2.62)$$

^{‡‡}Obviously there is no way to give d -dimensional integration a meaning in terms of a (Lebesgue) measure. The d -dimensional integration operator has to be understood as linear, *analytic* functional, that coincides with the usual notion of integration for $d \in \mathbb{N}$ [54].

so that the strong coupling renormalization in the $\overline{\text{MS}}$ scheme reads (see also e.g. [56])

$$\delta_{g_s} = \frac{\alpha_s}{4\pi} \left[\left(\frac{2N_f T_r}{3} - \frac{11C_A}{6} \right) \bar{\mathcal{S}}^{\text{UV}}(\mu_R) + \frac{2T_r}{3} \bar{\mathcal{S}}^{\text{UV}}(m_t) \right]. \quad (2.63)$$

This counterterm amounts to a five-flavor running of the strong coupling, as can easily be seen from the RGE for the strong coupling (2.49),

$$\beta(g_s) = \lim_{\varepsilon \rightarrow 0} \frac{\partial g_s}{\partial \log \mu_R} = \lim_{\varepsilon \rightarrow 0} g_s \frac{\partial \log Z_{g_s}}{\partial \log \mu_R} = \lim_{\varepsilon \rightarrow 0} g_s \frac{\partial \delta_{g_s}}{\partial \log \mu_R}, \quad (2.64)$$

i.e. the top-quark contribution is subtracted from the vertex correction at zero momentum transfer [55]. The dependence on μ_R is of type $(\mu^2/\mu_R^2)^\varepsilon$ so that only the coefficient of the UV pole of the first part of (2.63) contributes,

$$\beta(g_s) = -\frac{g_s^3}{16\pi^2} \left(\frac{11C_A}{3} - \frac{4N_f T_r}{3} \right) = -\frac{g_s^3}{16\pi^2} \beta_0, \quad (2.65)$$

where $N_F = 5$ is the number of massless flavors: The top quark has been entirely absorbed into the renormalization constants.

Eq. (2.65) is the one-loop approximation of the famous β function of QCD [57],

$$\beta(g_s) = -\frac{g_s^3}{16\pi^2} \beta_0 - \frac{g_s^5}{(16\pi^2)^2} \beta_1 - \frac{g_s^7}{(16\pi^2)^3} \beta_3 + \dots, \quad (2.66)$$

which guarantees asymptotic freedom for $N_f < 16$. Solving (2.65) for $\alpha_s = g_s^2/4\pi$,

$$\alpha_s(Q^2) = \frac{4\pi \alpha_s(\mu_R)}{4\pi + \alpha_s(\mu_R) \beta_0 \log(Q^2/\mu_R^2)}, \quad (2.67)$$

amounts to resumming the leading logarithms $\log^n(Q^2/\mu_R^2)$ to all orders of perturbation theory, where Q is a characteristic energy scale of the process. The running coupling (2.67) along with the scale dependence of the pdfs can be used for *renormalization-group improved* calculations by choosing an appropriate (dynamical) renormalization scale Q for the process under consideration, so that the dominating corrections from large logarithms get absorbed into α_s and the pdfs.

Clearly, the renormalization point μ_R is arbitrary, and technically only needed to separate-off the UV degrees of freedom in (2.63), while the bare quantities remain unaffected. This leads to renormalization group equations such as (2.64), which provide the scaling prescription of the renormalized quantities to keep the bare quantities fixed, i.e. the RGE express the independence of physical results of the renormalization scheme. The fact that renormalization constants are scale-dependent signals a conformal anomaly of QCD in the chiral limit: Massless QCD exhibits no mass scale at the classical level and is conformally invariant. At the loop level, however, a characteristic scale is introduced e.g. the scale of the Landau-pole of (2.67)

$$\Lambda_{\text{QCD}}^{\overline{\text{MS}},0} = \mu_R \exp \left[-\frac{2\pi}{\beta_0 \alpha_s(\mu_R)} \right], \quad (2.68)$$

so that

$$\alpha_s(Q^2) = \frac{4\pi}{\beta_0 \log(Q^2/[\Lambda_{\text{QCD}}^{\overline{\text{MS}},0}]^2)} \quad (2.69)$$

at one-loop, and

$$\alpha_s(Q^2) = \frac{4\pi}{\beta_0 \log(Q^2/[\Lambda_{\text{QCD}}^{\overline{\text{MS}},1}]^2)} \left(1 - \frac{2\beta_1}{\beta_0} \frac{\log \left[\log(Q^2/[\Lambda_{\text{QCD}}^{\overline{\text{MS}},1}]^2) \right]}{\log(Q^2/[\Lambda_{\text{QCD}}^{\overline{\text{MS}},1}]^2)} \right) \quad (2.70)$$

at two-loop, with the two-loop coefficient [58] in (2.66)

$$\beta_1 = \frac{34}{3}C_A^2 - \frac{20}{3}C_A N_F T_r - 4C_F N_F T_r, \quad (2.71)$$

and

$$\Lambda_{\text{QCD}}^{\overline{\text{MS}},1} = \mu_F \left(\frac{\beta_0^2}{\beta_1} \right)^{-\frac{\beta_1}{2\beta_0^2}} \exp \left[\frac{-8\pi^2}{\beta_0 g_s^2(\mu_R)} - \frac{\beta_1}{2\beta_0^2} \log \frac{\beta_1 g_s^2(\mu_R)}{16\pi^2 \beta_0 + \beta_1 g_s^2(\mu_R)} \right]. \quad (2.72)$$

Moreover, operators depart from their canonical scaling dimension by additional anomalous dimensions which result from the scale dependent normalization. This is spelled out in the Callen-Symanzik equation [59].

The μ_R dependence cancels between the renormalization constants and the renormalized quantities by construction. Yet, applying fixed-order perturbation theory renders the μ_R cancellation incomplete. In fact, the renormalization group equation at perturbative order $\mathcal{O}(\alpha_s^n)$, rearranges the coefficients of the perturbative series such that the μ_R -dependence drops out at $\mathcal{O}(\alpha_s^{n-1})$ with α_s probed at the characteristic scale Q . Therefore, one assumes that the dependence of physical cross sections and observables should decrease when going to higher orders in perturbation theory. This can be misleading, as the RGE contains no additional information on the process such as new channels opening up.

2.2.5 Event generation using Monte-Carlo methods

Multi-parton processes typically involve complicated analytical structures of matrix elements, so that closed analytical results of the involved high-dimensional phase space integration are either very tough to determine, or, in most of the cases, even do not exist. Furthermore, if selection criteria, that result from finite detector coverage and acceptance levels as well as from signal-over-background improvements, are taken into account, the phase space is limited to a domain, which is analytically hard to mod out from the integration in (2.28). One is forced to invoke numerical methods to perform the phase space integration. Due to the high dimensionality of the integration it is necessary to apply statistical Monte-Carlo methods [60], as straightforward numerical integration becomes too time-consuming. More precisely, the integration

$$\sigma = \int_V d^n x \mathcal{I}(x_1, x_2, \dots, x_n) = \int_V d^n x g(\vec{x}) \frac{\mathcal{I}(\vec{x})}{g(\vec{x})} = \mathbb{E}_g \left(\frac{\mathcal{I}}{g} \right) \quad (2.73)$$

where g is a probability density function, is done in a statistical manner. We can choose $0 \leq x_i \leq 1$ for all i by appropriate variable transformations in the integral, multiplying the according Jacobian determinant. The VEGAS algorithm [61] evaluates the integrand \mathcal{I} N times, and estimates the expectation value \mathbb{E} by the average of the evaluations,

$$\sigma_{\text{est}} = \frac{V}{N} \sum_{i=1}^N \frac{\mathcal{I}(\vec{x}_i)}{g(\vec{x}_i)}, \quad (2.74)$$

where the sample points \vec{x}_i are chosen according to the probability density g . The g -variance

$$\mathbb{V}_g(\sigma_{\text{est}}) = \mathbb{E}_g [(\sigma_{\text{est}} - \mathbb{E}_g(\sigma_{\text{est}}))^2] = \frac{V^2}{N} \mathbb{V}_g \left(\frac{\mathcal{I}}{g} \right), \quad (2.75)$$

where we make use of the statistical independence of the \vec{x}_i , gives an estimate of the error inherent to (2.74). Theoretically, the variance becomes minimal [61] for

$$g(\vec{x}) = \frac{|\mathcal{I}(\vec{x})|}{\int_V d^n x' |\mathcal{I}(\vec{x}')|}, \quad (2.76)$$

i.e. when we sample the integrand where the contributions are large. Therefore, VEGAS is a so-called *importance-sampling* algorithm. The estimates (2.74) are repeated in subsequent iterations, and the distribution g gets modified from iteration to iteration to minimize the variance (2.75). Technically this is done by splitting up the integration domain into a rectangular grid of hypercubes with an equal density of sample points \vec{x}_i . From iteration to iteration the grid is aligned such to concentrate more hypercubes (and thus more sample points) in regions with large relative $|\mathcal{I}|$. The FORTRAN subroutine set MONACO, which is modified version of VEGAS and part of the parton-level Monte-Carlo framework VBFNLO [11], was used for the purpose of this thesis.

2.2.6 Constructing the phase space

Applying the Monte Carlo integration techniques of the previous section to the calculation of integrated and differential cross sections, it is customary to parametrize the phase space integration in (2.31) in terms of observables which are directly related to the framework of detectors and experimentally measurable quantities. This is a somewhat standard method of collider phenomenology (see e.g. [62]), so that it is enough to only sketch our approach at this point.

Convenient choices of observables are, given a four-vector k^μ , transverse momentum,

$$p_T(k^\mu) = \sqrt{(k^1)^2 + (k^2)^2} \quad (2.77)$$

and rapidity

$$y(k^\mu) = \frac{1}{2} \log \frac{k^0 + k^3}{k^0 - k^3}, \quad (2.78)$$

which defines the pseudorapidity observable in the massless limit,

$$\eta(k^\mu) = \frac{1}{2} \log \frac{1 + \cos \theta}{1 - \cos \theta}, \quad (2.79)$$

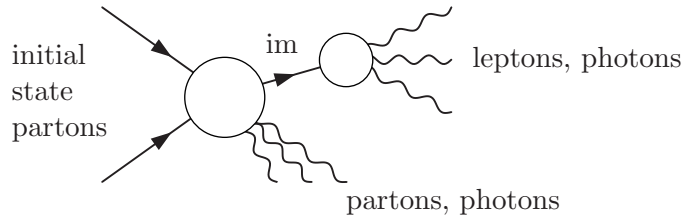


Figure 2.8: Schematic representation of the used phase space set-up, which is used for the purpose of this thesis. The intermediate massive pseudo-particle of the factorization (2.81) is denoted by “im”.

where θ is the polar angle. Note that we choose the beam axis to coincide with the z direction. This way the integration domain can efficiently be adjusted in signal-over-background-improving studies, by mapping the random numbers $x_j \in [0, 1]$, which are involved in the Monte Carlo integration to evaluate (2.73), onto the new domain. Constructing the four-momenta of the initial and final state particles from these observables, i.e. from the mapped random numbers, we can calculate different (final state) observables we would like or need to further constrain. If the phase space point agrees with the event selection criteria we impose, we subsequently evaluate the differential cross section (2.28) for this phase space point as part of the sum in eq. (2.74). The probability density g plays then the role of pointing out the “right” random numbers that translate into events via a one-to-one correspondence.

In this thesis we are interested in generating up to two partons and, depending on the process, four leptons or two leptons and a photon in the final state. The phase space in (2.31) reads

$$\begin{aligned} \text{dLIPS} \left(p_a + p_b; \sum_i p_f^{(i)} + \sum_j q_j \right) = \\ (2\pi)^4 \delta \left(p_a + p_b - \sum_i p_f^{(i)} - \sum_j q_j \right) \left(\prod_i \frac{d^3 p_f^{(i)}}{(2\pi)^3 2 E_i} \right) \left(\prod_j \frac{d^3 q_j}{(2\pi)^3 2 E_j} \right), \end{aligned} \quad (2.80)$$

where the q_j denote the momenta of all non-partons. By noting that this phase space can be factorized (see e.g. [63]),

$$\begin{aligned} \text{dLIPS} \left(p_a + p_b; \sum_i p_f^{(i)} + \sum_j q_j \right) \\ = \text{dLIPS} \left(p_a + p_b; \sum_i p_f^{(i)} + p_{\text{im}} \right) \frac{dp_{\text{im}}^2}{2\pi} \text{dLIPS} \left(p_{\text{im}}; \sum_j q_j \right), \end{aligned} \quad (2.81)$$

we can separate the parton integration from the generation of the lepton momenta, with an additional integration over the massive intermediate state pseudo-particle p_{im} . Exploiting the above factorization, we can also shuffle the photon between the two terms

on the right hand side of (2.81) to arrive at the typical phase space set-up used for the purpose of this thesis depicted in fig. 2.8. The final state partons (and the photon if shuffled to the parton integration) are generated from random variables mapped onto the allowed pseudorapidity and transverse momentum ranges, which, in the numerical program, are global parameters p_T^{cut} , y^{cut} and set by the user. With the available center-of-mass energy in the lab frame \sqrt{s} and the azimuthal angle ϕ , the final state parton momenta are generated by

$$(p_f^{(i)})^\mu = \begin{pmatrix} p_T^i \cosh y_i \\ p_T^i \cos \phi_i \\ p_T^i \sin \phi_i \\ p_T^i \sinh y_i \end{pmatrix} \quad (2.82)$$

with

$$p_T^i \in \left[p_T^{\text{cut}}, \frac{\sqrt{s}}{2} \right], \quad (2.83a)$$

$$\phi^i \in [0, 2\pi], \quad (2.83b)$$

$$y^i \in \left[-\text{Arcosh} \left(\frac{\sqrt{s}}{2p_T^i} \right), -y^{\text{cut}} \right) \cup \left(y^{\text{cut}}, \text{Arcosh} \left(\frac{\sqrt{s}}{2p_T^i} \right) \right]. \quad (2.83c)$$

Subsequently, we generate the the center-of-mass rapidity from the final state partons $p_\oplus = \sum_i p_f^{(i)}$ and p_{im}^2 in the lab frame,

$$y_{\text{CM}} \in [y_\oplus - \tilde{y}, y_\oplus + \tilde{y}], \quad (2.84)$$

where

$$\tilde{y} = \text{Arcosh} \left[\frac{s - (\sqrt{p_{\text{im}}^2} + \sqrt{p_\oplus^2})^2 - 4p_{\oplus,T}^2}{4[(p_\oplus^0)^2 - (p_\oplus^3)^2]} \right] \quad (2.85)$$

is determined analogously to (2.83c). We can then arrive at the center-of-mass four-momentum

$$p_{\text{cm}} = \begin{pmatrix} \sqrt{\hat{s}} \cosh y_{\text{CM}} \\ 0 \\ 0 \\ \sqrt{\hat{s}} \sinh y_{\text{CM}} \end{pmatrix}, \quad (2.86)$$

where $\sqrt{\hat{s}} = 4\sqrt{p_a \cdot p_b} = \Phi/2$ is the partonic center-of-mass energy, to determine the Feynman- x values,

$$x_{a,b} = \frac{p_{\text{cm}}^0 \pm p_{\text{cm}}^3}{\sqrt{s}/2} \quad (2.87)$$

and initial state momenta $p_{a,b} = x_{a,b} k_{1,2}$, cf. (2.28). The Jacobian factors that follow from the transformation of the random variables to the observables that eventually

determine the event are tabulated in the appendix of [63], so that we may skip over them and move on to the discussion of the remaining integration, which involves the decay of the intermediate pseudo-particle in 2.8. Here, including photons raises some subtleties. A photon can be radiated off from either a final state parton or a massive electroweak boson or lepton that both result from p_{im} . In the former case we can treat it as a parton from the phase space generation point of view. The latter case amounts to e.g. a three-body decay of the pseudo-particle in $W\gamma j$ production, i.e.

$$\text{dLIPS}(p_{\text{im}}; q_1 + q_2 + q_3) = \frac{1}{(2\pi)^5} \frac{1}{8\sqrt{p_{\text{im}}^2}} dq_1^0 dq_2^0 d\alpha d\cos\beta d\gamma \quad (2.88a)$$

$$= \frac{1}{(2\pi)^5} \frac{1}{32\sqrt{p_{\text{im}}^2}} dm_{12}^2 dm_{23}^2 d\alpha d\cos\beta d\gamma, \quad (2.88b)$$

with Euler angles

$$\alpha, \gamma \in [0, 2\pi], \quad \beta \in [0, \pi]. \quad (2.88c)$$

In second line we transform the two energies to the Dalitz variables $m_{ij}^2 = (q_i + q_j)^2$, which yields the standard form of the Dalitz plot [64], when integrated over the flat directions α, β, γ for the decay of a scalar particle. The construction of the the four-momenta q_i in both lines is straightforward [65] (see also [66]). From the Jacobian factor of e.g. (2.88a),

$$\text{dLIPS}(p_{\text{im}}; q_1 + q_2 + q_3) = \frac{1}{(2\pi)^3} \frac{x_1 p_{\text{im}}^2}{16} \prod_i^5 dx_i, \quad (2.89)$$

we can read off the corresponding phase space weight for eq.(2.73).

If we consider WZj production we first decay the pseudo-particle to Breit-Wigner W and Z distributions, using again (2.81). This two-body phase space is well-known from the literature (e.g. [21]),

$$\text{dLIPS}(p_{\text{im}}; \tilde{q}_1 + \tilde{q}_2) = \frac{1}{16\pi^2} \frac{|\mathbf{p}_{\text{im}}|}{p_{\text{im}}^2} d\phi d\cos\beta, \quad (2.90)$$

with $\phi \in [0, 2\pi]$ and $\beta \in [0, \pi]$. The construction of the four-momenta \tilde{q}_1, \tilde{q}_2 is clear from the spherical coordinates and energy-momentum conservation. Applying (2.90) again to \tilde{q}_1, \tilde{q}_2 ($p_{\text{im}} \rightarrow \tilde{q}_1$ and $p_{\text{im}} \rightarrow \tilde{q}_2$ in (2.90), respectively) yields the four decay leptons of the WZ cluster; all Jacobian factors can be inferred from [?].

While the integration over the broad pseudo-particle does not require additional transformations for the Monte Carlo integration, the Breit-Wigner propagators yield the largest differential cross sections in a very limited domain of the random variables. The integration over the pseudo-particle therefore provides the most dominant contributions for $p_{\text{im}}^2 \approx m_W^2$ or $p_{\text{im}}^2 \approx m_Z^2$, depending on the the process. This can be efficiently reflected in the numerical integration by a variable transformation called “tan-mapping”. Neglecting all non-resonant Feynman graphs, the integrated squared

amplitude is

$$\begin{aligned}
\int \frac{dp_{\text{im}}^2}{2\pi} |\mathcal{M}|^2 &= \int \frac{dp_{\text{im}}^2}{2\pi} \frac{1}{(p_{\text{im}}^2 - m_i^2)^2 + m_i^2 \Gamma_i^2} |\tilde{\mathcal{M}}|^2 \\
&\approx |\tilde{\mathcal{M}}|^2 \int \frac{dp_{\text{im}}^2}{2\pi} \frac{1}{(p_{\text{im}}^2 - m_i^2)^2 + m_i^2 \Gamma_i^2} \\
&= \frac{|\tilde{\mathcal{M}}|^2}{2\pi m_i \Gamma_i} \int_{-m_i/\Gamma_i}^{(s-m_i^2)/(m_i \Gamma_i)} \frac{dp_{\text{im}}}{1 + p_{\text{im}}^2} = \frac{|\tilde{\mathcal{M}}|^2}{2\pi m_i \Gamma_i} \int_a^b dp_{\text{im}}^2
\end{aligned} \tag{2.91a}$$

with

$$a = -\text{Arctan}\left(\frac{m_i}{\Gamma_i}\right), \quad b = \text{Arctan}\left(\frac{s - m_i^2}{m_i \Gamma_i}\right). \tag{2.91b}$$

The numerical integration becomes approximately flat (and efficient) in the cross section-dominating phase space region by the transformation

$$p_{\text{im}}^2 \longrightarrow \tan\left(\frac{p_{\text{im}}^2 - m_i^2}{m_i \Gamma_i}\right). \tag{2.91c}$$

Chapter 3

Elements of the calculation

3.1 Leading order contributions

The leading order contribution, at $\mathcal{O}(\alpha^3\alpha_s)$, to the processes $pp, p\bar{p} \rightarrow \ell^- \bar{\nu}_\ell \gamma j + X$ and $pp, p\bar{p} \rightarrow \ell^- \bar{\nu}_\ell \ell'^- \ell'^+ j + X$ yields the partonic subprocesses

$$q(p_a)\bar{Q}(p_b) \longrightarrow \ell^-(q_1)\bar{\nu}_\ell(q_2)\gamma(q_3)g(p_1) \quad (3.1a)$$

$$\bar{Q}(p_a)g(p_b) \longrightarrow \ell^-(q_1)\bar{\nu}_\ell(q_2)\gamma(q_3)\bar{q}(p_1) \quad (3.1b)$$

$$q(p_a)g(p_b) \longrightarrow \ell^-(q_1)\bar{\nu}_\ell(q_2)\gamma(q_3)Q(p_1) \quad (3.1c)$$

in case of $W^- \gamma j$ production, and the partonic subprocesses

$$q(p_a)\bar{Q}(p_b) \longrightarrow \ell^-(q_1)\bar{\nu}_\ell(q_2)\ell'^+(q_3)\ell'^-(q_4)g(p_1) \quad (3.2a)$$

$$\bar{Q}(p_a)g(p_b) \longrightarrow \ell^-(q_1)\bar{\nu}_\ell(q_2)\ell'^+(q_3)\ell'^-(q_4)\bar{q}(p_1) \quad (3.2b)$$

$$q(p_a)g(p_b) \longrightarrow \ell^-(q_1)\bar{\nu}_\ell(q_2)\ell'^+(q_3)\ell'^-(q_4)Q(p_1) \quad (3.2c)$$

for $W^- Z j$ production. There are three additional subprocesses, which can be recovered from (3.1a) and (3.2a) by interchanging the momentum-assignment of the initial state, $p_a \leftrightarrow p_b$, i.e. by interchanging the proton beams.

The three subprocesses are related by crossing symmetry. It is therefore enough to only consider the $q\bar{Q}$ -induced processes. All other partonic subprocesses are then given by analytical continuation of the $q\bar{Q}$ scattering amplitude; the W^+ cases can be treated accordingly.

For the purpose of this thesis, we take the CKM matrix to be diagonal, and neglect bottom contributions*, i.e. $q = (d, s)$, and $Q = (u, c)$. The leptons are assumed to be

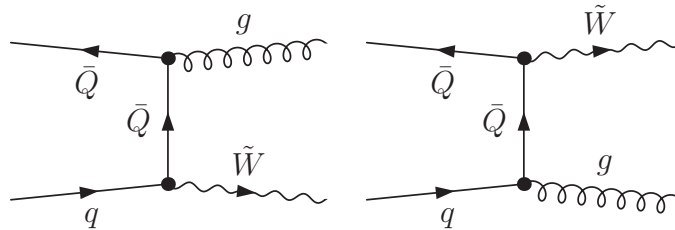


Figure 3.1: Feynman diagrams of the partonic subprocess $q\bar{Q} \rightarrow \tilde{W}^- g$. \tilde{W} denotes the effective polarization vector of the three-body decay current $\tilde{W} \rightarrow \ell^- \bar{\nu}_\ell \gamma$, and the four-body decay current $\tilde{W} \rightarrow \ell^- \bar{\nu}_\ell \ell'^+ \ell'^-$ of fig. 3.2.

*For a quantitative analysis of these approximations see below.

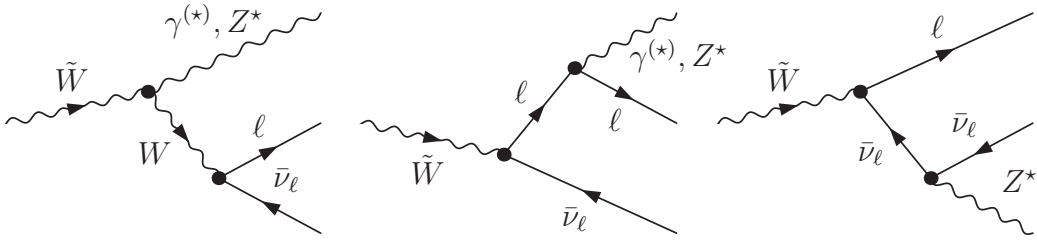


Figure 3.2: Feynman graphs of the decay currents $\tilde{W} \rightarrow \ell^- \bar{\nu}_\ell \gamma$, and $\tilde{W} \rightarrow \ell^- \bar{\nu}_\ell \ell'^+ \ell'^-$ via the off-shell decay $\gamma^*, Z^* \rightarrow \ell'^+ \ell'^-$ that follows from the vertex of eq. (2.26).

massless, disallowing decays of the Z, γ to massive τ s. The Feynman graphs of $W\gamma j$ and WZj production are quite alike, and it is economical to discuss both processes at the same time. In fact, they do only differ by the additional Z boson, and off-shellness of the further decaying, neutral electroweak gauge bosons.

The Feynman graphs decompose into two sets of topologies. The first set is characterized by two gauge bosons attached to the quark line, fig. 3.1, where the \tilde{W} is to be understood as the effective electroweak current, which is calculated from the Feynman graphs of fig. 3.2, contracted with the appropriate propagator factor. The leptonic decay of the photon and the Z boson in WZj production is included in an analogous manner. In fig. 3.2 the γ^*, Z^* denote effective polarization vectors, calculated from the propagator-contracted decay vertices (2.26). The second set combines all remaining

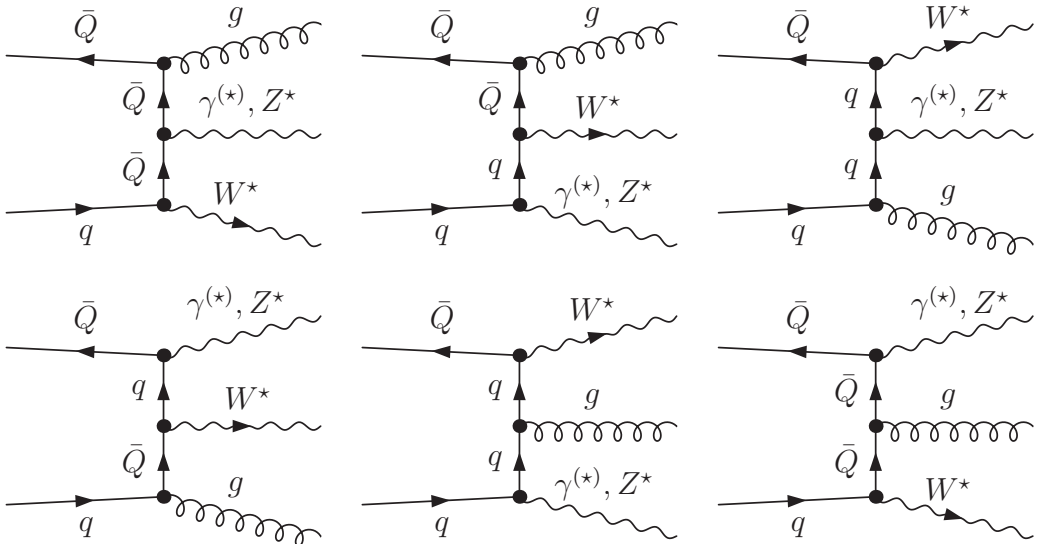


Figure 3.3: Feynman diagrams of the partonic subprocess $q\bar{Q} \rightarrow W^* g \gamma$, and $q\bar{Q} \rightarrow W^* (\gamma, Z)^* g$. W^* and $(\gamma, Z)^*$ denote the effective polarization vectors of the decay currents $W^* \rightarrow \ell^- \bar{\nu}_\ell$, $\gamma^* \rightarrow \ell'^+ \ell'^-$, and $Z^* \rightarrow \ell'^+ \ell'^-$, respectively.

	$pp \rightarrow e^- \bar{\nu}_e \gamma j + X$ [fb]
mod. VBFNLO	268.38 ± 0.12
SHERPA	268.14 ± 0.37
MADeVENT	268.24 ± 0.69

Table 3.1: Comparison of integrated $pp \rightarrow e^- \bar{\nu}_e \gamma j + X$ tree-level cross sections at the LHC. The cross sections were calculated with a modified version of VBFNLO, MADeVENT, and SHERPA, using CTEQ6L1 parton distributions and $\mu_F = \mu_R = 100$ GeV. The separation of the photon and the jet in the azimuthal-angle – pseudo rapidity plane is required to be $R_{j\gamma} \geq 1$. We also demand $R_{\ell\gamma} \geq 0.4$, and $p_T^j \geq 50$ GeV, $p_T^\gamma \geq 50$ GeV, $p_T^\ell \geq 30$ GeV, $|y_j| \leq 4.5$, $|\eta_\ell| \leq 2.5$, and $|\eta_\gamma| \leq 4.5$.

Feynman graphs where the three effective gauge boson polarization vectors are directly attached to the quark line, fig. 3.3.

3.1.1 Numerical implementation, speed and comparisons

The tree-level amplitude for all three partonic subprocesses has been implemented using HELAS routines [67], generated with MADGRAPH [68]. The code was slightly modified to avoid helicity-configurations which yield matrix elements equal to zero. The HELAS-amplitudes are set up in the way described in the above section, while the effective polarization vectors are calculated only once per subprocess and phase space point. Due to the simple color- and chirality structure of the amplitudes, the numerical evaluation is fast and requires no further optimization, so that the color- and helicity summation and -averaging is adopted from the MADGRAPH-implementation.

The phase space integration is performed numerically, cf. sec. 2.2.5 and applies the strategies of sec. 2.2.6. Integrated leading order cross sections

$$\sigma^B = \sum_{\{a,b\}} \iiint d\text{LIPS}_{1+\text{elw}}(p_a, p_b, p_1, q_1, \dots, q_n) dx_a dx_b \Theta(\mathcal{C}) \mathcal{F}(p_1, q_1, \dots, q_n) \times \frac{f_{a/P}(x_a, \mu_F^2) f_{b/P}(x_b, \mu_F^2)}{\Phi(p_a \cdot p_b) n_s(a) n_s(b) n_c(a) n_c(b)} \sum_{\{n_s, n_c\}} |\mathcal{M}_{ab}^B(p_a, p_b, p_1, p_2, q_1, \dots, q_n)|^2 \quad (3.3)$$

were checked against SHERPA v.1.1.3 [69] and MADeVENT v4.4.21 [68], yielding agreement at the per mill level for different input parameter choices and event selection criteria. In (3.3) the index “elw” denotes the electroweak part of the phase space, n_s , n_c are the spin and color numbers of the incoming particles. The summation in the lower line in (3.3) is performed over all final and initial state colors and spins.

Our numerical code is faster by at least a factor five compared to MADeVENT, and a factor three compared to SHERPA. Tab. 3.1 representatively gives the comparison of integrated $W^- \gamma j$ leading order production cross sections at the LHC using the three different programs. For leading order WZj production we find equally good agreement. Additional checks are discussed in sec. 3.5.

The event generation strategies of both $W\gamma j$ and WZj production employ modified versions of routines that are provided as part of the VBFNLO framework. Throughout this thesis, the finite width effects of the massive electroweak bosons are taken into account using a modified version of the complex mass scheme of [70, 71]: The weak mixing angle is taken to be real, while using Breit-Wigner-propagators for the massive electroweak boson. This scheme corresponds to the implementation in MADGRAPH.

$pp, p\bar{p} \rightarrow \ell^- \bar{\nu}_\ell \gamma j + X$ event generation

To optimize for different emissions of the massless final-state photon, the phase space is divided into disjoint parts by specifying a particular value m_3^c for the $\ell^- \bar{\nu}_\ell \gamma$ -invariant mass and a value m_2^c for the $\ell^- \gamma$ -invariant mass. The integration proceeds in two steps:

- (i) Integrate events satisfying

$$m(\ell^- \bar{\nu}_\ell \gamma) > m_3^c \quad \text{and} \quad m(\ell^- \gamma) > m_2^c,$$

and selection cuts, applying a phase space-generator optimized for the two-body decay, e.g. $W^- \rightarrow \ell^- \bar{\nu}_\ell$, with the W recoiling against the photon-parton-system.

- (ii) Integrate events that do not satisfy (i) but fulfill the selection criteria, applying a phase space-generator, which is optimized for the three-body decay $W^- \rightarrow \ell^- \bar{\nu}_\ell \gamma$. The parton thereby recoils against the $\ell^- \bar{\nu}_\ell \gamma$ -system.

This prescription guarantees that we efficiently generate momenta for ℓ^- , $\bar{\nu}_\ell$, and γ , which are not in the vicinity of the W mass pole, $(q_1 + q_2 + q_3)^2 \neq m_W^2$. In addition, the photon-lepton-, and the photon-parton-collinear behavior of the squared matrix element in the phase space regions selected by typical selection criteria get sufficiently sampled. m_2^c, m_3^c are roughly determined by the W mass m_W . In practice the efficient integration-optimization of the VEGAS-algorithm allows for a wide range of m_2^c, m_3^c , of which $m_2^c = 95$ GeV and $m_3^c = 100$ GeV turns out to be a reasonable choice. The quality of the phase space implementation was verified by explicitly checking the random number's differential distributions.

To also account for rather stringent cuts on photon, lepton and \not{p}_T , which are applied in anomalous couplings' searches, m_2^c can be steered by external values. Depending on the input value and the chosen cuts, the second channel is switched off and m_3^c, m_2^c are set to zero in (i).

$pp, p\bar{p} \rightarrow \ell^- \bar{\nu}_\ell \ell'^+ \ell'^- j + X$ event generation

Detection criteria for the leptons mostly remove the photon contribution from the squared matrix element. Additionally, the decay $W^* \rightarrow \ell^- \bar{\nu}_\ell \ell'^+ \ell'^-$ implies a highly off-shell W , so that these contributions are subdominant in the phase space region of interest. Consequently, the phase space implements Breit-Wigner W and Z resonances, with the parton recoiling against the WZ system.

Impact of the non-diagonal CKM matrix

Including the non-diagonal CKM matrix of eq. (2.20) decreases the LO cross sections at the Tevatron by about 3% and by $\lesssim 1\%$ at the LHC. These corrections are phenomenologically irrelevant and well below the residual scale dependence at NLO at both the LHC and the Tevatron, secs. 4 and 5. In total the approximation of a diagonal CKM matrix is adequate for our purposes.

The unequal impact of the CKM matrix on the cross sections at the different colliders is due to the dominance of distinct subprocesses at the different center-of-mass energies \sqrt{s} : At the Tevatron ($\sqrt{s} = 1.96$ TeV) $W\gamma j$ and WZj production are dominated by quark-induced processes, while at the LHC (expected $\sqrt{s} = 14$ TeV) quark-gluon-initiated processes provide the largest share of the cross sections. This is an immediate consequence of the pdfs as a function of the momentum fraction x , fig 2.1: At the LHC the proton is typically probed at low values of $x \sim 0.01$ (see chapter 4) where the gluon pdf is very large, whereas at the Tevatron typically $x \sim 0.2$, where the (anti)proton's valence quarks dominate.

Additionally, for massless fermions, we find for the final state-summed matrix elements of $gq \rightarrow Q + \dots$

$$\begin{aligned} \sum_Q f_{g/P}(x_1) f_{q/P}(x_2) |V_{qQ}|^2 |\mathcal{M}(gq \rightarrow Q)|^2 \\ = f_{g/P}(x_1) f_{q/P}(x_2) |\mathcal{M}|^2 \sum_Q |V_{qQ}|^2 = f_{g/P}(x_1) f_{q/P}(x_2) |\mathcal{M}|^2, \end{aligned} \quad (3.4)$$

because the V_{qQ} -stripped amplitude is flavor-blind, we do not tag flavor, and the CKM matrix is unitary. Indeed, the approximation is exact for the gluon-induced processes, and the only dependence on the CKM matrix comes from subprocesses $q\bar{Q} \rightarrow g + \dots$ as the above factorization does not hold due to the pdfs.

3.1.2 Anomalous $WW\gamma$ couplings

Along the line of sec. 2.1.2, we can study the impact of non-SM interactions in the electroweak sector by including anomalous couplings. For $W\gamma$ production, which is the theoretically favored channel to look for such effects due to radiation zeros[†] of the amplitude, this has already been performed in [12] at NLO QCD.

The most general Lorentz and \mathcal{CP} -invariant vertex that is in accordance with electromagnetic gauge invariance up to operator-dimension six, is described by the effective Lagrangian [72]

$$\mathcal{L}_{WW\gamma} = -ie \left[W_{\mu\nu}^\dagger W^\mu A^\nu - W_\mu^\dagger A_\nu W^{\mu\nu} + \kappa W_\mu^\dagger W_\nu F^{\mu\nu} + \frac{\lambda}{m_W^2} W_{\lambda\mu}^\dagger W_\nu^\mu F^{\nu\lambda} \right]. \quad (3.5)$$

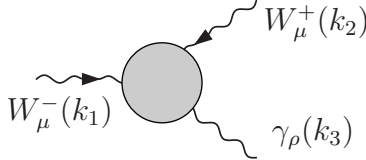
It is customary to measure the κ -induced deviation from the SM operators ($\kappa = 1$, and $\lambda = 0$) by introducing $\Delta\kappa = \kappa - 1$. The parameters $\Delta\kappa$ and λ are related to the electric

[†]A detailed discussion of phenomenological implications of the anomalous couplings, including current bounds are postponed to sec. 4.4.

quadrupole moment Q_W and magnetic dipole moment μ_W of the W boson,

$$\begin{aligned}\mu_W &= \frac{e}{2m_W}(2 + \Delta\kappa + \lambda), \\ Q_W &= -\frac{e}{m_W^2}(1 + \Delta\kappa - \lambda).\end{aligned}\tag{3.6}$$

The anomalous $WW\gamma$ Lagrangian yields a modified $WW\gamma$ vertex,



$$\begin{aligned}W_\mu^-(k_1) \quad W_\mu^+(k_2) \quad \gamma_\rho(k_3) &= g^{\mu_1\mu_2} \left[(\Delta\kappa - 1 + (\lambda k_2 \cdot k_3)/m_W^2) k_1^{\mu_3} \right. \\ &\quad \left. + (1 - (\lambda k_1 \cdot k_3)/m_W^2) k_2^{\mu_3} \right] \\ &+ g^{\mu_2\mu_3} \left[(-1 + (\lambda k_1 \cdot k_3)/m_W^2) k_2^{\mu_1} \right. \\ &\quad \left. + (1 - (\lambda k_1 \cdot k_2)/m_W^2) k_3^{\mu_1} \right] \\ &+ g^{\mu_1\mu_3} \left[(1 - \Delta\kappa - (\lambda k_2 \cdot k_3)/m_W^2) k_1^{\mu_2} \right. \\ &\quad \left. + (-1 + (\lambda k_1 \cdot k_2)/m_W^2) k_3^{\mu_2} \right] \\ &+ \lambda/m_W^2 \left[k_1^{\mu_2} k_2^{\mu_3} k_3^{\mu_1} - k_1^{\mu_3} k_2^{\mu_1} k_3^{\mu_2} \right].\end{aligned}\tag{3.7}$$

For $\Delta\kappa = \lambda = 0$ we obviously recover the SM-vertex (2.25).

Retaining unitarity at high energies is a crucial ingredient to meaningfully model beyond-the-SM physics in a Monte Carlo setting. If probability conservation is violated, the cross section is dominated by the behavior at large invariant masses of the matrix element, even though the parton luminosities are steeply falling. On the other hand, if unitarity is conserved, the phenomenology gets no significant contribution from large invariant masses by the same reason. Therefore, the parameters $\Delta\kappa = \kappa - 1$ and λ have to be merely understood as low-energy limits of form factors, whose precise momentum dependence highly depends on the BSM model. A phenomenological parametrization is [12, 72]

$$\Delta\kappa = \frac{\Delta\kappa_0}{(1 + m_{W\gamma}^2/\Lambda^2)^{n_\kappa}}, \quad \lambda = \frac{\lambda_0}{(1 + m_{W\gamma}^2/\Lambda^2)^{n_\lambda}},\tag{3.8}$$

where $m_{W\gamma}$ denotes the invariant mass of the final state lepton-photon-neutrino system. Unitarity requires $n_\kappa > 1/2$ and $n_\lambda > 1$, and customary choices are dipole profiles $n_\kappa = n_\lambda = 2$. Note that, we have not included anomalous \mathcal{CP} -violating operators, as they are already heavily constrained from measurements of the neutron electric dipole moment [21].

Numerical implementation

The Feynman rule resulting from (3.5) has been determined with FEYNRULES [73]. Algebraic checks and comparisons have been performed by means of FEYNCALC [74].

The vertex and the form factors are numerically implemented via newly set up HELAS-routines, which are then called when calculating the matrix elements and currents. The Standard Model limit $\Delta\kappa = \lambda = 0$ has been checked numerically for the vertex implementation, as well as for the entire implementation.

3.2 Real emission contributions

3.2.1 Real emission matrix elements

At $\mathcal{O}(\alpha_s^2)$, the real emission part of the NLO matrix element contains 90 subprocesses. A MADGRAPH-based implementation as done for the leading order matrix elements has thus been discarded, in order not to compromise on the speed of the implementation. The calculation in the chiral limit also heavily simplifies by noting that the real emission correction can be constructed from the leading order graphs, by attaching a gluon or a quark-pair in all possible ways, fig. 3.4. Flavor-blindness and the assumed diagonal CKM matrix then allow to recycle parts of the amplitude of one subprocess into others, by noting that the electroweak part of the amplitude remains algebraically unaffected by additional QCD radiation. Following this prescription, the partonic subprocesses for $W^- \gamma j$ production can be classified, modulo crossing, flavor summation, and initial state interchange, into

$$\bar{u}(p_a)u(p_b) \rightarrow \ell^-(q_1)\bar{\nu}_\ell(q_2)\gamma(q_3)\bar{d}(p_1)u(p_2) \quad 28 \text{ Graphs} \quad (3.9a)$$

$$\bar{u}(p_a)u(p_b) \rightarrow \ell^-(q_1)\bar{\nu}_\ell(q_2)\gamma(q_3)\bar{s}(p_1)c(p_2) \quad 14 \text{ Graphs} \subset (3.9a) \quad (3.9b)$$

$$\bar{d}(p_a)d(p_b) \rightarrow \ell^-(q_1)\bar{\nu}_\ell(q_2)\gamma(q_3)\bar{u}(p_1)d(p_2) \quad 28 \text{ Graphs} \quad (3.9c)$$

$$\bar{d}(p_a)d(p_b) \rightarrow \ell^-(q_1)\bar{\nu}_\ell(q_2)\gamma(q_3)\bar{c}(p_1)s(p_2) \quad 14 \text{ Graphs} \subset (3.9c) \quad (3.9d)$$

$$\bar{u}(p_a)d(p_b) \rightarrow \ell^-(q_1)\bar{\nu}_\ell(q_2)\gamma(q_3)g(p_1)g(p_2) \quad 46 \text{ Graphs}, \quad (3.9e)$$

while the electroweak part can be provided globally for all subprocesses. The subprocesses for $W^+ \gamma j$ and $W^\pm Z j$ production can be written down accordingly, by replacing $\gamma(q_3) \rightarrow \ell'^-(q_3)\ell'^+(q_4)$, etc., in (3.9). For the color-stripped amplitude $\bar{Q}_i q_j \rightarrow \ell^- \bar{\nu}_\ell \gamma g_a g_b$ with $\mathfrak{su}(3)$ indices i, j, a, b , the amplitude can be cast into the form

$$\begin{aligned} \mathcal{M}_{\bar{q}Q,R}^{ij,ab} = & \left[(t^a t^b)_{ij} \tilde{J}_{\bar{q}Q}^{\mu,(ab)}(\tilde{W}) + (t^b t^a)_{ij} \tilde{J}_{\bar{q}Q}^{\mu,(ba)}(\tilde{W}) \right] J_\mu(\tilde{W}) \\ & + \left[(t^a t^b)_{ij} \tilde{J}_{\bar{q}Q}^{\mu,(ab)}(W^*) + (t^b t^a)_{ij} \tilde{J}_{\bar{q}Q}^{\mu,(ba)}(W^*) \right] J_\mu(W^*). \end{aligned} \quad (3.10)$$

The current $J_{\bar{q}Q}^{\mu,(ab)}(\tilde{W})$ is evaluated from the sum of the Feynman graphs in fig. 3.4, and $J_\mu(\tilde{W})$ follows from the sums of figs. 3.2 and 3.4 with the effective polarization vectors of the γ^* and the Z^* already contracted. $J_\mu(W^*)$ is computed from the vertex diagram of (2.26) and the corresponding hadronic current $J_{\bar{q}Q}^{\mu,(ba)}(W^*)$ is evaluated from the Feynman graph topologies where four gauge bosons are radiated off the quark leg in total, contracting with the effective γ^* and Z^* polarization vectors. There is a subtlety concerning how to treat the electroweak boson propagators when defining the effective currents. Massless decay leptons guarantee that the part of the electroweak boson

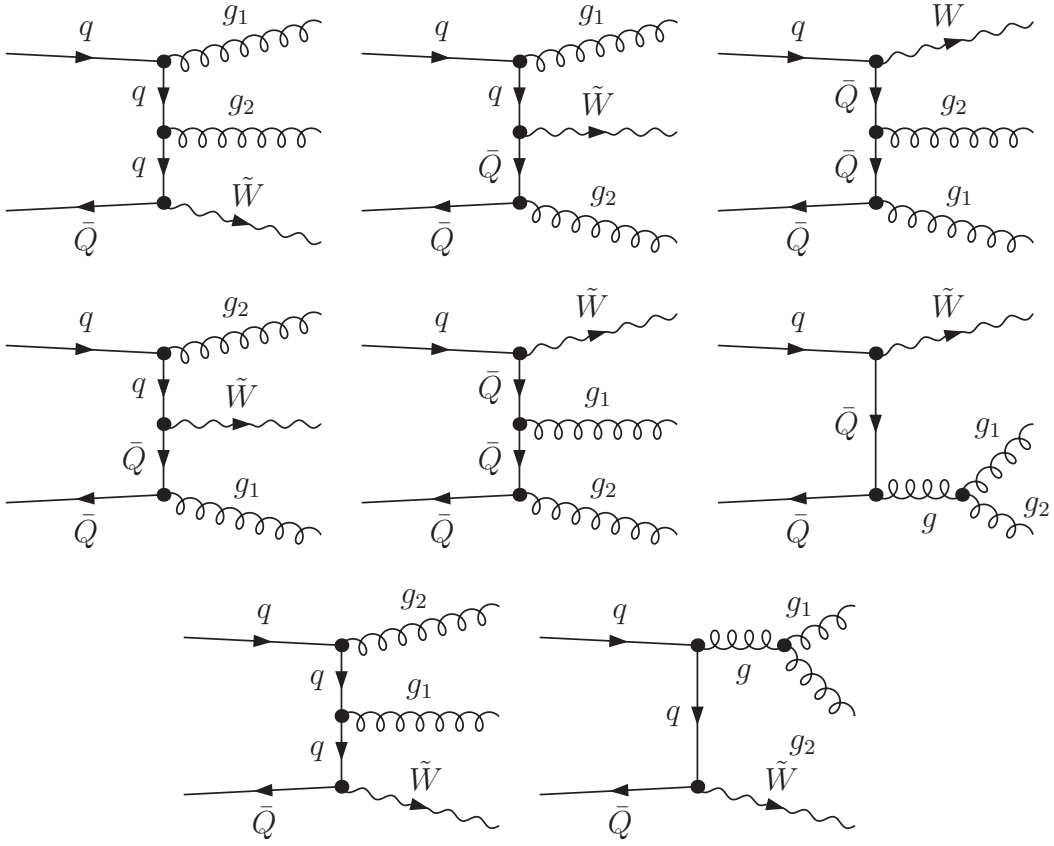


Figure 3.4: Sample Feynman graphs contributing to the partonic real emission subprocess $q\bar{Q} \rightarrow \tilde{W}gg$ at $\mathcal{O}(\alpha^3\alpha_s^2)$. The \tilde{W} denotes the effective decay current of fig. 3.2. Comparing to fig. 3.1, the additional gluon is attached to the quark and gluon lines in all possible places. Not shown are real emission topologies that follow from fig. 3.3.

propagator (2.21c) proportional to its four momentum has vanishing contributions and the propagator factor is simply the Breit-Wigner distribution that can be read off (2.21c):

$$\begin{aligned}
 J_{\bar{q}Q}^\mu(W^*)J_\mu(W^*) &= \frac{-i}{k^2 - m_W^2 + im_W\Gamma_W} J_{\bar{q}Q}^\mu(W^*)j_\mu(W^*) \\
 &= \frac{1}{k^2 - m_W^2 + im_W\Gamma_W} J_{\bar{q}Q}^\mu(W^*) \left[\frac{e}{\sqrt{2}\sin\theta_w} \bar{u}(e^-)\gamma_\mu\mathbb{P}_L v(\bar{\nu}_e) \right], \quad (3.11)
 \end{aligned}$$

where we have introduced j for the propagator-stripped version of $J^\mu(W^*)$ and have suppressed the color indices. Note, that the part in brackets is, of course, the Feynman rule of (2.26). This is a simple example of how to make contact between the notion of effective currents and the Feynman rules of interactions by splitting off the propagator factors. For the current $J_\mu(\tilde{W})$ this is more involved; we include the non-vanishing

contributions by writing

$$J_{\tilde{q}Q}^\mu(\tilde{W})J_\mu(\tilde{W}) = \frac{-i}{k^2 - m_W^2 + im_W\Gamma_W} \left[\tilde{j}^\mu - \frac{\tilde{J} \cdot k}{k^2 - m_W^2 + im_W\Gamma_W} k_\mu \right] j^\mu(\tilde{W}(k)). \quad (3.12)$$

The propagator-stripped currents $j^\mu(W^*)$ and $j^\mu(\tilde{W})$ can be evaluated directly from the vertex (2.26) and fig. 3.2 as indicated in (3.11).

The remaining subprocesses in (3.9) can be straightforwardly decomposed in similar manner by providing the appropriate hadronic currents, which involve two contracted fermion lines. Eq. (3.10) also shows that the amplitude of $W\gamma jj$ can be directly extended to include anomalous couplings, and to $WZjj$ production, including full leptonic decays with all off-shell effects, by replacing the photon by the respective effective polarization vector in the definition of the effective currents of (3.10).

The color structure is slightly more complicated compared to the leading order matrix elements' one, as there are two color configurations in (3.10) that interfere,

$$\text{Tr}(t^a t^b t^a t^b) = d_r C_F \left(C_F - \frac{C_A}{2} \right), \quad (3.13)$$

whereas they yield individual color factors of the squared matrix element

$$\text{Tr}(t^a t^a t^b t^b) = \text{Tr}(t^b t^b t^a t^a) = d_r C_F^2. \quad (3.14)$$

A complete list of subprocesses can be found in Tab. 3.3 on page 43.

3.2.2 Numerical implementation, speed and di-jet comparisons

The and color- and helicity-averaged and -summed matrix elements, associated with the hadronic currents in (3.10), are set up using the spinor helicity formalism of [34]. Intermediate numerical results are stored and re-used, thus speeding up the numerical code. Exploiting (3.10), the effective electroweak currents are calculated only once per phase space point, so that we can rely on modified MADGRAPH-generated code without jeopardizing numerical speed. Entire subprocesses' matrixelements are recycled as indicated in (3.9) before multiplying with the corresponding parton densities.

The real emission matrix elements have been checked numerically against code generated with MADGRAPH for every subprocess. Integrated di-jet cross sections were again checked against SHERPA and MADEVENT. Tab. 3.2 representatively gives the integrated cross sections for $W^-\gamma jj$ production at the LHC for the selection cuts that are quoted in Tab. 3.1. Compared to MADEVENT and SHERPA, we find a considerable speed-improvement of the VBFNLO-implementation, gaining at least factors of ~ 7 compared to SHERPA, and factors of ~ 20 compared to MADEVENT.

Table 3.2: Comparison of integrated $W^-\gamma jj$ production cross sections at the LHC for selection cuts of Tab. 3.1.

	$pp \rightarrow e^- \bar{\nu}_e \gamma jj + X$ [fb]
mod. VBFNLO	124.74 ± 0.10
SHERPA	124.35 ± 0.59
MADEVENT	123.80 ± 0.40

The event generation is set up analogously to the leading order part of the numerical program, sec. 3.1.1, extending the phase space generation to the two-parton final state.

3.2.3 Dipole subtraction

The dipole subtraction is performed by straightforwardly applying the algorithm of Catani and Seymour [37], which is sketched in sec. 2.2.2. There are, in principle, 5 different momentum configurations that give rise to IR-divergent real emission matrix elements in the context of NLO QCD mono-jet production. The divergencies factorize in the respective phase space regions,

$$\mathcal{M}_{ab}^{\text{R}}(p_a, p_b, p_1, p_2, q_1, \dots, q_n) = \begin{cases} \mathcal{D}^{ai,b}(p_1, p_2; p_a, p_b) + \mathcal{D}_k^{ai}(p_1, p_2; p_a, p_b) + \dots & , p_a \cdot p_i \rightarrow 0 \\ \mathcal{D}^{bi,a}(p_1, p_2; p_b, p_a) + \mathcal{D}_k^{bi}(p_1, p_2; p_b, p_a) + \dots & , p_b \cdot p_i \rightarrow 0 \\ \mathcal{D}_{12}^a(p_1, p_2; p_a, p_b) + \mathcal{D}_{12}^b(p_1, p_2; p_a, p_b) + \dots & , p_1 \cdot p_2 \rightarrow 0 \end{cases} \quad (3.15)$$

where $i, k = 1, 2, k \neq i$, and the dots correspond to IR-finite terms. The IR-singular behavior of the real emission amplitude is numerically mended by subtracting the dipoles of (3.15) from the real emission matrix element. This is due to the fact that in the critical regions of phase space, (3.15) exactly reproduces the real emission IR-behavior, which is encoded in three distinct Feynman topologies that are given for the example of soft and collinear emission off the $\bar{u}d \rightarrow g + \text{electroweak}$ – graph in figs. 3.5 and 3.6. The divergencies are cancelled by subtracting dipoles with initial, or final state spectator, e.g. either the final-state gluon or the initial state \bar{u} quark can recoil against the emitter $d \rightarrow dg$ in the emitter-spectator system in fig. 3.6 (a). The radiating particle can thereby be an initial or a final state parton, cf. fig. 3.5. A complete table of the dipoles, together with the partonic real emission subprocess they render IR-finite, is given in Tab. 3.3.

In the following we discuss the dipoles of (3.15) for the initial state emitter or spectator particle chosen to be a . The other dipoles follow from the formulae upon trivial exchange $a \leftrightarrow b$.

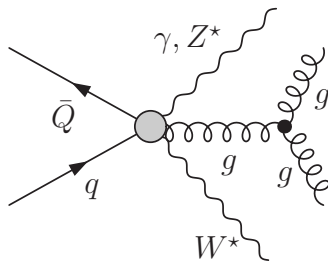


Figure 3.5: Representative topology leading to IR singularities of the final-initial dipoles. The shaded vertex denotes the Born-level insertions of figs. 3.1 and 3.3.

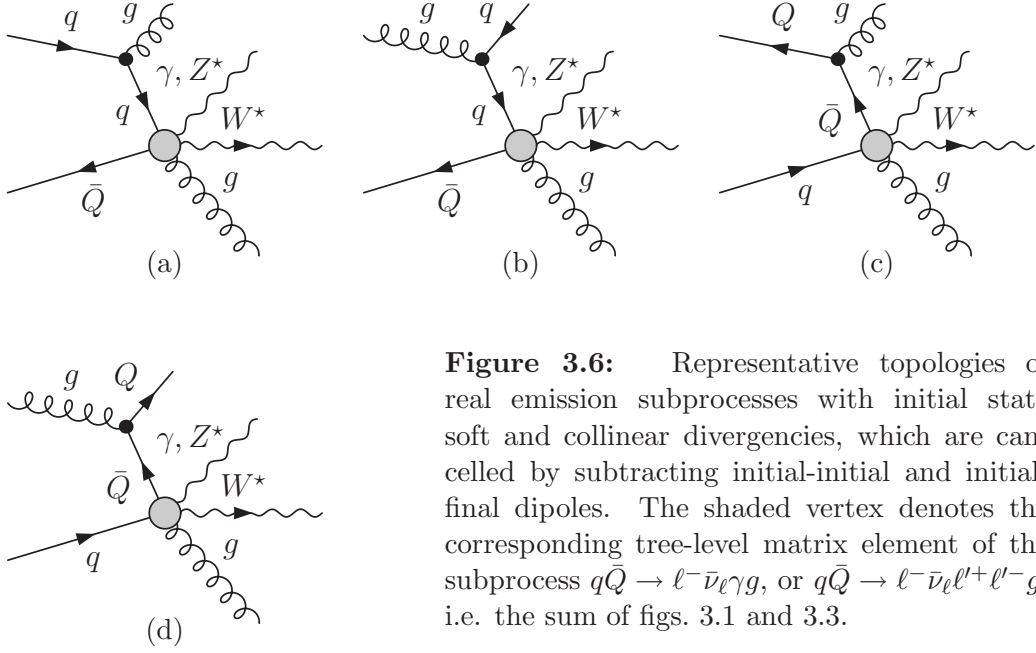


Figure 3.6: Representative topologies of real emission subprocesses with initial state soft and collinear divergencies, which are cancelled by subtracting initial-initial and initial-final dipoles. The shaded vertex denotes the corresponding tree-level matrix element of the subprocess $q\bar{Q} \rightarrow \ell^- \bar{\nu}_\ell \gamma g$, or $q\bar{Q} \rightarrow \ell^- \bar{\nu}_\ell \ell'^+ \ell'^- g$, i.e. the sum of figs. 3.1 and 3.3.

Initial state singularities with final state spectators (initial-final dipoles)

The dipoles for an initial state emitter with a final state spectator in (3.15) read [37]

$$\mathcal{D}_k^{ai}(p_1, p_2; p_a, p_b) = -\frac{1}{2p_a \cdot p_i} \frac{1}{x_{ik,a}} \langle \tilde{k}; \tilde{a}i, b | \frac{\mathbf{T}_k \cdot \mathbf{T}_{ai}}{\mathbf{T}_{ai}^2} \mathbf{V}_k^{ai} | \tilde{k}; \tilde{a}i, b \rangle \quad (3.16)$$

where $i, k = 1, 2$, $k \neq i$, and the subtraction kinematics are

$$\tilde{p}_{ai}^\mu = x_{ik,a} p_a^\mu, \quad \tilde{p}_k^\mu = p_k^\mu + p_i^\mu - (1 - x_{ik,a}) p_a^\mu, \quad x_{ik,a} = 1 - \frac{p_i \cdot p_k}{(p_k + p_i) \cdot p_a}. \quad (3.17)$$

The bra-ket notation used for the subtraction terms in the Catani-Seymour formalism is an abbreviation for the Born amplitude and its complex conjugate, respectively, suppressing the non-QCD part. In (3.16) the bra explicitly means

$$|\tilde{k}; \tilde{a}i, b\rangle = \mathcal{M}^{\text{B}\{c_k, c_{ai}, c_b\}, \{s_k, s_{ai}, s_b\}}(\tilde{p}_{ai}, p_b, \tilde{p}_k, q_1, \dots, q_n), \quad (3.18)$$

where the color and spin indices of the partons are denoted by c and s , on which the color and spin operators \mathbf{T} and \mathbf{V} act.

The transformation (3.17) correctly implements four-momentum conservation in the Born matrix element on the right-hand side of the dipole in (3.16),

$$p_a + p_b - p_1 - p_2 - \sum_i q_i = \tilde{p}_{ai} - \tilde{p}_k + p_b - \sum_i q_i = 0. \quad (3.19)$$

Hence, the dipole kinematics can be understood as the partons from the splitting process recoiling against the spectator parton. The emitter-spectator color correlation follows

from color conservation $\mathbf{T}_{ai} + \mathbf{T}_k + \mathbf{T}_b = \mathbf{0}$,

$$\mathbf{T}_k \cdot \mathbf{T}_{ai} = \frac{1}{2} (\mathbf{T}_b^2 - \mathbf{T}_k^2 - \mathbf{T}_{ai}^2) = \begin{cases} -C_A/2 & ai = q, \bar{q}; k = g \\ -C_A/2 & ai = g; k = q, \bar{q} \\ C_A/2 - C_F & ai = q, \bar{q}; k = Q, \bar{Q} \end{cases}, \quad (3.20)$$

i.e. the correlation is fixed upon specifying the emitter and spectator gauge representation. This is special to mono-jet production processes, as the charge of the electroweak final state fixes the QCD-representation of single remaining parton upon specifying emitter and spectator.

The spin-correlated splitting matrix elements \mathbf{V}_k^{ai} of the color dipole read

$$\begin{aligned} \langle s | \mathbf{V}_k^{g a \bar{q} i}(x_{ik,a}) | s' \rangle &= 8\pi\alpha_s T_R [1 - 2x_{ik,a}(1 - x_{ik,a})] \delta_{ss'}, \\ \langle s | \mathbf{V}_k^{q a g i}(x_{ik,a}, u_i) | s' \rangle &= 8\pi\alpha_s C_F \delta_{ss'} \left[\frac{2}{1 - x_{ik,a} + u_i} - (1 + x_{ik,a}) \right], \\ \langle \mu | \mathbf{V}_k^{q a q i}(x_{ik,a}, u_i) | \nu \rangle &= 8\pi\alpha_s C_F [-g^{\mu\nu} x_{ik,a} \\ &\quad + \frac{1 - x_{ik,a}}{x_{ik,a}} \frac{2u_i(1 - u_i)}{p_i \cdot p_k} \left(\frac{p_i^\mu}{u_i} - \frac{p_k^\mu}{1 - u_i} \right) \left(\frac{p_i^\nu}{u_i} - \frac{p_k^\nu}{1 - u_i} \right)], \\ \langle \mu | \mathbf{V}_k^{g a g i}(x_{ik,a}, u_i) | \nu \rangle &= 16\pi\alpha_s C_A \left[-g^{\mu\nu} \left(\frac{1}{1 - x_{ik,a} + u_i} - 1 + x_{ik,a}(1 - x_{ik,a}) \right) \right. \\ &\quad \left. + \frac{1 - x_{ik,a}}{x_{ik,a}} \frac{u_i(1 - u_i)}{p_i \cdot p_k} \left(\frac{p_i^\mu}{u_i} - \frac{p_k^\mu}{1 - u_i} \right) \left(\frac{p_i^\nu}{u_i} - \frac{p_k^\nu}{1 - u_i} \right) \right], \end{aligned} \quad (3.21)$$

with

$$u_i = \frac{p_i \cdot p_a}{(p_i + p_k) \cdot p_a}, \quad (3.22)$$

where, comparing to [37], the limit $d \rightarrow 4$ in d -dimensional regularization has already been taken. The spin-convention of \mathbf{V}_k^{ai} is μ, ν for spin-1 vectorial representations, and s, s' for spin-1/2 fermionic representations of the Lorentz group (2.1). Note that splittings with $ai = q, \bar{q}$ do not introduce spin correlations in the absolute-squared amplitude, as opposed to splittings with $ai = g$.

Initial state singularities with initial state spectator (initial-initial dipoles)

The dipole for emitting initial state and initial state spectator reads [37]

$$\mathcal{D}^{ai,b}(p_1, p_2; p_a, p_b) = -\frac{1}{2p_a \cdot p_i} \frac{1}{x_{i,ab}} \langle \tilde{1}, \tilde{a}\tilde{i}, b | \frac{\mathbf{T}_b \cdot \mathbf{T}_{ai}}{\mathbf{T}_{ai}^2} \mathbf{V}^{ai,b} | \tilde{1}, \tilde{a}\tilde{i}, b \rangle, \quad (3.23)$$

with subtraction kinematics

$$\tilde{p}_{a\tilde{i}}^\mu = x_{i,ab} p_a^\mu, \quad x_{i,ab} = 1 - \frac{(p_a - p_b) \cdot p_i}{p_a \cdot p_b}, \quad (3.24)$$

where $i = 1, 2$. The momentum of the spectator parton b remains unchanged, while the final state parton and the electroweak momenta are lorentz-transformed,

$$\tilde{k}_j^\mu = k_j^\mu - \frac{2k_j \cdot (K + \tilde{K})}{(K + \tilde{K})^2} (K + \tilde{K})^\mu + \frac{2k_j \cdot K}{K^2} \tilde{K}^\mu, \quad (3.25)$$

with $k_j \in \{p_1, p_2, q_1, \dots, q_4\}$ and transformation momenta

$$K^\mu = p_a^\mu + p_b^\mu - p_i^\mu, \quad \tilde{K}^\mu = \tilde{p}_{ai}^\mu + p_b^\mu. \quad (3.26)$$

Four-momentum conservation of the real emission matrix element is reflected in the matrix element of (3.23),

$$\tilde{p}_{ai}^\mu + p_b^\mu - \tilde{p}_1 - \sum_i \tilde{q}_i = 0. \quad (3.27)$$

The color correlation of emitter and spectator is given in (3.20), and the spin-correlation in (3.23) is

$$\begin{aligned} \langle s | \mathbf{V}^{q_a g_i, b}(x_{i,ab}) | s' \rangle &= 8\pi\alpha_s C_F \delta_{ss'} \left[\frac{2}{1 - x_{i,ab}} - (1 + x_{i,ab}) \right], \\ \langle s | \mathbf{V}^{g_a \bar{q}_i, b}(x_{i,ab}) | s' \rangle &= 8\pi\alpha_s T_R [1 - 2x_{i,ab}(1 - x_{i,ab})] \delta_{ss'}, \\ \langle \mu | \mathbf{V}^{q_a q_i, b}(x_{i,ab}) | \nu \rangle &= 8\pi\alpha_s C_F \left[-g^{\mu\nu} x_{i,ab} \right. \\ &\quad \left. + \frac{1 - x_{i,ab}}{x_{i,ab}} \frac{2p_a \cdot p_b}{p_i \cdot p_a p_i \cdot p_b} \left(p_i^\mu - \frac{p_i p_a}{p_b p_a} p_b^\mu \right) \left(p_i^\nu - \frac{p_i p_a}{p_b p_a} p_b^\nu \right) \right], \\ \langle \mu | \mathbf{V}^{g_a g_i, b}(x_{i,ab}) | \nu \rangle &= 16\pi\alpha_s C_A \left[-g^{\mu\nu} \left(\frac{x_{i,ab}}{1 - x_{i,ab}} + x_{i,ab}(1 - x_{i,ab}) \right) \right. \\ &\quad \left. + \frac{1 - x_{i,ab}}{x_{i,ab}} \frac{p_a \cdot p_b}{p_i \cdot p_a p_i \cdot p_b} \left(p_i^\mu - \frac{p_i p_a}{p_b p_a} p_b^\mu \right) \left(p_i^\nu - \frac{p_i p_a}{p_b p_a} p_b^\nu \right) \right]. \end{aligned} \quad (3.28)$$

Final state singularities with initial state spectators (final-initial dipoles)

The dipole in (3.21) for a final state singularity with an initial state parton as spectator, fig. 3.5, reads [37]

$$\mathcal{D}_{12}^a(p_1, p_2; p_a, p_b) = -\frac{1}{2p_1 \cdot p_2} \frac{1}{x_{12,a}} \langle \tilde{1}\tilde{2}; \tilde{a}, b | \frac{\mathbf{T}_a \cdot \mathbf{T}_{12}}{\mathbf{T}_{12}^2} \mathbf{V}_{12}^a | \tilde{1}\tilde{2}; \tilde{a}, b \rangle, \quad (3.29)$$

with subtraction dipole-kinematics

$$\tilde{p}_a^\mu = x_{12,a} p_a^\mu, \quad \tilde{p}_{12}^\mu = p_1^\mu + p_2^\mu - (1 - x_{12,a}) p_a^\mu, \quad x_{12,a} = 1 - \frac{p_1 \cdot p_2}{(p_1 + p_2) \cdot p_a}. \quad (3.30)$$

Energy and momentum conservation in the dipole's Born matrix element applies analogously to the initial-final dipole kinematics of (3.19). The color coefficient of the

final-initial dipoles can be computed similarly to (3.20), and the spin correlation matrix \mathbf{V}_{12}^a is given by

$$\begin{aligned}
\langle s | \mathbf{V}_{q_1 g_2}^a(\tilde{z}_i, x_{12,a}) | s' \rangle &= 8\pi\alpha_s C_F \left[\frac{2}{1 - \tilde{z}_i + (1 - x_{12,a})} - (1 + \tilde{z}_i) \right] \delta_{ss'}, \\
\langle \mu | \mathbf{V}_{g_1 g_2}^a(\tilde{z}_i, x_{12,a}) | \nu \rangle &= 16\pi\alpha_s C_A \left[-g^{\mu\nu} \left(\frac{1}{1 - \tilde{z}_1 + (1 - x_{12,a})} - 2 \right. \right. \\
&\quad \left. \left. + \frac{1}{1 - \tilde{z}_2 + (1 - x_{12,a})} \right) + \frac{1}{p_1 \cdot p_2} (\tilde{z}_1 p_1^\mu - \tilde{z}_2 p_2^\mu)(\tilde{z}_1 p_1^\nu - \tilde{z}_2 p_2^\nu) \right], \\
\langle \mu | \mathbf{V}_{q_1 \bar{q}_2}^a(\tilde{z}_1) | \nu \rangle &= 8\pi\alpha_s T_R \left[-g^{\mu\nu} - \frac{2}{p_1 \cdot p_2} (\tilde{z}_1 p_1^\mu - \tilde{z}_2 p_2^\mu)(\tilde{z}_1 p_1^\nu - \tilde{z}_2 p_2^\nu) \right],
\end{aligned} \tag{3.31}$$

where

$$\tilde{z}_1 = \frac{p_1 \cdot \tilde{p}_a}{\tilde{p}_{12} \cdot \tilde{p}_a}, \quad \tilde{z}_2 = 1 - \tilde{z}_1. \tag{3.32}$$

Numerical implementation of the dipoles and checks

The dipoles that are needed to render the real emission matrix elements of (3.9) IR-finite, following (3.15), have been numerically set up using modified HELAS routines generated with MADGRAPH. The modifications are such that the HELAS-code calculates the spin-1 Born-level currents with subtraction kinematics (3.17), (3.24), and (3.30), which are globally provided for every phase space point. From these currents the spin-correlated, color and helicity-summed and -averaged matrix elements (3.21), (3.28), and (3.31) are evaluated numerically, multiplying the color coefficient, which is determined according to the rule of (3.20). If needed, the spin-diagonal dipoles are easily recovered from these four-vector currents, via

$$\begin{aligned}
\sum_\lambda \mathcal{M}^\mu \varepsilon_\mu^{(\lambda)} (\mathcal{M}^\nu \varepsilon_\nu^{(\lambda)})^* &= \sum_\lambda \mathcal{M}^\mu (\mathcal{M}^\nu)^* \varepsilon_\mu^{(\lambda)} (\varepsilon_\nu^{(\lambda)})^* \\
&\hookrightarrow \sum_\lambda \mathcal{M}^\mu (\mathcal{M}^\nu)^* (-g_{\mu\nu}) = - \sum_\lambda |\mathcal{M}|^2,
\end{aligned} \tag{3.33}$$

avoiding redundant evaluations of matrix elements. The replacement in the second line follows from current conservation and the construction of the dipoles' tilded momenta ($k^\mu \mathcal{M}_\mu = 0$).

Throughout, unnecessary re-evaluation of leading order matrix elements and currents is avoided, i.e. the calculated Born current for a single phase space point is stored, and entirely recycled into the numerics of other subprocesses' dipoles with identical kinematics by multiplying and contracting with the appropriate color and spin functions, respectively. Entire dipoles are re-used if possible, by using, e.g. $\mathcal{D}_{Q\bar{Q}}^{\bar{q}q} = \mathcal{D}_{Q\bar{Q}}^{qq}$, $\mathcal{D}_{q\bar{q}}^Q = \mathcal{D}_{q'\bar{q}'}^Q$ etc.

Besides avoiding redundancy, (3.33) provides a method to check the previously mentioned modifications directly against squared helicity amplitudes from MADGRAPH.

Table 3.3: List of the partonic subprocess of the real emission contribution $W^- \gamma j(j)$ and $W^- Z j(j)$ production at $\mathcal{O}(\alpha_s^2 \alpha^3)$, described in sec. 3.2.1. The dashed arrow stands for the suppressed electroweak part of the amplitude, i.e. $\bar{Q}q \rightarrow gg$ should be understood as $\bar{Q}q \rightarrow \ell^- \bar{\nu}_\ell \gamma gg$ or $\bar{Q}q \rightarrow \ell^- \bar{\nu}_\ell \ell'^+ \ell'^- gg$. The right column displays the needed dipoles for the IR-subtracted real emission cross section. Flavor-blindness of the dipoles in the chiral limit guarantees that the dipoles, for the subprocesses that are separated by a comma in the first column, are identical. Not shown are subprocesses and corresponding dipoles that follow from initial-state momenta-interchange. We also do not quote multiple dipoles for subprocesses with identical quark flavors or two gluons, i.e. for $\bar{u}(p_a)\bar{u}(p_b) \rightarrow \bar{u}d$, both $\bar{u}(p_a)$ and $\bar{u}(p_b)$ may act as emitter and spectator. This leads to a doubling of dipoles for the considered subprocess, which amounts computing algebraically identical dipoles with, however, different kinematics ($p_a \leftrightarrow p_b$).

Real emission subprocess	dipoles
$\bar{u}\bar{u} \rightarrow \bar{u}d, \bar{c}\bar{c} \rightarrow \bar{c}\bar{s}$	$\mathcal{D}_{\bar{d}}^{\bar{u}\bar{u}}, \mathcal{D}^{\bar{u}\bar{u},\bar{u}}$
$\bar{u}u \rightarrow u\bar{d}, \bar{c}c \rightarrow c\bar{s}$	$\mathcal{D}_{\bar{d}}^{uu}, \mathcal{D}^{uu,\bar{u}}$
$\bar{u}d \rightarrow u\bar{u}, \bar{c}s \rightarrow c\bar{c}$	$\mathcal{D}_u^{\bar{u}\bar{u}}, \mathcal{D}^{\bar{u}\bar{u},d},$ $\mathcal{D}_{u\bar{u}}^{\bar{u}}, \mathcal{D}_{u\bar{u}}^d$
$ud \rightarrow uu, cs \rightarrow cc$	$\mathcal{D}_u^{uu}, \mathcal{D}^{uu,d}$
$dd \rightarrow du, ss \rightarrow sc$	$\mathcal{D}_u^{dd}, \mathcal{D}^{dd,d}$
$\bar{d}\bar{u} \rightarrow \bar{d}\bar{d}, \bar{s}\bar{c} \rightarrow \bar{s}\bar{s}$	$\mathcal{D}_{\bar{d}}^{\bar{d}\bar{d}}, \mathcal{D}^{\bar{d}\bar{d},\bar{u}}$
$\bar{u}d \rightarrow d\bar{d}, \bar{c}s \rightarrow s\bar{s}$	$\mathcal{D}_{\bar{d}}^{dd}, \mathcal{D}^{dd,\bar{u}},$ $\mathcal{D}_{d\bar{d}}^{\bar{u}}, \mathcal{D}_{d\bar{d}}^{\bar{d}}$
$\bar{d}d \rightarrow u\bar{d}, \bar{s}s \rightarrow c\bar{s}$	$\mathcal{D}_{\bar{d}}^{\bar{d}d}, \mathcal{D}^{\bar{d}d,d}$
$\bar{u}u \rightarrow \bar{s}c, \bar{c}c \rightarrow \bar{d}u$	none
$\bar{u}d \rightarrow \bar{s}s, \bar{c}s \rightarrow \bar{d}d$	$\mathcal{D}_{\bar{s}s}^{\bar{u}}, \mathcal{D}_{\bar{s}s}^d$
$\bar{u}d \rightarrow \bar{c}\bar{c}, \bar{c}s \rightarrow u\bar{u}$	$\mathcal{D}_{\bar{c}\bar{c}}^{\bar{u}}, \mathcal{D}_{\bar{c}\bar{c}}^d$
$\bar{u}s \rightarrow \bar{u}c, \bar{c}d \rightarrow \bar{c}u$	$\mathcal{D}_c^{\bar{u}\bar{u}}, \mathcal{D}^{\bar{u}\bar{u},s}$
$\bar{u}\bar{s} \rightarrow \bar{d}\bar{s}, \bar{c}\bar{d} \rightarrow \bar{s}\bar{d}$	$\mathcal{D}_{\bar{d}}^{\bar{s}\bar{s}}, \mathcal{D}^{\bar{s}\bar{s},\bar{u}}$
$\bar{u}s \rightarrow \bar{d}s, \bar{c}d \rightarrow \bar{s}d$	$\mathcal{D}_{\bar{d}}^{ss}, \mathcal{D}^{ss,\bar{u}}$
$\bar{u}\bar{c} \rightarrow \bar{u}\bar{s}, \bar{c}\bar{u} \rightarrow \bar{c}\bar{d}$	$\mathcal{D}_{\bar{s}}^{\bar{u}\bar{u}}, \mathcal{D}^{\bar{u}\bar{u},\bar{c}}$
$\bar{u}c \rightarrow \bar{d}c, \bar{c}u \rightarrow \bar{s}u$	$\mathcal{D}_{\bar{d}}^{cc}, \mathcal{D}^{cc,\bar{u}}$
$us \rightarrow uc, cd \rightarrow cu$	$\mathcal{D}_c^{uu}, \mathcal{D}^{cc,s}$
$\bar{d}d \rightarrow \bar{s}c, \bar{s}s \rightarrow \bar{d}u$	none
$\bar{d}s \rightarrow \bar{d}c, \bar{s}d \rightarrow \bar{s}u$	$\mathcal{D}_c^{\bar{d}\bar{d}}, \mathcal{D}^{\bar{d}\bar{d},s}$
$ds \rightarrow us, sd \rightarrow cd$	$\mathcal{D}_u^{ss}, \mathcal{D}^{ss,d}$
$\bar{u}d \rightarrow gg, \bar{c}s \rightarrow gg$	$\mathcal{D}_g^{\bar{u}g}, \mathcal{D}^{\bar{u}g,d}$ $\mathcal{D}_g^{dg}, \mathcal{D}^{dg,\bar{u}},$ $\mathcal{D}_{gg}^{\bar{u}}, \mathcal{D}_{gg}^d$
$\bar{u}g \rightarrow dg, \bar{c}g \rightarrow sg$	$\mathcal{D}_g^{\bar{u}g}, \mathcal{D}^{\bar{u}g,g}$ $\mathcal{D}_d^{gg}, \mathcal{D}^{gg,\bar{u}}$
$dg \rightarrow ug, sg \rightarrow cg$	$\mathcal{D}_g^{dg}, \mathcal{D}^{dg,g}$ $\mathcal{D}_u^{gg}, \mathcal{D}^{gg,d}$
$gg \rightarrow u\bar{d}, gg \rightarrow c\bar{s}$	$\mathcal{D}_{\bar{d}}^{gu}, \mathcal{D}^{gu,g},$ $\mathcal{D}_u^{g\bar{d}}, \mathcal{D}^{g\bar{d},g}$

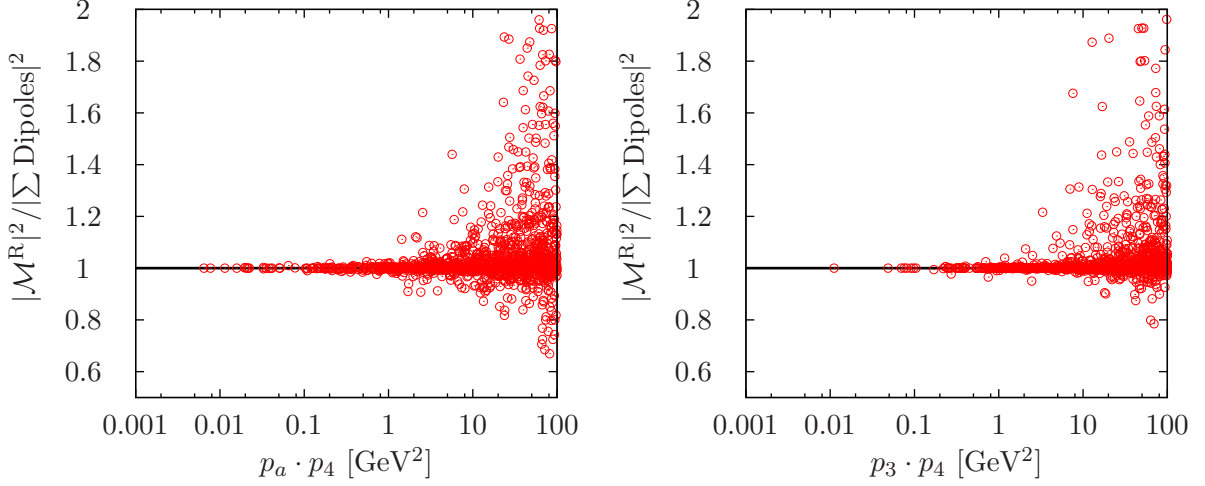


Figure 3.7: Ratio of the real emission matrix element for the process $pp \rightarrow W\gamma j(j) + X$ at $\mathcal{O}(\alpha_s^2\alpha^3)$ and the subtraction dipoles, Tab. 3.3, in the limits $p_a \cdot p_4 \rightarrow 0$ (left panel) and $p_3 \cdot p_4 \rightarrow 0$ (right panel) for 10^5 randomly chosen phase space points.

Furthermore, numerical checks have been performed at the dipole-level against the automated MADDIPOLES [75] framework, yielding agreement of all dipoles involved in the calculation. Numerical stability over the whole phase space is assured by comparing phase space-integrated dipoles (or to be more precise, by checking that the integrated difference of the two implementation is numerically compatible with zero). Additionally, the cancellation of the IR-singular behavior of the real matrix element against the dipoles in the respective phase space regions has been checked explicitly for the sum, as well as for individual subprocesses. Fig. 3.7 demonstrates these numerical cancellations for the sum of all subprocesses. Writing

$$\begin{aligned} \tilde{\sigma}_{ab}^{\text{R-A}} = & \frac{f_{a/P}(x_a, \mu_F^2) f_{b/P}(x_b, \mu_F^2)}{n_s(a)n_s(b)n_c(a)n_c(b)S_f} \frac{1}{\Phi(p_a \cdot p_b)} \\ & \times \left[|\mathcal{M}_{ab}^{\text{R}}(p_a, p_b, p_1, p_2, q_1, \dots, q_n)|^2 \mathcal{F}(p_1, p_2, q_1, \dots, q_n) \right. \\ & - \left(\sum_{i=1,2, k \neq i} \mathcal{D}_k^{ai}(p_a, p_1, p_2) \mathcal{F}(\tilde{p}_1, q_1, \dots, q_n) + \sum_{i=1,2} \mathcal{D}^{ai,b}(p_a, p_1, p_2) \mathcal{F}(\tilde{p}_1, \tilde{q}_1, \dots, \tilde{q}_n) \right. \\ & \left. \left. + \mathcal{D}_{12}^a(p_a, p_1, p_2) \mathcal{F}(\tilde{p}_1, q_1, \dots, q_n) \right) - (a \leftrightarrow b) \right], \quad (3.34a) \end{aligned}$$

with the final state symmetry factor S_f , we can take the $\varepsilon \rightarrow 0$ limit, and the Monte-Carlo integration of the IR-subtracted differential real emission cross section is performed by summing the pdf-weighted differential partonic cross sections, multiplied by the corresponding phase space factor,

$$\sigma^{\text{R-A}} = \sum_{\{a,b\}} \iiint d\text{LIPS}_{2+\text{elw}}(p_a, p_b, p_1, p_2, q_1, \dots, q_n) dx_a dx_b \Theta(\mathcal{C}) \tilde{\sigma}_{ab}^{\text{R-A}}. \quad (3.34b)$$

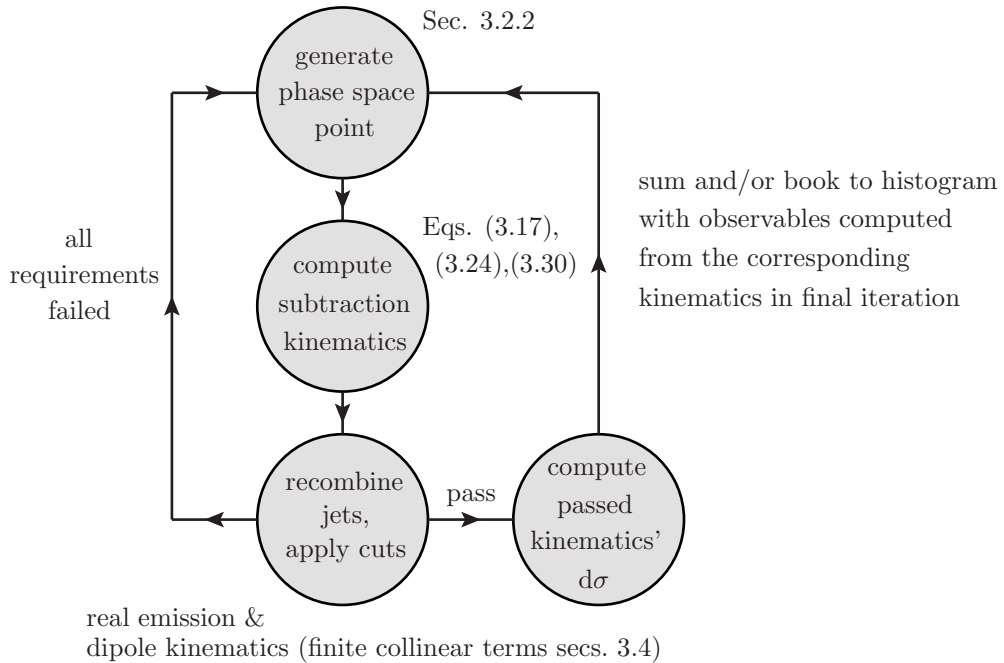


Figure 3.8: Flow chart of the Monte Carlo integration of the IR-subtracted real emission differential cross section.

The event generation is steered as described in secs. 3.2.2 and 2.2.6. Fig. 3.8 sketches the translation of (3.34) into our Monte-Carlo implementation.

To avoid numerical instabilities that result from numerically incomplete cancellations in the very soft and very collinear phase space region, we introduce a technical cut-off on the invariant parton-parton masses, which we choose to be larger than $(100 \text{ MeV})^2$. In these regions of phase space the squared matrix elements and the dipoles diverge, and the level, at which the cancellation is required, tests numerical precision, which is limited by the number of available digits. In fact, the phase space weights for these momentum configurations are small, so that these points do not spoil the numerical implementation but they tend to slow down the numerical convergence of the Monte Carlo program. By construction, the cancellations in these phase space regions are exact (cf. also fig. 3.7). Introducing this technical cut-off amounts to numerically stabilizing the implementation, with a numerical impact on the cross sections well below the statistical integration error.

3.3 Virtual contributions

The calculation of the virtual amplitude comprises all loop corrections to the Born-level topologies of figs. 3.1 and 3.3. These give rise to loop diagrams up to boxes and pentagons, respectively. We can use the fact that all divergencies, either of UV- or IR-character, will reproduce the Born matrix element as coefficient of the divergencies at the one loop level. This is formally expressed by a simple multiplicative renormalization

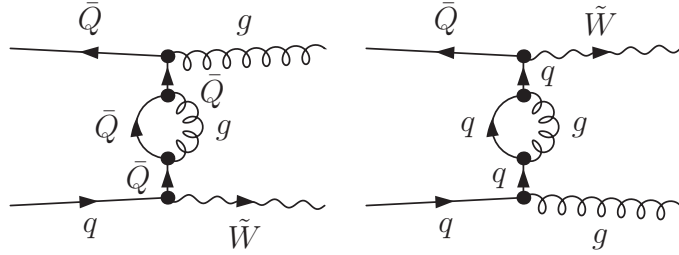


Figure 3.9: Self-energy corrections contained in the boxline building block, i.e. the self-energy contribution to $q\bar{Q} \rightarrow \tilde{W}g$ at $\mathcal{O}(g_s^3)$. The \tilde{W} decay current follows from fig. 3.2.

of the amplitude and factorization of soft and collinear divergencies, e.g. the Catani-Seymour subtraction method.

As the SM is a product-group gauge theory, the QCD-corrections are also entirely independent of the electroweak sector, except for kinematical invariants determined by the electroweak masses. This is simply a more precise formulation of the loose consistency-requirement, that "QCD does not renormalize electroweak charge". A conventional choice for our purposes would therefore be calculating the virtual corrections to $q\bar{Q} \rightarrow W^\pm g$ and $qq \rightarrow W^+W^-g$ production with triple-gauge boson couplings set to zero and stripping off the chiral electroweak couplings from the amplitude. Replacing one of the effective W polarization vectors in the latter case by, e.g. the photon polarization vector multiplying the appropriate vectorial coupling, effectively amounts to calculating half of the one-loop Feynman graphs which are involved in the virtual corrections. The remaining set is easily recovered by permuting the remaining W and the photon. We explicitly demonstrate this strategy in secs. 3.3.1, A.1, and A.2.

This method effectively describes how to build one-loop amplitudes from a generic set of building blocks, which are assembled for the specific process under consideration. In our case, the building blocks consist of all self-energy-, triangle-, box-, and pentagon-corrections, combined to a single routine, i.e. the corrections to $q(p_a)\bar{Q}(p_b) \rightarrow \tilde{W}g$ yield topologies up to boxes, and virtual contributions to $q(p_a)\bar{Q}(p_b) \rightarrow W^*\gamma^{(*)}g$, $q(p_a)\bar{Q}(p_b) \rightarrow W^*Z^*g$ giving rise to topologies up to pentagons. We will refer to these building blocks as "boxline" and "pentline" corrections. The effective currents \tilde{W} , W^* , etc. follow from sec. 3.1, and the remaining subprocesses (3.1), and (3.2) are then related by crossing.

3.3.1 'Boxline' corrections

The virtual corrections to $q(p_a)\bar{Q}(p_b) \rightarrow \tilde{W}g$, using the methods of sec. 2.2, are calculated from the sum of self-energy diagrams (fig. 3.9), triangle- and box-diagrams (figs. 3.10 and 3.11). While the topologies of fig. 3.10 are QED-like, the color factors are mixed abelian – non-abelian,

$$t^a t^c t^a = \left(C_F - \frac{C_A}{2} \right) t^c, \quad (3.35)$$

if the gluon couples to the loop-fermion in fig. 3.10 (b), (c), (e), (f). The triple-gluon-vertex in the diagrams of fig. 3.11 give rise to purely non-abelian color structures,

$$-if^{abc}t^at^b = \frac{C_A}{2}t^c, \quad (3.36)$$

while the remaining diagrams in fig. 3.10 with the \tilde{W} attached to the loop, and the self-energy diagrams are purely abelian

$$t^at^at^c = t^ct^at^a = C_F t^c. \quad (3.37)$$

Note that the color factors (3.35) and (3.36) do only differ by the sign from the ones encountered in the dipoles (3.20). Moreover, the color and spin structure of the one-loop amplitude is identical to one encountered in the leading order amplitude, so that averaging and summing over spins and colors of the interference term $\mathcal{M}^V(\mathcal{M}^B)^*$ follows immediately from the leading order part of the calculation. We therefore suppress the $\mathfrak{su}(3)$ generators in the following and focus on color-stripped amplitudes, also suppressing the spin indices.

As we consider a diagonal CKM matrix and neglect bottom quark contributions, massive top-quarks are absent. Therefore, the counter term amplitude to order $\mathcal{O}(g_s^3)$, fig. 3.12, factorizes

$$\begin{aligned} \mathcal{M}_{\text{CT}}^{\text{1loop},\tilde{W}} &= \mathcal{M}_{\text{LO}}^{\tilde{W}}\delta_1 \\ &= \mathcal{M}_{\text{LO}}^{\tilde{W}}\left(\delta_{g_s} + \delta_\psi + \frac{1}{2}\delta_A\right), \end{aligned} \quad (3.38)$$

where the on-shell and $\overline{\text{MS}}$ renormalization constants have already been provided in

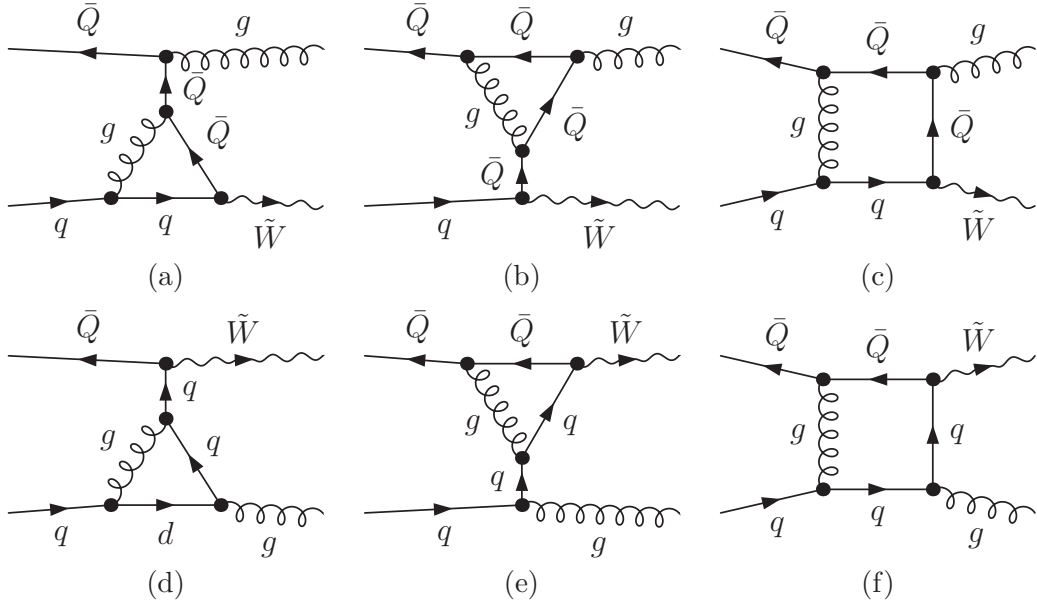


Figure 3.10: Abelian (left column) and mixed abelian – non-abelian triangle- and box corrections of the boxline building block, i.e. the triangle and box contribution to $q\bar{q}\tilde{W}g$ at $\mathcal{O}(g_s^3)$. The decay current \tilde{W} can be found in fig. 3.2.

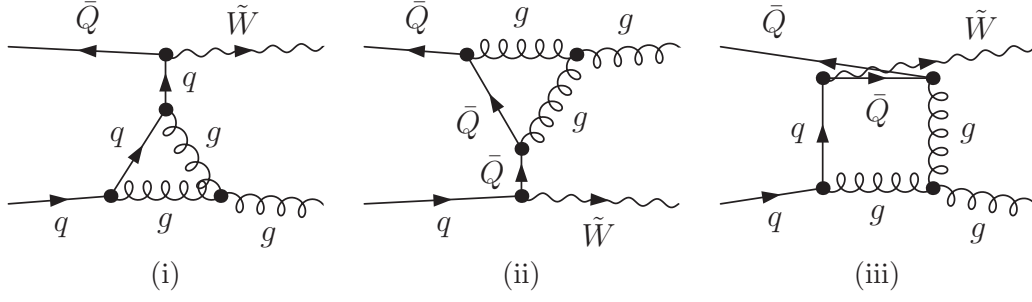


Figure 3.11: Non-abelian triangle- and box contributions to the non-abelian boxline building block, e.g. to $q\bar{Q} \rightarrow \tilde{W}g$ at $\mathcal{O}(g_s^3)$. The decay currents can be found in fig. 3.2.

eqs. (2.61) and (2.63),

$$\begin{aligned} \delta_\psi &= 0, \\ \delta_A &= -\frac{\alpha_s}{4\pi} \frac{4T_r}{3} \bar{\mathcal{S}}^{\text{UV}}(m_t), \\ \delta_{g_s} &= \frac{\alpha_s}{4\pi} \left[\left(\frac{2N_f T_r}{3} - \frac{11C_A}{6} \right) \bar{\mathcal{S}}^{\text{UV}}(\mu_R) + \frac{2T_r}{3} \bar{\mathcal{S}}^{\text{UV}}(m_t) \right], \end{aligned} \quad (3.39)$$

so that

$$\mathcal{M}_{\text{CT}}^{\text{1loop}, \tilde{W}} = \mathcal{M}_{\text{LO}}^{\tilde{W}} \left(\frac{2N_f T_r}{3} - \frac{11C_A}{6} \right) \bar{\mathcal{S}}^{\text{UV}}(\mu_R), \quad (3.40)$$

where we have also used $\bar{\mathcal{S}}^{\text{UV}}(\tilde{\mu}) = \bar{\mathcal{S}}^{\text{IR},1}(\tilde{\mu})$ of (2.58).

The renormalization does only depend on the number of external fermion and gluon fields, and the number of strong couplings. Emitting two gauge bosons from the same

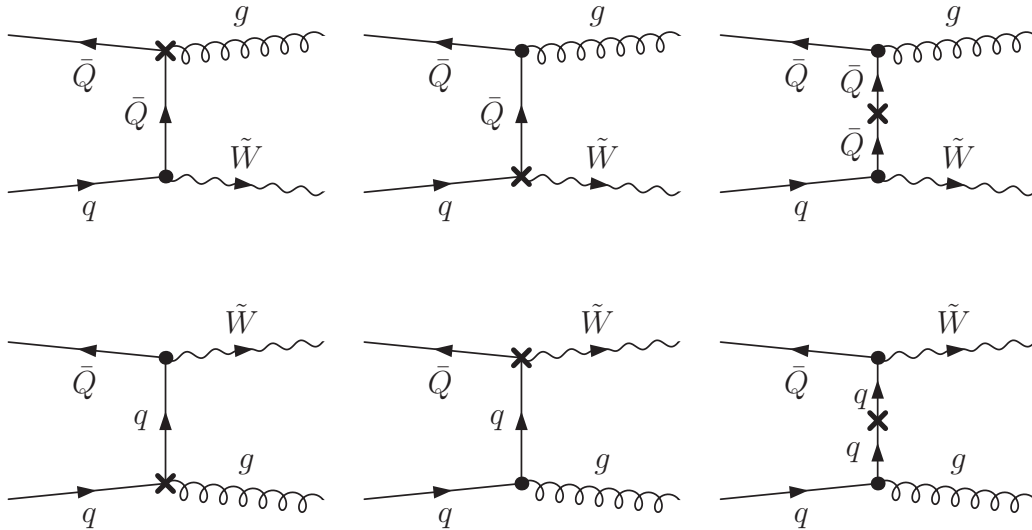


Figure 3.12: Counter term diagrams contributing to $q\bar{Q} \rightarrow \tilde{W}g$ at $\mathcal{O}(g_s^3)$.

quark line, i.e. for the pentline contribution $q\bar{Q} \rightarrow W^*\gamma g$ (cf. fig 3.3) to be discussed in sec. 2.2.4, the renormalization constants are identical. Having renormalized the amplitude's UV divergencies, we quote the result of the virtual corrections in $d = 4 - 2\varepsilon$ conventional dimensional regularization, which now only contains IR singularities.

$$\begin{aligned} \mathcal{M}_{\text{Virt+CT}}^{\text{1Loop},\tilde{W}} &= \frac{\alpha_s(\mu_R^2)}{4\pi} \frac{\mathcal{M}_{\text{LO}}^{\tilde{W}}}{\Gamma(1-\varepsilon)} \left[\frac{1}{2} \left\{ \left(\frac{4\pi\mu_R^2}{-u} \right)^\varepsilon + \left(\frac{4\pi\mu_R^2}{-t} \right)^\varepsilon \right\} \left(-\frac{C_A}{\varepsilon^2} - \frac{\gamma_g}{\varepsilon} \right) \right. \\ &+ \frac{C_A}{2C_F} \left\{ \left(\frac{4\pi\mu_R^2}{-u} \right)^\varepsilon + \left(\frac{4\pi\mu_R^2}{-t} \right)^\varepsilon - 2 \left(\frac{4\pi\mu_R^2}{-s} \right)^\varepsilon \right\} \left(-\frac{C_F}{\varepsilon^2} - \frac{\gamma_q}{\varepsilon} \right) \\ &\left. + 2 \left(\frac{4\pi\mu_R^2}{-s} \right)^\varepsilon \left(-\frac{C_F}{\varepsilon^2} - \frac{\gamma_q}{\varepsilon} \right) \right] + \widetilde{\mathcal{M}}_{\text{Virt}}^{\tilde{W}}(-s, -t, -u). \end{aligned} \quad (3.41)$$

$\widetilde{\mathcal{M}}_{\text{Virt}}^{\tilde{W}}$ represents finite contributions. These embrace tensor coefficients that multiply fermion chains, and additional constants and logarithms proportional to the leading order amplitude, which arise from putting the virtual contribution to the algebraic form of (3.41). Also included are the rational terms of UV origin. The parameters γ_q, γ_g are fixed by the $\mathfrak{su}(3)$ representation, under which the quarks and gluons transform. They are quoted as part of the Catani-Seymour formulae in appendix B. s, t, u are the well-known Mandelstam variables of $2 \rightarrow 2$ processes,

$$s = (p_a + p_b)^2, \quad t = (p_a - p_1)^2, \quad u = (p_b - p_1)^2. \quad (3.42)$$

The logarithms that appear in the virtual corrections can be analytically continued from the space-like momentum configuration to physical regions by restoring the ε -prescription of the propagators, which amounts to replacements, e.g.

$$\log(-s) = \log(|s|) - i\pi \Theta(-s). \quad (3.43)$$

These replacements are performed automatically in the numerical code.

Possible complications arising from d -dimensional formulations of γ_5 are avoided by choosing identical prescriptions for γ_5 in both the virtual and the real emission calculations by neglecting terms from γ_5 permutations in $d \neq 4$ throughout. This method is described in [76]. It is also known from various calculations, e.g. [77, 78], that applying dimensional reduction [79] or the 't Hooft-Veltman-Breitenlohner-Maison scheme [14, 80] reproduces identical results at the cross section level compared to the method laid out.

We are now ready to construct the boxline building-blocks. By combining the upper lines of Feynman diagrams and counter terms of figs. 3.10 and 3.12 and the first diagram of fig. 3.9 we end up with the set of diagrams of fig. 3.13, which we refer to as abelian boxline

$$\mathcal{B}^A(p_a, p_b; p_1, \{q_i\}; \varepsilon_g^*, J(\tilde{W})) = C_F (\mathcal{M}_{\text{ren}}^{(a)} + \mathcal{M}_{\text{ren}}^{(b)}) + \left(C_F - \frac{C_A}{2} \right) (\mathcal{M}_{\text{ren}}^{(c)} + \mathcal{M}_{\text{ren}}^{(d)}), \quad (3.44)$$

where the various renormalized one-loop contributions are in one-to-one correspondence to the diagrams depicted in fig. 3.13, suppressing again color and spin indices. The

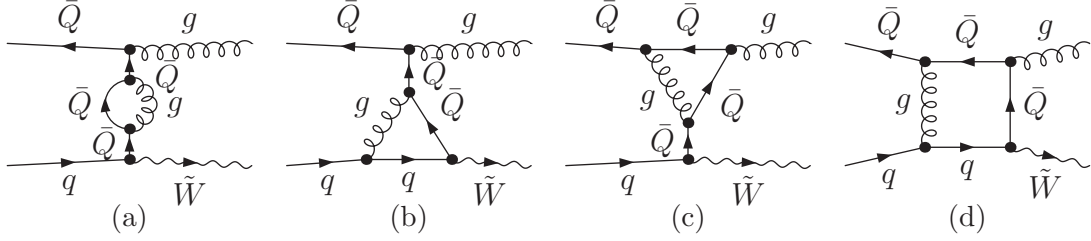


Figure 3.13: Feynman graph topologies contributing to the abelian boxline building block. Not shown are the counter term graphs of fig. 3.12 that renormalize the corresponding graphs.

numerical implementation of the abelian boxline building block calculates the diagram combinations which are quoted in the parentheses in 3.44 without specific couplings or color factors. The color factors and the couplings, that are not already included in the definition of the effective currents, are multiplied[‡] with the numerical result of the boxline routine subsequently. The purely abelian limit that follows from changing the gluon polarization vector to an (effective) electroweak current is recovered by setting $C_A = 0$.

The remaining abelian-like topologies which contribute to the full one-loop amplitude with up two gauge boson attached to the quark line can be evaluated from this building block by making the replacements $p_1 \leftrightarrow p_{\tilde{W}} = \sum_i q_i$ for the momenta accompanied by $J(\tilde{W}\{q_i\}) \leftrightarrow \varepsilon_g^*(p_1)$ and the permutation $\mathcal{M}^{(b)} \leftrightarrow \mathcal{M}^{(c)}$ in fig. 3.13 and eq. (3.44).

The remaining non-abelian diagrams are combined to the non-abelian boxline, which computes numerically

$$\mathcal{B}^{\text{NA}}(p_a, p_b; p_1, \{q_i\}; \varepsilon_g^*, J(\tilde{W})) = C_A (\mathcal{M}_{\text{ren}}^{(i)} + \mathcal{M}_{\text{ren}}^{(ii)} + \mathcal{M}_{\text{ren}}^{(iii)}) , \quad (3.45)$$

where the renormalized one-loop contributions on the right-hand side correspond again to the Feynman graphs of fig. 3.11. Coupling constants associated with quarks and gluons, and color factors are again multiplied outside the numerical loop calculation. We can write the complete one-loop contribution to the topologies that involve up to two gauge bosons and the effective \tilde{W} current as

$$\begin{aligned} \widetilde{\mathcal{M}}_{\text{Virt}}^{\tilde{W}}(-s, -t, -u) &= \mathcal{B}^{\text{A}}(p_a, p_b; p_1, \{q_i\}; \varepsilon_g^*, J(\tilde{W})) + \mathcal{B}^{\text{A}}(p_a, p_b; \{q_i\}, p_1; J(\tilde{W}), \varepsilon_g^*) \\ &+ \mathcal{B}^{\text{NA}}(p_a, p_b; p_1; \{q_i\}; \varepsilon_g^*; J(\tilde{W})) . \end{aligned} \quad (3.46)$$

It is technically desirable to code the abelian and non-abelian boxlines as tensors, that later get contracted with the respective polarizations and effective currents

$$\begin{aligned} \mathcal{B}^{\text{A}}(p_a, p_b; p_1, \{q_i\}; \varepsilon_g^*, J(\tilde{W})) &= (\varepsilon_g^\mu)^* J^\nu(\tilde{W}) \widetilde{\mathcal{B}}_{\mu\nu}^{\text{A}}(p_a, p_b; p_1, \{q_i\}) , \\ \mathcal{B}^{\text{NA}}(p_a, p_b; p_1, \{q_i\}; \varepsilon_g^*, J(\tilde{W})) &= (\varepsilon_g^\mu)^* J^\nu(\tilde{W}) \widetilde{\mathcal{B}}_{\mu\nu}^{\text{NA}}(p_a, p_b; p_1, \{q_i\}) . \end{aligned} \quad (3.47)$$

[‡]Note, that the quarks are left-handed throughout.

This not only allows a more transparent summation over permutations (3.46), but also provides a method for numerical gauge checks, and numerical improvements by exploiting Ward identities, see sec. 3.3.5.

Eq. (3.41) has been determined using FEYNARTS [81] to generate the leading order, and one-loop Feynman diagrams. A modified version of FORMCALC [82] is used to translate the diagrams into a series of tensor coefficients and a basis of fermion chains, i.e. the standard matrix elements [49]. The modifications are such that the full d -dimensional dependence is kept throughout, incorporating all IR singularities. The output is then further processed with purpose-built MATHEMATICA-routines based on FEYNCALC [74], that reduce the tensor coefficients to scalar integrals in dimensional regularization, which are known from the literature, see e.g. [50]. After renormalization by counter terms, this allows to extract the infrared poles of the one-loop amplitudes. Matching the one-loop standard matrix elements onto the leading order ones, we recover the Born-level amplitude in (3.41).

This method allows to fully keep track of the rational terms (cf. the discussion below (2.46)), which turn out to be entirely of UV-origin. This is generic to all one-loop QCD calculations, as shown in [44]. There are specific representations of the unrenormalized, truncated QCD-loop diagrams for collinear and soft loop momenta, which are manifestly free of rational terms of IR-origin. This allows to deduce that, although appearing in intermediate steps of the calculation, the amplitude is free of IR-rational terms. Thus, the absence of IR-rational terms in our calculation provides a strong algebraic test. Moreover, this can be used to calculate the virtual amplitude fully automated in $d = 4 - 2\epsilon$ dimensions by mere use of the FEYNARTS, FORMCALC, and LOOPTOOLS tool-chain [3, 44, 83]. Trading LOOPTOOLS' internal mass-regularized scalar integrals against IR-divergent scalar functions in dimensional regularization, FEYNARTS, FORMCALC, and LOOPTOOLS supply FORTRAN-Code for one-loop virtual amplitudes up to pentagons "out of the box". This reveals a very economical way to perform an independent calculation to numerically check the entire virtual calculation, sec. 3.5.

The IR-divergent part of the virtual amplitude (3.41) is already known from the dominant NLO QCD corrections to Higgs-production associated with three jets in vector boson-fusion [84], and reduces in the limit of only electroweak gauge bosons, $C_A \rightarrow 0$, to the results of W and Z production in vector boson-fusion [71].

3.3.2 'Pentline' corrections

In analogy to figs. 3.9 - 3.11, there are 12 self-energy diagrams to the quark line with three attached gauge bosons (fig. 3.3), 18 triangle diagrams of mixed abelian–non-abelian color structure, 6 purely non-abelian triangles, 12 mixed abelian–non-abelian boxes, 4 non-abelian box diagrams and 6 abelian and 2 non-abelian pentagon diagrams. We can again deconstruct these topologies to a minimal set of graphs, which are then combined in six different ways to recover the full correction to a quark line with three attached gauge bosons per subprocess. Just as with the boxline routine, we define an abelian pentline and a non-abelian pentline set. Representatively, we just show the abelian (i.e. mixed abelian–non-abelian according to (3.35)) and non-abelian pentagon contributions in fig. 3.14. We postpone a more detailed documentation of the pentline

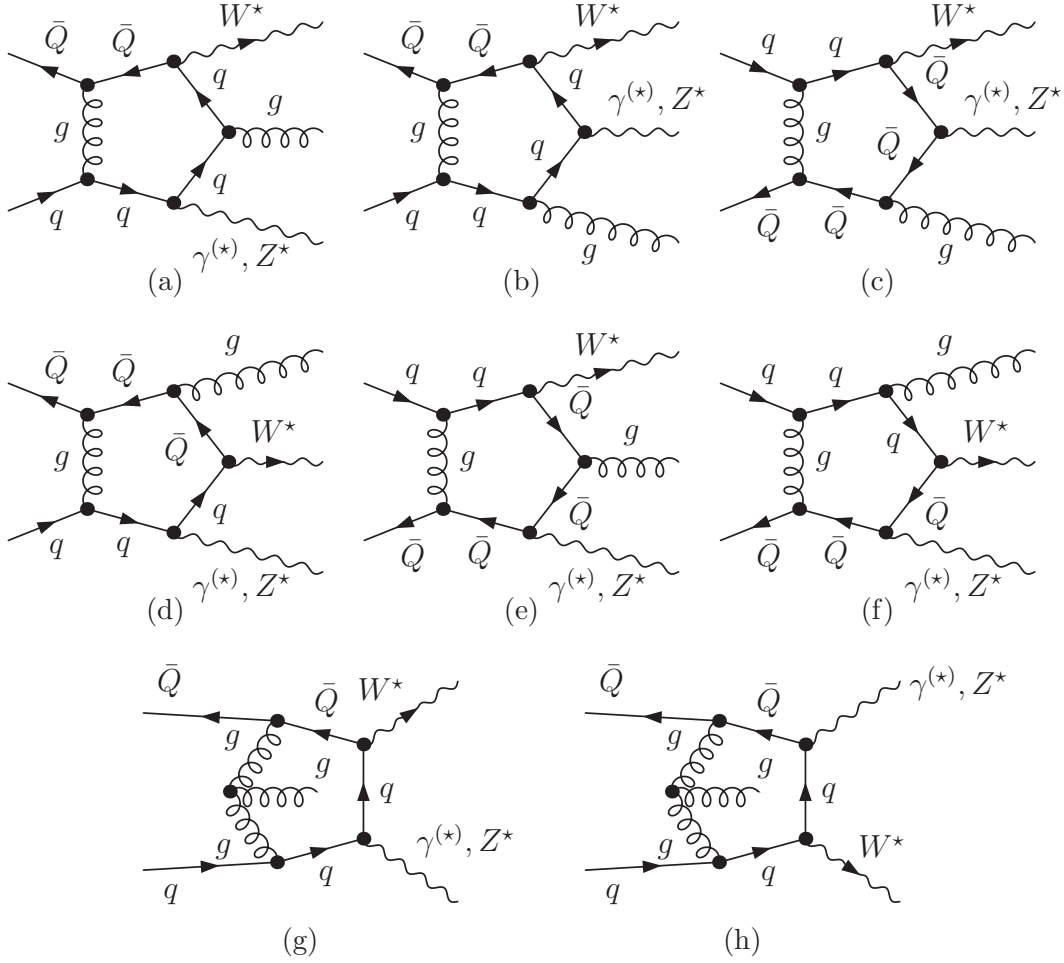


Figure 3.14: Mixed abelian–non-abelian and purely non-abelian pentagon contributions to $\bar{u}d \rightarrow g\ell^-\bar{\nu}_\ell\gamma$ via the off-shell decay of W^* at $\mathcal{O}(g_s^3)$. In $q\bar{Q} \rightarrow g\ell^-\bar{\nu}_\ell\ell'^+\ell'^-$.

building blocks along the lines of the previous section to the appendix A, where also complete diagrammatic representations of the abelian and non-abelian pentline building blocks are given.

Our strategy is already visible from fig. 3.14, however. Once fig. 3.14 (a) and (g) are known, all other pentagon graph contributions (fig. 3.14 (b)-(f),(h)) can be recovered upon summing over all allowed permutations Π of gauge bosons (cf. secs. A.1 and A.2),

$$\begin{aligned} \widetilde{\mathcal{M}}_{\text{Virt}}^{W^*} = & \sum_{(ijk) \in \Pi\{W^*, \widetilde{Z}\gamma, g\}} \mathcal{P}^{\text{A}}(p_a, p_b; p_i, p_j, p_k; \varepsilon_i, \varepsilon_j, \varepsilon_k) \\ & + \sum_{(i,j) \in \Pi\{W^*, \widetilde{Z}\gamma\}} \mathcal{P}^{\text{NA}}(p_a, p_b; p_g; p_j, p_k; \varepsilon_g^*, \varepsilon_j, \varepsilon_k), \end{aligned} \quad (3.48)$$

where we have introduced

$$\varepsilon_{W^*} = J(W^*), \quad \varepsilon_{\widetilde{Z}\gamma} = \begin{cases} J(Z^*) + J(\gamma^*), & WZj \text{ production} \\ \varepsilon_\gamma^*, & W\gamma j \text{ production} \end{cases}, \quad (3.49)$$

and

$$p_{W^*} = q_1 + q_2, \quad p_{\widetilde{Z}\gamma} = \begin{cases} q_3 + q_4, & WZj \text{ production} \\ q_3, & W\gamma j \text{ production} \end{cases} \quad (3.50)$$

for convenience.

We choose a fixed order of the electroweak gauge bosons to perform the algebra, and evaluate all diagrams by mapping the graphs onto this set of topologies, as explained in the beginning of this section. The color factors reproduce (3.35)–(3.37). The renormalization procedure follows analogously to the boxline configuration, and the result of the counter term amplitude and the UV-renormalized, IR-divergent one-loop amplitude is identical to (3.41), except for the replacement $\mathcal{M}_{\text{LO}}^{\widetilde{W}} \rightarrow \mathcal{M}_{\text{LO}}^{W^*}$, and different finite contributions. This, of course, is not accidental: Within the SM only the sum of figs. 3.1 and 3.3 gives an electroweak gauge invariant amplitude. Gauge invariance therefore dictates $\mathcal{M}_{\text{LO}}^{\widetilde{W}} \rightarrow \mathcal{M}_{\text{LO}}^{\widetilde{W}} + \mathcal{M}_{\text{LO}}^{W^*}$ in (3.41). This is also reflected in the structure of the dipoles, e.g. (3.15), which subtract identical divergencies for figs. 3.1 and 3.3.

3.3.3 Fermionic loop corrections to WZj production

Furry's theorem [85] guarantees the absence of closed fermion loop corrections to $W\gamma j$ production. However, due to the $V - A$ structure of the electroweak boson's couplings to fermions, we will have non-vanishing fermionic corrections from nested anomaly diagrams $gg \rightarrow Z^*$ to WZj production, fig. 3.15. The triangle is identically zero for the massless fermion generations, as they transform under the doublet representation of $SU(2)_W$. The third generation, with only the top-quark taken to be massiv in our

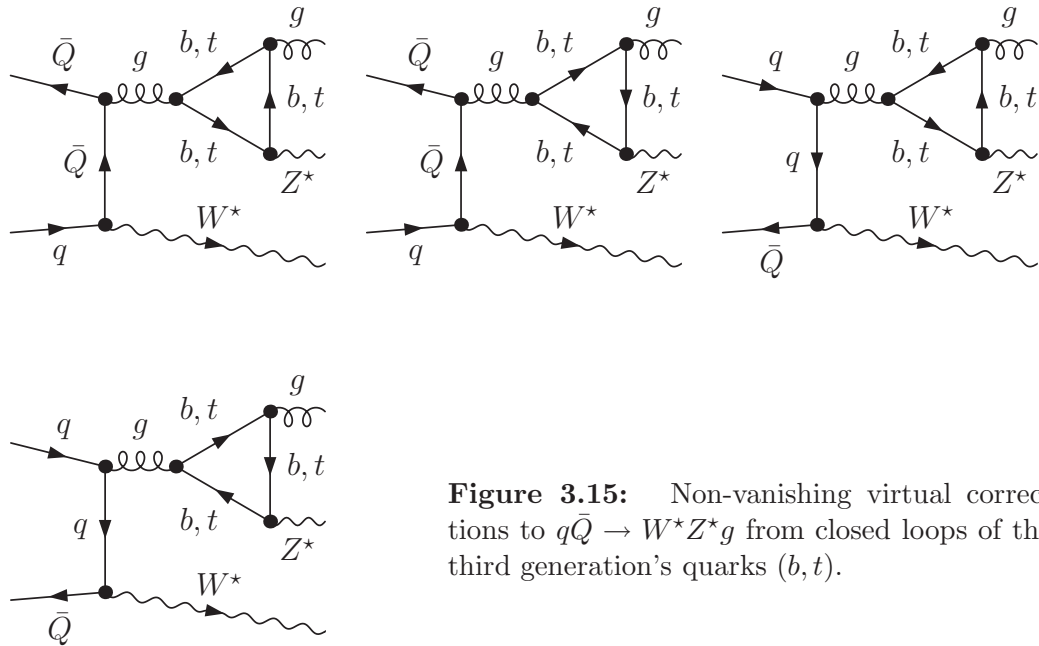


Figure 3.15: Non-vanishing virtual corrections to $q\bar{Q} \rightarrow W^*Z^*g$ from closed loops of the third generation's quarks (b, t).

approximation, yields an incompletely cancelled sum of fermion loops. The Feynman diagrams can be written

$$\mathcal{M}_{\text{Virt, ferm}}^{q_j \bar{Q}_i} = T_r t_{ij}^a (\tilde{J}^{q\bar{Q}})^\mu (W^*) \mathcal{T}_{\mu\nu\delta} (m_b - m_t; \bar{p}_g, p_1, q_3 + q_4) \Big|_{m_b=0} (\varepsilon_g^\nu)^* J^\delta(Z^*) \quad (3.51)$$

with $\bar{p}_g = p_a + p_b - q_1 - q_2$. $\tilde{J}^{q\bar{Q}}(W^*)$ denotes the effective $q\bar{Q}W^* \rightarrow g$ -current that results from embracing the first column of fig 3.15, and cutting the gluon-propagator. The color-stripped tensor \mathcal{T} is then straightforwardly calculated by summing the quark-triangle-traces with top and bottom running in both directions in the loop. We revert to the FEYNARTS-modified FORMCALC-MATHEMATICA tool-chain, described below (3.47), to show the absence of UV- and IR-divergencies, and subsequently generate the FORTRAN core-function of the tensor \mathcal{T} fully automated, by means of MATHEMATICA. The current $\tilde{J}^{q\bar{Q}}$ is set up in terms of modified HELAS routines, and the scalar integrals are inferred from the Ellis-Zanderighi library [50]. The fermionic corrections turn out to be numerically insignificant compared to the Born-, boxline- and pentline contributions. They only contribute at the sub-per mill level to the Born-plus-virtual cross section.

3.3.4 Cancellation of IR divergencies and finite remainders

Collecting the results of secs. 3.3.1, 3.3.2, and 3.3.3, we write the renormalized $q\bar{Q}$ -induced virtual matrix element

$$\begin{aligned} & 2 \operatorname{Re} \left(\mathcal{M}_{\text{Virt+CT}}^{\text{1Loop}, q\bar{Q} \rightarrow g} \left[\mathcal{M}_{\text{LO}}^{q\bar{Q} \rightarrow g} \right]^* \right) \\ &= \frac{\alpha_s(\mu_R^2)}{2\pi} \frac{|\mathcal{M}_{\text{LO}}^{q\bar{Q} \rightarrow g}|^2}{\Gamma(1-\varepsilon)} \left[\frac{1}{2} \left\{ \left(\frac{4\pi\mu_R^2}{-u} \right)^\varepsilon + \left(\frac{4\pi\mu_R^2}{-t} \right)^\varepsilon \right\} \left(-\frac{C_A}{\varepsilon^2} - \frac{\gamma_g}{\varepsilon} \right) \right. \\ &+ \frac{C_A}{2C_F} \left\{ \left(\frac{4\pi\mu_R^2}{-u} \right)^\varepsilon + \left(\frac{4\pi\mu_R^2}{-t} \right)^\varepsilon - 2 \left(\frac{4\pi\mu_R^2}{s} \right)^\varepsilon \right\} \left(-\frac{C_F}{\varepsilon^2} - \frac{\gamma_q}{\varepsilon} \right) \\ &\left. + 2 \left(\frac{4\pi\mu_R^2}{s} \right)^\varepsilon \left(-\frac{C_F}{\varepsilon^2} - \frac{\gamma_q}{\varepsilon} \right) \right] + 2 \operatorname{Re} \left(\widetilde{\mathcal{M}}'_{\text{Virt}} \left[\mathcal{M}_{\text{LO}}^{q\bar{Q} \rightarrow g} \right]^* \right), \quad (3.52) \end{aligned}$$

where the analytical continuation to time-like $s > 0$ according to (3.43) has already been performed. The analytical continuation causes modifications in the finite part, along with the triangle corrections of (3.51).

The IR-divergencies cancel against the \mathbf{I} operator of (B.1). For the Born configuration with $q\bar{Q}$ initial state, we find

$$\begin{aligned} & \langle 1^g; a^q b^{\bar{Q}} | \mathbf{I} | 1^g; a^q b^{\bar{Q}} \rangle \\ &= \frac{\alpha_s(\mu_R^2)}{2\pi} \frac{\mathcal{M}_{\text{LO}}^{q\bar{Q} \rightarrow g}}{\Gamma(1-\varepsilon)} \left[\frac{1}{2} \left\{ \left(\frac{4\pi\mu_R^2}{-t} \right)^\varepsilon + \left(\frac{4\pi\mu_R^2}{-u} \right)^\varepsilon \right\} \left(\frac{C_A}{\varepsilon^2} + \frac{\gamma_g}{\varepsilon} - \frac{\pi^2 C_A}{3} + K_g + \gamma_g \right) \right. \\ &- \frac{\alpha_s(\mu_R^2)}{2\pi} \frac{\mathcal{M}_{\text{LO}}^{q\bar{Q} \rightarrow g}}{\Gamma(1-\varepsilon)} \left(\frac{C_F}{\varepsilon^2} + \frac{\gamma_q}{\varepsilon} - \frac{\pi^2 C_F}{3} + K_q + \gamma_q \right) \\ &\quad \times \left[\frac{C_A - 2C_F}{C_F} \left(\frac{4\pi\mu_R^2}{s} \right)^\varepsilon - \frac{C_A}{2C_F} \left(\frac{4\pi\mu_R^2}{-t} \right)^\varepsilon - \frac{C_A}{2C_F} \left(\frac{4\pi\mu_R^2}{-u} \right)^\varepsilon \right]. \quad (3.53) \end{aligned}$$

K_g, K_q are again fixed by the gauge representation of the quarks and gluons and their explicit definitions are given in appendix B.

Combining the \mathbf{I} operator with the virtual NLO QCD matrix element yields

$$\begin{aligned}
2 \operatorname{Re} \left(\mathcal{M}_{\text{Virt+CT}}^{\text{1Loop}, q\bar{Q} \rightarrow g} \left[\mathcal{M}_{\text{LO}}^{q\bar{Q} \rightarrow g} \right]^* \right) + \langle 1^g; a^q b^{\bar{Q}} | \mathbf{I} | 1^g; a^q b^{\bar{Q}} \rangle &= \frac{\alpha_s(\mu_R^2)}{2\pi} \frac{\mathcal{M}_{\text{LO}}^{\bar{q}Q \rightarrow g}}{\Gamma(1-\varepsilon)} \\
&\times \left[\frac{1}{2} \left\{ \left(\frac{4\pi\mu_R^2}{-t} \right)^\varepsilon + \left(\frac{4\pi\mu_R^2}{-u} \right)^\varepsilon \right\} \left(K_g + \gamma_g - \frac{\pi^2 C_A}{3} \right) - \left(K_q + \gamma_q - \frac{\pi^2 C_F}{3} \right) \right. \\
&\times \left. \left\{ \frac{C_A - 2C_F}{C_F} \left(\frac{4\pi\mu_R^2}{s} \right)^\varepsilon - \frac{C_A}{2C_F} \left(\frac{4\pi\mu_R^2}{-t} \right)^\varepsilon - \frac{C_A}{2C_F} \left(\frac{4\pi\mu_R^2}{-u} \right)^\varepsilon \right\} \right] \\
&+ 2 \operatorname{Re} \left(\widetilde{\mathcal{M}}'_{\text{Virt}} \left[\mathcal{M}_{\text{LO}}^{q\bar{Q} \rightarrow g} \right]^* \right), \quad (3.54)
\end{aligned}$$

which is $\mathcal{O}(\varepsilon^0)$. We can therefore perform the limit $\varepsilon \rightarrow 0$, which yields the finite NLO QCD virtual matrix element, ready to be integrated over the leading order phase space, cf. sec. 3.1.1. The processes $\bar{Q}g \rightarrow \bar{q}\ell^- \bar{\nu}_\ell \gamma$, $qg \rightarrow \bar{Q}\ell^- \bar{\nu}_\ell \gamma$, follow from crossing the Mandelstam variables, and replacing the Born matrix element accordingly. The extension to WZj production is straightforwardly performed by contracting the loop topologies with the respective effective polarization vectors.

3.3.5 Numerical implementation and gauge checks

The numerical implementation employs the loop building-block representation of (3.46), (3.48), (3.51), and (3.54). The loops up to boxes are evaluated using the Passarino-Veltman reduction scheme [47] for tensor integrals. For the pentagons we rely on the Denner-Dittmaier reduction [48]. Altogether, this already guarantees numerical stability of the virtual cross section

$$\begin{aligned}
\tilde{\sigma}_{ab}^{\text{V+A}} &= \frac{f_{a/P}(x_a, \mu_F^2) f_{b/P}(x_b, \mu_F^2)}{n_s(a)n_s(b)n_c(a)n_c(b)} \frac{1}{\Phi(p_a \cdot p_b)} \\
&\times \left[2 \operatorname{Re} \left(\mathcal{M}_{\text{Virt+CT}}^{\text{1Loop}, ab} \left[\mathcal{M}_{\text{LO}}^{ab} \right]^* \right) + \langle 1; a^a b^b | \mathbf{I} | 1; a^a b^b \rangle \right] \mathcal{F}(p_1, q_1, \dots, q_n)
\end{aligned} \quad (3.55a)$$

over the phase space integration

$$\sigma^{\text{V+A}} = \sum_{\{a,b\}} \iiint d\text{LIPS}_{1+\text{elw}}(p_a, p_b, p_1, q_1, \dots, q_n) dx_a dx_b \Theta(\mathcal{C}) \tilde{\sigma}_{ab}^{\text{V+A}}. \quad (3.55b)$$

The Born-amplitudes and matrix elements make use of the implementation of sec. 3.1.1.

Numerical instabilities typically arise from momentum configurations at the phase space edges. The Monte Carlo code checks each phase space point for violation of gauge invariance via Ward identities [14, 25]: Replacing a polarization vector by its four

momentum[§] yields, e.g.,

$$\begin{aligned}
 & p_2^\nu \cdot \left(\begin{array}{c} \text{Diagram 1: Triangle graph with external momenta } p_a, p_b \text{ and internal momenta } p_1, p_2, p_3. \text{ External indices } \mu, \nu, \rho. \end{array} \right) \\
 &= \left(\begin{array}{c} \text{Diagram 2: Triangle graph with external momenta } p_a, p_b \text{ and internal momenta } p_1, p_2+p_3. \text{ External indices } \mu, \rho. \end{array} \right) \\
 &\quad - \left(\begin{array}{c} \text{Diagram 3: Triangle graph with external momenta } p_a, p_b \text{ and internal momenta } p_1+p_2, p_3. \text{ External indices } \mu, \rho. \end{array} \right), \tag{3.56}
 \end{aligned}$$

and similar equations for the box contributions mapped onto triangle graph differences. Note, that the quark-tensor current in (3.56) is a *S-matrix current* in the sense of the LSZ reduction. Depending on position of the index, which is contracted with the respective four momentum, there is also contribution to the Green's function in momentum space with changed quark momentum. For the box graphs the Green's functions' Ward identities are, e.g.,

$$\begin{aligned}
 & p_2^\nu \cdot \left(\begin{array}{c} \text{Diagram 4: Triangle graph with external momenta } p_a, p_b \text{ and internal momenta } p_1, p_2. \text{ External indices } \mu, \nu. \end{array} \right) \\
 &= \left(\begin{array}{c} \text{Diagram 5: Triangle graph with external momenta } p_a, p_b+p_2 \text{ and internal momenta } p_3. \text{ External index } \mu. \end{array} \right) \\
 &\quad - \left(\begin{array}{c} \text{Diagram 6: Triangle graph with external momenta } p_a, p_b \text{ and internal momenta } p_2+p_3. \text{ External index } \mu. \end{array} \right), \tag{3.57}
 \end{aligned}$$

where the first term on the right hand side does not contribute p_b -residue and thus vanishes for the *S-matrix* quark current. Subsequent application of the Ward identities

[§]Eq.(3.56) follows from expressing the contracted four momentum by the difference of the momenta of the adjacent propagators.

(3.56) and (3.57) to all graphs of the pentline and boxline routines therefore allows to numerically compare the pentline routine with up to two boxlines, and the boxline with a single triangle diagram.

For the typical cuts of chapters 4 and 5, we find that, without any additional improvements, $\sim 2\%$ of the abelian pentagon evaluations, $\sim 0.2\%$ of the non-abelian evaluations, and $\sim 10^{-4}\%$ of the box evaluations violate gauge invariance at the level of 1%. The error made by rejecting the phase space points, that numerically violate gauge invariance at that level is however always well below the statistical integration error, as the finite virtual loop contributions (3.54) only contribute at around 5% to the total NLO cross section for reasonable scale choices $\mu_R \sim \mu_F \sim m_W$.

To improve the code's performance and even increase the numerical stability of the pentagon calculations over the whole parameter space (especially for massive WZj production), we can invert the gauge checks, and partially map a pentagon configuration onto the difference of the two boxes, by writing the electroweak polarization vectors

$$\varepsilon_j^\mu(p_j) = x_j p_j^\mu + \tilde{\varepsilon}_j^\mu(p_j). \quad (3.58)$$

in (3.48). A convenient choice of x_q is given by requiring

$$\tilde{\varepsilon}_j \cdot \left(\sum_i q_i \right) = \varepsilon \cdot p^{\text{elw}} = 0 \quad \Rightarrow \quad x_j = \frac{\varepsilon \cdot p^{\text{elw}}}{p_j \cdot p^{\text{elw}}}, \quad (3.59)$$

see also [8]. In fact, try-and-error of different parameterizations of x_j shows, that for improved numerical stability, the precise form of (3.58) is rather unimportant. Yet, by exploiting the Ward identities, the fraction of pentagon cross section can be decreased to a large extent, thus offering a method to speed up the numerical code via reduced statistics. In addition, a potential error that arises from incomplete electroweak cancellations among the box- and pentline topologies by different QCD gauge check acceptance, is thus numerically ruled out. This is also confirmed by explicit checks against integrated results of independent implementations, sec. 3.5.

3.4 Finite collinear remainders

The remaining initial-state collinear divergencies are mended by factorizing them into a redefinition of the parton distribution functions [42]. The finite terms, that remain after cancelling all IR divergencies as described in sec. 2.2.3 are formally expressed by

$$\begin{aligned} d\sigma_{\text{coll}}^{ab} = \int_0^1 dx \left\{ \left[\sum_{a'} (\mathbf{P}(x, xp_a, p_b, \mu_F^2) + \mathbf{K}(x))^{aa'} \otimes d\sigma_{\text{LO}}^{a'b \rightarrow j} \right] \right. \\ \left. + \left[\sum_{b'} (\mathbf{P}(x, p_a, xp_b, \mu_F^2) + \mathbf{K}(x))^{bb'} \otimes d\sigma_{\text{LO}}^{ab' \rightarrow j'} \right] \right\}. \end{aligned} \quad (3.60)$$

The explicit result of (3.60) is rather lengthy, and is given in the appendix B.2 for the sake of clarity. Here, we only sketch the result and its implementation. Eq. (3.60) can

be written in terms of modified parton distribution functions $\tilde{f}_{a/P}$ (B.29)-(B.34):

$$\begin{aligned}
\sigma_{\text{coll.}}^{\text{NLO}} &= \iint_0^1 dx_a dx_b \int d\text{LIPS}_{1+\text{elw}}(k_1, k_2, k_3, k_4; p_a, p_b) \frac{1}{\hat{s}} \\
&\times \left\{ \left[\tilde{f}_{\bar{q}/P}(x_a, \mu_F^2) \tilde{f}_{Q/P}^{(1)}(x_b, \mu_F^2) + \tilde{f}_{\bar{q}/P}^{(1)}(x_a, \mu_F^2) f_{Q/P}(x_b, \mu_F^2) \right] \right. \\
&\times \left| \mathcal{M}_{\text{LO}}^{\bar{q}Q \rightarrow g}(k_1, k_2, k_3, k_4; p_a, p_b) \right|^2 + (\bar{q} \leftrightarrow Q) \\
&+ \left[f_{g/P}(x_a, \mu_F^2) \tilde{f}_{Q/P}^{(2)}(x_b, \mu_F^2) + \tilde{f}_{g/P}^{(2)}(x_a, \mu_F^2) f_{Q/P}(x_b, \mu_F^2) \right] \\
&\times \left| \mathcal{M}_{\text{LO}}^{gQ \rightarrow q}(k_1, k_2, k_3, k_4; p_a, p_b) \right|^2 + (g \leftrightarrow Q) \\
&+ \left[\tilde{f}_{\bar{q}/P}(x_a, \mu_F^2) \tilde{f}_{g/P}^{(3)}(x_b, \mu_F^2) + \tilde{f}_{\bar{q}/P}^{(3)}(x_a, \mu_F^2) f_{g/P}(x_b, \mu_F^2) \right] \\
&\times \left. \left| \mathcal{M}_{\text{LO}}^{\bar{q}g \rightarrow \bar{Q}}(k_1, k_2, k_3, k_4; p_a, p_b) \right|^2 + (\bar{q} \leftrightarrow g) \right\}, \tag{3.61}
\end{aligned}$$

which have the generic form

$$\begin{aligned}
\tilde{f}_{a/P}^{(i)}(\tilde{x}, \mu_F^2) &= \frac{\alpha_s(\mu_R^2)}{2\pi} \int_{\tilde{x}}^1 \frac{dx}{x} \left\{ \mathcal{A}_{aa}^{(i)} \left(f_{a/P} \left(\frac{\tilde{x}}{x}, \mu_F^2 \right) - x f_{b/P}(\tilde{x}, \mu_F^2) \right) \right. \\
&+ \mathcal{B}_{ab}^{(i)} f_{b/P} \left(\frac{\tilde{x}}{x}, \mu_F^2 \right) + \mathcal{C}_{ac}^{(1)} f_{c/P} \left(\frac{\tilde{x}}{x}, \mu_F^2 \right) \left. \right\} + \frac{\alpha_s(\mu_R^2)}{2\pi} \mathcal{D}_{aa}^{(i)} f_{a/P}(\tilde{x}, \mu_F^2). \tag{3.62}
\end{aligned}$$

The coefficients $\mathcal{A}_{aa}^{(i)}$, $\mathcal{B}_{ab}^{(i)}$, $\mathcal{C}_{ab}^{(i)}$, and $\mathcal{D}_{aa}^{(i)}$ are determined by the QCD-splittings.

It is also desirable from a technical point of view to perform the integration of (3.61) over the real emission (2+elw)-particle phase space as opposed to over the Born-level (1+elw)-particle configurations [78]. This way, the Born matrix element of the dipoles can be recycled, and MONACO can adapt the numerical integration to the subtracted real emission and the finite collinear terms at the same time, thus speeding up the numerics while keeping the statistical integration error small.

We can use the definition of the tilde-kinematics (3.24) of the initial-initial dipoles $\mathcal{D}^{ai,b}$ to map the real emission phase space onto the Born-level phase space,

$$\int d\text{LIPS}_{2+\text{elw}}(p_a, p_b) \frac{1}{2p_a \cdot p_b} = \int_0^1 dx \int d\text{LIPS}_{1+\text{elw}}(\tilde{p}_a, p_b) \frac{1}{8\pi^2} \int_0^{1-x} dv, \tag{3.63}$$

where $v = (p_a \cdot p_i)/(p_a \cdot p_b)$, $x = x_{i,ab}$. By rewriting

$$1 - x_a = \int_{x_a}^1 dx = \int_{x_a}^1 dx \int_0^{1-x} dv \frac{1}{1-x}, \tag{3.64}$$

for the $\mathcal{D}_{ab}^{(i)}$ terms and using the generic form of (3.62), we find

$$\begin{aligned}
& \int_0^1 dx_a \int d\text{LIPS}_{1+\text{elw}}(p_a, p_b) \frac{1}{2p_a \cdot p_b} \tilde{f}_{a/P}^{(i)}(x_a, \mu_F^2) |\mathcal{M}(p_a, p_b)|^2 \\
&= \int_0^1 dx_a \int_{x_a}^1 \frac{dx}{x} \int d\text{LIPS}_{1+\text{elw}} \frac{8\pi^2}{2\tilde{p}_a \cdot p_b} \frac{4\pi\alpha_s(\mu_R^2)}{8\pi^2} |\mathcal{M}(p_a, p_b)|^2 \left(\mathcal{B}_{ab}^{(i)} f_{b/P} \left(\frac{x_a}{x}, \mu_F^2 \right) \right. \\
&+ \mathcal{A}_{ab}^{(i)} \left(f_{b/P} \left(\frac{x_a}{x}, \mu_F^2 \right) - x f_{b/P} \left(x_a, \mu_F^2 \right) \right) + \mathcal{C}_{ac}^{(i)} f_{c/P} \left(\frac{x_a}{x}, \mu_F^2 \right) + \frac{x}{1-x_a} \mathcal{D}_{ab}^{(i)} f_{b/P}(xx_a) \Big) \\
&= \int_0^1 dx_a \int d\text{LIPS}_{2+\text{elw}} \frac{1}{2p_a \cdot p_b} \frac{4\pi\alpha_s(\mu_R^2)}{2\tilde{p}_a \cdot p_b} \frac{1}{1-x} \left(\mathcal{B}_{ab}^{(i)}(x) f_{b/P} \left(x_a, \mu_F^2 \right) \right. \\
&\quad + \mathcal{A}_{ab}^{(i)}(x) \left(f_{b/P} \left(x_a, \mu_F^2 \right) - x f_{b/P} \left(xx_a, \mu_F^2 \right) \right) + \mathcal{C}_{ac}^{(i)}(x) f_{c/P} \left(x_a, \mu_F^2 \right) \\
&\quad \left. + \frac{x}{1-xx_a} \mathcal{D}_{ab}^{(i)}(xx_a) f_{b/P}(xx_a) \right) |\mathcal{M}(\tilde{p}_a, p_b)|^2.
\end{aligned} \tag{3.65}$$

In the last line the substitution $x_a \rightarrow x_a x$ ($p_a \rightarrow \tilde{p}_a$) was performed, applying (3.63).

3.5 Test and Comparisons

All parts of the NLO amplitude have been cross-checked either analytically or numerically against independent calculations or implementations, respectively. In detail, these checks involve numerical cross-checks of the one-loop amplitudes against code generated with modified versions of FEYNARTS, FORMCALC, and LOOPTOOLS, as described in sec. 3.3.1, yielding perfect agreement. The gauge checks of 3.3.5, applied to each phase space point during the numerical integration, provide a powerful test of the virtual implementation's validity.

The divergent pieces of the one-loop amplitude have been determined independently and the cancellation against the dipole's IR poles was shown analytically (sec. 3.3.4). The finite collinear remainders have been calculated redundantly, yielding analytical agreement. Their implementation and phase space integration was computed as part of the leading-order and real emission phase space and cross-checked to verify (3.63).

Throughout, partial to full automation is invoked whenever feasible, strongly relying on computer-algebra-driven code generation, which avoids human shortcomings. This includes fully automated MATHEMATICA routines to determine the IR-divergencies from the tensor reduction as described in sec. 3.3.4, and automated generation of the finite collinear remainders along the lines of secs. 3.4 and B.2. For verification reasons the results of [8, 84] were algebraically reproduced.

For the WZj results of [10] two entirely independent Monte Carlo implementations were cross-checked in narrow-width approximation (i.e. on-shell W s and Z s), as well as for full leptonic decays. The two independently coded matrix elements agree to 7-8 digits, and integrated cross sections at per mill-level for the individual parts σ^B , σ^{V+A} , σ^{R-A} , and σ^C .

Chapter 4

$W^\pm\gamma j$ production at hadron colliders

4.1 General Monte-Carlo input parameters

We use CTEQ6M parton distributions [39] with $\alpha_s(m_Z) = 0.118$ at NLO, and the CTEQ6L1 set at LO. We choose $m_Z = 91.188$ GeV, $m_W = 80.419$ GeV and $G_F = 1.16639 \times 10^{-5}$ GeV⁻² as electroweak input parameters and derive the electromagnetic coupling α and the weak mixing angle $\sin\theta_w$ via Standard Model-tree level relations. The one- and two-loop runnings of α_s for the LO and NLO calculations, respectively, are determined by (2.69) with $\Lambda_{\text{QCD}}^{\overline{\text{MS}},0} = 165.2$ MeV, and by (2.70) with $\Lambda_{\text{QCD}}^{\overline{\text{MS}},1} = 226.2$ MeV.

The center-of-mass energy is fixed to 14 TeV for LHC and 1.96 TeV for Tevatron collisions. In the following, we only consider W^\pm decays to one family of light leptons, i.e. $W^- \rightarrow e^- \nu_e$ or $\mu^- \nu_\mu$, and treat these leptons as massless.

Jets are recombined via the k_T algorithm [86] from massless partons of pseudorapidities $|\eta| \leq 5$ with resolution parameter $D = 0.7$. The jets are required to lie in the rapidity range

$$|y_j| \leq 4.5 \tag{4.1a}$$

to account for finite detector coverage. For the photons and leptons, we request

$$|y_\gamma| \leq 2.5, \quad |y_\ell| \leq 2.5. \tag{4.1b}$$

To avoid the collinear photon-lepton configurations, we require a finite separation in the azimuthal angle – pseudorapidity plane of

$$R_{\ell\gamma} = \sqrt{[\Delta\phi(\ell\gamma)]^2 + [\Delta\eta(\ell\gamma)]^2} \geq 0.2, \tag{4.1c}$$

for the jet-lepton separation we impose

$$R_{j\ell} \geq 0.2. \tag{4.1d}$$

We adopt the photon isolation of (2.42) and choose $\mathcal{E} = p_T^\gamma$ unless specified differently.

4.2 Scale dependence of production cross sections

To analyze the $W^\pm\gamma j$ cross sections and their dependence on the unphysical factorization and renormalization scales μ_R, μ_F , we choose a rather inclusive set of selection

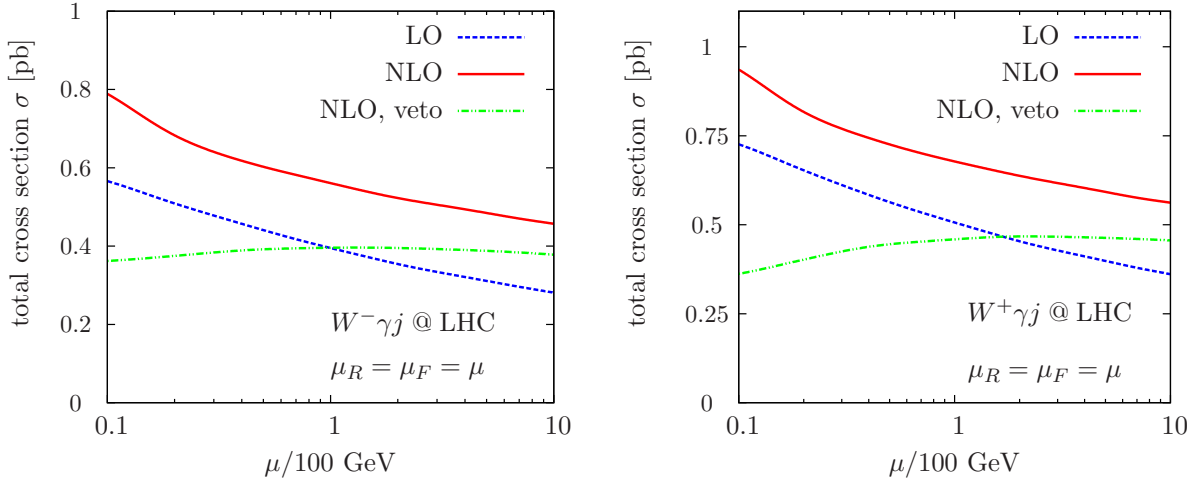


Figure 4.1: Scale dependence of the leading order, next-to-leading order inclusive, and next-to-leading order exclusive $W^\pm\gamma j$ cross sections at the LHC for $\delta_0 = 1.0$.

criteria. On top of the cuts mentioned above, we require the jets, the charged lepton, and the photon to have transverse momenta

$$p_T^j \geq 50 \text{ GeV}, \quad p_T^\ell \geq 20 \text{ GeV}, \quad p_T^\gamma \geq 50 \text{ GeV}, \quad (4.2a)$$

The IR-safe photon-jet separation is chosen to be $\delta_0 = 1.0$. It is customary to also analyze the cross sections' behavior with an additional 'no resolvable 2nd jet'-criterion [3], i.e. a veto on the second jet, if it gets resolved,

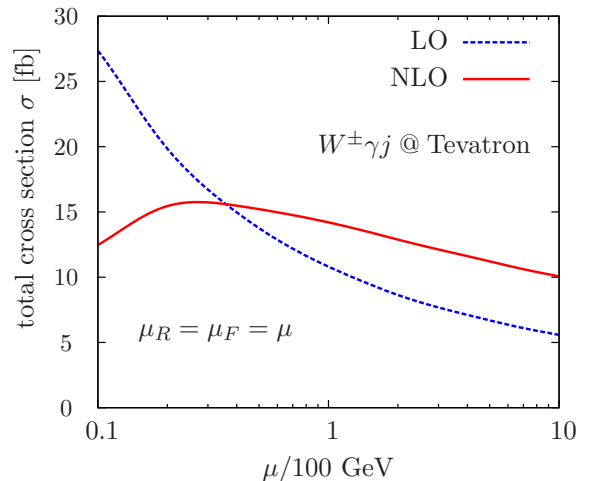
$$p_T^{j,\text{veto}} \geq 50 \text{ GeV}, \quad |y_j^{\text{veto}}| \leq 4.5 \quad (\text{exclusive NLO}). \quad (4.2b)$$

Figs. 4.1 and 4.2 show the behavior of the $W\gamma j$ cross sections for these cut choices and identified scales $\mu_R = \mu_F = \mu$ at the LHC and the Tevatron. Tab. 4.1 explicitly gives the computed inclusive cross sections at the LHC for $\mu = 100$ GeV, including the total correction factor $k^{\text{tot}} = \sigma^{\text{NLO}}/\sigma^{\text{LO}}$. Also shown are total cross sections for the choice $\delta_0 = 0.6$, which is later on used to study differential distributions and the veto's impact in detail in sec. 4.3. The larger cross section and different scale dependence for $W^+\gamma j$ production compared to $W^-\gamma j$ production is predominantly due to different parton luminosities in the dominating (anti)quark-gluon subprocesses (cf. fig. 2.1). In particular $W^+\gamma j$ production involves initial state up-quarks as opposed to $W^-\gamma j$ production.

The NLO exclusive production projects onto "genuine" $W\gamma j$ events, and one is tempted to conjecture improved QCD-stability for the vetoed sample. In fact, vetoed $W\gamma j$ production* exhibits an almost flat scale dependence. At leading order, we find a dependence on the unphysical scales μ_F, μ_R of approximately 11% for inclusive $W^\pm\gamma j$ production cross sections at the LHC, when varying $\mu_R = \mu_F$ by a factor two around 100 GeV in fig. 4.1. This scale dependence is reduced to about 7% when including

*Apart from small modifications this is qualitatively reproduced by all other NLO massive di-boson+jet cross sections [3, 6, 10].

Figure 4.2: Scale dependence of the leading order and next-to-leading order inclusive $W^\pm\gamma j$ cross sections at the Tevatron for $\delta_0 = 1.0$. The cross sections correspond to either $W^-\gamma j$ or $W^+\gamma j$ production, i.e. we do not sum over the two W^\pm bosons.



NLO QCD precision for $W^\pm\gamma j$. For the NLO exclusive cross section, however, the scale dependence in this range is only 0.5% for $W^-\gamma j$ and 2% for $W^+\gamma j$. While jet-vetoing is a straightforward Monte-Carlo exercise, its experimental and phenomenological implications are delicate. Relying on fixed-order Monte Carlo input to an experimental analysis, the veto amounts to subtraction of a leading order cross section, which is plagued with typical QCD scale uncertainties. This also turns out to be problematic for anomalous $W\gamma$ couplings searches, where significance-enhancing strategies involve jet-vetos. We discuss these issues in detail in secs. 4.3 and 4.4.

For $W\gamma j$ production at NLO QCD, the di-jet contribution introduces a significant dependence on the renormalization scale μ_R (which is also the source of scale dependence at LO), that eventually translates into an only mild reduction of scale dependence of the total NLO cross section in fig 4.1. This can also be inferred from Fig. 4.3, which displays the separate variations[†] of μ_R and μ_F , respectively. We also note that the numerical value at small scales of $\mu_R = \mu_F$ results from cancellations among large positive-definite Born- and negative one-loop contributions which exhibit a non-trivial dependence on μ_R .

As a matter of fact, the only slight taming of the μ_R dependence is a purely kine-

	$\sigma_{\text{incl}}^{\text{NLO}}$ [fb]	$\sigma_{\text{incl}}^{\text{NLO}}/\sigma^{\text{LO}}$	
$W^-\gamma j$	615.3 ± 2.8	1.491	$\delta_0 = 0.6$
$W^+\gamma j$	736.5 ± 3.5	1.411	
$W^-\gamma j$	558.7 ± 2.4	1.413	$\delta_0 = 1.0$
$W^+\gamma j$	676.9 ± 3.2	1.339	

Table 4.1: Inclusive next-to-leading order cross sections and k^{tot} -factors for the processes $pp \rightarrow e^+\nu_e\gamma j + X$ and $pp \rightarrow e^-\bar{\nu}_e\gamma j + X$ at the LHC for identified renormalization and factorization scales, $\mu_R = \mu_F = 100$ GeV. The cuts are chosen as described in the text.

[†]Here, the interpretation of the cross sections' variations requires caution. The pdfs do also depend on the renormalization scale via the strong coupling. Yet, figs. 4.3, 4.3 clearly reveal the origin of the additionally introduced μ_R -dependence by the di-jet contribution.

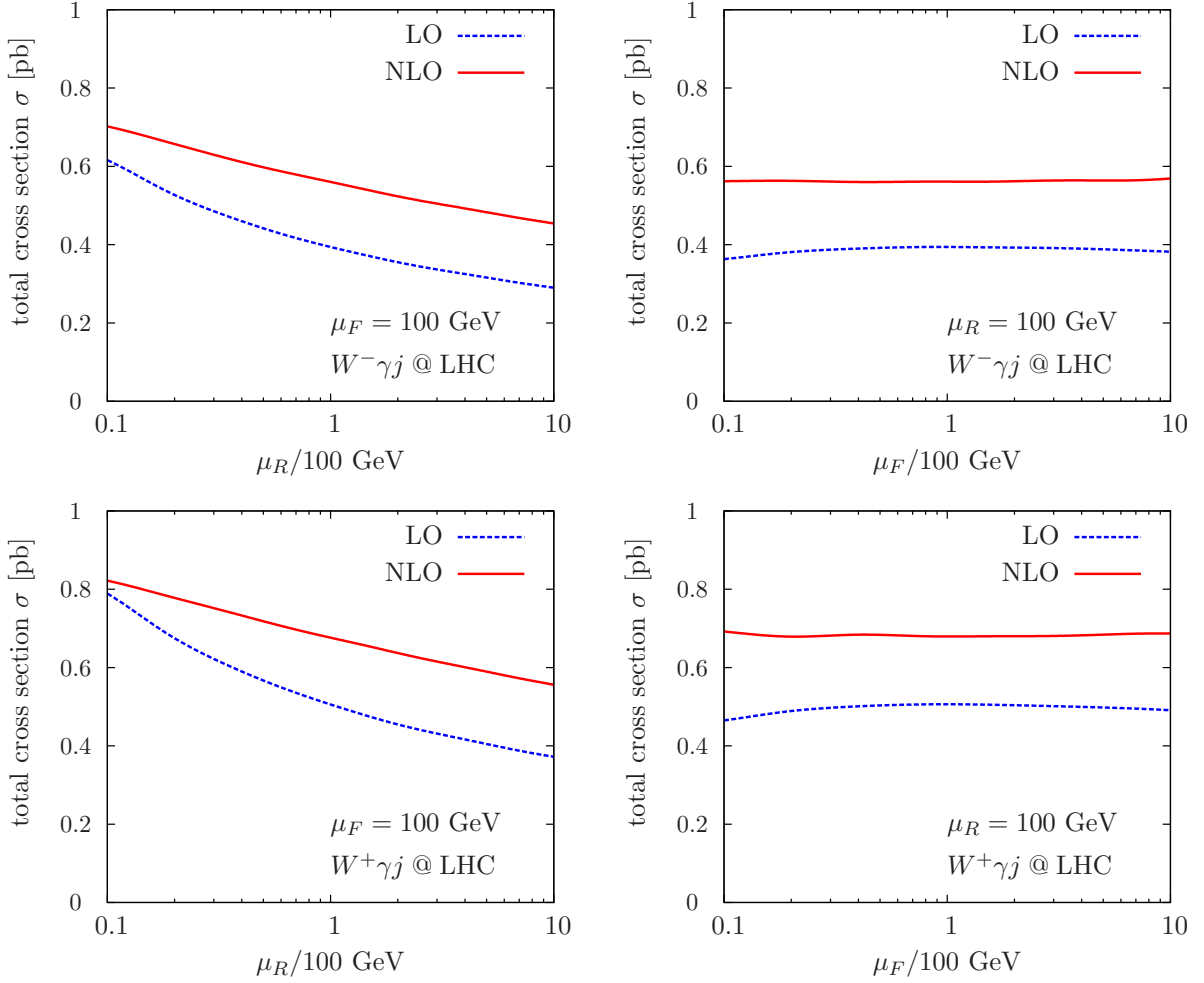


Figure 4.3: Individual renormalization and factorization scale dependencies of the leading order and next-to-leading order inclusive $W^\pm \gamma j$ cross sections at the LHC for $\delta_0 = 1.0$.

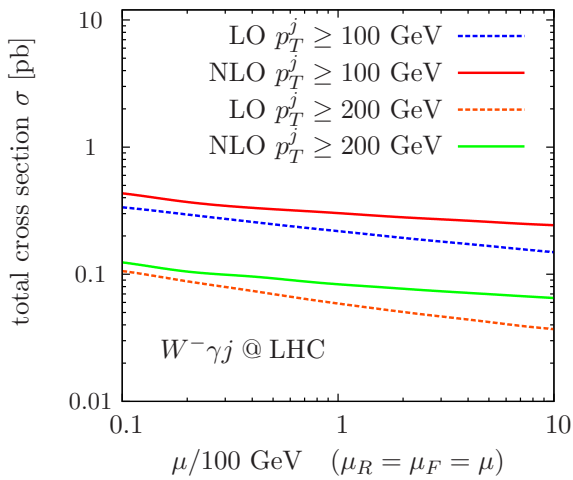


Figure 4.4: Scale dependence of the leading order and next-to-leading order inclusive $W^- \gamma j$ cross sections ($\delta_0 = 1.0$) at the LHC for identified scales $\mu_R = \mu_F = \mu$ and different cuts on the transverse momentum of the jet.

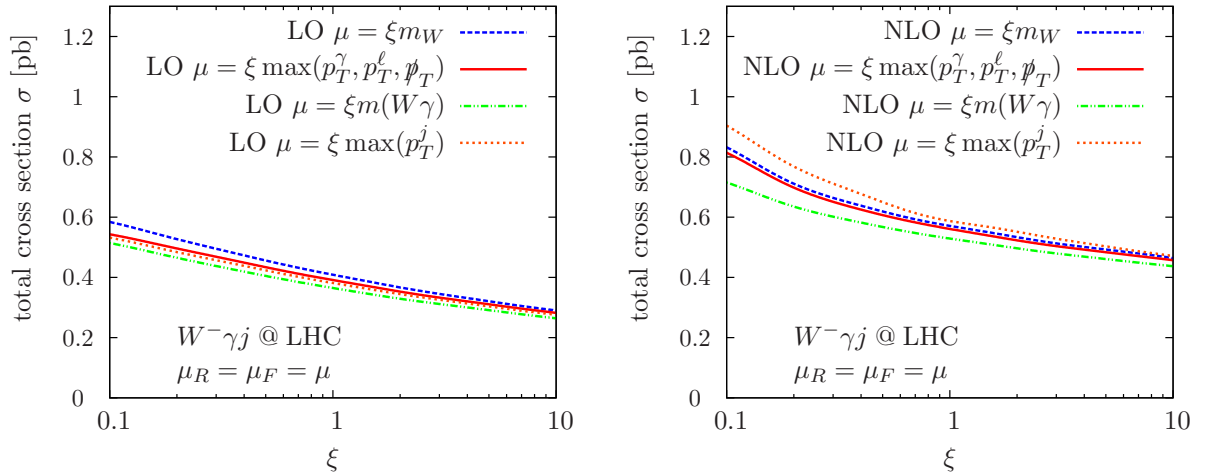


Figure 4.5: Scale dependence of the leading order and next-to-leading order $W^- \gamma j$ cross sections at the LHC for different dynamical scales and $\delta_0 = 1.0$.

mathematical effect: At the LHC the proton is probed at very small momentum fractions $x \sim 0.01$ in $W \gamma j$ production (see below). While the involved mass scales are not too large to make extra QCD radiation naively probable, the α_s -suppression is considerably compensated by accessing the proton's high gluon luminosity at small momentum fractions $x_{a,b}$ with the two parton-final state contribution. This is also the reason why the two-jet rate is not lower than about one-half the one-jet rate, comparing Tabs. 3.1 and 3.2.

The overall qualitative features of the $W \gamma j$ cross section are rather independent of the selection cuts of (4.1)-(4.2). Increasing e.g. the scale of the jet p_T at the LHC in (4.2a) leads to a kinematically decreased available phase space for the real emission compared to LO. As a result, the cross section slowly stabilizes artificially at lower total rates, fig. 4.4. Fig. 4.5 gives a comparison of dynamical scale choices $\mu_F = \mu_R$ for $W^- \gamma j$ production, with typical scales inherent to the process. Again, the qualitative behavior of fig. 4.1 is reproduced, which underlines the conclusion that the inclusive NLO cross section is dominated by the contribution of additional parton emission and not by large logarithms from bad scale choices. For scaling parameters $\xi = 1$ the LO- and NLO-uncertainties due to the different dynamical scales are about 6%.

The totally different cross section's scale dependence at the Tevatron, fig. 4.2 is predominantly due to lowering the available center-of-mass energy at fixed final state mass scales. The proton is probed at large values of $x \sim 0.2$, rendering quark induced channels dominating. Additional jet radiation for the chosen selection cuts is suppressed, so that the scale dependence decreases from 23% at LO to about 8% at NLO QCD when varying $\mu_R = \mu_F$ again by a factor two around 100 GeV.

4.3 Photon isolation and differential distributions

In figs. 4.6 and 4.7, we compare distinct photon isolation criteria based on (2.42) with different choices for the characteristic energy scale \mathcal{E} . Representative dynamical scales

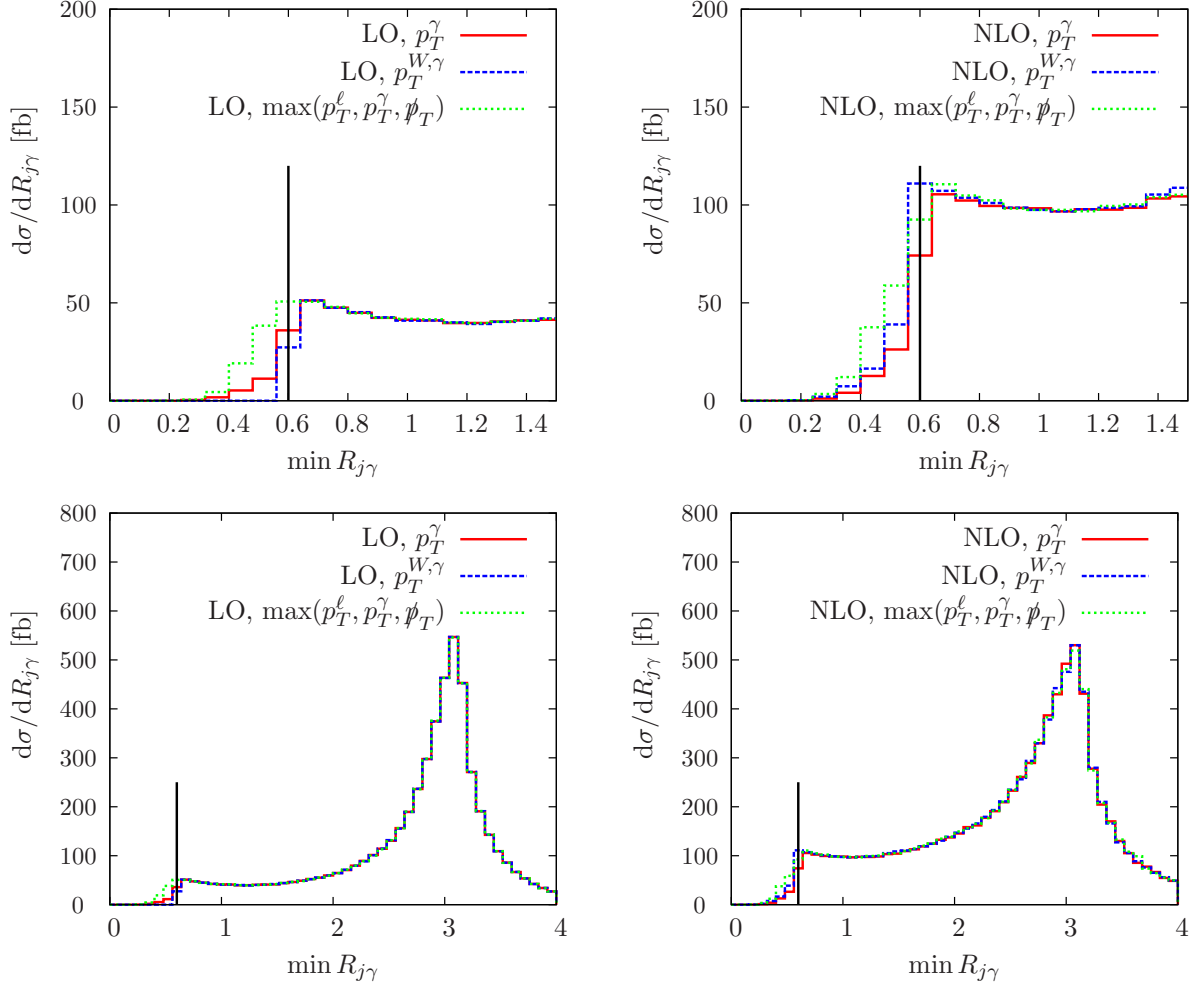


Figure 4.6: Minimal photon-jet separation in the azimuthal angle – pseudorapidity plane at leading order and next-to-leading order for different isolation scales, $\mathcal{E} = p_T^\gamma, p_T^{W,\gamma}, \max(p_T^\ell, p_T^\gamma, p_T^\nu)$ in (2.42). The isolation parameter is $\delta_0 = 0.6$ (denoted by the vertical line), and $\mu_F = \mu_R = 100$ GeV.

for the electroweak system are the previously chosen transverse momentum of the photon p_T^γ , the p_T the $W\gamma$ pair,

$$p_T^{W,\gamma} = |\mathbf{p}_T^\gamma + \mathbf{p}_T^\ell + \mathbf{p}_T^\nu|, \quad (4.3)$$

or the maximum p_T among the final state photon, lepton, and neutrino, $\mathcal{E} = \max(p_T^\ell, p_T^\gamma, p_T^\nu)$. The dominating effect of this scale choice is given by rigidity ($\mathcal{E} \sim$ low scale) or softness ($\mathcal{E} \sim$ large scale) of the photon cone against QCD radiation, as can be inferred from the very definition of the isolation cut (2.42). The experimentally distinguishable isolation scenarios differ at about 1% at LO for the total rates and the cut choice (4.1), (4.2a). This difference does not receive any notable QCD-correction for our cuts, as the shape only gets modified around the isolation cone where the differential cross section dips before rising again when approaching the collinear singularity (which is of course cut away by the isolation criterion). Consequently, for smaller minimal distances, the

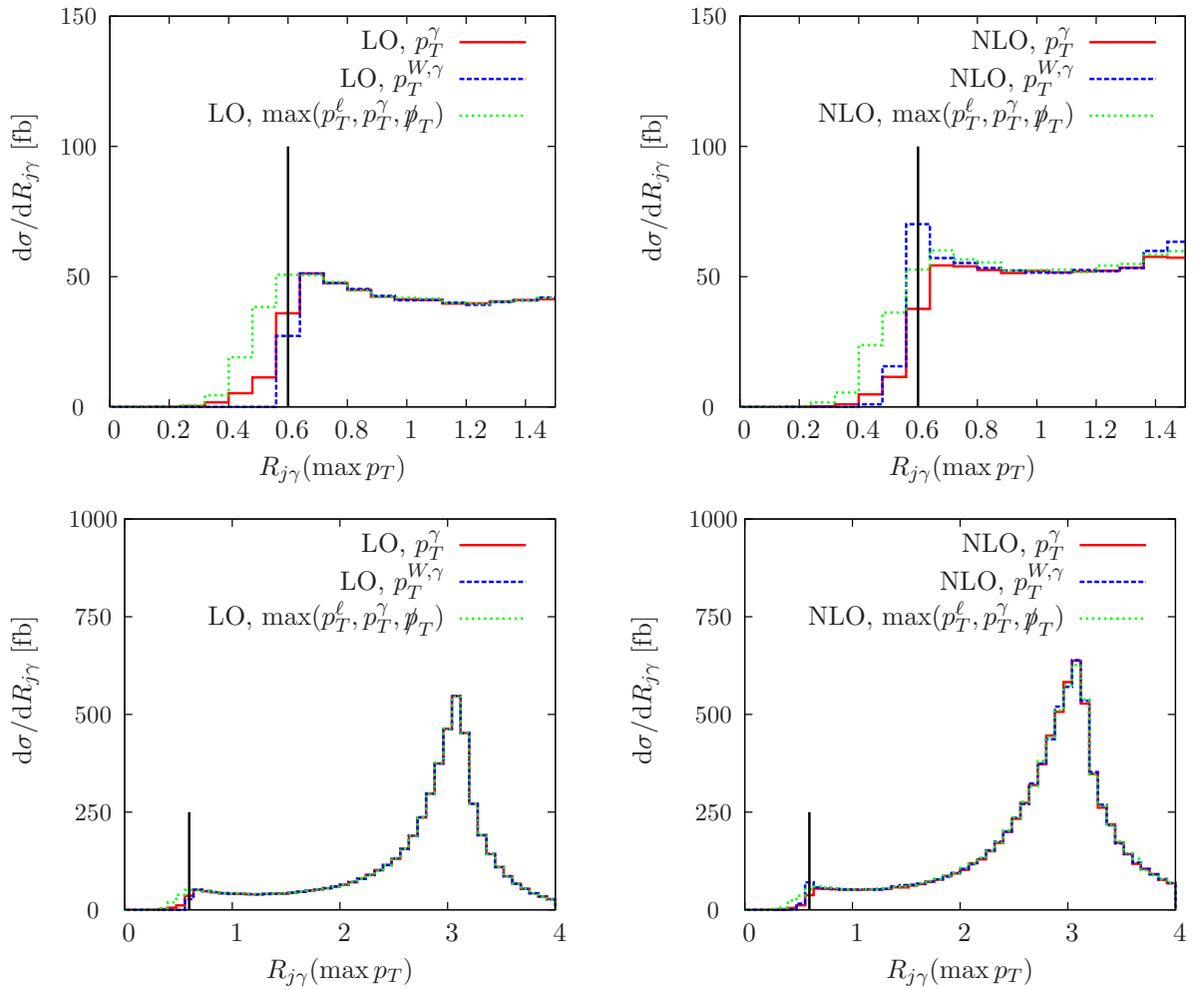


Figure 4.7: Separation of the photon from the jet with highest p_T in the azimuthal angle – pseudorapidity plane at leading order and next-to-leading order for different isolation scales with isolation parameter $\delta_0 = 0.6$ (denoted by the vertical line), and $\mu_F = \mu_R = 100$ GeV.

impact of the isolation scale choice is larger, but also fragmentation effects will become non-negligible. For the isolation scale $\mathcal{E} = p_T^{W,\gamma}$ the threshold behavior changes most significantly when including NLO precision. This is a consequence of $p_T^{W,\gamma} = p_T^j$ at LO, and the W recoiling against the photon-jet pair for configurations where the jet is close to the photon cone. The closer the centrally produced parton gets to the photon inside the photon cone, the larger is the transverse momentum of the W , but the isolation scale is still set by the jet itself. Due to the steeply falling p_T^W spectrum these configurations die off very fast, which explains the steep drop-off for $\mathcal{E} = p_T^{W,\gamma}$ in figs. 4.6 and 4.7 for the LO distributions. At NLO these configurations are heavily modified (this is further explained below). Now the kinematical LO correlation of jet and $W\gamma$ -system is distorted by additional parton emission, which allows the W to “climb up” the steep p_T -hill. Thus, the probability of QCD radiation into the photon cone gets larger around the threshold δ_0 . As, however, at the same time $p_T^{W,\gamma}$ decreases, more partons get vetoed at distances smaller than δ_0 , which explains the still steep

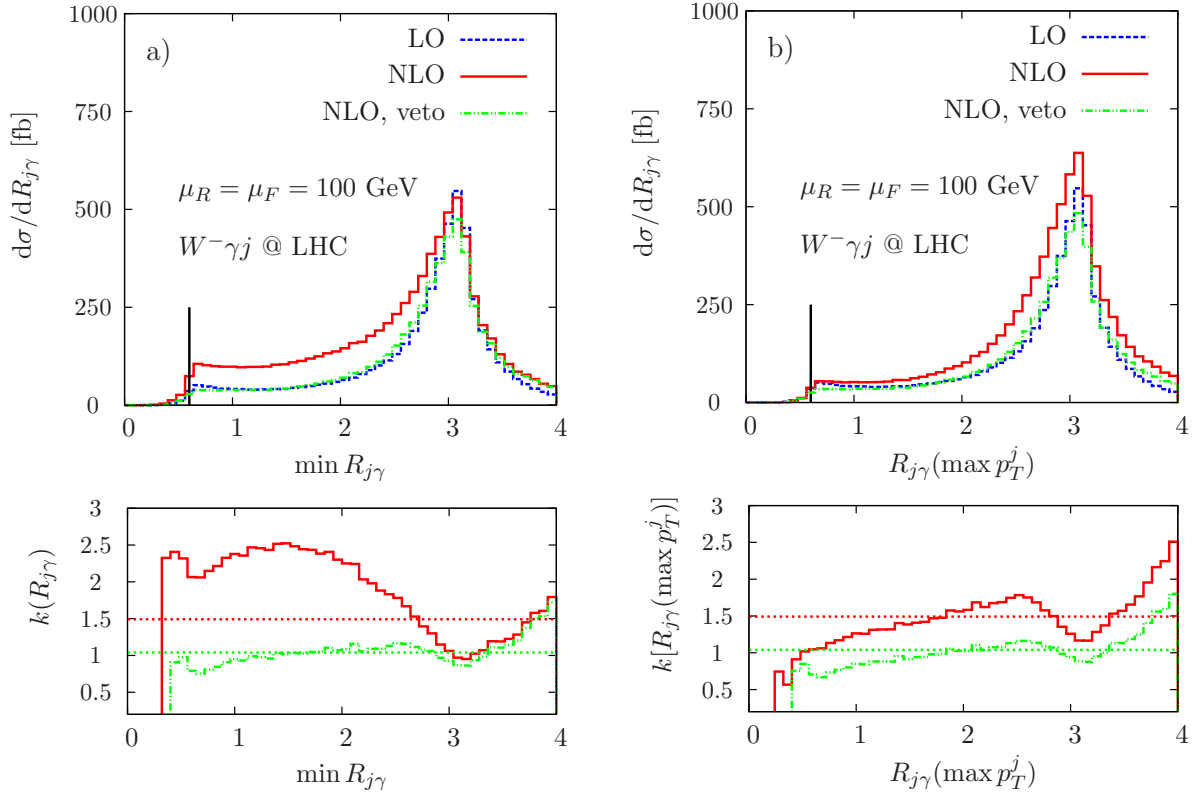


Figure 4.8: LO and NLO separation of the photon from a) the closest jet, and b) from the jet with largest p_T in the azimuthal angle – pseudorapidity plane. The isolation parameter $\delta_0 = 0.6$ is denoted by the vertical line. The isolation scale choice is $\mathcal{E} = p_T^\gamma$ in (2.42), and the differential k factor with k^{tot} plotted as horizontal line is depicted in the lower panels.

drop-off around δ_0 in the NLO curve for $\mathcal{E} = p_T^{W,\gamma}$ in figs. 4.6 and 4.7. In addition, we add (positive-weight) configurations to the minimum-separation distribution with the second resolved jet approximately balancing the jet-photon- W system in p_T . This configurations are not present at LO, but are disfavored for the observable in fig. 4.7.

The distributions for different isolation scale choices \mathcal{E} highly resemble each other outside the photon cone, and the dominant effect that alters the distribution’s shape from LO to NLO is additional jet radiation. This becomes visible by comparing the shape changes of figs. 4.8 and 4.10 when going from LO to NLO. The minimal photon-jet separation is highly affected by the additional hard jet radiation into the jet-photon cone one defines at LO.

This behavior confirms the well-known fact that total k factors and scale variations tend to be misleading when quantifying the impact of QCD quantum corrections to a given process. A better understanding of the QCD effects can be gained from differential k -factors of (IR-safe) observables \mathcal{O} ,

$$k(\mathcal{O}) = \frac{d\sigma^{\text{NLO}}}{d\mathcal{O}} \bigg/ \frac{d\sigma^{\text{LO}}}{d\mathcal{O}}, \quad (4.4)$$

which encode the phase space dependence of the corrections, projected onto the respective observable. In figs. 4.6-4.15 we give sample distributions alongside differential

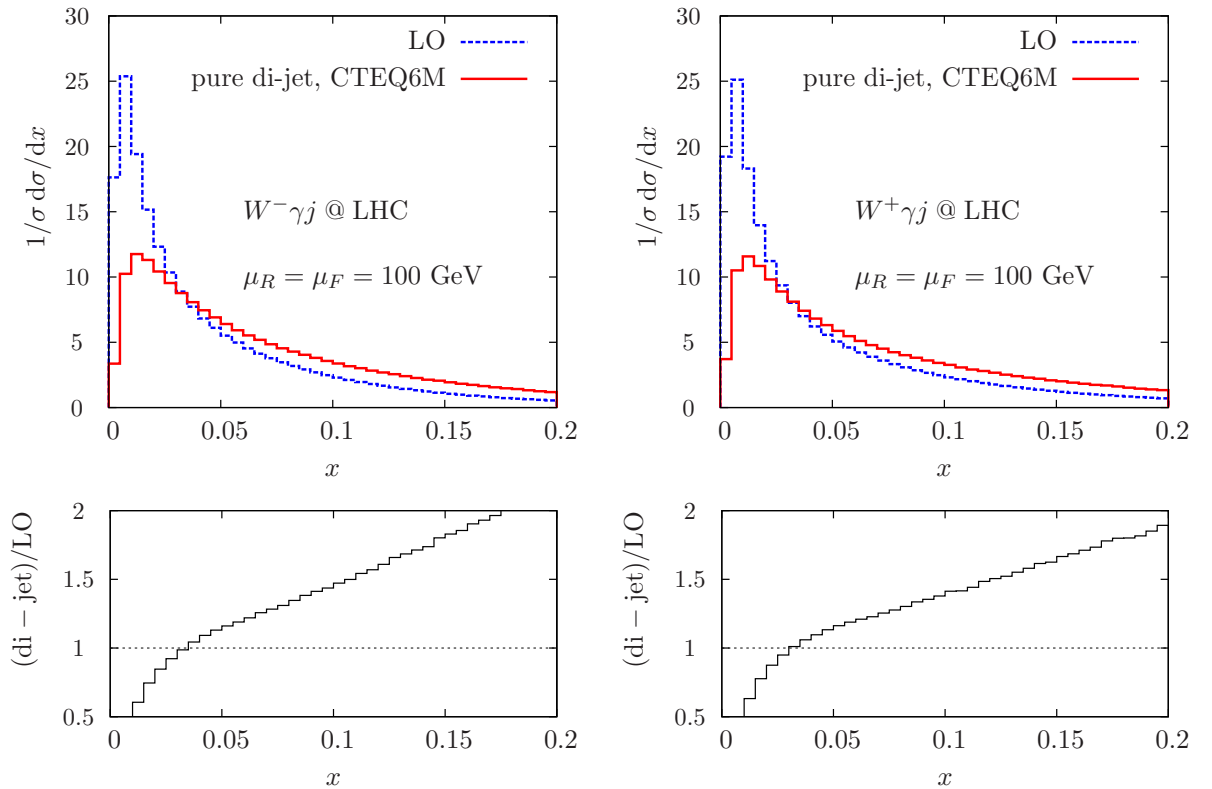


Figure 4.9: Comparison of the parton momentum fractions of the incoming partons of the leading order and the pure di-jet part at NLO for $W^\pm\gamma j$ production. We choose $\delta_0 = 0.6$. The lower panel shows the ratio of the two distributions.

k factors of common observables at the LHC for the cut set (4.1), (4.2). It is apparent that the differential corrections sizably depart from the total k factor-rescaled LO distribution, by comparing the differential k factors in figs. 4.6-4.15 to the respective total correction, which are always plotted as dashed horizontal lines. To generate these histograms we have chosen

$$\delta_0 = 0.6, \quad \mathcal{E} = p_T^\gamma \quad (4.5)$$

throughout. The quantitative differences in the corrections of $W^+\gamma j$ compared to $W^-\gamma j$ production are again due to the different pdf distributions, while the qualitative impact of the QCD-corrections is obviously identical.

The additional hard jet-radiation can highly affect the NLO distributions. While most of the purely leptonic and photonic observables' leading order shapes survive to NLO QCD in the dominant region of phase space (except for significant modifications in the p_T tails due to recoil against the additional hard jet, see below), observables that involve the hadronic part of the process develop large relative corrections: In addition to the minimum separation of the photon from the jet in fig. 4.8, also the minimum lepton-jet separation in fig. 4.10 receives major modifications due to the extra jet, which tends to be more collinear to the lepton at NLO. The lepton-photon separation exhibits an almost flat relative correction over the bulk of the important phase space. This behavior is also reproduced by the rapidity differences $|y_W - \eta_\gamma|$, $|\eta_\ell - \eta_\gamma|$, fig. 4.11, and the lepton

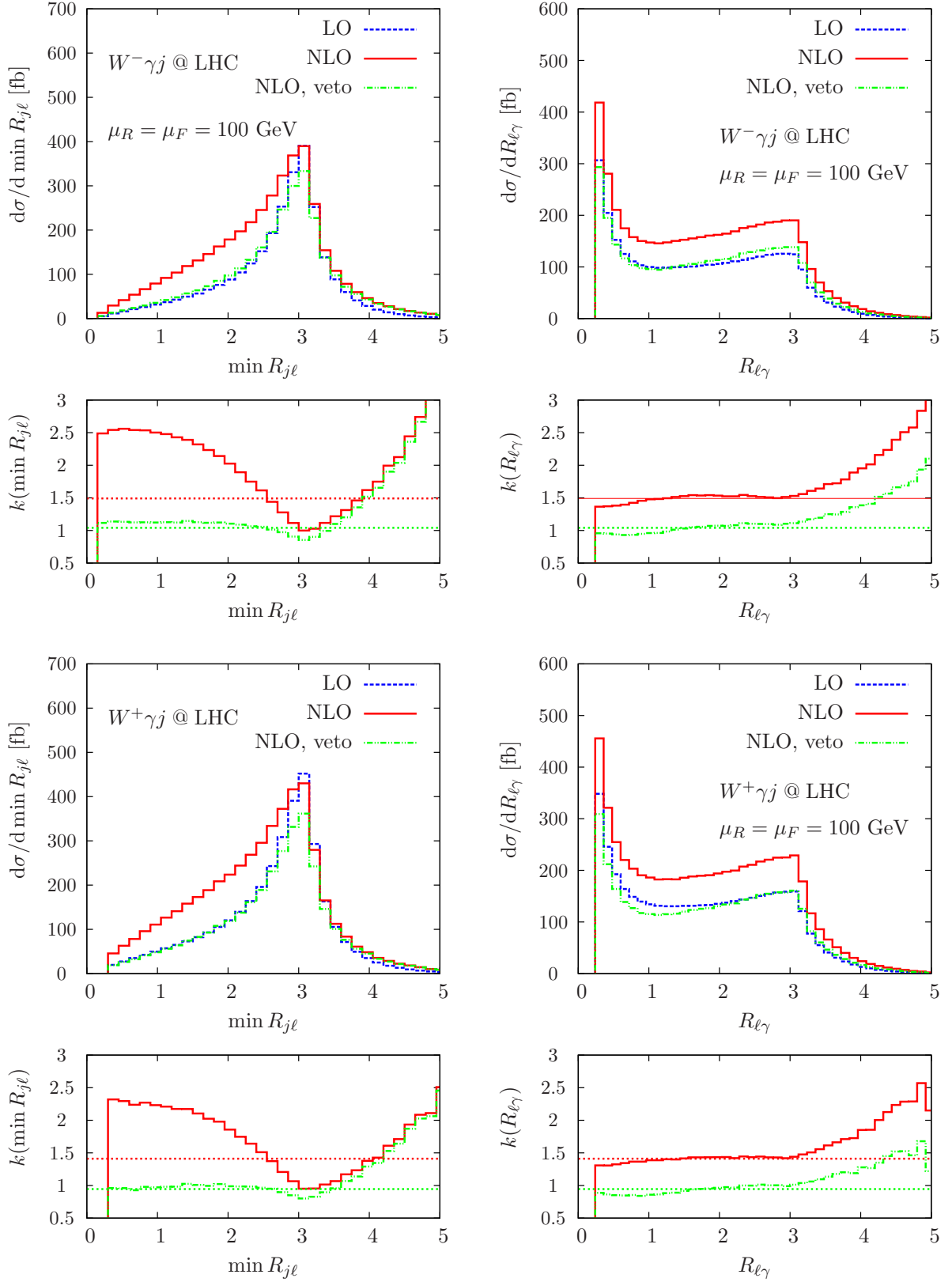


Figure 4.10: Leading order and next-to-leading order distributions of the minimum jet-lepton separation (left panel) and the lepton-photon separation (right panel) in the azimuthal angle – pseudorapidity plane, including the respective differential k factors. The horizontal dashed lines display the corresponding k^{tot} .

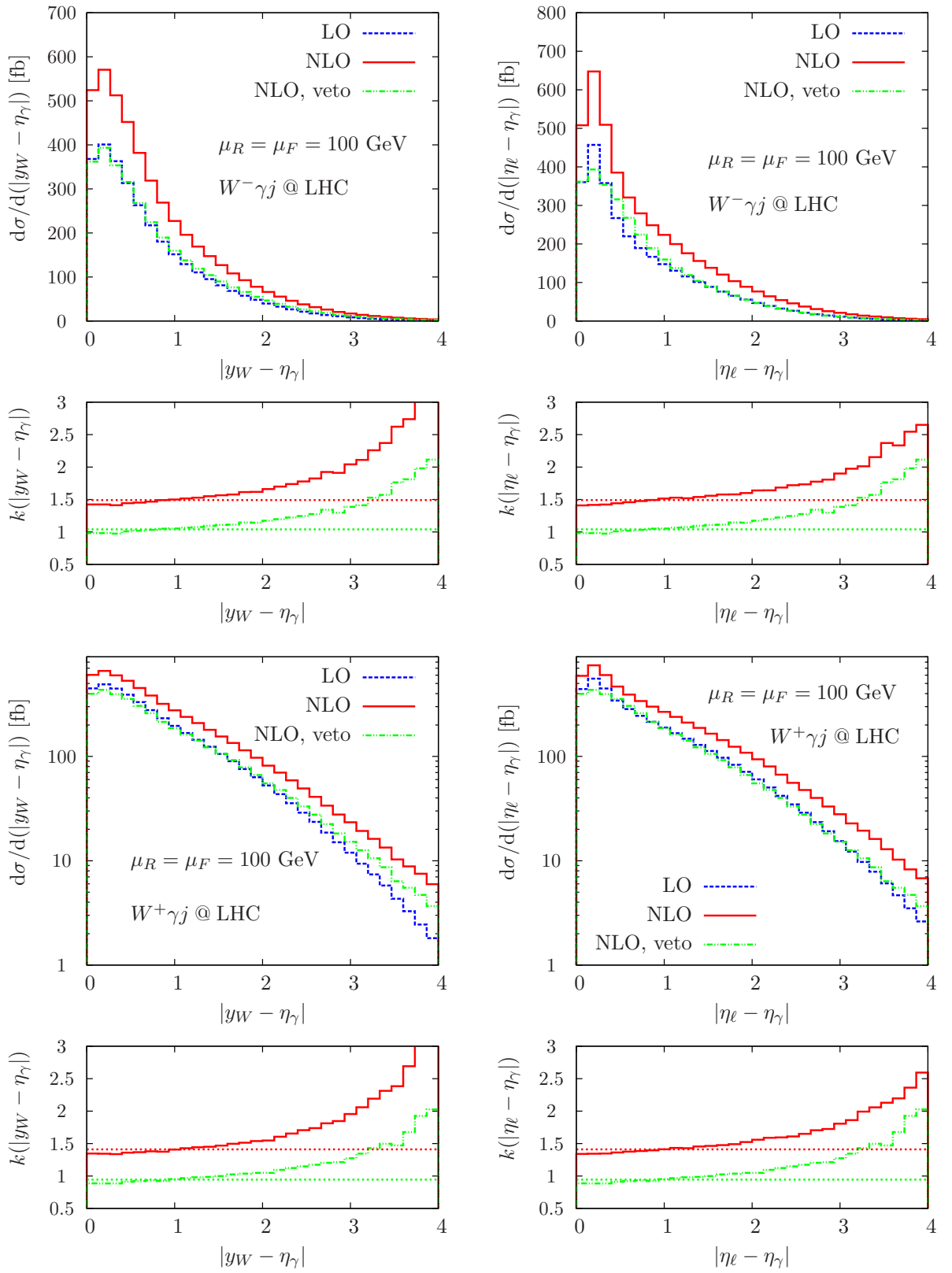


Figure 4.11: Leading order and next-to-leading order distributions of (pseudo)rapidity differences $|y_W - \eta_\gamma|$ (left panel) and $|\eta_\ell - \eta_\gamma|$ (right panel), including the respective differential k factors. The horizontal dashed lines display the corresponding k^{tot} .

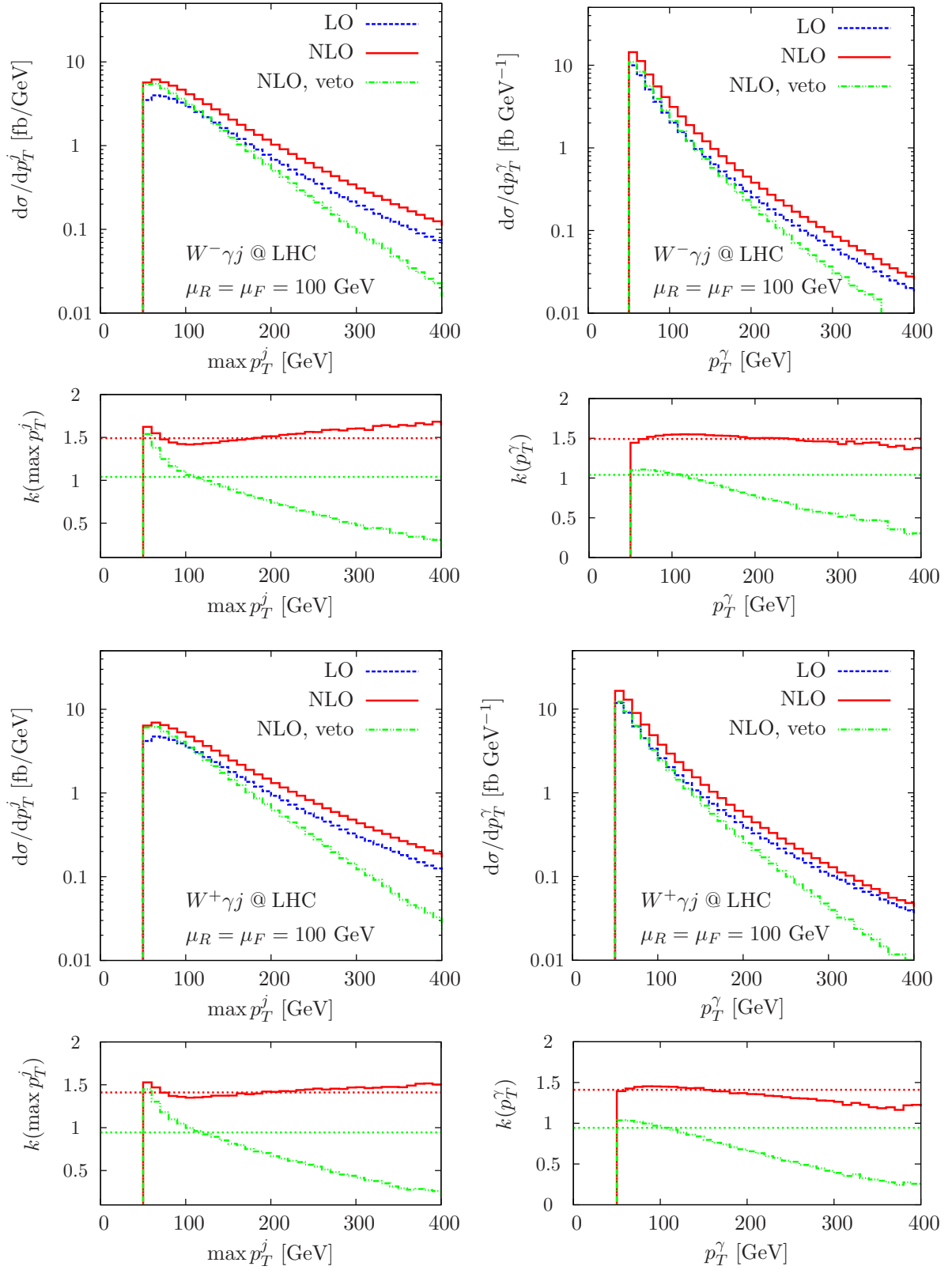


Figure 4.12: Leading order and next-to-leading order distributions of the maximum transverse jet momentum (left panel) and the photon transverse momentum (right panel), including the respective differential k factors. The horizontal dashed lines display the corresponding k^{tot} .

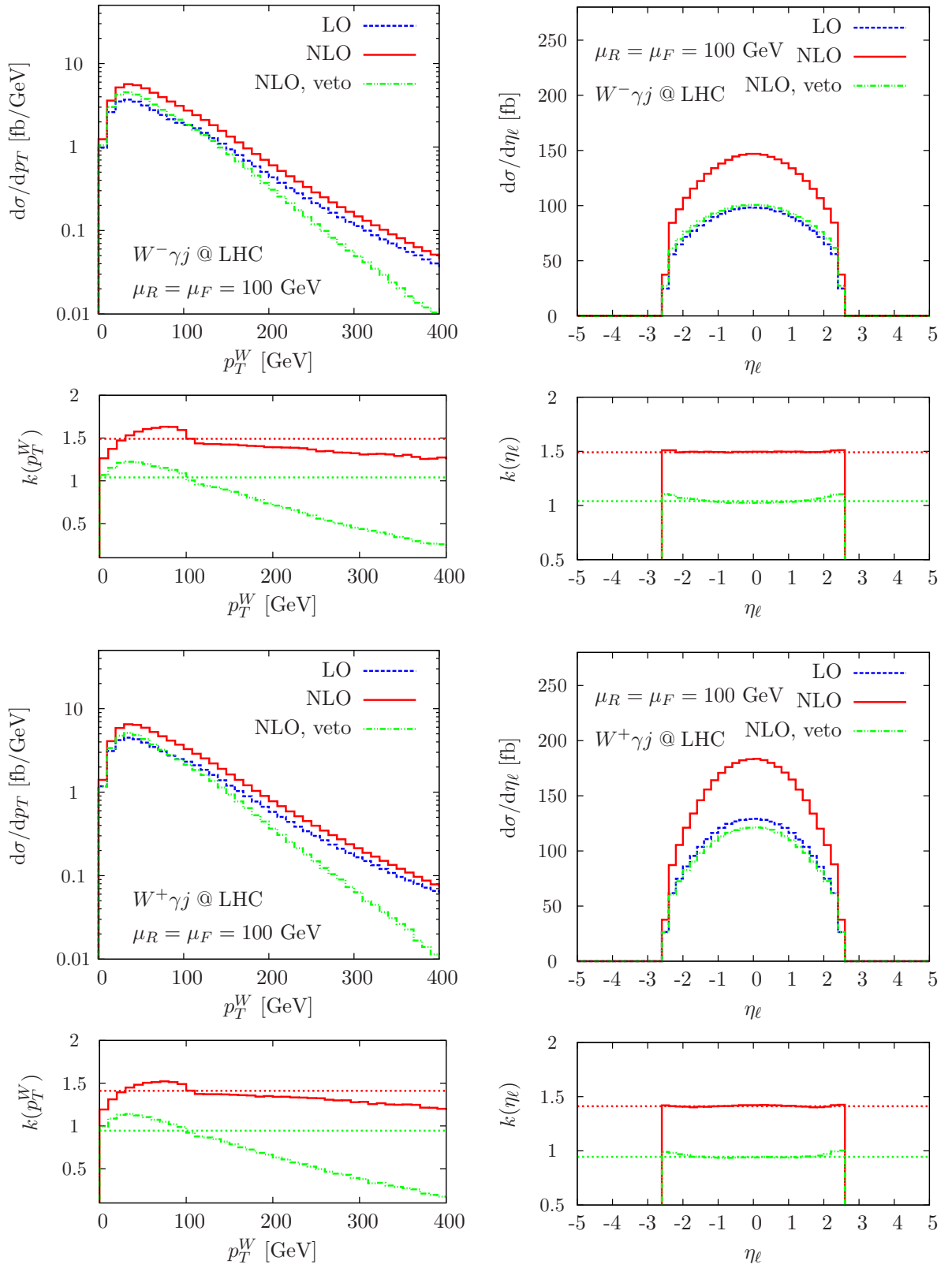


Figure 4.13: Leading order and next-to-leading order distributions of the W transverse momentum (left panel) and the lepton rapidity (right panel), including the respective differential k factors. The horizontal dashed lines display the corresponding k^{tot} .

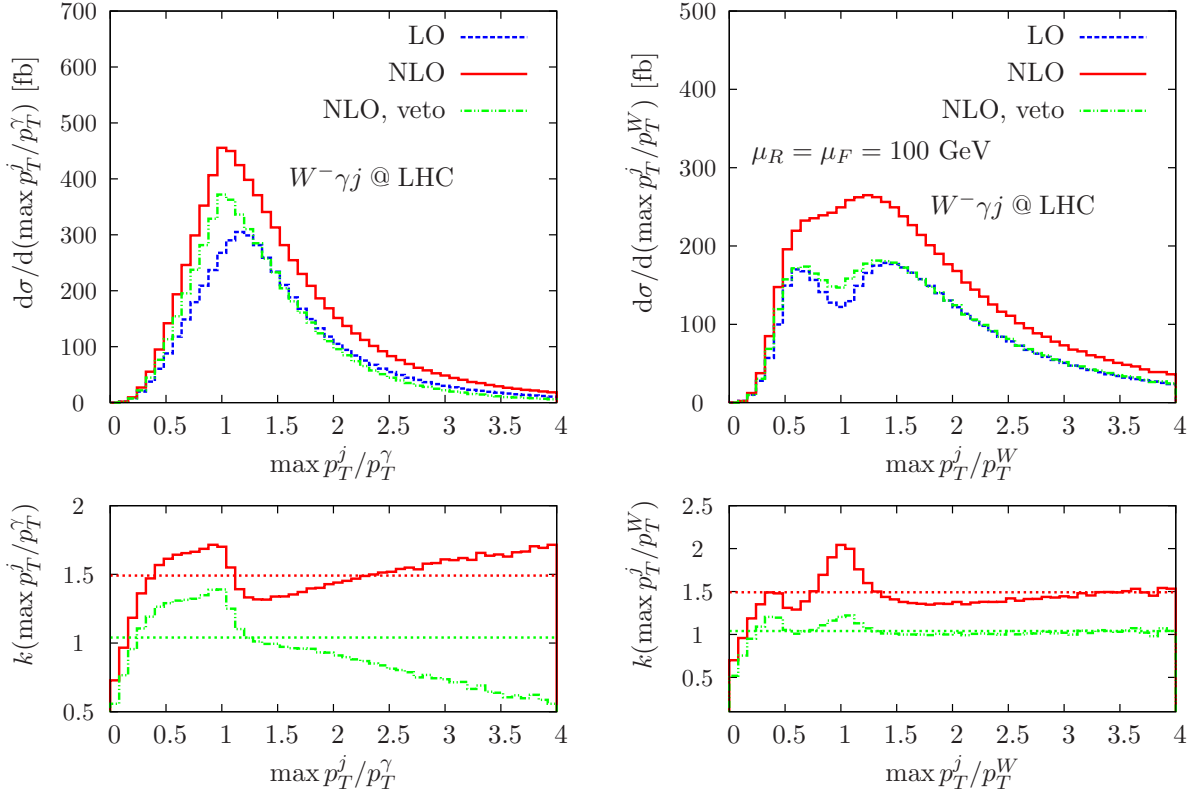


Figure 4.14: Leading order and next-to-leading order distributions of the ratios $\max(p_T^j)/p_T^\gamma$ (left panel) and $\max(p_T^j)/p_T^W$ (right panel), including the respective differential k factors.

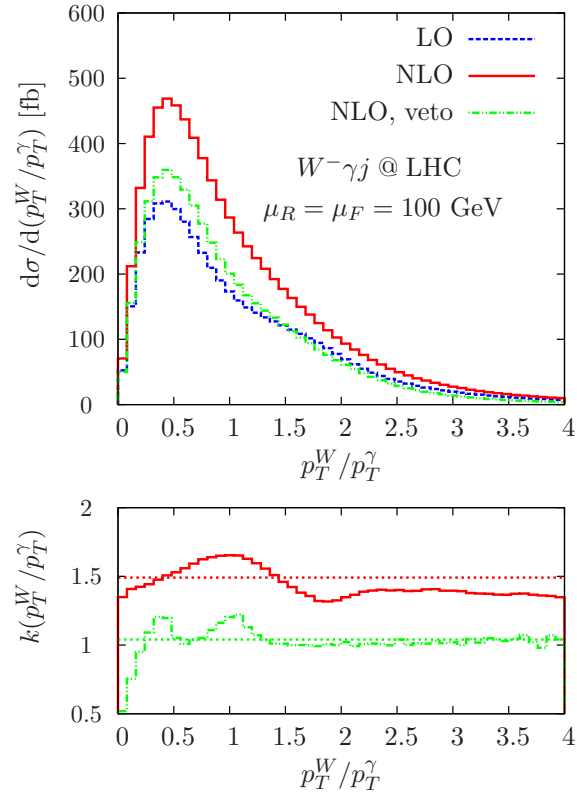


Figure 4.15: Leading order and next-to-leading order distributions of the ratio p_T^W/p_T^γ , including the respective differential k factor.

rapidity in fig. 4.13, where the W 's four-momentum is given by the sum of lepton and neutrino momenta.

Fig. 4.9 depicts the shapes of the longitudinal parton momentum fraction, at which the proton is probed in $W\gamma j$ production and in the NLO di-jet part $W\gamma jj$ for the specified cuts. It also underlines quantitatively the rationale of sec. 4.2, by remembering that the di-jet part has a significant contribution to the NLO cross section. The di-jet part probes the proton at larger momentum fractions, indicated by $\tilde{k}(x) > 1$ for values $x \gtrsim 0.02$. The x -distribution, however, still peaks at small values $x \sim 0.01$ for both contributions due to the subprocess-dominating gluon pdfs at the LHC.

Turning to the transverse momentum distributions (figs. 4.12-4.13), it is evident that the NLO cross section becomes larger in the tails of the p_T^j distribution of fig. 4.12. This results from configurations where the hard jet recoils against the collinear photon- W pair and the additional softer jet. From the softer p_T^γ and p_T^W tails we infer that additional QCD radiation is dominant. The relatively higher jet rate at threshold is mainly compensated by the less constrained W , fig. 4.13. This is also visible from the softer $\max p_T^j$ spectrum compared to p_T^γ and the peak in $k(\max p_T^j/p_T^W)$ at values $\max p_T^j/p_T^W \sim 1$ at NLO in fig. 4.14. The dip in $k(p_T^W)$ around $p_T^W \approx 100$ GeV results from additional parton emission modifying the situation where photon and jet at threshold recoil against the W at LO.

The ratio distributions in figs. 4.14 and 4.15 are also quite helpful in understanding the typical signatures of $W\gamma j$ production at the LHC for the given inclusive cuts: The events are dominated by low p_T configurations due to the (steeply) falling spectra; the entire event is central with lepton and photon preferably at small angular distances in the transverse plane. In fig. 4.16 we show that in the transverse plane with respect to the reconstructible W , the photon is preferably emitted collinearly (three-body decay $W \rightarrow W\gamma$). Yet, there is a considerable fraction of back-to-back events (γ -radiation off the jet). The jet recoils against the electroweak system, so that it points in the opposite direction of the W and the photon in the azimuthal angle distribution. This typical signature also provides an interpretation for the large differential k factor for large photon- W (or photon-lepton) (pseudo)rapidity differences in fig. 4.11, which communicates to the R -separation in fig. 4.10. Such configurations are affected by additional parton emission, i.e. also by the finite collinear contributions, which misaligns the event in the beam direction with respect to the situation at LO. On top, due to the larger x value of the di-jet contribution compared to LO, fig. 4.9, the events exhibit larger boosts along the beam axis, giving rise to larger rapidity differences than at LO. In addition to both these reasons the finite collinear terms reproduce The same reason contributes to the leptons depopulating the central region in fig. 4.13 and e.g. $k(|y_W - \eta_\gamma|) < k^{\text{tot}}$ at small values in fig. 4.11. These effects can not be circumvented by the veto on the second jet. Quite contrary, they are more pronounced for the exclusive distributions. This is because the situation where the two jets recoil against the W - γ system in the transverse plane tend to re-collimate the lepton in central region. Similar modifications can be also be found in the azimuthal angle distributions, e.g. fig. 4.16, where the differential k factors of the vetoed distributions exhibit almost identical shapes as the inclusive differential cross sections.

The NLO QCD corrections to the hadronic observables in the region of phase space

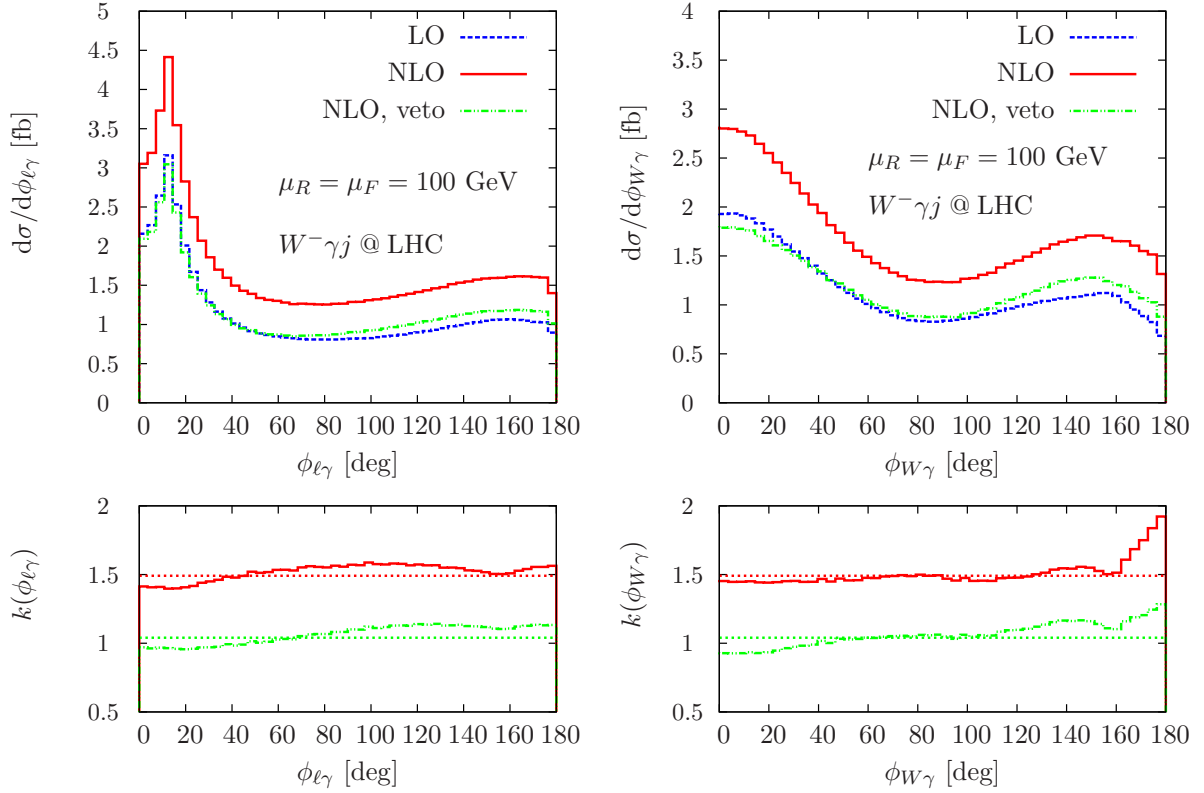


Figure 4.16: Leading order and next-to-leading order distributions of the azimuthal angle between photon and lepton, and photon and W .

selected by our inclusive cuts are dominated by the additional jet activity, which occurs central at small rapidity differences $|\Delta y_{jj} \approx 1|$. This is due to the real emission-dominating quark-gluon-induced processes, which involve distinct momentum fractions of the incoming partons. There is an only weak accentuation of back-to-back di-jet configurations in the almost flat radiation pattern of $\Delta\phi_{jj}$. This behavior can be anticipated from the large relative modifications of minimum distance observables that involve a jet at LO. Pronounced effects of the additional jet activity are also visible in the ratio distributions. While at LO the region $\max p_T^j \sim p_T^W$ is kinematically disfavored by the chosen acceptance criteria, the dip for $\max p_T^j/p_T^W \sim 1$ is entirely smeared out at NLO. This becomes even more apparent for W - γ back-to-back configurations with e.g. $|\Delta\phi_{W\gamma}| \geq 150$ deg, where the energetic W s that recoil against the jet and the photon at LO get suppressed because of additional hard jet radiation into the direction of the W s. As these configurations amount to large momentum transfers in the trilinear $WW\gamma$ coupling, our corrections are highly important for understanding deviations that result from anomalous couplings. We will discuss this in more detail in sec. 4.4, but as the anomalous couplings effects generically show at large values of p_T^γ , it is worth commenting on the impact of the NLO corrections onto this region of phase space already at this point. Hence, turning to more energetic events in the tails of the p_T distributions (e.g. $p_T^\gamma > 1$ TeV), we find a quite different picture compared to one analyzed before. At large transverse momentum of the photon, jet emission is logarithmically enhanced

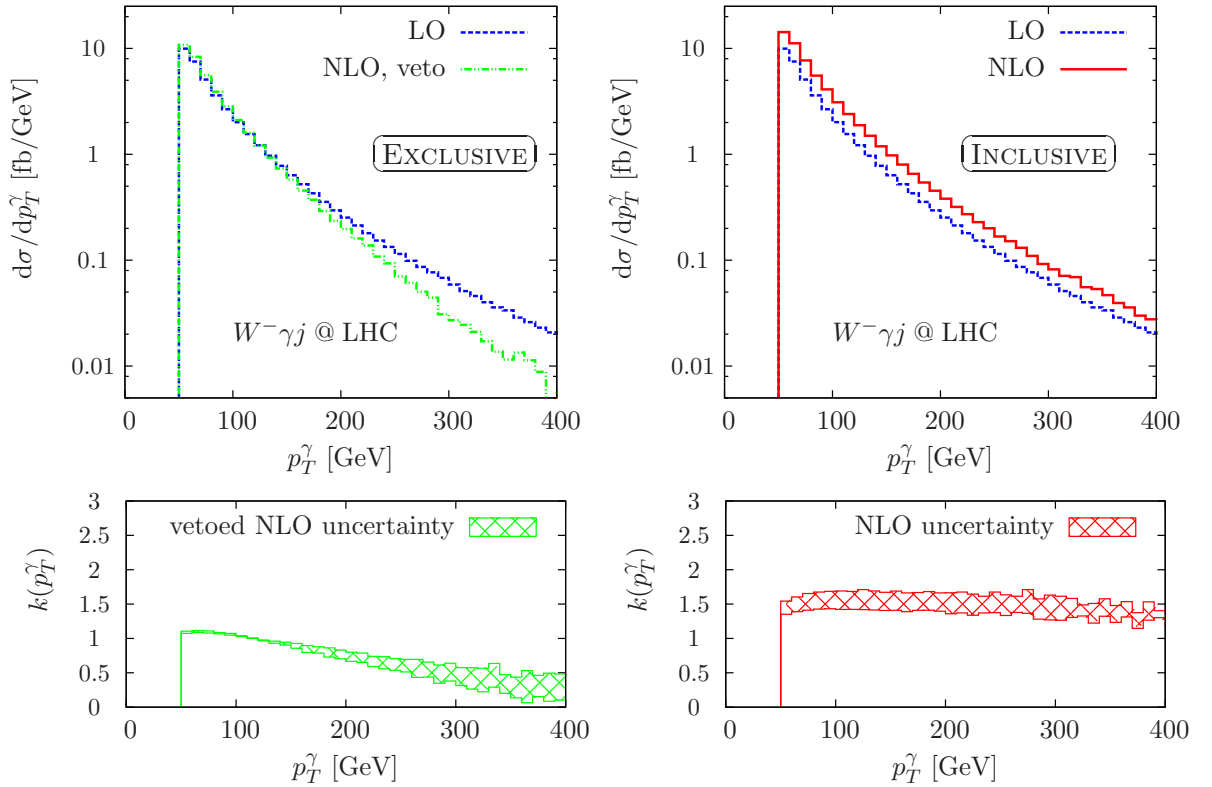


Figure 4.17: Leading order and next-to-leading order uncertainty bands for the p_T^γ distribution, for exclusive and inclusive $W\gamma$ production. The band widths are determined from varying the factorization and renormalization scales by a factor two around $\mu_R = \mu_F = 100$ GeV only in the NLO distributions, while keeping the scale fixed for the LO distribution.

in the dominating gluon-induced channels $qg \rightarrow W\gamma Q$ already at LO, which can easily be seen from the Altarelli-Parisi approximation of collinear emission $q \rightarrow QW$ [12]

$$d\sigma(qg \rightarrow W\gamma Q) = d\sigma(qg \rightarrow q\gamma) \frac{e^2}{32\pi^2 \sin^2 \theta_w} \log^2 \frac{p_T^{\gamma 2}}{m_W^2}, \quad (4.6)$$

where we again assume a diagonal CKM matrix. The preferred situation is therefore a collinear W -jet pair that recoils against the hard photon. This region of phase space receives sizable QCD corrections. Compared to the other hard jet, the extra jet emission for these events is nearly isotropic in the azimuthal angle at small rapidity differences $|\Delta y_{jj}|$. The situation where the photon recoils against the W -jet pair is therefore again heavily modified as the additional jet emission becomes kinematically unsuppressed. By the same reason the p_T^W distribution is affected.

Applying the jet veto of (4.2b) the described characteristics of additional jet radiation vanishes in figs. 4.6-4.15 to large extent at total rates of

$$\begin{aligned} \sigma_{\text{excl}}^{\text{NLO}}(W^-\gamma j) &= (429.2 \pm 0.8) \text{ fb} & (k^{\text{tot}} = 1.04), \\ \sigma_{\text{excl}}^{\text{NLO}}(W^+\gamma j) &= (495.1 \pm 1.0) \text{ fb} & (k^{\text{tot}} = 1.06). \end{aligned} \quad (4.7)$$

As we can see in figs. 4.12 and 4.13, the small total corrections are due to approximate cancellations among large differential corrections to different regions of phase space.

The small k^{tot} along with the stability against variations of $\mu_R = \mu_F$ of the exclusive cross sections should therefore not be misinterpreted as a guideline to stable LHC predictions *per se*, but as a significant, yet still purely *theoretical* perturbative improvement of $W\gamma j$ production up to the specified threshold value of p_T^j , which characterizes genuine $W\gamma j$ production. Above this threshold the new channels opening up at NLO as part of the real emission get expelled from the total cross section in exclusive production. Whether the veto actually does provide a sufficiently stable theoretical approximation in the sense of an experimentally applicable strategy, thus depends highly on the phenomenological question we ask, i.e. on the phase-space region we are interested in[‡]. From the direct comparison of differential inclusive and exclusive distributions it is evident that additional jet radiation is kinematically unsuppressed. This especially holds for hard events with large jet-transverse momenta, where the di-jet contribution favors recoil of the jet with largest p_T against the new softer jet, instead of exclusively against the $W\gamma$ system, which corresponds to the typical situation at LO. Vetoing additional radiation in a region of phase space where it becomes likely is crucial to the flat scale dependence of the exclusive cross section as can be seen from comparing the perturbative uncertainties of the p_T^γ distribution in fig. 4.17. While the scale dependence is rather uniformly distributed for inclusive NLO, the threshold region (where we can really speak of “genuine $W\gamma j$ production”) of the vetoed sample is perturbatively stabilized, and the small overall scale dependence arises from a significant uncertainty at large p_T^γ with only little contribution to the total rate. Perturbative stability against variations of factorization and renormalization scales of vetoed $pp \rightarrow \ell\nu\gamma j + X$ hereby appears as subtraction of a leading order contribution from a rather stable inclusive distribution at large p_T^γ . The vetoed di-jet contribution is kinematically well-accessible in this very region of phase space and unsuppressed by QCD dynamics. Thus, the relatively larger scale variation in the vetoed distribution compared to inclusive production remains as an echo thereof. On top of this uncertainty, some distributions, e.g. $|y_W - \eta_\gamma|$ and therefore also $R_{\ell\gamma}$, are still heavily modified by additional parton emission in phase space regions which are close to the cut-determined edges, where kinematical distortion and boost effects become visible.

Lowering the available center-of-mass energy by turning to Tevatron collisions, we find a qualitatively similar situation to the LHC-veto set-up at a lower overall rate of

$$\sigma^{\text{NLO}} = (14.86 \pm 0.03) \text{ fb} \quad (k^{\text{tot}} = 1.351), \quad (4.8)$$

with dominating quark-induced channels. This is due to the fact that additional jet-radiation is suppressed for the chosen selection cuts, giving effectively rise to a jet veto; as additional jet radiation is kinematically suppressed compared to the LHC, the semi-hadronic observables receive smaller corrections. Yet, QCD radiation-effects are still visible, and events tend to be re-distributed to smaller minimum separations of the hadronic jets with respect to the lepton and the photon, figure 4.18.

[‡]There are various other sources of uncertainty, which we do not address here. These range from NLO-showering and hadronization to underlying event and pile-up. Nonetheless it is clear from QCD factorization that a perturbatively stable hard matrix element calculation is a *condicio sine qua non* for sensibly modelling high energy particle physics.

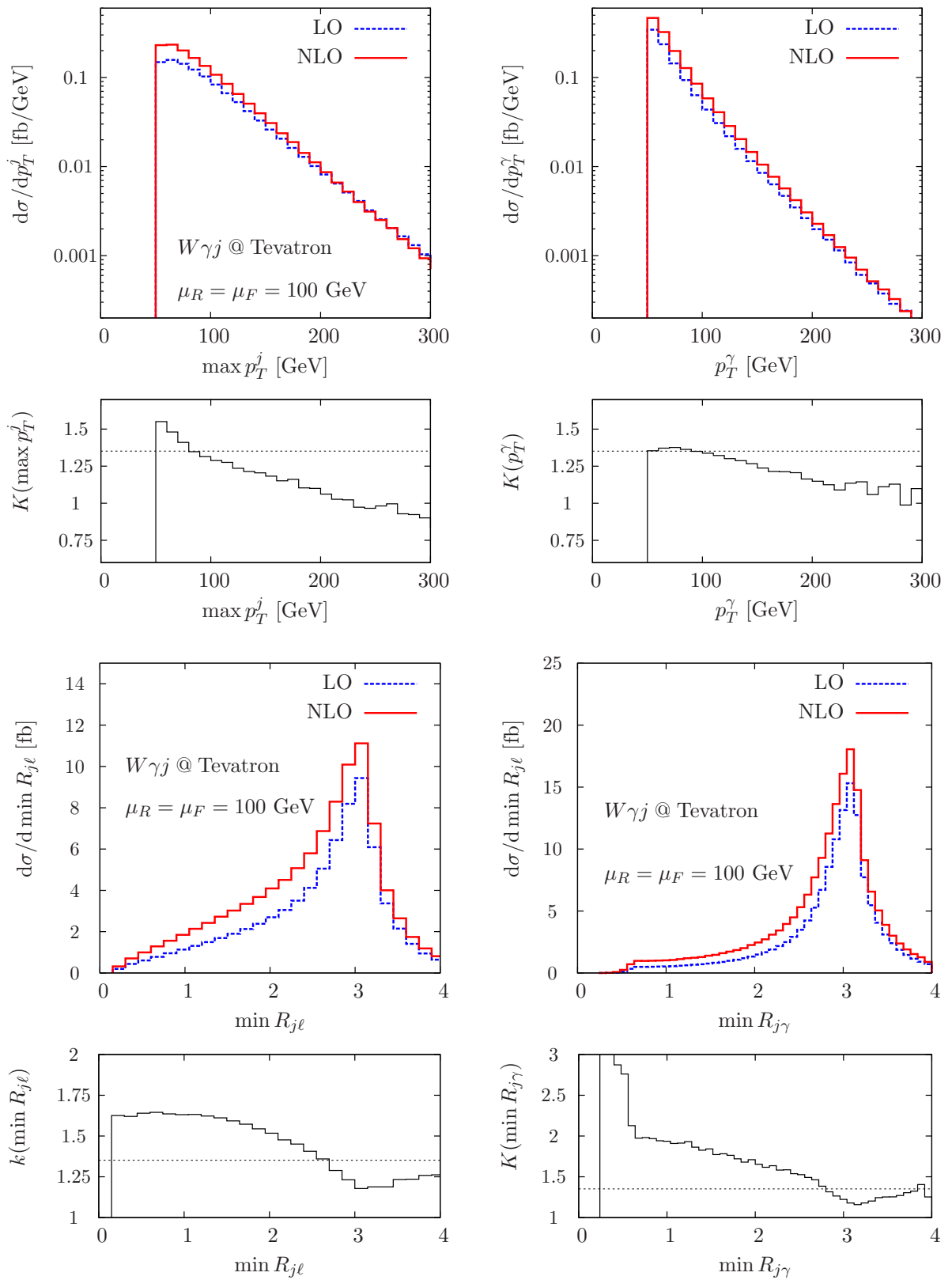


Figure 4.18: Leading order and next-to-leading order distributions of $\max p_T^j$, p_T^γ , $\min R_{j\ell}$, and $\min R_{j\gamma}$ at the Tevatron, including the respective differential k factors. The total k factor is plotted as horizontal line.

4.4 Impact of non-standard $WW\gamma$ couplings

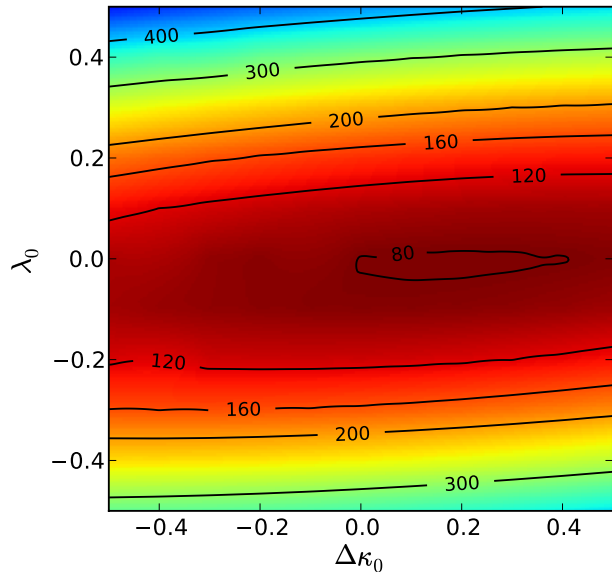
Searches for anomalous couplings represent benchmark tests for non-SM interactions at the LHC. Consequently, measurement and discovery strategies have received lots of attention, both from the theoretical (e.g. [12, 87, 88]) and the experimental side (cf. [89–93]). Quite obviously, di-boson production is an important channel at the LHC as it exhibits sizable rates, and, in case of $W^\pm\gamma$ production, is sensitive to SM-deviations through so-called radiation zeros [94]. These classical zeros of the amplitude in the $q\bar{Q} \rightarrow W^\pm\gamma$ channels at the photon’s scattering angle in the center-of-mass frame at $\cos\theta_\gamma^* = \mp 1/3$ is special to the completely destructive interference of gauge boson-radiation in an unbroken renormalizable field theory from incoming and outgoing charged lines. Any deviation from QED by additional non-SM operators of (2.27) and (3.5) ultimately destroys this characteristic radiation pattern. However, as the radiation zero is physically not present in the gluon-induced channels, which dominate at the LHC via the larger pdf luminosities, and the antiquark direction is indistinguishable from the quark direction for the LHC’s proton-proton initial state, the radiation zero gets considerably washed out. ”Signing” the quark direction according to the event’s overall boost, which was considered in the context of di-lepton asymmetries and electroweak mixing angle measurements [95], efficiently lifts this proton-proton initial state’s degeneracy [91].

The radiation zero remains only present if additional neutral (gluonic) radiation is collinear to the photon. Hence, additional QCD emission, as part of the NLO contribution to $W\gamma$ production, is potentially lethal to the radiation zero. At the same time it becomes impossible to measure the radiation zero in $W\gamma j$ production [88]. Additionally, extra radiation in the channel $qg \rightarrow W\gamma Q$ is logarithmically enhanced in regions $p_T^\gamma \gg m_W$ as shown in (4.6), and affects fits to the p_T^γ distribution, which are additionally used by experimentalists to infer the numerical values of $\Delta\kappa_0$ and λ_0 for a given scale Λ [91, 92]. In the high- p_T^γ phase space region, where anomalous couplings’ effects are pronounced, the NLO inclusive $W\gamma$ cross section is therefore dominated by collinear W -jet pairs with suppressed contributions of the graphs that involve the trilinear $WW\gamma$ coupling with a large momentum transfer. Hence, the inclusive sample is less sensitive to electroweak deviations.

A straightforward (Monte Carlo) way to avoid this dilemma is to impose a veto on additional hard jets, which, for $W\gamma$ production, exhibits similar implications as for the $W\gamma + \text{jet}$ production, discussed in the beginning of this chapter: The scale dependence is reduced, the radiation zero is restored and deviations from the SM in the high p_T^γ tail are mostly due to anomalous couplings. Therefore, some experimental studies (e.g. [91]) are based on total k -factor corrected leading order cross sections applying a jet veto; systematic uncertainties due to higher order effects are estimated by varying fixed renormalization and factorization scales by an overall factor.

This procedure involves at present theoretical as well as experimental uncertainties. On the one hand, systematic uncertainties attached to jet vetoing can be sizeable as they do highly depend on the experimental situation and therefore require precise knowledge of detector performance, jet energy scales, pile-up and underlying event effects. A realistic assessment of these uncertainties is clearly way beyond current Monte Carlo-

Figure 4.19: Total leading order cross section contours at the LHC (in fb) for anomalous input parameters $|\Delta\kappa_0|, |\lambda_0| \leq 0.5$ with dipole form factor $n = 2$ and cutoff scale $\Lambda = 1$ TeV. The selection cuts are adopted from typical experimental studies [89–93], extended by inclusive criteria for the jets. They are quoted in (4.10). All other input parameters are chosen as described in sec. 4.1.



driven studies and should be addressed with early LHC data. On the other hand, from a more theoretical point of view, a jet veto is a questionable procedure in fixed order perturbation theory. For typical cut-choices that are applied in anomalous couplings searches, the inclusive k^{tot} factor is larger than 4, and the LO $W\gamma$ cross section of approximately 20 fb is pushed to inclusive rates well above 100 fb by gluon-initial states opening up as part of $W\gamma j$ real emission contribution at very small momentum fractions x . This way NLO $W\gamma$ production is still dominated by leading order $W\gamma j$ uncertainties – the jet-veto amounts to subtraction of a cross section, which is considerably larger than the LO approximation and which, at the moment, exhibits typical LO QCD-scale uncertainties. Neuronal net algorithms, trained to these LO distributions, consequently inherit large perturbative uncertainties. Additionally, the differential k factor sizably departs from the total k factor in the tails of the distributions [90], ranging up to factors of five in the p_T^γ regions. Not only is this the region of phase space where anomalous couplings effects are well-pronounced, but we also have to raise the question how reliable the predictions are in this particular region, given their huge size.

Most stringent bounds on anomalous $WW\gamma$ couplings currently follow from combined LEP data [93]

$$1 + \Delta\kappa_0 = 0.984_{-0.047}^{+0.042} \quad \lambda = -0.016_{-0.023}^{+0.021}, \quad (4.9a)$$

and most recent fits at hadron colliders are from the Tevatron $D\bar{0}$ experiment [92]

$$1 + \Delta\kappa_0 = 1.07_{-0.20}^{+0.16} \quad \lambda = -0.0_{-0.04}^{+0.05}. \quad (4.9b)$$

Both bounds are at 68% confidence level, with a choice of $\Lambda = 2$ TeV. The numbers quoted in (4.9b) are based on fits assuming full $SU(2)_L \times U(1)_Y$ invariance. Note, that both experiments are consistent with the SM prediction $\Delta\kappa_0 = \lambda_0 = 0$. These bounds

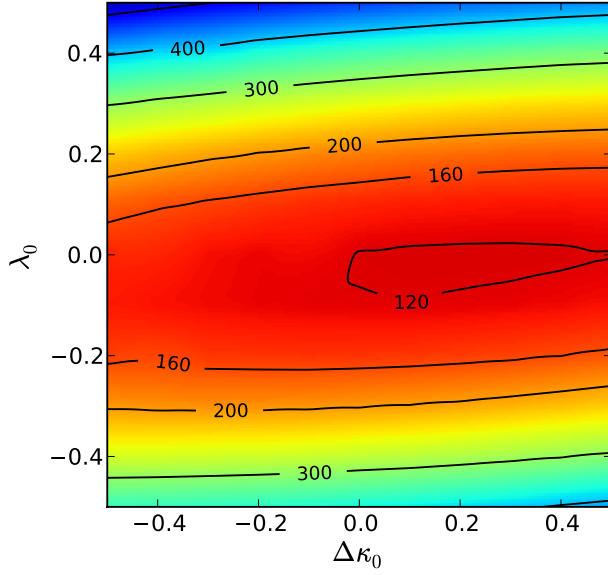


Figure 4.20: Total next-to-leading order cross section contours at the LHC (in fb) for anomalous input parameters $|\Delta\kappa_0|, |\lambda_0| \leq 0.5$ with dipole form factor $n = 2$ and cutoff scale $\Lambda = 1$ TeV. Cuts and parameters are chosen as described in fig. 4.20.

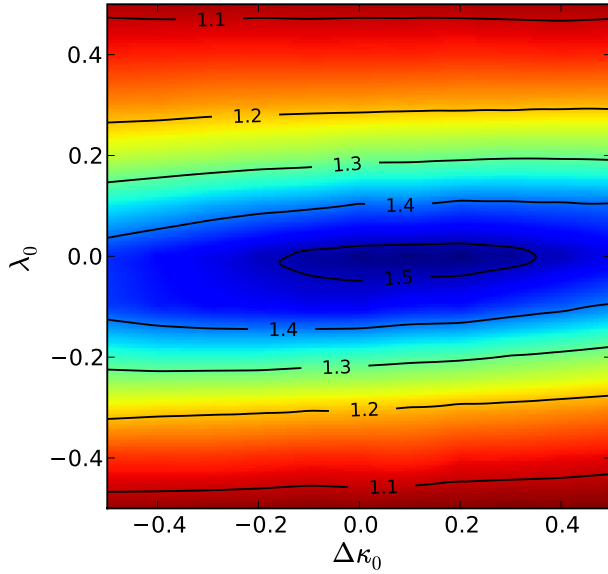


Figure 4.21: Total k factor contours at the LHC for anomalous input parameters $|\Delta\kappa_0|, |\lambda_0| \leq 0.5$ with dipole form factor $n = 2$ and cutoff scale $\Lambda = 1$ TeV. Cuts and parameters are chosen as described in fig. 4.20.

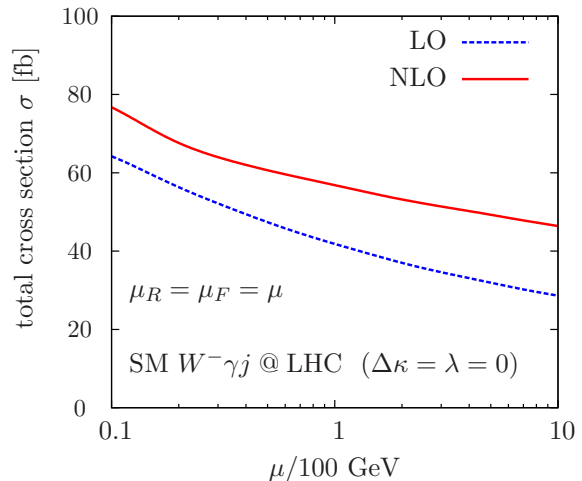
select the region of parameter space where the QCD corrections are most sizable for $W\gamma j$ production (explained further below), i.e. where they are relevant to the veto procedure. This can be seen from figs. 4.19-4.21, which are produced with the cut set of [91],

$$p_T^\gamma \geq 100 \text{ GeV}, \quad p_T^\ell, \not{p}_T \geq 25 \text{ GeV}, \quad R_{\ell\gamma} \geq 1.0, \quad (4.10a)$$

with the additional hadronic jet cuts

$$p_T^j \geq 20 \text{ GeV}, \quad \delta_0 = 0.4, \quad R_{j\ell} \geq 0.2, \quad (4.10b)$$

Figure 4.22: Scale dependence of the leading order, next-to-leading order inclusive $W^- \gamma j$ in the SM $\Delta\kappa = \lambda = 0$ for the cut choice (4.10), (4.11), which we use to study the impact of anomalous couplings (4.9) on the cross sections in fig. 4.23. Varying around $\mu = 100$ GeV by a factor two yields a NLO scale uncertainty of 6.5% with an upper bound of 60.6 fb.



i.e. very inclusive hadronic cuts. All other cuts and input parameters are adopted from sec. 4.1. These cuts already remove efficiently the collinear $W\gamma$ configurations of fig. 4.16. Yet, there is still a sizable fraction of events where the photon recoils against the jet, instead of against the W , which would be the preferred situation to generate large momentum transfers in the anomalous vertex. This can be rectified by requiring harder leptons and more missing transverse momentum.

Confronted with the allowed anomalous coupling range (4.9), NLO $W\gamma j$ production with the additional cut

$$\Delta\phi(W\gamma) \geq 150 \text{ deg} \quad (4.11)$$

to mimic $W\gamma$ events with large invariant mass, shows a variation of the $W^- \gamma j$ cross section of about 10% over the allowed parameter range of (4.9). Comparing to the uncertainty attached to the SM expectation fig. 4.22, which e.g. yields $\sigma \simeq 60.6$ fb for $\mu_R = \mu_F = 50$ GeV, we see that the cross sections' increase due to the anomalous couplings is entirely covered by the SM scale uncertainty, signaling a vanishing sensitivity of the total rate to anomalous couplings.

This statement, however, does not hold for differential distributions. The differential $k(p_T^\gamma)$ factor shows that the NLO inclusive cross section receives a larger contribution from the threshold region compared to the p_T^γ -tail. In addition, at low transverse momenta the distributions exhibit a rather uniform shape, which is largely independent of the chosen anomalous couplings. Hence, not only a large fraction of the cross section, but also a large share of its increase compared to LO, is insensitive to the underlying electroweak deviation in the allowed parameter range. The NLO inclusive cross section is therefore less sensitive to the anomalous couplings than the LO cross section, and k^{tot} is large in regions, where the distributions are solely dominated by their low p_T behavior: k^{tot} peaks around the SM, $\Delta\kappa = \lambda = 0$, figs. 4.21 and 4.22. The anomalous couplings cause deviations from the SM shape at values $p_T^\gamma < \Lambda$ in the transverse momentum spectrum (or, equally, at large invariant $W\gamma$ masses), fig. 4.24, before they get tamed at $p_T^\gamma \sim \Lambda$. The resulting deviations are well outside the SM-uncertainty band for larger values of anomalous couplings, with a particular sensitivity to λ_0 , which dials the dimension six operator new to the electroweak part of the Lagrangian. Approaching the SM, the characteristic enhancements decrease and become

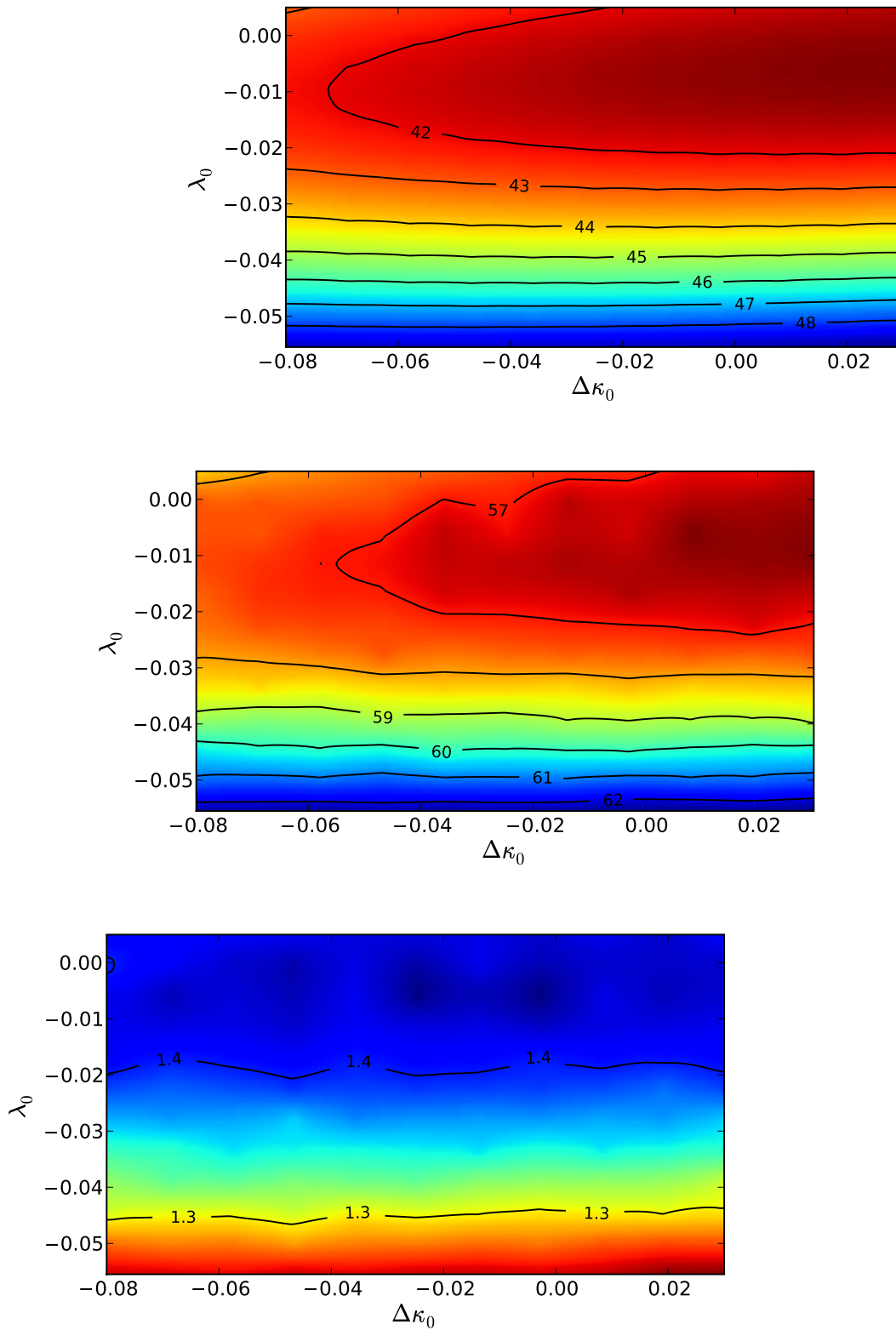


Figure 4.23: Leading order (top right) next-to-leading order (middle) cross sections in fb, and total k factor (bottom) for the anomalous couplings parameters (4.9) with dipole form factor $n = 2$ and cutoff scale $\Lambda = 2$ TeV [91,92] at the LHC. The cuts are chosen as described in the text, eqs. (4.10) and (4.11).

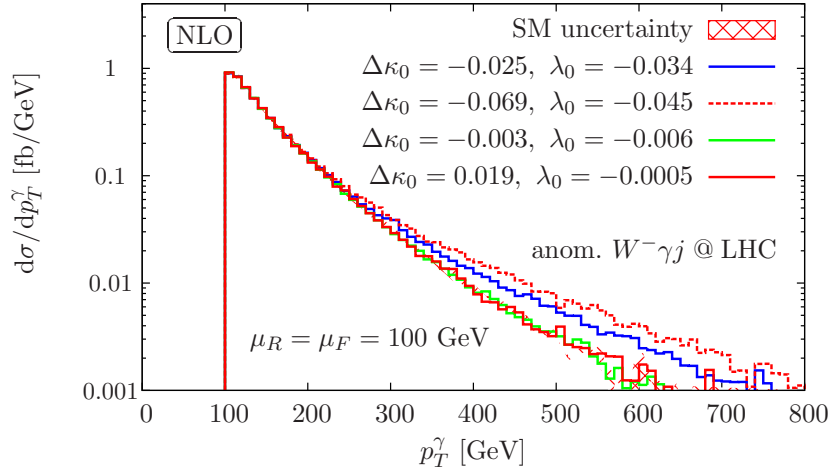


Figure 4.24: NLO- p_T^γ distributions for different anomalous couplings and $\Lambda = 2$ TeV and cuts (4.10), (4.11). The shaded band depicts the SM uncertainty, derived from varying the $\mu_R = \mu_F = 100$ GeV by a factor two around the central value. Note that the uncertainty band is covered by the green and red curve.

comparable to the distributions uncertainty. A more inclusive strategy that supplements traditional techniques appears to be practicable, especially given that the overall theoretical uncertainty of order 10% becomes comparable to the estimated experiments’ systematics.

We can “replace” the LO $W\gamma j$ contribution of NLO $W\gamma$ production at the LHC by our NLO-improved cross section to arrive at an improved inclusive estimate of the differential $W\gamma$ cross section at large transverse momenta of the photon. To do this we define

$$\begin{aligned} \left[\frac{d\sigma^{\text{NLO}}(W^- \gamma)}{dp_T^\gamma} \right]_{\text{improved}} &= \frac{d\sigma_{\text{incl}}^{\text{NLO}}(W^- \gamma)}{dp_T^\gamma} \Big|_{p_T^j \leq 50 \text{ GeV}} + \frac{d\sigma_{\text{incl}}^{\text{NLO}}(W^- \gamma j)}{dp_T^\gamma} \Big|_{p_T^j > 50 \text{ GeV}} \\ &= \frac{d\sigma_{\text{excl}}^{\text{NLO}}(W^- \gamma)}{dp_T^\gamma} \Big|_{p_T^j > 50 \text{ GeV}} + \frac{d\sigma_{\text{incl}}^{\text{NLO}}(W^- \gamma j)}{dp_T^\gamma} \Big|_{p_T^j > 50 \text{ GeV}}. \end{aligned} \quad (4.12)$$

and choose cuts

$$\begin{aligned} p_T^\gamma \geq 100 \text{ GeV}, \quad p_T^j, p_T^\ell \geq 25 \text{ GeV}, \quad \geq 25 \text{ GeV}, \\ R_{j\ell} \geq 0.2, \quad \delta_0 = 0.7, \quad \mathcal{E} = p_T^\gamma, \end{aligned} \quad (4.13)$$

and general Monte Carlo parameter choices and (pseudo)rapidity cuts for photon, jets and leptons as in sec. 4.1. The p_T^j cut, which is used for defining the exclusive $W\gamma$ and the inclusive $W\gamma j$ cross sections according to the above selection criteria follows from (4.12). Note that (4.12) explicitly depends on the chosen jet- p_T (matching-)scale. This again underlines that (4.12) is on only an approximation of the a NNLO calculation.

To generate the $W\gamma$ events we use MCFM v5.5 [96], which does not include anomalous couplings effects, and only considers the decay $W \rightarrow \ell\nu$ [§]. For our cuts and an

[§]For typical section criteria to study anomalous couplings effects, the three-body decay of the W

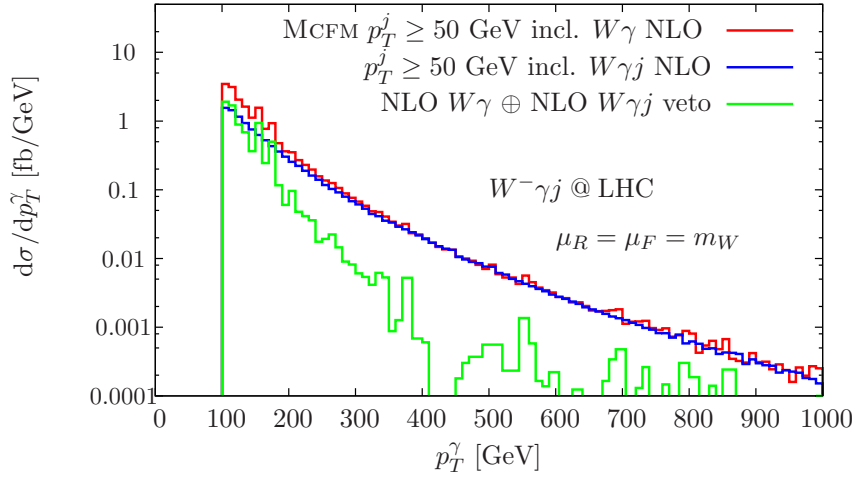


Figure 4.25: NLO- p_T^γ distributions for $W^- \gamma$ and $W^- \gamma + \text{jet}$ production the selection cuts of (4.13), combined to estimate the veto-performance at NLO in the large p_T^γ region.

appropriately modified $W\gamma j$ implementation, the NLO one-jet rate very well approximates the inclusive-NLO $W\gamma$ production at large values of p_T^γ , fig 4.25. At large values of p_T^γ , where LO $W\gamma j$ production dominates the NLO $W\gamma$ inclusive cross section, the NLO-improvement of this one-jet contribution, should provide an improvement of inclusive NLO $W\gamma$ production. This is also the region, where anomalous couplings effects are visible. Our approximation yields only minor modifications on top of the inclusive-NLO $W\gamma$ distribution.

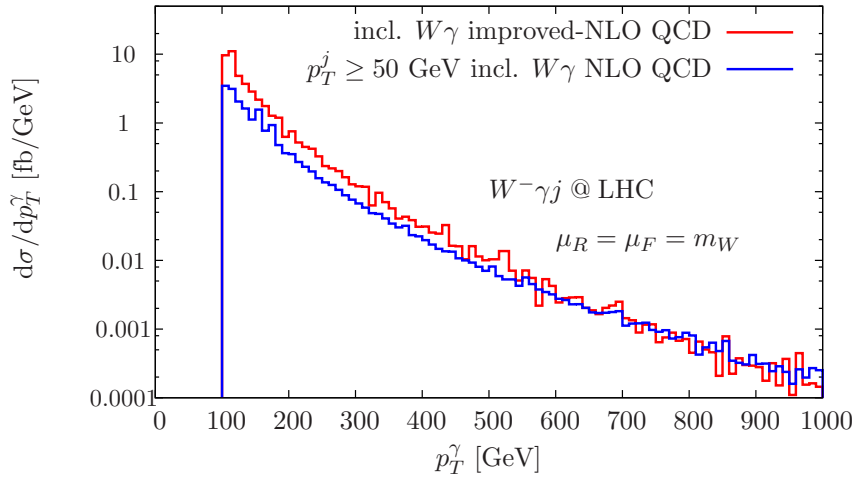


Figure 4.26: NLO- p_T^γ distributions for $W^- \gamma$ production modified with NLO- $W^- \gamma j$ contributions to yield an approximation to the NNLO distribution. Details are described in the text.

is a highly suppressed as pointed out below eq. (4.10). The key selection criteria are the cuts on the transverse momenta of the photon and W (i.e. the lepton and p_T). We therefore relax the cut on $R_{\ell\gamma} \geq 1.0$ in (4.13) compared to (4.10) without changing quantitatively our results in the large p_T^γ region.

We summarize two important points stated by figs. 4.25 and 4.26. On the one hand the veto-procedure applied for $p_T^{j,\text{veto}} \lesssim 50$ GeV does not give a perturbatively reliable result at the given order in perturbation theory. This is already indicated at the exclusive-NLO level of $W\gamma$ production, that yields negative weights at large values of p_T^γ , depending on the jet's p_T scale. This picture does not change, unfortunately, by an NLO-improvement of the vetoed $W\gamma j$ cross section (which is still sensitive to QCD radiation), cf. fig. 4.25, where the veto is shown to leave only statistical noise and negative bins. A full NNLO calculation seems therefore mandatory to give a reasonable estimate of the veto performance at large p_T^γ .

On the other hand, an inclusive strategy towards measurements of anomalous $WW\gamma$ parameters from fits to p_T -distributions that supplement traditional radiation zero measurements, that are mostly result from perturbatively stable low- p_T configurations as opposed to fits to the p_T^γ distribution at large values, should not be obscured by QCD effects beyond typical uncertainties of order 10%, as our calculation shows. As a fortunate side effect this yields sensitivity at much lower integrated luminosities from accessing low- x gluons compared to the small and uncertainty-plagued veto-rates.

Clearly, both statements deserve more detailed investigation and we leave this to future work.

Chapter 5

$W^\pm Z j$ production at hadron colliders

5.1 General Monte-Carlo input parameters

We use identical pdf and parameter sets for the general Monte Carlo input as for $W\gamma j$ production in chapter 4. For the fermionic loop corrections we fix the top quark mass to

$$m_t = 174.3 \text{ GeV}, \quad (5.1)$$

and consider the decays of the W and Z to massless leptons of different generation to avoid identical fermion interference. In addition we do not sum over the final state lepton flavors, i.e. we focus on the processes

$$\begin{aligned} \bar{p}p, pp &\rightarrow e^+ \nu_e \mu^+ \mu^- j + X && \text{(referred to as } W^+ Z j \text{ production)}, \\ \bar{p}p, pp &\rightarrow e^- \bar{\nu}_e \mu^+ \mu^- j + X && \text{(referred to as } W^- Z j \text{ production)} \end{aligned} \quad (5.2)$$

throughout this chapter.

We again recombine jets via the k_T algorithm [86] from massless partons of pseudo-rapidities $|\eta| \leq 5$ with resolution parameter $D = 0.7$ and require the jets to lie in the rapidity range

$$|y_j| \leq 4.5 \quad (5.3a)$$

to account for finite detector coverage. The leptons are detected in rapidity-range

$$|y_\ell| \leq 2.5. \quad (5.3b)$$

To avoid the collinear singularity associated with the virtual photon that couples to the decay leptons, we require a finite lepton-lepton separation in the azimuthal angle-pseudorapidity plane by

$$R_{\ell\ell'} \geq 0.3, \quad (5.3c)$$

	$\sigma_{\text{incl}}^{\text{NLO}}$ [fb]	$k^{\text{tot}} = \sigma_{\text{incl}}^{\text{NLO}} / \sigma^{\text{LO}}$
$W^- Z j$	12.35 ± 0.01	1.295
$W^+ Z j$	17.39 ± 0.02	1.261

Table 5.1: Next-to-leading order inclusive cross sections and k^{tot} -factors for the processes $pp \rightarrow e^+ \nu_e \mu^+ \mu^- j + X$ and $pp \rightarrow e^- \bar{\nu}_e \mu^+ \mu^- j + X$ at the LHC for identified renormalization and factorization scales, $\mu_R = \mu_F = 100 \text{ GeV}$. The cuts are chosen as described in the text.

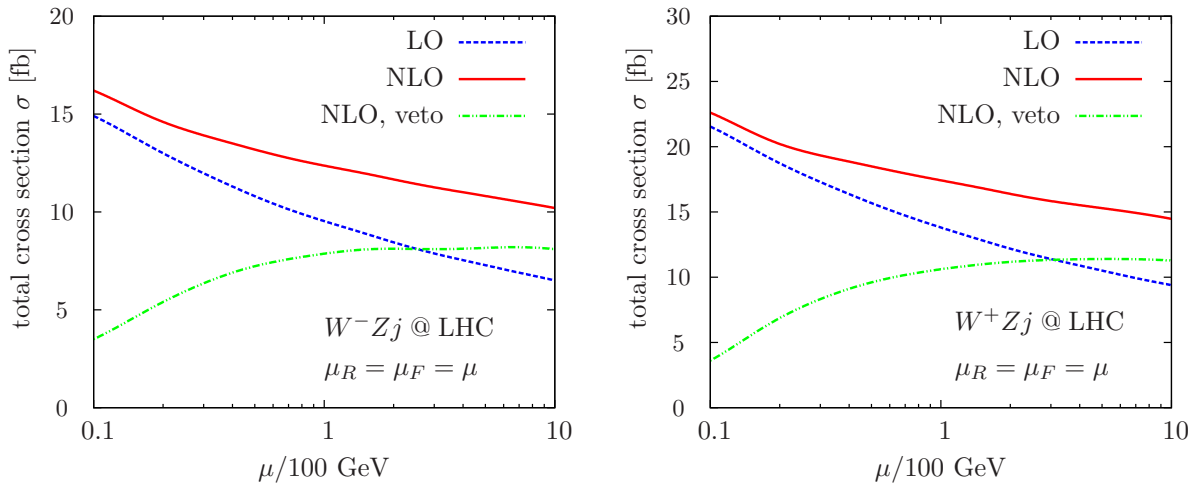


Figure 5.1: Scale dependence of the leading order, next-to-leading order inclusive, and next-to-leading order exclusive $W^\pm Z j$ cross sections at the LHC.

for all leptons, which are at the same time required to be isolated from all jets

$$R_{\ell j} \geq 0.2. \quad (5.3d)$$

5.2 Scale dependence of production cross sections

In the following we analyze the cross sections scaling behavior for the transverse momentum cuts

$$p_T^j \geq 50 \text{ GeV}, \quad p_T^\ell \geq 20 \text{ GeV}, \quad (5.4a)$$

also comparing to the cross sections with the 'no resolvable 2nd jet'-criterion,

$$p_T^{j,\text{veto}} \geq 50 \text{ GeV}, \quad |y_j^{\text{veto}}| \leq 4.5 \quad (\text{exclusive NLO}). \quad (5.4b)$$

The cross sections and total correction factors are listed in tabs 5.1 and 5.2, respectively. The overall scaling behavior highly resembles $W\gamma j$ production, including the μ_R dependence, which is introduced by the di-jet contribution at NLO, figs. 5.1-5.3. This is evident from algebraically identical corrections with the exception of the additional electroweak decay of the massive Z , that amounts to larger final state mass scales compared to the results of chapter 4. Therefore, the bulk of the $W\gamma j$ findings generalize to WZj production in a qualitative manner. Hence we can be shorter discussing the QCD corrections to WZj production. Nonetheless we will address the key differences (especially concerning the second-jet-veto), which quantitatively are due to the fact that the processes test different mass scales and typical selection cuts leave more constraints on the events compared to $W\gamma j$.

The LO scale uncertainties of $\sim 25\%$, estimated by varying $\mu_F = \mu_R$ by a factor two around 100 GeV, are reduced to about 13% for inclusive NLO production. Quite different from the stabilization of the vetoed sample of $W\gamma j$ production at the cross section level, the veto does not yield a perturbative improvement in terms of flat scale

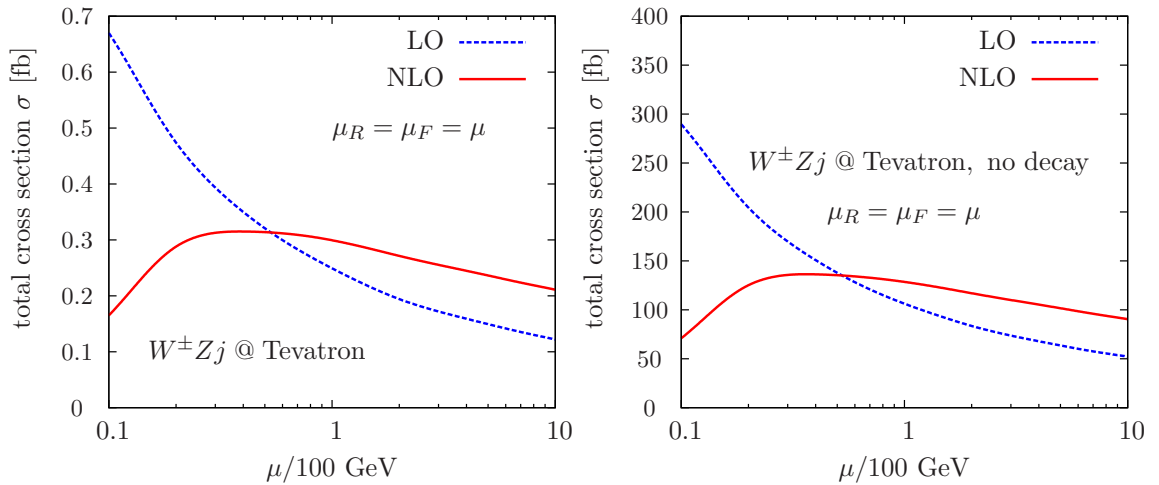


Figure 5.2: Scale dependence of the leading order and next-to-leading order inclusive $W^\pm Zj$ cross sections at the Tevatron. The cross sections correspond to either $W^- Zj$ or $W^+ Zj$ production, i.e. we do not sum over the two W^\pm bosons.

variations. The exclusive WZj production cross sections still exhibit scale dependencies of $\sim 10\%$. The impact of dynamically chosen scales $\mu_F = \mu_R$, depicted in fig. 5.3 is about 7% for $\xi = 1$ at NLO.

The total rate at the Tevatron is very low, given the collected luminosity of about 8 fb^{-1} . Lowering the p_T^j selection criterion to 20 GeV and summing over light lepton flavors drives the total NLO cross section from $(298.5 \pm 0.5) \text{ ab}$ ($k^{\text{tot}} = 1.2$) up to 3 fb, which is still a too low rate to be relevant to phenomenological studies. Hence, in the following we only mention the Tevatron findings at the side, focussing on LHC predictions. While leptonic decays of the massive gauge bosons exhibit low rates at the Tevatron this is not true for WZj production without further decay of the gauge bosons taken into account. Here the production rate is sizable, fig. 5.2. Including the

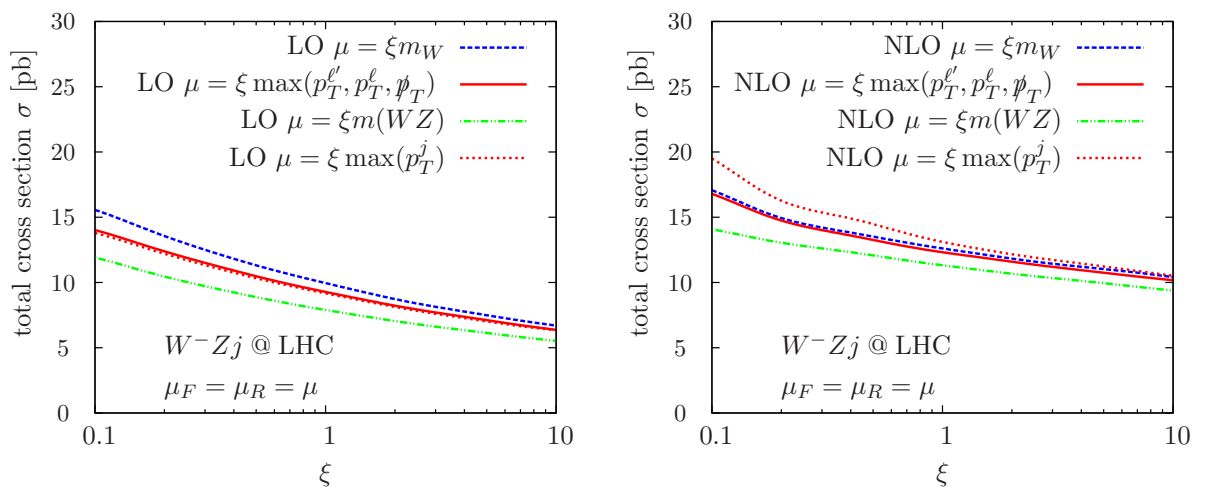


Figure 5.3: Scale dependence of the leading order and next-to-leading order $W^- Zj$ cross sections at the LHC for different dynamical scales.

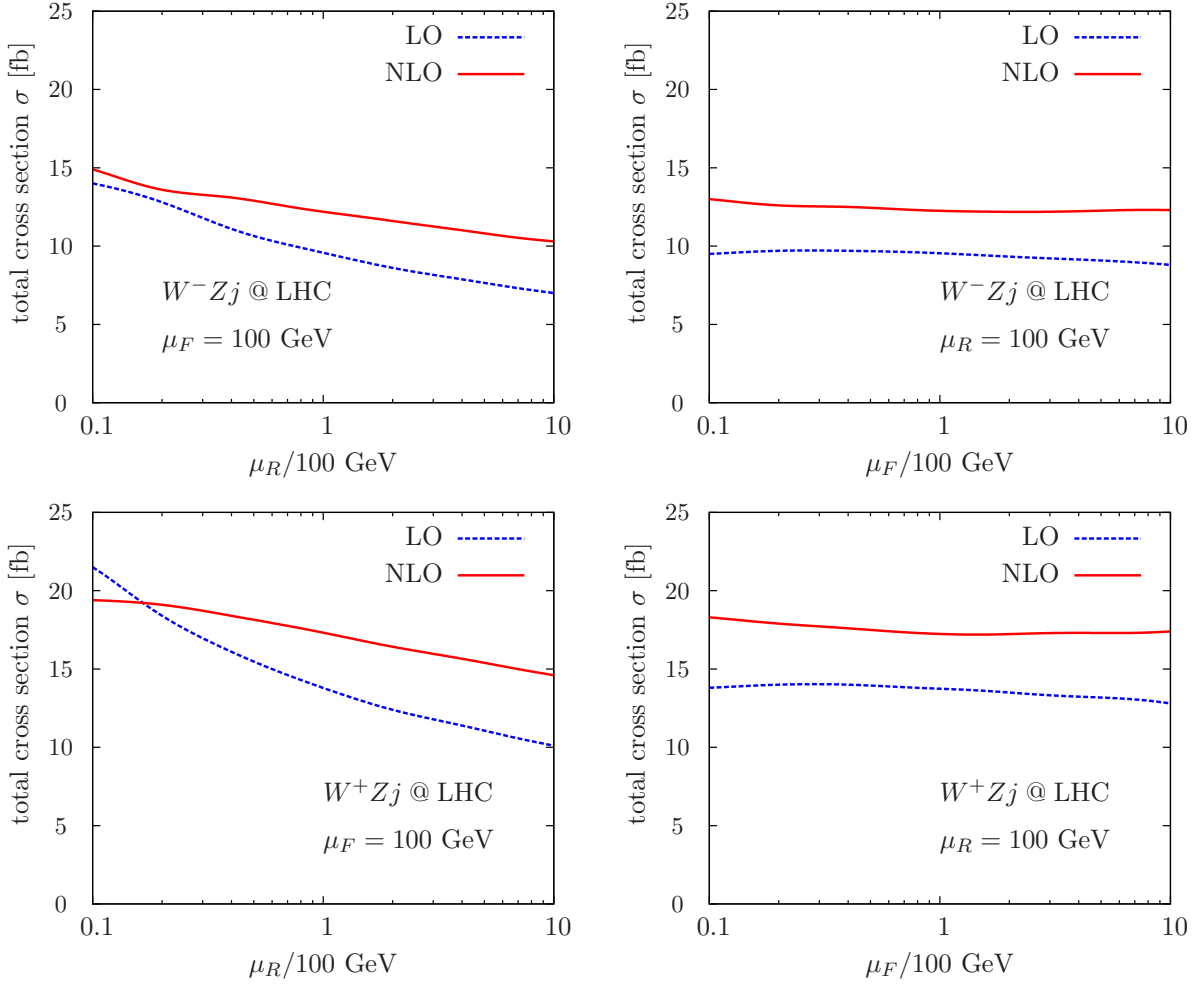


Figure 5.4: Individual renormalization and factorization scale dependencies of the leading order and next-to-leading order $W^\pm Z j$ cross sections at the LHC.

(semi-) hadronic decays of the bosons, with branching ratios 67% for the W and 69% for the Z , and the corresponding NLO corrections is, however, beyond the scope of this thesis.

5.3 Differential distributions

In figs. 5.6-5.8 we exemplarily plot distributions at the LHC and the Tevatron for the cuts (5.3), (5.4a). We again find that semi-hadronic observables, e.g. the minimum jet-lepton separation in fig. 5.5, are heavily affected by additional hard jet radiation. The purely leptonic observables, e.g. the maximum lepton pseudorapidity fig. 5.7 or the transverse WZ mass in fig 5.6, receive only small modifications around the LO-rescaled distributions, with the exception of the lepton-transverse momentum distributions and the neutrino's missing transverse momentum \cancel{p}_T . We discuss them in detail below. NLO jet vetoing obviously exhibits similar properties as in chapter 4. In total the corrections are, however, less sizable, for overall rates and differential distributions of NLO $W\gamma j$

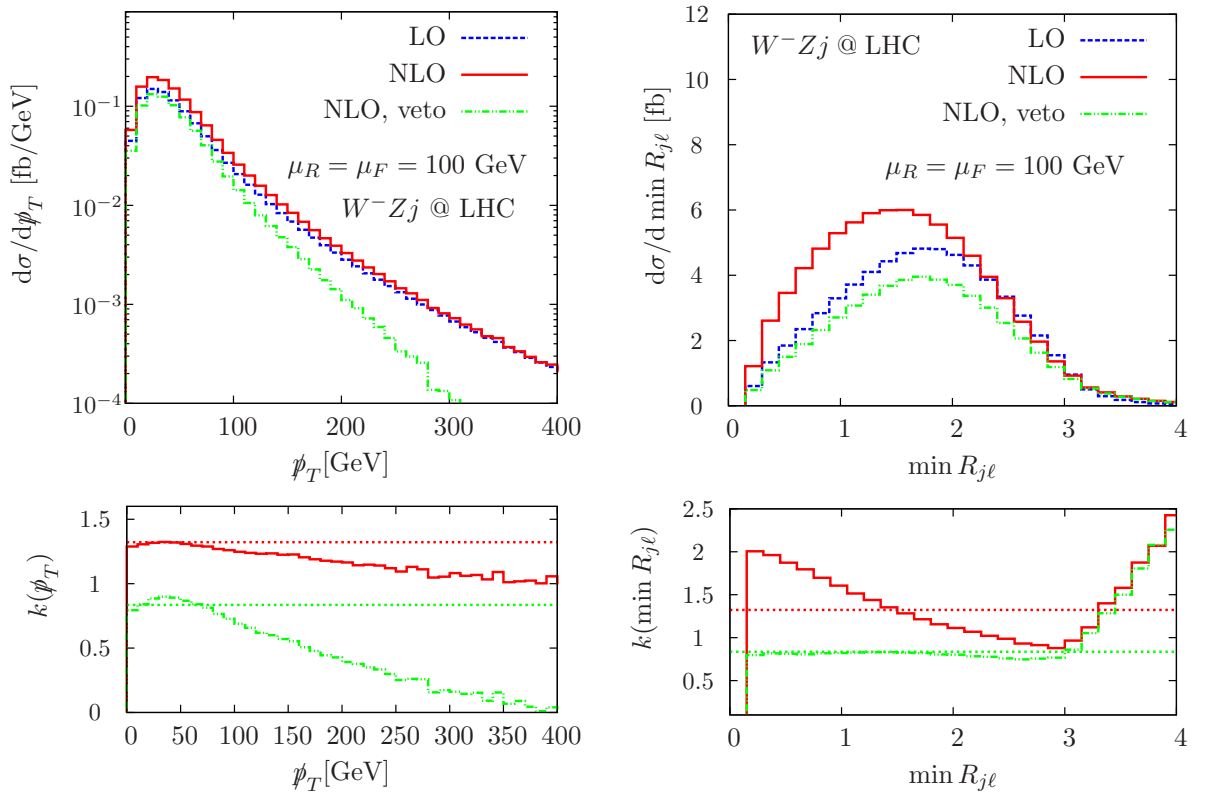


Figure 5.5: Minimum jet-lepton separation and missing transverse momentum at leading and next-to-leading in W^-Zj production including the differential k factors. The horizontal dashed line displays the corresponding k^{tot} .

production.

In more detail, the leading order underestimates the $\max p_T^j$ distribution in the tail of the distribution for inclusive production, fig. 5.6. While the tail receives larger corrections due to hard jet emission compared to the $k^{\text{tot}} = \sigma^{\text{NLO}}/\sigma^{\text{LO}}$ -rescaled LO distribution, the $\max p_T^j$ shape is overestimated in the threshold region by the LO approximation. The maximum lepton transverse momentum is slightly softer for large values and receives modifications above k^{tot} around the threshold. The additional soft parton emission is mainly compensated by the leptons as an additional jet is preferably emitted into the direction of the hard jet due to an approximately flat radiation pattern

	$\sigma_{\text{excl}}^{\text{NLO}}$ [fb]	$\sigma_{\text{excl}}^{\text{NLO}}/\sigma^{\text{LO}}$
W^-Zj	7.81 ± 0.01	0.819
W^+Zj	10.67 ± 0.13	0.772

Table 5.2: Exclusive next-to-leading order cross sections and total correction factors for the processes $pp \rightarrow \ell^+ \nu_\ell \ell'^+ \ell'^- + X$ and $pp \rightarrow \ell^- \bar{\nu}_\ell \ell'^+ \ell'^- j + X$ at the LHC for identified renormalization and factorization scales, $\mu_R = \mu_F = 100$ GeV. The cuts are chosen as described in the text.

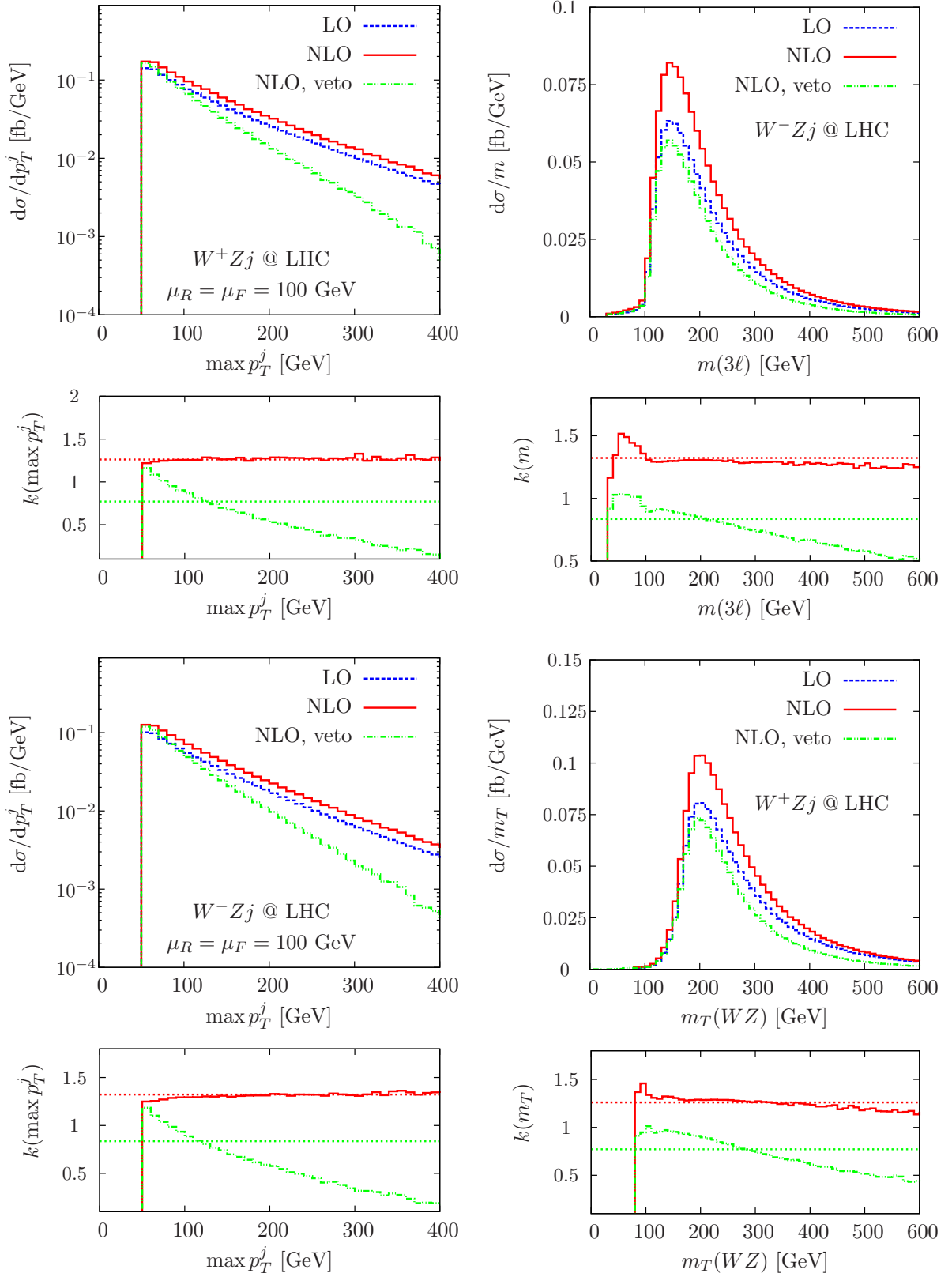


Figure 5.6: Maximum jet p_T , invariant charged lepton mass, and transverse cluster mass at leading and next-to-leading order in WZj production including the differential k factors. The horizontal dashed line displays the corresponding k^{tot} .

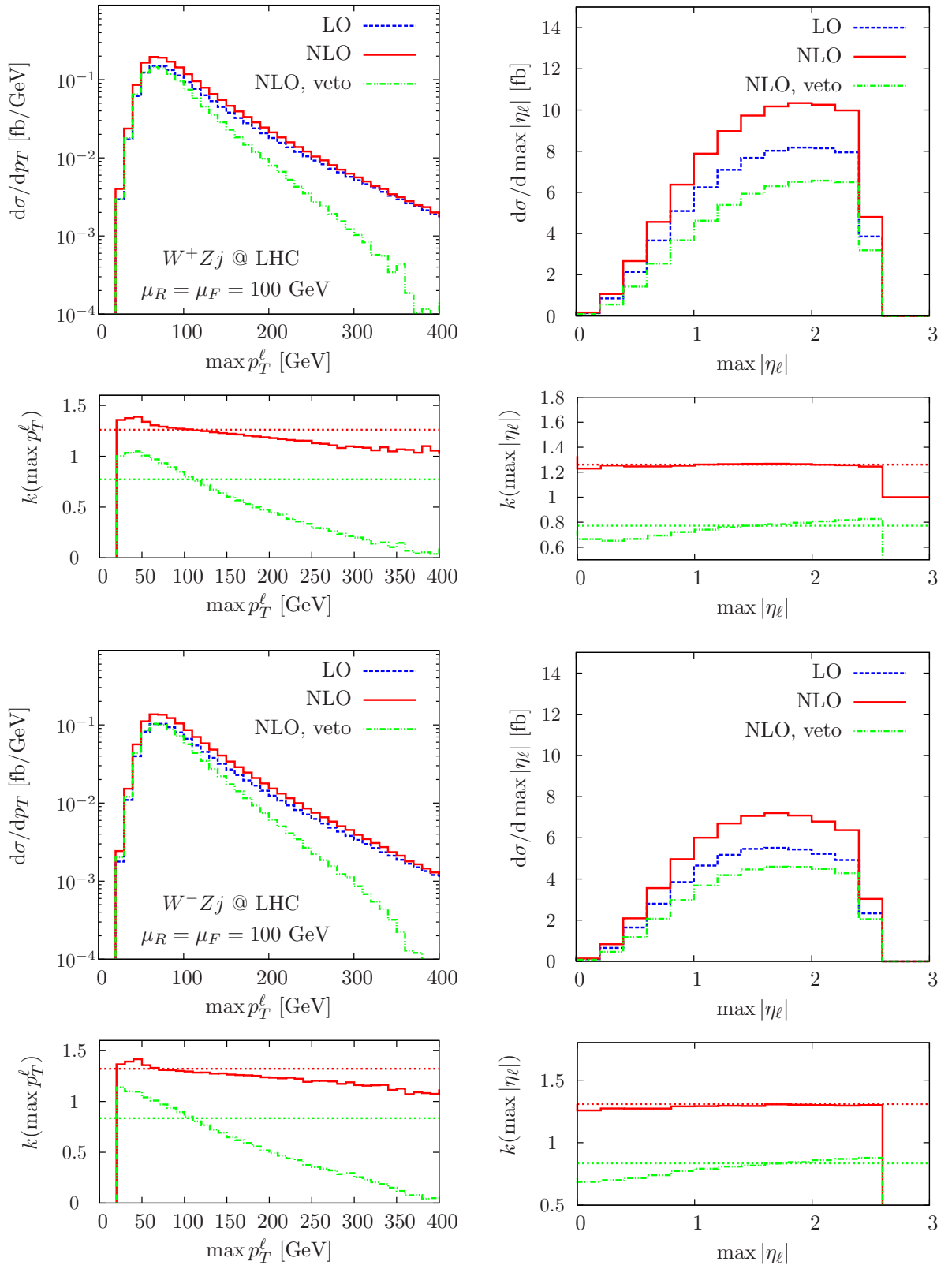


Figure 5.7: Maximum jet and lepton p_T at leading and next-to-leading in WZj production including the differential k factors. The horizontal dashed line displays the corresponding k^{tot} .

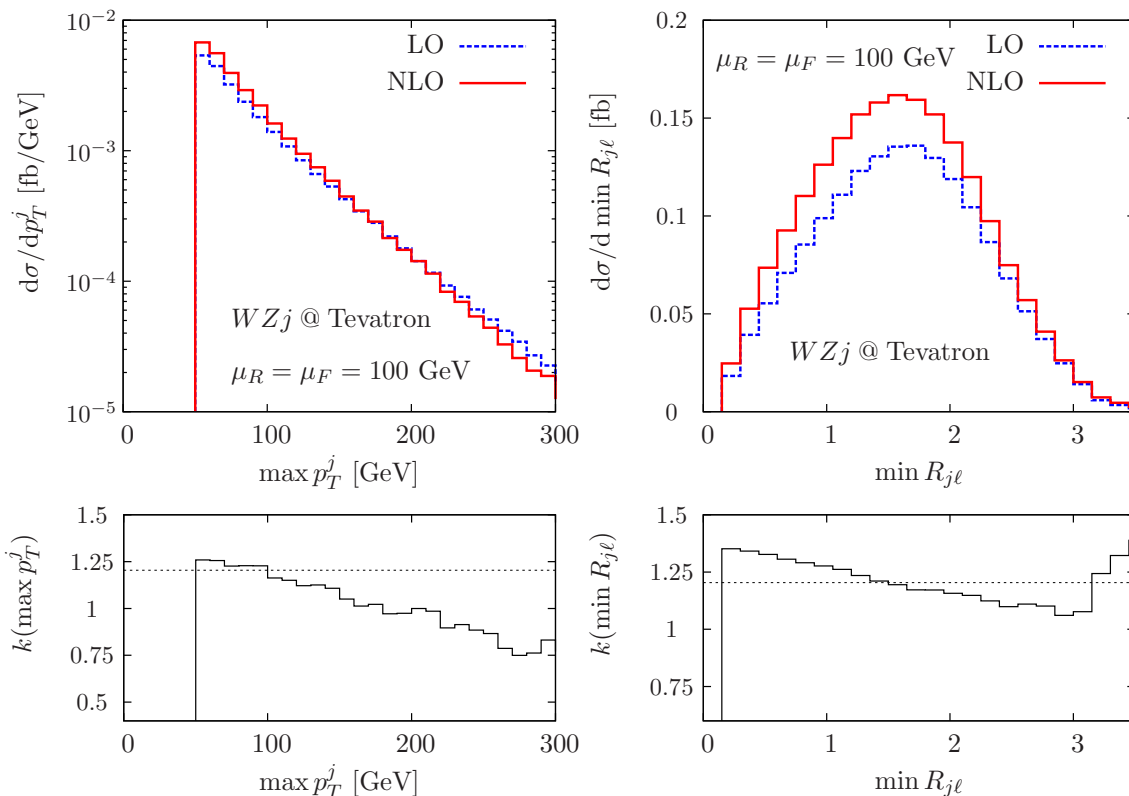


Figure 5.8: Maximum p_T^j , minimum jet-lepton separation at leading and next-to-leading in WZj production including the differential k factor at the Tevatron.

in $\Delta\phi_{jj}$. On the other hand, hard QCD radiation recoils against the hard jet points in the direction of the W and Z , as can be seen from the large modifications in the minimum $R_{j\ell}$ -separation in fig. 5.5. This situation is qualitatively identical to the one encountered in the discussion of the $\max p_T^j$ spectrum in chapter 4 and is also apparent from the invariant lepton mass distribution in fig. 5.6. At small invariant masses the additional parton recoils against the WZ pair until the parton reaches the threshold at 50 GeV, eq. (5.4a). Then all isolation criteria have to be fulfilled, and the differential correction drops as the jets have to be emitted into roughly the same direction which is not preferred for hard events with large invariant mass.

The central partons force the leptons to move to larger rapidities in fig. 5.7 to balance the additional parton's momentum component along the beam direction. This is more pronounced for the vetoed distribution as the two energetic jets recoiling against the W and Z tend to re-focus the leptons in the central region. The effect of the additional parton emission at small pseudorapidity difference $\Delta\eta$ is also well-observable in the minimum jet-lepton separation at large values.

For exclusive production at the LHC (total cross sections are quoted in table 5.2) the high p_T behavior is heavily suppressed with respect to LO. This is exemplarily shown in fig. 5.6. Additionally, the characteristics of extra jet radiation vanish in observables that involve the hadronic jet at leading order, cf. fig. 5.5. In fact, because inclusive corrections tend to be less sizable, which nonetheless include a considerable contribu-

tion of the positive-definite di-jet contribution, the exclusive cross sections exhibit a larger phase space dependence compared to $W\gamma j$ production. Comparing the shapes of exclusive cross sections for $W\gamma j$ production and WZj production, and bearing in mind the large- p_T^γ behavior for exclusive $W\gamma j$ events, we anticipate a bad perturbative jet veto-performance when applied to the WZj processes. Indeed, the $\max p_T^\ell$ momentum receives relative modifications of order five in fig. 5.6, and even becomes negative at still small values $\max p_T^\ell \gtrsim 400$ GeV. This also qualitatively applies for the various other p_T distributions, signaling a breakdown of perturbation theory at the given order for the vetoed sample at already low scales. This can be understood along the lines of the discussion of the vetoed $W\gamma j$ cross sections: The veto stabilizes the distributions around the p_T -thresholds, but does not provide perturbatively reliable predictions for hard momentum configurations. For the massive WZj production case this is even more apparent compared to chap. 4 — clearly the jet veto does not yield to the experimental strategy at all and should be discarded in any phenomenological study that uses WZj production, either as signal or as background.

The lowered center of mass energy when turning to Tevatron collisions effectively introduces a jet veto for the chosen selection criteria, which reproduces the typical differential k factor shapes, cf. fig. 5.8, also encountered in the vetoed WZj sample of fig. 5.6, and the vetoed $W\gamma j$ production of chapter 4.

Chapter 6

Summary and Outlook

In this thesis the NLO QCD corrections to $W^\pm Z j$ and $W^\pm \gamma j$ production at hadron colliders, including full leptonic decays of the massive electroweak gauge bosons, have been computed. Anomalous $WW\gamma$ couplings have been included to the $W\gamma j$ production channels. The results are implemented into a Monte Carlo program in a numerically stable way. We have applied a dedicated system of checks and balances to verify this numerical implementation. Checks include verification against available automated matrix element-, Catani-Seymour dipole- and phase space generators wherever possible, and independently performed computations relying on different approaches. In addition gauge checks are applied to every phase space point during virtual corrections' integration to ensure numerical stability of this part of the numerical code.

We have reviewed the Standard Model and QCD-improved hadron collider calculations in chapter 2. Special care has there been devoted to a detailed introduction to infrared singularities and their bookkeeping via the Catani-Seymour formalism. We have also discussed the anatomy of one-loop calculations, and our strategy to efficiently perform the numerical phase space integration to make this thesis self-consistent.

In chapter 3 we have given details on the actual calculation and the numerical implementation of (differential) $W^\pm \gamma j$ and $W^\pm Z j$ cross sections, including leptonic decays. Our strategy, that heavily makes use of effective currents and process-universal building blocks for the virtual part of the computation, is explained in necessary detail. We also comment on the design of these numerical building blocks, and perform the renormalization and the dipole subtraction explicitly to demonstrate the absence of singularities in the NLO cross section.

Chapters 4 and 5 are devoted to numerical results. In summary, the next-to-leading order QCD corrections to the considered processes, are sizable and highly phase space-dependent. With total inclusive corrections in the range of $1.2 \lesssim k^{\text{tot}} \lesssim 1.5$, depending on process, experiment and cuts, they are relevant to any phenomenological study which includes these processes, either as signal or as background. The differential distributions get significantly modified with respect to their leading order approximations, a characteristic trait which is, at the LHC, predominantly due to unsuppressed jet radiation. This suggests a jet-veto to suppress the additional jet radiation to arrive at a perturbatively stable exclusive production cross section. Indeed, vetos remove the di-jet induced distortion of differential distributions compared to LO in the cross section-dominating phase space region and superficially cure the substantial theoretical uncertainties re-introduced by the leading order- α_s di-jet cross section. However, the small total k -factor for exclusive production entirely follows from a cancellation of the

p_T distributions' tails ($k(p_T) \lesssim 0.25$) against the threshold region ($k(p_T) \gtrsim 1.2$). We show that in regions of large transverse momenta where jet-radiation turns out to be sizable, the exclusive NLO cross section exhibits considerably larger uncertainties than the inclusive cross section. Hence, the veto amounts to improved NLO stability almost exclusively in the threshold region, and the substantial uncertainty a large p_T is not visible in the total exclusive rate due to the small differential k factor there. In addition to that, the veto distribution still receives major modifications in some regions of phase space. For WZj production the veto yields negative weights already at low transverse momentum scales, and hence does not provide a reasonable procedure at all.

At the Tevatron, where, due to the limited center-of-mass energy, additional jet emission is less favored for the considered cuts and quark-induced channels are preferred, the differential k factors interpolate between the NLO-exclusive and the NLO-inclusive LHC results. While taking leptonic decays into account exhibits too low rates for WZj production to be phenomenologically relevant, the corrections to $W\gamma j$ production are important. The effects of additional jet radiation, though kinematically suppressed for our cut choices, are still visible in the differential corrections. Vetos do not offer applicable means here at all as they tend to produce negative weights at the given order in perturbation theory.

In chapter 4 we also analyze the veto strategy that is applied to anomalous $WW\gamma$ couplings searches at the LHC. After having reviewed the contemporary approaches to measurements of the parameters of the anomalous couplings operators in the effective field theory (introduced in chapter 3), we have provided the full NLO QCD corrections to anomalous inclusive $W\gamma j$ production. We find that the anomalous couplings' effect is considerably washed out in the total NLO rate and becomes comparable to the theoretical uncertainty of the NLO cross section in the parameter range that is still allowed by LEP data. However, we also demonstrate that the large- p_T^γ region exhibits remaining sensitivity to anomalous couplings in this very same parameter range beyond the perturbative uncertainty inherent to the fixed order calculation. This points to inclusive measurement strategies that supplement traditional radiation-zero methods. Whether the effects of anomalous couplings that are visible in our fixed-order parton-level Monte Carlo study carry over to sensitivity in a more realistic experimental framework deserves a more careful investigation. We leave this to future work.

Finally, in chapter 4, we comment on the veto strategy applied in approaches that measure anomalous couplings in vetoed $W\gamma$ production via fits to the p_T^γ distribution. Here we show that instabilities marked by negative NLO-weights are not cured by including the NLO precision to the vetoed cross section. This is an immediate consequence of accessing the low- x gluon luminosities, which not only dominate the NLO-inclusive $W\gamma$ rate via the real emission contribution, but also increases $W\gamma j$ -production at NLO.

The Monte Carlo code will become publicly available as part of an upcoming update of the VBFNLO suite [11].

Appendix A

Pentline building block

A.1 Abelian pentline

The abelian pentline introduced in sec. 3.3.2 consists of the Feynman graphs that involve the effective W^* current, i.e. from topologies where up to three gauge bosons are radiated off the quark line. Analogous to the boxline building block, a specific order of

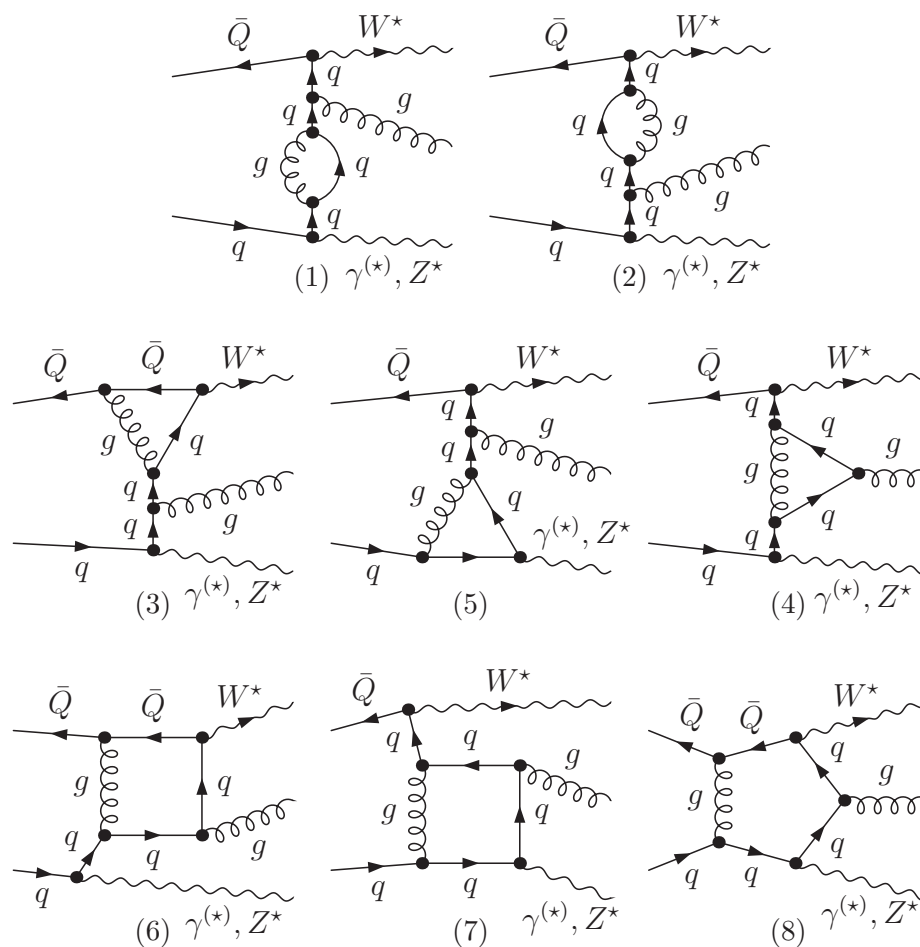


Figure A.1: Feynman graph topologies contributing to the abelian pentline building block. Not shown are the counter term graphs that renormalize the corresponding graphs.

the gauge bosons is chosen for the design of the numerical routine, fig. A.1. All other one-loop contributions are then calculated by subsequent calls to the same numerical routine with permuted effective polarization vectors and specified gluon position.

We define the abelian pentline building block, suppressing color and spin indices,

$$\begin{aligned} & \mathcal{P}^A(p_a, p_b; p_{\widetilde{Z}\gamma}, p_g, p_{W^*}; \varepsilon_{\widetilde{Z}\gamma}, \varepsilon_g^*, \varepsilon_{W^*}) \\ &= C_F (\mathcal{M}_{\text{ren}}^{(1)} + \mathcal{M}_{\text{ren}}^{(2)} + \mathcal{M}_{\text{ren}}^{(3)} + \mathcal{M}_{\text{ren}}^{(4)}) + \left(C_F - \frac{C_A}{2} \right) (\mathcal{M}_{\text{ren}}^{(5)} + \mathcal{M}_{\text{ren}}^{(6)} + \mathcal{M}_{\text{ren}}^{(7)} + \mathcal{M}_{\text{ren}}^{(8)}), \end{aligned} \quad (\text{A.1})$$

with the definitions of eq. (3.49). The various renormalized contributions $\mathcal{M}^{(i)}$ are in one-to-one correspondence with the diagrams of fig. A.1. The numerical implementation calculates the diagram-combinations in the parentheses, in complete analogy to the boxline routine. The color coefficients and the coupling constants of the hadronic current are not part of the loop calculation, but are subsequently multiplied with the numerical pentline result.

Due to the different color factors of the individual diagrams $\sim C_F$ or $\sim C_F - C_A/2$, the permutations to construct the full mixed abelian – non-abelian part of the one-loop amplitude induce non-trivial permutations in the part of the abelian pentline that is proportional to C_A . Put in another way, the evaluation of the pentline building block,

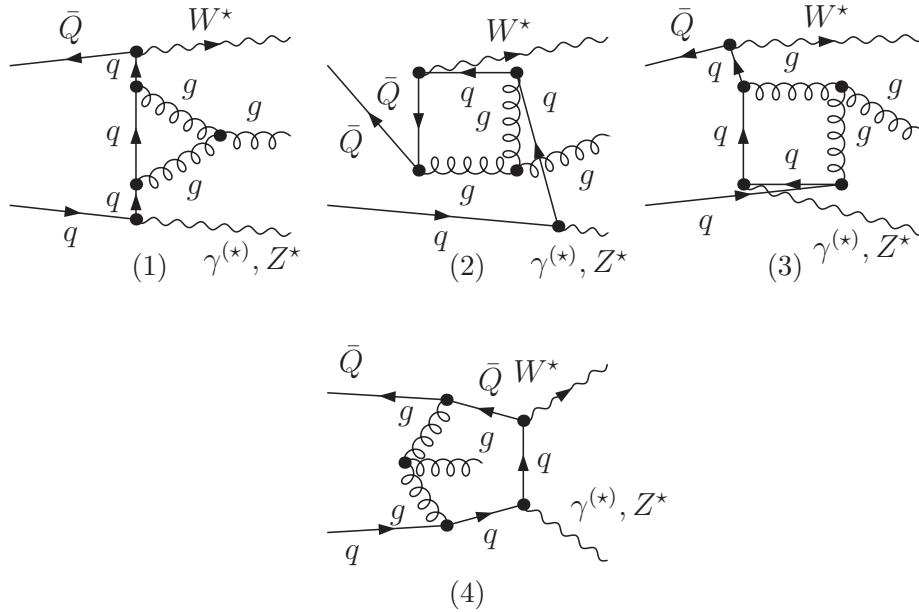


Figure A.2: Feynman graph topologies contributing to the non-abelian pentline building block. Not shown are the counter term contributions that renormalize the corresponding graphs.

just as for the boxline routine, depends on the position of the gluon:

$$(\widetilde{Z}\gamma, g, W^*) \quad (\text{A.1}) \quad (\text{A.2a})$$

$$(W^*, \widetilde{Z}\gamma, g) \quad \mathcal{M}_{\text{ren}}^{(4)} \leftrightarrow \mathcal{M}_{\text{ren}}^{(5)} \text{ with respect to (A.1)} \quad (\text{A.2b})$$

$$(g, \widetilde{Z}\gamma, W^*) \quad \mathcal{M}_{\text{ren}}^{(4)} \leftrightarrow \mathcal{M}_{\text{ren}}^{(3)} \text{ with respect to (A.1)}. \quad (\text{A.2c})$$

Permutations that follow from (A.2) upon interchanging $\widetilde{Z}\gamma \leftrightarrow W^*$ do not affect the position of the gluon along the quark line and, hence, do not induce non-trivial permutations in the terms proportional to C_A in (A.1).

A.2 Non-abelian pentline

The remaining diagrams to construct the full one-loop amplitude are purely non-abelian and involve a trilinear gluon coupling, fig. A.2. The non-abelian pentline building block is defined in analogy to the depicted (renormalized) Feynman graphs via

$$\mathcal{P}^{\text{NA}}(p_a, p_b; p_g; p_j, p_k; \varepsilon_g^*; \varepsilon_{\widetilde{Z}\gamma}, \varepsilon_{W^*}) = C_A (\mathcal{M}_{\text{ren}}^{(1)} + \mathcal{M}_{\text{ren}}^{(2)} + \mathcal{M}_{\text{ren}}^{(3)} + \mathcal{M}_{\text{ren}}^{(4)}) . \quad (\text{A.3})$$

Coupling constants associated with quarks and gluons, and the color factor are multiplied with the non-abelian pentline result outside of the actual loop calculation. The remaining non-abelian Feynman graphs can be calculated from (A.3) by interchanging $\varepsilon_{\widetilde{Z}\gamma} \leftrightarrow \varepsilon_{W^*}$, see also fig. 3.14.

Appendix B

Catani Seymour Dipole Formulae

This section summarizes the relevant algebra for the Catani-Seymour dipole subtraction [37], which is introduced in sec. 2.2.2, and performed for the processes subject of this thesis in chapter 3. Throughout, we assume dimensional regularization in $d = 4 - 2\varepsilon$ dimensions.

B.1 The \mathbf{I} operator

The \mathbf{I} insertion operator, that cancels the IR poles of the virtual NLO matrix element, can be written in the compact form

$$\mathbf{I}(\{p\}; \varepsilon) = -\frac{\alpha_s}{2\pi} \frac{1}{\Gamma(1-\varepsilon)} \sum_I \frac{1}{\mathbf{T}_I^2} \mathcal{V}_I(\varepsilon) \sum_{J \neq I} \mathbf{T}_I \cdot \mathbf{T}_J \left(\frac{4\pi\mu^2}{2p_I \cdot p_J} \right)^\varepsilon, \quad (\text{B.1})$$

where the summation indices run over all colored partons of the Born amplitude $I, J = a, b, 1$. The color algebra $\mathbf{T}_I \cdot \mathbf{T}_J$, and \mathbf{T}_I^2 , follows from (3.20). The divergent coefficients $\mathcal{V}_I(\varepsilon)$ are

$$\mathcal{V}_I(\varepsilon) = \mathbf{T}_I^2 \left(\frac{1}{\varepsilon^2} - \frac{\pi^2}{3} \right) + \frac{\gamma_I}{\varepsilon} + \gamma_I + K_I + \mathcal{O}(\varepsilon), \quad (\text{B.2})$$

with

$$\gamma_q = \gamma_{\bar{q}} = \frac{3}{2}C_F, \quad \gamma_g = \frac{11}{6}C_A - \frac{2}{3}T_r N_F, \quad (\text{B.3})$$

and

$$K_q = K_{\bar{q}} = \left(\frac{7}{2} - \frac{\pi^2}{6} \right) C_F, \quad K_g = \left(\frac{67}{18} - \frac{\pi^2}{6} \right) C_A - \frac{10}{9} T_r N_F. \quad (\text{B.4})$$

B.2 Finite Collinear Terms

After cancelling the IR divergencies of the integrated Dipoles' \mathbf{I} operator against the virtual poles, there remains a finite collinear term, schematically expressed for the partonic initial state $|p_a p_b\rangle$

$$\sigma_{\text{coll.}}^{ab} = \int_0^1 dx \left\{ \left[\sum_{a'} (\mathbf{P}(x, xp_a, p_b, p_1, \mu_F^2) + \mathbf{K}(x))^{aa'} \otimes d\sigma_{a'b \rightarrow j}^{\text{B}}(xp_a, p_b) \right] + \left[\sum_{b'} (\mathbf{P}(x, p_a, xp_b, p_1, \mu_F^2) + \mathbf{K}(x))^{bb'} \otimes d\sigma_{ab' \rightarrow j'}^{\text{B}}(p_a, xp_b) \right] \right\}, \quad (\text{B.5})$$

where p_1 denotes the final state momentum of the colored final state parton j, j' , that are entirely determined by the electroweak dynamics for the considered processes, i.e. $j = j(a', b)$. The precise form of the kernel operators \mathbf{K} and \mathbf{P} is determined by the splitting and the color connection of the colored partons,

$$\mathbf{K}^{aa'}(x) = \frac{\alpha_s}{2\pi} \left\{ \bar{K}^{aa'}(x) + \delta^{aa'} \mathbf{T}_j \cdot \mathbf{T}_a \frac{\gamma_j}{\mathbf{T}_j^2} \left[\left(\frac{1}{1-x} \right)_+ + \delta(1-x) \right] \right\} - \frac{\alpha_s}{2\pi} \mathbf{T}_b \cdot \mathbf{T}_{a'} \frac{1}{\mathbf{T}_{a'}^2} \tilde{K}^{aa'}(x), \quad (\text{B.6})$$

$$\mathbf{P}^{aa'}(x, p_a, xp_b, p_1, \mu_F^2) = \frac{\alpha_s}{2\pi} P^{aa'}(x) \frac{1}{\mathbf{T}_{a'}^2} \left[\mathbf{T}_j \cdot \mathbf{T}_{a'} \log \frac{\mu_F^2}{2xp_a \cdot p_1} + \mathbf{T}_b \cdot \mathbf{T}_{a'} \log \frac{\mu_F^2}{2xp_a \cdot p_b} \right], \quad (\text{B.7})$$

where we have introduced the plus-distribution, defined by

$$\int dx g(x) [f(x)]_+ = \int dx (g(x) - g(1)) f(x). \quad (\text{B.8})$$

The four-dimensional Altarelli-Parisi splitting kernels in these equations, that arise when integrating the dipoles of sec. 3.2.3 over the one-parton phase space, read

$$\begin{aligned} P^{qg}(x) &= P^{\bar{q}g}(x) = C_F \frac{1 + (1-x)^2}{x}, \\ P^{gq}(x) &= P^{g\bar{q}}(x) = T_r [x^2 + (1-x)^2], \\ P^{qq}(x) &= P^{\bar{q}\bar{q}}(x) = C_F \left(\frac{1+x^2}{1-x} \right)_+, \\ P^{gg}(x) &= 2C_A \left[\left(\frac{1}{1-x} \right)_+ + \frac{1-x}{x} - 1 + x(1-x) \right] \\ &\quad + \delta(1-x) \left(\frac{11}{6} C_A - \frac{2}{3} N_F T_r \right), \end{aligned} \quad (\text{B.9})$$

The $\bar{K}^{aa'}$ and $\tilde{K}^{aa'}$ are, explicitly,

$$\begin{aligned} \bar{K}^{qg}(x) &= \bar{K}^{\bar{q}g}(x) = P^{qg}(x) \ln \frac{1-x}{x} + C_F x, \\ \bar{K}^{gq}(x) &= \bar{K}^{g\bar{q}}(x) = P^{gq}(x) \ln \frac{1-x}{x} + 2T_r x(1-x), \\ \bar{K}^{qq}(x) &= \bar{K}^{\bar{q}\bar{q}}(x) = C_F \left[\left(\frac{2}{1-x} \ln \frac{1-x}{x} \right)_+ - (1+x) \ln \frac{1-x}{x} + (1-x) \right] \\ &\quad - \delta(1-x) (5 - \pi^2) C_F, \\ \bar{K}^{gg}(x) &= 2C_A \left[\left(\frac{1}{1-x} \ln \frac{1-x}{x} \right)_+ + \left(\frac{1-x}{x} - 1 + x(1-x) \right) \ln \frac{1-x}{x} \right] \\ &\quad - \delta(1-x) \left[\left(\frac{50}{9} - \pi^2 \right) C_A - \frac{16}{9} T_r N_F \right] \end{aligned} \quad (\text{B.10})$$

and

$$\tilde{K}^{ab}(x) = P_{\text{reg}}^{ab}(x) \ln(1-x) + \delta^{ab} \mathbf{T}_a^2 \left[\left(\frac{2}{1-x} \ln(1-x) \right)_+ - \frac{\pi^2}{3} \delta(1-x) \right], \quad (\text{B.11})$$

where we have introduced the regular part of the Altarelli-Parisi-kernels (B.9),

$$\begin{aligned} P_{\text{reg}}^{qq}(x) &= -C_F (1+x), \\ P_{\text{reg}}^{gg}(x) &= 2C_A \left[\frac{1-x}{x} - 1 + x(1-x) \right], \\ P_{\text{reg}}^{ab}(x) &= P^{ab}(x), \quad \text{if } a \neq b. \end{aligned} \quad (\text{B.12})$$

The color algebra $\mathbf{T}_a \cdot \mathbf{T}_b$, \mathbf{T}_a^2 , etc., follows from (3.20).

The sum over the initial partonic states in the hadronic cross section allows to convert (B.5) into splittings corresponding to specific Born-level configurations by writing

$$\begin{aligned} \sigma_{\text{coll.}} &= \sum_{a,b} \iint dx_a dx_b f_{a/P}(x_a, \mu_F^2) f_{b/P}(x_b, \mu_F^2) \sigma_{\text{coll.}}^{ab} \\ &= \sum_{a'} \left(\sum_{a,b} \iiint_0^1 dx_a dx_b dx f_{a/P}(x_a, \mu_F^2) f_{b/P}(x_b, \mu_F^2) \left[(\mathbf{P} + \mathbf{K})^{aa'} \otimes d\sigma_{a'b \rightarrow j}^{\text{B}} \right] \right) \\ &+ \sum_{b'} \left(\sum_{a,b} \iiint_0^1 dx_a dx_b dx f_{a/P}(x_a, \mu_F^2) f_{b/P}(x_b, \mu_F^2) \left[(\mathbf{P} + \mathbf{K})^{bb'} \otimes d\sigma_{ab' \rightarrow j'}^{\text{B}} \right] \right). \end{aligned} \quad (\text{B.13})$$

Note, that at hadron colliders the two lines are related by interchanging partonic initial state. The findings of this section have been calculated using MATHEMATICA functions, that allow to directly translate the analytical results to FORTRAN code. The results have been analytically cross-checked via independent calculations, and the MATHEMATICA functions have been validated by reproducing existing results of other scenarios [8, 84].

B.2.1 Finite collinear terms related to $\mathcal{M}^{\bar{q}Q \rightarrow g}$

Following (B.13), we have to calculate the kernels

$$\begin{aligned} \mathcal{F}_1 &= \left(\frac{\alpha_s}{2\pi} \right)^{-1} \iiint_0^1 dx_{\bar{q}} dx_Q dx f_{\bar{q}/P}(x_{\bar{q}}, \mu_F^2) f_{Q/P}(x_Q, \mu_F^2) \left[(\mathbf{P} + \mathbf{K})^{\bar{q}\bar{q}} \otimes d\sigma_{\bar{q}Q \rightarrow g}^{\text{B}} \right] \\ \mathcal{F}_2 &= \left(\frac{\alpha_s}{2\pi} \right)^{-1} \iiint_0^1 dx_g dx_Q dx f_{g/P}(x_g, \mu_F^2) f_{Q/P}(x_Q, \mu_F^2) \left[(\mathbf{P} + \mathbf{K})^{g\bar{q}} \otimes d\sigma_{\bar{q}Q \rightarrow g}^{\text{B}} \right] \end{aligned} \quad (\text{B.14})$$

The needed splitting operators read

$$\begin{aligned}
\langle \bar{q}Q; g | \mathbf{K}^{\bar{q}\bar{q}}(x) + \mathbf{P}^{\bar{q}\bar{q}}(x, xp_{\bar{q}}, p_Q, p_g, \mu_F^2) | g; \bar{q}Q \rangle &= \frac{\alpha_s}{2\pi} |\mathcal{M}^{\bar{q}Q \rightarrow g}(xp_{\bar{q}}, p_Q, q_1, q_2, q_3, p_g)|^2 \\
&\times \left\{ \left[\frac{C_A - 2C_F}{2} \log\left(\frac{\mu_F^2}{2xp_a \cdot p_b}\right) - \frac{C_A}{2} \log\left(\frac{\mu_F^2}{2xp_a \cdot p_g}\right) \right] \left(\frac{x^2 + 1}{1-x}\right)_+ \right. \\
&+ \frac{C_A - 2C_F}{2} \left[\left(\frac{2 \log(1-x)}{1-x}\right)_+ - \frac{\pi^2}{3} \delta(1-x) - (x+1) \log(1-x) \right] \\
&- C_F \left[(5 - \pi^2) \delta(1-x) - \frac{\gamma_g}{2} \left[\delta(1-x) + \left(\frac{1}{1-x}\right)_+ \right] \right. \\
&\left. \left. + 1 - x - (x+1) \log\left(\frac{1-x}{x}\right) + \left(\log\left(\frac{1-x}{x}\right) \frac{2}{1-x}\right)_+ \right] \right\}
\end{aligned} \tag{B.15}$$

$$\begin{aligned}
\langle \bar{q}Q; g | \mathbf{K}^{g\bar{q}}(x) + \mathbf{P}^{g\bar{q}}(x, xp_{\bar{q}}, p_Q, p_g, \mu_F^2) | g; \bar{q}Q \rangle &= \frac{\alpha_s}{2\pi} |\mathcal{M}^{\bar{q}Q \rightarrow g}(xp_{\bar{q}}, p_Q, q_1, q_2, q_3, p_g)|^2 \\
&\times \left\{ T_r \left((1-x)x + ((1-x)^2 + x^2) \log\left(\frac{1-x}{x}\right) - \frac{C_A - 2C_F}{2C_F} \right. \right. \\
&\times \left. \left. ((1-x^2) + x^2) \log(1-x) \right) + T_r((1-x)^2 + x^2) \right. \\
&\times \left. \left[\left(\frac{C_A - 2C_F}{2C_F}\right) \log\left(\frac{\mu_F^2}{2xp_a \cdot p_b}\right) - \frac{C_A}{2C_F} \log\left(\frac{\mu_F^2}{2xp_a \cdot p_b}\right) \right] \right\}.
\end{aligned} \tag{B.16}$$

with the plus-distribution of (B.8) and a substitution involving the Feynman- x of the splitting-associated mother particle, e.g. $\tilde{x}_a = xx_a$ in (B.13). This gives, using the tabulated integrals of section B.2.5 while keeping in mind that $p_{\bar{q},g}^\mu = x_{\bar{q},g} P^\mu$,

$$\begin{aligned}
\mathcal{F}_1 &= \left(\frac{\alpha_s}{2\pi}\right)^{-1} \iint_0^1 d\tilde{x}_{\bar{q}} dx_Q \int_0^1 \frac{dx}{x} f_{Q/P}(x_Q, \mu_F^2) \\
&\times f_{\bar{q}/P}\left(\frac{\tilde{x}_{\bar{q}}}{x}, \mu_F^2\right) \langle \bar{q}Q; g | \mathbf{K}^{\bar{q}\bar{q}}(x) + \mathbf{P}^{\bar{q}\bar{q}}(x, \tilde{x}_{\bar{q}}P, p_Q, p_g, \mu_F^2) | g; \bar{q}Q \rangle \Theta(x - \tilde{x}_{\bar{q}}).
\end{aligned} \tag{B.17}$$

and

$$\begin{aligned}
\mathcal{F}_2 &= \left(\frac{\alpha_s}{2\pi}\right)^{-1} \iint_0^1 d\tilde{x}_g dx_Q \int_0^1 \frac{dx}{x} f_{Q/P}(x_Q, \mu_F^2) \\
&\times f_{g/P}\left(\frac{\tilde{x}_g}{x}, \mu_F^2\right) \langle \bar{q}Q; g | \mathbf{K}^{g\bar{q}}(x) + \mathbf{P}^{g\bar{q}}(x, \tilde{x}_gP, p_Q, p_g, \mu_F^2) | g; \bar{q}Q \rangle \Theta(x - \tilde{x}_g).
\end{aligned} \tag{B.18}$$

Plugging in the integration kernels (B.15) and (B.16) yields

$$\begin{aligned}
\mathcal{F}_1 = & \iint_0^1 d\tilde{x}_{\bar{q}} dx_Q \int_{\tilde{x}_{\bar{q}}}^1 \frac{dx}{x} f_{Q/P}(x_Q, \mu_F^2) \left\{ \left(f_{\bar{q}/P} \left(\frac{\tilde{x}_{\bar{q}}}{x}, \mu_F^2 \right) - x f_{\bar{q}/P}(\tilde{x}_{\bar{q}}, \mu_F^2) \right) \right. \\
& \times \left[2 \left(C_F - \frac{C_A}{2} \right) \log(1-x) - \frac{\gamma_g}{2} - 2 \left(C_F - \frac{C_A}{2} \right) \log \left(\frac{\mu_F^2}{2(1-x)\tilde{p}_{\bar{q}} \cdot p_Q} \right) \right. \\
& \left. \left. - C_A \log \left(\frac{\mu_F^2}{2(1-x)\tilde{p}_{\bar{q}} \cdot p_g} \right) \right] + f_{\bar{q}/P} \left(\frac{\tilde{x}_{\bar{q}}}{x}, \mu_F^2 \right) \left[C_F(1-x) - (1+x) \right. \right. \\
& \times \left(\left(C_F - \frac{C_A}{2} \right) \log(1-x) - \left(C_F - \frac{C_A}{2} \right) \log \left(\frac{x\mu_F^2}{2(1-x)\tilde{p}_{\bar{q}} \cdot p_Q} \right) \right. \\
& \left. \left. - \frac{C_A}{2} \log \left(\frac{x\mu_F^2}{2(1-x)\tilde{p}_{\bar{q}} \cdot p_g} \right) \right) + \frac{2}{x-1} C_F \log(x) \right] \left. \right\} \times |\mathcal{M}^{\bar{q}Q \rightarrow g}|^2 \quad (\text{B.19}) \\
& + \iint_0^1 d\tilde{x}_{\bar{q}} dx_Q f_{Q/P}(x_Q, \mu_F^2) f_{\bar{q}/P}(\tilde{x}_{\bar{q}}, \mu_F^2) \left[\left(C_F - \frac{C_A}{4} \right) \log^2(1-\tilde{x}_{\bar{q}}) \right. \\
& + \log(1-\tilde{x}_{\bar{q}}) \left(\frac{\gamma_g}{2} - 2 \left(C_F - \frac{C_A}{2} \right) \log \left(\frac{\mu_F^2}{2\tilde{p}_{\bar{q}} \cdot p_Q} \right) - C_A \log \left(\frac{\mu_F^2}{2\tilde{p}_{\bar{q}} \cdot p_g} \right) \right) \\
& \left. - \frac{3}{2} \left(\left(C_F - \frac{C_A}{2} \right) \log \left(\frac{\mu_F^2}{2\tilde{p}_{\bar{q}} \cdot p_Q} \right) + \frac{C_A}{2} \log \left(\frac{\mu_F^2}{2\tilde{p}_{\bar{q}} \cdot p_g} \right) \right) \right. \\
& \left. + \frac{\pi^2}{2} C_F - 5C_F + \frac{\pi^2}{6} C_A - \frac{\gamma_g}{2} \right] \times |\mathcal{M}^{\bar{q}Q \rightarrow g}|^2
\end{aligned}$$

and

$$\begin{aligned}
\mathcal{F}_2 = & \iint_0^1 d\tilde{x}_g dx_Q \int_{\tilde{x}_g}^1 \frac{dx}{x} f_{Q/P}(x_Q, \mu_F^2) f_{g/P} \left(\frac{\tilde{x}_g}{x}, \mu_F^2 \right) \left\{ \frac{T_r(2(x-1)x+1)}{C_F} \right. \\
& \times \left[\left(C_F - \frac{C_A}{2} \right) \log(1-x) - \left(C_F - \frac{C_A}{2} \right) \log \left(\frac{x\mu_F^2}{2(1-x)\tilde{p}_g \cdot p_Q} \right) \right. \\
& \left. \left. - \frac{C_A}{2} \log \left(\frac{x\mu_F^2}{2(1-x)\tilde{p}_g \cdot p_g} \right) \right] - 2T_r(x-1)x \right\} \times |\mathcal{M}^{\bar{q}Q \rightarrow g}|^2 \quad (\text{B.20})
\end{aligned}$$

B.2.2 Finite collinear terms related to $\mathcal{M}^{gQ \rightarrow q}$

Following (B.13), we calculate the kernels

$$\begin{aligned}
\mathcal{F}_1 = & \left(\frac{\alpha_s}{2\pi} \right)^{-1} \iiint_0^1 dx_g dx_Q dx f_{g/P}(x_g, \mu_F^2) f_{Q/P}(x_Q, \mu_F^2) [(\mathbf{P} + \mathbf{K})^{gg} \otimes d\sigma_{gQ \rightarrow q}^B] \\
\mathcal{F}_2 = & \left(\frac{\alpha_s}{2\pi} \right)^{-1} \iiint_0^1 dx_{q'} dx_Q dx f_{g/P}(x_g, \mu_F^2) f_{Q/P}(x_Q, \mu_F^2) [(\mathbf{P} + \mathbf{K})^{q'g} \otimes d\sigma_{gQ \rightarrow q}^B] \\
\mathcal{F}_3 = & \left(\frac{\alpha_s}{2\pi} \right)^{-1} \iiint_0^1 dx_{\bar{q}} dx_Q dx f_{\bar{q}/P}(x_g, \mu_F^2) f_{Q/P}(x_Q, \mu_F^2) [(\mathbf{P} + \mathbf{K})^{\bar{q}g} \otimes d\sigma_{gQ \rightarrow q}^B] \quad (\text{B.21})
\end{aligned}$$

yielding

$$\begin{aligned}
\mathcal{F}_1 = & \iint_0^1 d\tilde{x}_g dx_Q \int_{\tilde{x}_g}^1 \frac{dx}{x} f_{Q/P}(x_Q, \mu_F^2) \left\{ \left(f_{g/P} \left(\frac{\tilde{x}_g}{x}, \mu_F^2 \right) - x f_{g/P}(\tilde{x}_g, \mu_F^2) \right) \right. \\
& \times \left(C_A \log(1-x) - \frac{C_A \gamma_q}{2C_F} - C_A \log \left(\frac{\mu_F^2}{2(1-x)\tilde{p}_g \cdot p_Q} \right) - C_A \log \left(\frac{\mu_F^2}{2(1-x)\tilde{p}_g \cdot p_q} \right) \right) \\
& + f_{g/P} \left(\frac{\tilde{x}_g}{x}, \mu_F^2 \right) \left[-2C_A \frac{\log(x)}{1-x} - \frac{x((x-1)x+2)-1}{x} \left(C_A \log(1-x) \right. \right. \\
& \left. \left. - C_A \log \left(\frac{x\mu_F^2}{2(1-x)\tilde{p}_g \cdot p_Q} \right) - C_A \log \left(\frac{x\mu_F^2}{2(1-x)\tilde{p}_g \cdot p_q} \right) \right) \right] \left. \right\} \times |\mathcal{M}^{gQ \rightarrow q}|^2 \\
& + \iint_0^1 d\tilde{x}_g dx_Q f_{Q/P}(x_Q, \mu_F^2) f_{g/P}(\tilde{x}_g, \mu_F^2) \left[\frac{3}{2} C_A \log^2(1-\tilde{x}_g) - \log(1-\tilde{x}_g) \right. \\
& \times \left(\frac{C_A \gamma_q}{2C_F} + C_A \log \left(\frac{\mu_F^2}{\tilde{p}_g \cdot p_Q} \right) + C_A \log \left(\frac{\mu_F^2}{\tilde{p}_g \cdot p_q} \right) \right) + \frac{16N_F T_r}{9} - \frac{C_A \gamma_q}{2C_F} \\
& \left. - \frac{50C_A}{9} + \frac{4N_F T_r - 11C_A}{12} \left(\log \left(\frac{\mu_F^2}{2\tilde{p}_g \cdot p_Q} \right) + \log \left(\frac{\mu_F^2}{2\tilde{p}_g \cdot p_q} \right) \right) + \frac{C_A \pi^2}{2} \right] \times |\mathcal{M}^{gQ \rightarrow q}|^2
\end{aligned} \tag{B.22}$$

and

$$\begin{aligned}
\mathcal{F}_2 = & \iint_0^1 d\tilde{x}_{q'} dx_Q \int_{\tilde{x}_{q'}}^1 \frac{dx}{x} f_{Q/P}(x_Q, \mu_F^2) f_{q'/P} \left(\frac{\tilde{x}_{q'}}{x}, \mu_F^2 \right) \left\{ C_F x + \frac{C_F(x^2 - 2x + 2)}{2x} \right. \\
& \times \left[\log(1-x) - \log \left(\frac{x\mu_F^2}{(1-x)\tilde{p}_{q'} \cdot p_Q} \right) - \log \left(\frac{x\mu_F^2}{(1-x)\tilde{p}_{q'} \cdot p_q} \right) \right] \left. \right\} \times |\mathcal{M}^{gQ \rightarrow q}|^2
\end{aligned} \tag{B.23}$$

By observing $(\mathbf{P} + \mathbf{K})^{qq} = (\mathbf{P} + \mathbf{K})^{\bar{q}g}$, we can infer \mathcal{F}_3 directly from $\mathcal{F}_2 = \mathcal{F}_2 [f_{q'/P}]$ by replacing the pdf in the integration kernel:

$$\mathcal{F}_3 [f_{\bar{q}'/P}] = \mathcal{F}_2 [f_{q'/P}] \tag{B.24}$$

B.2.3 Finite collinear terms related to $\mathcal{M}^{\bar{q}g \rightarrow \bar{Q}}$

According to (B.13), we need to calculate the kernels

$$\begin{aligned}
\mathcal{F}_1 = & \left(\frac{\alpha_s}{2\pi} \right)^{-1} \iiint_0^1 dx_q dx_g dx f_{q/P}(x_q, \mu_F^2) f_{g/P}(x_g, \mu_F^2) \left[(\mathbf{P} + \mathbf{K})^{qq'} \otimes d\sigma_{q'g \rightarrow \bar{Q}}^B \right] \\
\mathcal{F}_2 = & \left(\frac{\alpha_s}{2\pi} \right)^{-1} \iiint_0^1 dx_g dx_{g'} dx f_{g/P}(x_g, \mu_F^2) f_{g'/P}(x_{g'}, \mu_F^2) \left[(\mathbf{P} + \mathbf{K})^{gq} \otimes d\sigma_{gg' \rightarrow \bar{Q}}^B \right]
\end{aligned} \tag{B.25}$$

Following again the steps of Sec. B.2.3, we find

$$\begin{aligned}
\mathcal{F}_1 = & \int \int_0^1 d\tilde{x}_q dx_g \int_{\tilde{x}_q}^1 \frac{dx}{x} f_{g/P}(x_g, \mu_F^2) \left\{ \left(f_{q/P} \left(\frac{\tilde{x}_q}{x}, \mu_F^2 \right) - x f_{q/P}(\tilde{x}_q, \mu_F^2) \right) \right. \\
& \times \left[C_A \log(1-x) - \left(C_F - \frac{C_A}{2} \right) \frac{\gamma_q}{C_F} - 2 \left(C_F - \frac{C_A}{2} \right) \log \left(\frac{\mu_F^2}{2(1-x)\tilde{p}_q \cdot p_{\bar{Q}}} \right) \right. \\
& - C_A \log \left(\frac{\mu_F^2}{2(1-x)\tilde{p}_q \cdot p_g} \right) \left. \right] + f_{q/P} \left(\frac{\tilde{x}_q}{x}, \mu_F^2 \right) \left[C_F(1-x) + \frac{2 \log(x) C_F}{x-1} \right. \\
& - (x+1) \left\{ \frac{C_A}{2} \log(1-x) - \frac{C_A}{2} \log \left(\frac{x \mu_F^2}{2(1-x)\tilde{p}_q \cdot p_g} \right) - \left(C_F - \frac{C_A}{2} \right) \right. \\
& \left. \left. \times \log \left(\frac{x \mu_F^2}{2(1-x)\tilde{p}_q \cdot p_{\bar{Q}}} \right) \right\} \right] \left. \right\} \times |\mathcal{M}^{\bar{q}g \rightarrow \bar{Q}}|^2 \\
& + \int \int_0^1 d\tilde{x}_q dx_g f_{g/P}(x_g, \mu_F^2) f_{q/P}(\tilde{x}_q, \mu_F^2) \left[\left(C_F + \frac{C_A}{2} \right) \log^2(1-\tilde{x}_q) \right. \\
& - \log(1-\tilde{x}_q) \left\{ \left(C_F - \frac{C_A}{2} \right) \frac{\gamma_q}{C_F} + \left(C_F - \frac{C_A}{2} \right) \log \left(\frac{\mu_F^2}{2\tilde{p}_q \cdot p_{\bar{Q}}} \right) \right. \\
& \left. \left. + C_A \log \left(\frac{\mu_F^2}{2\tilde{p}_q \cdot p_g} \right) \right\} - \frac{3}{2} \left\{ \left(C_F - \frac{C_A}{2} \right) \log \left(\frac{\mu_F^2}{2\tilde{p}_q \cdot p_{\bar{Q}}} \right) + \frac{C_A}{2} \log \left(\frac{\mu_F^2}{2\tilde{p}_q \cdot p_g} \right) \right\} \right. \\
& \left. \left. + (4C_F - C_A) \frac{\pi^2}{6} - 5C_F - \frac{\gamma_q}{C_F} \left(C_F - \frac{C_A}{2} \right) \right] |\mathcal{M}^{\bar{q}g \rightarrow \bar{Q}}|^2,
\end{aligned} \tag{B.26}$$

and

$$\begin{aligned}
\mathcal{F}_2 = & \int \int_0^1 d\tilde{x}_g dx_q \int_{\tilde{x}_g}^1 \frac{dx}{x} f_{q/P}(x_q, \mu_F^2) f_{g/P} \left(\frac{\tilde{x}_g}{x}, \mu_F^2 \right) \left[2T_r(1-x)x + \right. \\
& \frac{T_r(2(x-1)x+1)}{C_F} \left\{ \frac{C_A}{2} \log(1-x) - \frac{C_A}{2} \log \left(\frac{\mu_F^2}{2(1-x)\tilde{p}_q \cdot p_g} \right) \right. \\
& \left. \left. - \left(C_F - \frac{C_A}{2} \right) \log \left(\frac{\mu_F^2}{2(1-x)\tilde{p}_q \cdot p_{\bar{Q}}} \right) \right\} \right] \times |\mathcal{M}^{\bar{q}g \rightarrow \bar{Q}}|^2.
\end{aligned} \tag{B.27}$$

B.2.4 Compact Expressions

Using (B.19), (B.20), (B.22), (B.23), (B.24), (B.26), and (B.27), (B.13) can be written into a more compact formulation

$$\begin{aligned}
\sigma_{\text{coll.}}^{\text{NLO}} &= \iint_0^1 dx_a dx_b \int d\text{LIPS}_{1+\text{elw}}(k_1, k_2, k_3, k_4; p_a, p_b) \frac{1}{\hat{s}} \\
&\times \left\{ \left[f_{\bar{q}/P}(x_a, \mu_F^2) \tilde{f}_{Q/P}^{(1)}(x_b, \mu_F^2) + \tilde{f}_{\bar{q}/P}^{(1)}(x_a, \mu_F^2) f_{Q/P}(x_b, \mu_F^2) \right] \right. \\
&\times \left| \mathcal{M}_{\text{B}}^{\bar{q}Q \rightarrow g}(k_1, k_2, k_3, k_4; p_a, p_b) \right|^2 + (\bar{q} \leftrightarrow Q) \\
&+ \left[f_{g/P}(x_a, \mu_F^2) \tilde{f}_{Q/P}^{(2)}(x_b, \mu_F^2) + \tilde{f}_{g/P}^{(2)}(x_a, \mu_F^2) f_{Q/P}(x_b, \mu_F^2) \right] \\
&\times \left| \mathcal{M}_{\text{B}}^{gQ \rightarrow q}(k_1, k_2, k_3, k_4; p_a, p_b) \right|^2 + (g \leftrightarrow Q) \\
&+ \left[f_{\bar{q}/P}(x_a, \mu_F^2) \tilde{f}_{g/P}^{(3)}(x_b, \mu_F^2) + \tilde{f}_{\bar{q}/P}^{(3)}(x_a, \mu_F^2) f_{g/P}(x_b, \mu_F^2) \right] \\
&\times \left. \left| \mathcal{M}_{\text{B}}^{\bar{q}g \rightarrow \bar{Q}}(k_1, k_2, k_3, k_4; p_a, p_b) \right|^2 + (\bar{q} \leftrightarrow g) \right\}, \tag{B.28}
\end{aligned}$$

where we have introduced the modified pdfs

$$\begin{aligned}
\tilde{f}_{\bar{q}/P}^{(1)}(\tilde{x}, \mu_F^2) &= \frac{\alpha_s(\mu_R^2)}{2\pi} \int_{\tilde{x}}^1 \frac{dx}{x} \left\{ \mathcal{A}_{\bar{q}\bar{q}}^{(1)} \left(f_{\bar{q}/P} \left(\frac{\tilde{x}}{x}, \mu_F^2 \right) - x f_{\bar{q}/P}(\tilde{x}, \mu_F^2) \right) \right. \\
&\quad \left. + \mathcal{B}_{\bar{q}\bar{q}}^{(1)} f_{\bar{q}/P} \left(\frac{\tilde{x}}{x}, \mu_F^2 \right) + \mathcal{C}_{\bar{q}g}^{(1)} f_{g/P} \left(\frac{\tilde{x}}{x}, \mu_F^2 \right) \right\} + \frac{\alpha_s(\mu_R^2)}{2\pi} \mathcal{D}_{\bar{q}\bar{q}}^{(1)} f_{\bar{q}/P}(\tilde{x}, \mu_F^2), \tag{B.29}
\end{aligned}$$

$$\begin{aligned}
\tilde{f}_{Q/P}^{(1)}(\tilde{x}, \mu_F^2) &= \frac{\alpha_s(\mu_R^2)}{2\pi} \int_{\tilde{x}}^1 \frac{dx}{x} \left\{ \mathcal{A}_{QQ}^{(1)} \left(f_{Q/P} \left(\frac{\tilde{x}}{x}, \mu_F^2 \right) - x f_{Q/P}(\tilde{x}, \mu_F^2) \right) \right. \\
&\quad \left. + \mathcal{B}_{QQ}^{(1)} f_{Q/P} \left(\frac{\tilde{x}}{x}, \mu_F^2 \right) + \mathcal{C}_{Qg}^{(1)} f_{g/P} \left(\frac{\tilde{x}}{x}, \mu_F^2 \right) \right\} + \frac{\alpha_s(\mu_R^2)}{2\pi} \mathcal{D}_{QQ}^{(1)} f_{Q/P}(\tilde{x}, \mu_F^2), \tag{B.30}
\end{aligned}$$

$$\begin{aligned}
\tilde{f}_{Q/P}^{(2)}(\tilde{x}, \mu_F^2) &= \frac{\alpha_s(\mu_R^2)}{2\pi} \int_{\tilde{x}}^1 \frac{dx}{x} \left\{ \mathcal{A}_{QQ}^{(2)} \left(f_{Q/P} \left(\frac{\tilde{x}}{x}, \mu_F^2 \right) - x f_{Q/P}(\tilde{x}, \mu_F^2) \right) \right. \\
&\quad \left. + \mathcal{B}_{QQ}^{(2)} f_{Q/P} \left(\frac{\tilde{x}}{x}, \mu_F^2 \right) + \mathcal{C}_{Qg}^{(2)} f_{g/P} \left(\frac{\tilde{x}}{x}, \mu_F^2 \right) \right\} + \frac{\alpha_s(\mu_R^2)}{2\pi} \mathcal{D}_{QQ}^{(2)} f_{Q/P}(\tilde{x}, \mu_F^2), \tag{B.31}
\end{aligned}$$

$$\begin{aligned}
\tilde{f}_{g/P}^{(2)}(\tilde{x}, \mu_F^2) &= \frac{\alpha_s(\mu_R^2)}{2\pi} \int_{\tilde{x}}^1 \frac{dx}{x} \left\{ \mathcal{A}_{gg}^{(2)} \left(f_{g/P} \left(\frac{\tilde{x}}{x}, \mu_F^2 \right) - x f_{g/P}(\tilde{x}, \mu_F^2) \right) \right. \\
&\quad \left. + \mathcal{B}_{gg}^{(2)} f_{g/P} \left(\frac{\tilde{x}}{x}, \mu_F^2 \right) + \mathcal{C}_{gq}^{(2)} f_{q/P} \left(\frac{\tilde{x}}{x}, \mu_F^2 \right) + \mathcal{C}_{g\bar{q}'}^{(2)} f_{\bar{q}'/P} \left(\frac{\tilde{x}}{x}, \mu_F^2 \right) \right\} \\
&\quad + \frac{\alpha_s(\mu_R^2)}{2\pi} \mathcal{D}_{gg}^{(2)} f_{g/P}(\tilde{x}, \mu_F^2), \tag{B.32}
\end{aligned}$$

Table B.1: Cross-references of the modified pdfs' coefficient functions (B.29)-(B.34) to the results of Secs. B.2.1, B.2.2, and B.2.3.

Function of Secs. B.2.1-B.2.3	Coefficients
(B.19)	$\mathcal{A}_{\bar{q}q}^{(1)}, \mathcal{B}_{\bar{q}q}^{(1)}, \mathcal{D}_{\bar{q}q}^{(1)},$ $\mathcal{A}_{QQ}^{(1)}, \mathcal{B}_{QQ}^{(1)}, \mathcal{D}_{QQ}^{(1)}$
(B.20)	$\mathcal{C}_{\bar{q}g}^{(1)}, \mathcal{C}_{Qg}^{(1)}$
(B.22)	$\mathcal{A}_{gg}^{(2)}, \mathcal{B}_{gg}^{(2)}, \mathcal{D}_{gg}^{(2)},$ $\mathcal{A}_{gg}^{(3)}, \mathcal{B}_{gg}^{(3)}, \mathcal{D}_{gg}^{(3)}$
(B.23)	$\mathcal{C}_{gq}^{(2)}, \mathcal{C}_{gQ}^{(3)}$
(B.24)	$\mathcal{C}_{q\bar{q}'}^{(2)}, \mathcal{C}_{q\bar{q}'}^{(3)}$
(B.26)	$\mathcal{A}_{QQ}^{(2)}, \mathcal{B}_{QQ}^{(2)}, \mathcal{D}_{QQ}^{(2)},$ $\mathcal{A}_{\bar{q}q}^{(3)}, \mathcal{B}_{\bar{q}q}^{(3)}, \mathcal{D}_{\bar{q}q}^{(3)}$
(B.27)	$\mathcal{C}_{Qq}^{(2)}, \mathcal{C}_{\bar{q}g}^{(3)}$

$$\begin{aligned}
\tilde{f}_{g/P}^{(3)}(\tilde{x}, \mu_F^2) &= \frac{\alpha_s(\mu_R^2)}{2\pi} \int_{\tilde{x}}^1 \frac{dx}{x} \left\{ \mathcal{A}_{gg}^{(3)} \left(f_{g/P} \left(\frac{\tilde{x}}{x}, \mu_F^2 \right) - x f_{g/P}(\tilde{x}, \mu_F^2) \right) \right. \\
&+ \mathcal{B}_{gg}^{(3)} f_{g/P} \left(\frac{\tilde{x}}{x}, \mu_F^2 \right) + \mathcal{C}_{gQ}^{(3)} f_{Q/P} \left(\frac{\tilde{x}}{x}, \mu_F^2 \right) + \mathcal{C}_{g\bar{q}'}^{(3)} f_{\bar{q}'/P} \left(\frac{\tilde{x}}{x}, \mu_F^2 \right) \left. \right\} \quad (\text{B.33}) \\
&+ \frac{\alpha_s(\mu_R^2)}{2\pi} \mathcal{D}_{gg}^{(3)} f_{g/P}(\tilde{x}, \mu_F^2),
\end{aligned}$$

$$\begin{aligned}
\tilde{f}_{\bar{q}/P}^{(3)}(\tilde{x}, \mu_F^2) &= \frac{\alpha_s(\mu_R^2)}{2\pi} \int_{\tilde{x}}^1 \frac{dx}{x} \left\{ \mathcal{A}_{\bar{q}q}^{(3)} \left(f_{\bar{q}/P} \left(\frac{\tilde{x}}{x}, \mu_F^2 \right) - x f_{\bar{q}/P}(\tilde{x}, \mu_F^2) \right) \right. \\
&+ \mathcal{B}_{\bar{q}q}^{(3)} f_{\bar{q}/P} \left(\frac{\tilde{x}}{x}, \mu_F^2 \right) + \mathcal{C}_{\bar{q}g}^{(3)} f_{g/P} \left(\frac{\tilde{x}}{x}, \mu_F^2 \right) \left. \right\} + \frac{\alpha_s(\mu_R^2)}{2\pi} \mathcal{D}_{\bar{q}q}^{(3)} f_{\bar{q}/P}(\tilde{x}, \mu_F^2). \quad (\text{B.34})
\end{aligned}$$

As a consequence of the invariance of \mathbf{K} and \mathbf{P} with respect to charge conjugation, which follows directly from QCD being \mathcal{C} -invariant, all the coefficients $\mathcal{A}_{ab}^{(i)}, \mathcal{B}_{ab}^{(i)}, \mathcal{C}_{ab}^{(i)}, \mathcal{D}_{ab}^{(i)}$ as functions of x are related to the results of secs. B.2.1-B.2.3 upon trivial changes in of momenta-labels, cf. (B.24). The cross-references are summarized in Tab. B.1.

B.2.5 Integral Formulae

This section tabulates the integrals encountered by resolving the plus-distribution of the splitting operators of Secs. B.2.1-B.2.3.

$$\begin{aligned}
\int_0^1 \frac{dx}{x} \theta(x-z) f\left(\frac{z}{x}\right) \left[\frac{\log\{(1-x)/x\}}{1-x} \right]_+ &= \frac{\log^2(1-z) - \pi^2}{2} f(z) \\
&+ \int_0^1 \frac{dx}{x} \theta(x-z) \left\{ \frac{\log(1-x)}{1-x} \left(f\left(\frac{z}{x}\right) - x f(z) \right) - \frac{\log(x)}{1-x} f\left(\frac{z}{x}\right) \right\} \quad (\text{B.35})
\end{aligned}$$

$$\int_0^1 \frac{dx}{x} \theta(x-z) f\left(\frac{z}{x}\right) \left[\frac{\log(1-x)}{1-x} \right]_+ = \frac{\log^2(1-z)}{2} f(z) \\ + \int_0^1 \frac{dx}{x} \theta(x-z) \left\{ \frac{1}{1-x} \left(f\left(\frac{z}{x}\right) - x f(z) \right) - (x+1) f\left(\frac{z}{x}\right) \right\} \quad (\text{B.36})$$

$$\int_0^1 \frac{dx}{x} \theta(x-z) f\left(\frac{z}{x}\right) \left[\frac{x^2+1}{1-x} \right]_+ = \left(2 \log(1-z) + \frac{3}{2} \right) f(z) \\ + \int_0^1 \frac{dx}{x} \theta(x-z) \left(\frac{2}{1-x} \left(f\left(\frac{z}{x}\right) - x f(z) \right) - (x+1) f\left(\frac{z}{x}\right) \right) \quad (\text{B.37})$$

$$\int_0^1 \frac{dx}{x} \theta(x-z) f\left(\frac{z}{x}\right) \left[\frac{1}{1-x} \right]_+ = \log(1-z) f(z) \\ + \int_0^1 \frac{dx}{x} \theta(x-z) \left(\frac{1}{1-x} \left(f\left(\frac{z}{x}\right) - x f(z) \right) \right) \quad (\text{B.38})$$

Bibliography

- [1] M. E. Peskin and D. V. Schroeder, *An Introduction To Quantum Field Theory*, ADDISON-WESLEY, READING, USA (1995),
M. Böhm, A. Denner and H. Joos, *Gauge Theories of the Strong and Electroweak Interaction*, TEUBNER, STUTTGART, GERMANY (2001),
G. Dissertori, I. G. Knowles and M. Schmelling, *Quantum Chromodynamics: High Energy Experiments And Theory*, CLARENDON, OXFORD, UK (2003).
- [2] C. Buttar *et al.*, Les Houches Physics at TeV Colliders 2005, Standard Model and Higgs working group: Summary report, [hep-ph/0604120](#).
- [3] S. Dittmaier, S. Kallweit and P. Uwer, “NLO QCD corrections to WW +jet production at hadron colliders,” *Phys. Rev. Lett.* **100** (2008) 062003 [[arXiv:0710.1577](#)],
J. M. Campbell, R. Keith Ellis and G. Zanderighi, “Next-to-leading order predictions for $WW + 1$ jet distributions at the LHC,” *JHEP* **0712** (2007) 056 [[arXiv:0710.1832](#)].
- [4] T. Binoth, G. Ossola, C. G. Papadopoulos and R. Pittau, “NLO QCD corrections to tri-boson production,” *JHEP* **0806** (2008) 082 [[arXiv:0804.0350](#)].
- [5] A. Bredenstein, A. Denner, S. Dittmaier and S. Pozzorini, “NLO QCD corrections to $pp \rightarrow t\bar{t}b\bar{b} + X$ at the LHC,” *Phys. Rev. Lett.* **103** (2009) 012002 [[arXiv:0905.0110](#)].
- [6] T. Binoth, T. Gleisberg, S. Karg, N. Kauer and G. Sanguinetti, “NLO QCD corrections to ZZ +jet production at hadron colliders,” *Phys. Lett. B* **683** (2010) 154 [[arXiv:0911.3181](#)].
- [7] T. Binoth, N. Greiner, A. Guffanti, J. P. Guillet, T. Reiter and J. Reuter, “Next-to-leading order QCD corrections to $pp \rightarrow b\bar{b}b\bar{b} + X$ at the LHC: the quark induced case,” [arXiv:0910.4379](#).
- [8] V. Hankele and D. Zeppenfeld, *Phys. Lett. B* **661** (2008) 103 [[arXiv:0712.3544](#)],
F. Campanario, V. Hankele, C. Oleari, S. Prestel and D. Zeppenfeld, “QCD corrections to charged triple vector boson production with leptonic decay,” *Phys. Rev. D* **78** (2008) 094012 [[arXiv:0809.0790](#)].
- [9] F. Campanario, C. Englert, M. Spannowsky and D. Zeppenfeld, “NLO-QCD corrections to $W\gamma j$ production,” *Europhys. Lett.* **88**, 11001 (2009) [[arXiv:0908.1638](#)].

-
- [10] F. Campanario, C. Englert, S. Kallweit, M. Spannowsky and D. Zeppenfeld, “NLO QCD corrections to WZj production,” in preparation.
- [11] K. Arnold *et al.*, “VBFNLO: A parton level Monte Carlo for processes with electroweak bosons,” *Comput. Phys. Commun.* **180**, 1661 (2009) [arXiv:0811.4559]. Available from <http://www-itp.particle.uni-karlsruhe.de/vbfnlo/>
- [12] U. Baur, T. Han and J. Ohnemus, “QCD corrections to hadronic $W\gamma$ production with nonstandard $WW\gamma$ couplings,” *Phys. Rev. D* **48** (1993) 5140 [arXiv:hep-ph/9305314].
- [13] C. Grojean, “New theories for the Fermi scale,” arXiv:0910.4976, D. E. Morrissey, T. Plehn and T. M. P. Tait, “New physics at the LHC,” arXiv:0912.3259.
- [14] G. 't Hooft and M. J. G. Veltman, “Regularization and renormalization of gauge fields,” *Nucl. Phys. B* **44** (1972) 189.
- [15] S. R. Coleman and J. Mandula, “All possible symmetries of the S matrix,” *Phys. Rev.* **159** (1967) 1251.
- [16] F. A. Berezin, “The method of second quantization,” *Pure Appl. Phys.* **24** (1966) 1.
- [17] J. Glimm and A. M. Jaffe, *Quantum Physics, A Functional Integral Point Of View* SPRINGER, NEW YORK, USA (1987)
- [18] M. Kac, “On distributions of certain Wiener functionals,” *Trans. Amer. Math. Soc.* **65** (1949), 1.
- [19] R. F. Streater and A. S. Wightman, *\mathcal{PCT} , spin and statistics, and all that*, Addison-Wesley, Redwood City, USA: (1989).
- [20] C. N. Yang and R. L. Mills, “Conservation of isotopic spin and isotopic gauge invariance,” *Phys. Rev.* **96** (1954) 191,
R. Shaw, “The problem of particle types and other contributions to the theory of elementary particles,” doctoral thesis, Cambridge University, unpublished.
- [21] C. Amsler *et al.* [Particle Data Group], “Review of particle physics,” *Phys. Lett. B* **667** (2008) 1.
- [22] F. Wilczek, “Problem of strong \mathcal{P} and \mathcal{T} invariance in the presence of instantons,” *Phys. Rev. Lett.* **40** (1978) 279.
- [23] L. D. Faddeev and V. N. Popov, “Feynman diagrams for the Yang-Mills field,” *Phys. Lett. B* **25** (1967) 29,
B. S. DeWitt, “Quantum theory of gravity. II. The manifestly covariant theory,” *Phys. Rev.* **162**, 1195 (1967).

- [24] C. Becchi, A. Rouet and R. Stora, “Renormalization of gauge theories,” *Annals Phys.* **98** (1976) 287,
C. Becchi, A. Rouet and R. Stora, “Renormalization of the abelian Higgs-Kibble model,” *Commun. Math. Phys.* **42** (1975) 127,
I. V. Tyutin, Lebedev Institute preprint (1975, unpublished),
M. Z. Iofa and I. V. Tyutin, “Gauge invariance of spontaneously broken nonabelian theories in the Bogolyubov-Parasiuk-Hepp-Zimmerman method,” *Teor. Mat. Fiz.* **27** (1976) 38.
- [25] J. C. Taylor, “Ward identities and charge renormalization of the Yang-Mills field,” *Nucl. Phys. B* **33** (1971) 436,
A. A. Slavnov, “Ward identities in gauge theories,” *Theor. Math. Phys.* **10** (1972) 99 [*Teor. Mat. Fiz.* **10** (1972) 153],
G. 't Hooft, “Renormalization of massless Yang-Mills fields,” *Nucl. Phys. B* **33**, 173 (1971),
B. W. Lee and J. Zinn-Justin, “Spontaneously broken gauge symmetries. 1. Preliminaries,” *Phys. Rev. D* **5**, 3121 (1972),
B. W. Lee and J. Zinn-Justin, “Spontaneously broken gauge symmetries 2. Perturbation theory and renormalization,” *Phys. Rev. D* **5**, 3137 (1972) [Erratum-*ibid.* *D* **8**, 4654 (1973)],
B. W. Lee and J. Zinn-Justin, “Spontaneously broken gauge symmetries. 3. Equivalence,” *Phys. Rev. D* **5**, 3155 (1972),
B. W. Lee and J. Zinn-Justin, “Spontaneously broken gauge symmetries. 4. General gauge formulation,” *Phys. Rev. D* **7**, 1049 (1973).
- [26] J. C. Ward, “An identity in Quantum Electrodynamics,” *Phys. Rev.* **78** (1950) 182.
- [27] F. Englert and R. Brout, “Broken symmetry and the mass of gauge vector mesons,” *Phys. Rev. Lett.* **13** (1964) 321,
P. W. Higgs, “Broken symmetries and the masses of gauge bosons,” *Phys. Rev. Lett.* **13**, 508 (1964).
- [28] K. Fujikawa, B. W. Lee and A. I. Sanda, “Generalized renormalizable gauge formulation of spontaneously broken gauge theories,” *Phys. Rev. D* **6** (1972) 2923.
- [29] N. Cabibbo, “Unitary symmetry and leptonic decays,” *Phys. Rev. Lett.* **10** (1963) 531,
M. Kobayashi and T. Maskawa, “ \mathcal{CP} violation in the renormalizable theory of weak interaction,” *Prog. Theor. Phys.* **49** (1973) 652.
- [30] A. D. Sakharov, “Violation of \mathcal{CP} invariance, \mathcal{C} asymmetry, and baryon asymmetry of the universe,” *Pisma Zh. Eksp. Teor. Fiz.* **5** (1967) 32 [*JETP Lett.* **5** (1967) 24].
- [31] M. J. Strassler and K. M. Zurek, “Echoes of a hidden valley at hadron colliders,” *Phys. Lett. B* **651** (2007) 374 [[arXiv:hep-ph/0604261](https://arxiv.org/abs/hep-ph/0604261)].

- [32] K. M. Case and S. G. Gasiorowicz, “Can massless particles be charged?” *Phys. Rev.* **125** (1962) 1055,
S. Weinberg and E. Witten, “Limits on massless particles,” *Phys. Lett. B* **96** (1980) 59,
C. Quigg and R. Shrock, “Gedanken worlds without Higgs: QCD-induced electroweak symmetry breaking,” *Phys. Rev. D* **79** (2009) 096002 [[arXiv:0901.3958](#)].
- [33] T. D. Lee and M. Nauenberg, “Degenerate systems and mass singularities,” *Phys. Rev.* **133** (1964) B1549.
- [34] K. Hagiwara and D. Zeppenfeld, “Amplitudes for multiparton processes involving a current at e^+e^- , $e^\pm p$, and hadron colliders,” *Nucl. Phys. B* **313** (1989) 560.
- [35] T. Kinoshita, “Mass singularities of Feynman amplitudes,” *J. Math. Phys.* **3** (1962) 650.
- [36] R. K. Ellis, D. A. Ross and A. E. Terrano, “The perturbative calculation of jet structure in e^+e^- annihilation,” *Nucl. Phys. B* **178**, 421 (1981),
Z. Kunszt and D. E. Soper, “Calculation of jet cross-sections in hadron collisions at order α_s^3 ,” *Phys. Rev. D* **46**, 192 (1992),
S. D. Ellis, Z. Kunszt and D. E. Soper, “Two jet production in hadron collisions at order α_s^3 in QCD,” *Phys. Rev. Lett.* **69**, 1496 (1992),
S. Frixione, Z. Kunszt and A. Signer, “Three jet cross-sections to next-to-leading order,” *Nucl. Phys. B* **467**, 399 (1996) [[arXiv:hep-ph/9512328](#)].
- [37] S. Catani and M. H. Seymour, “A general algorithm for calculating jet cross sections in NLO QCD,” *Nucl. Phys. B* **485** (1997) 291 [Erratum-ibid. B **510** (1998) 503] [[arXiv:hep-ph/9605323](#)].
- [38] A. V. Belitsky and A. V. Radyushkin, “Unraveling hadron structure with generalized parton distributions,” *Phys. Rept.* **418** (2005) 1 [[arXiv:hep-ph/0504030](#)].
- [39] J. Pumplin, D. R. Stump, J. Huston, H. L. Lai, P. Nadolsky, and W. K. Tung, “New generation of parton distributions with uncertainties from global QCD analysis,” *JHEP* **0207** (2002), 012 [[arXiv:hep-ph/0201195](#)].
- [40] J. C. Collins, D. E. Soper and G. Sterman, “Factorization of hard processes in QCD,” *Adv. Ser. Direct. High Energy Phys.* **5** (1988) 1 [[arXiv:hep-ph/0409313](#)].
- [41] K. G. Wilson, “The renormalization group: Critical phenomena and the Kondo problem,” *Rev. Mod. Phys.* **47** (1975) 773.
- [42] V. N. Gribov and L. N. Lipatov, “Deep inelastic ep scattering in perturbation theory,” *Sov. J. Nucl. Phys.* **15** (1972) 438 [*Yad. Fiz.* **15** (1972) 781],
G. Altarelli and G. Parisi, “Asymptotic freedom in parton language,” *Nucl. Phys. B* **126** (1977) 298,

- Y. L. Dokshitzer, “Calculation of the structure functions for deep inelastic scattering and e^+e^- annihilation by perturbation theory in Quantum chromodynamics,” *Sov. Phys. JETP* **46** (1977) 641 [*Zh. Eksp. Teor. Fiz.* **73** (1977) 1216].
- [43] S. Dittmaier, “Separation of soft and collinear singularities from one-loop N -point integrals,” *Nucl. Phys. B* **675** (2003) 447 [[arXiv:hep-ph/0308246](#)].
- [44] A. Breckenstein, A. Denner, S. Dittmaier and S. Pozzorini, “NLO QCD corrections to top anti-top bottom anti-bottom production at the LHC: 1. quark-antiquark annihilation,” *JHEP* **0808** (2008) 108 [[arXiv:0807.1248](#)].
- [45] R. E. Cutkosky, “Singularities and discontinuities of Feynman amplitudes,” *J. Math. Phys.* **1** (1960) 429.
- [46] S. Frixione, “Isolated photons in perturbative QCD,” *Phys. Lett. B* **429** (1998) 369 [[arXiv:hep-ph/9801442](#)].
- [47] G. Passarino and M. J. G. Veltman, “One loop corrections for e^+e^- annihilation into $\mu^+\mu^-$ in the Weinberg model,” *Nucl. Phys. B* **160** (1979) 151.
- [48] A. Denner and S. Dittmaier, “Reduction of one-loop tensor 5-point integrals,” *Nucl. Phys. B* **658** (2003) 175 [[arXiv:hep-ph/0212259](#)],
A. Denner and S. Dittmaier, “Techniques for one-loop tensor integrals in many-particle processes,” *Nucl. Phys. Proc. Suppl.* **157** (2006) 53 [[arXiv:hep-ph/0601085](#)].
- [49] A. Denner, “Techniques for calculation of electroweak radiative corrections at the one loop level and results for W physics at LEP-200,” *Fortsch. Phys.* **41** (1993) 307 [[arXiv:0709.1075](#)].
- [50] R. K. Ellis and G. Zanderighi, “Scalar one-loop integrals for QCD,” *JHEP* **0802** (2008) 002 [[arXiv:0712.1851](#)].
- [51] H. Lehmann, “On the Properties of propagation functions and renormalization constants of quantized fields,” *Nuovo Cim.* **11** (1954) 342.
- [52] H. Lehmann, K. Symanzik and W. Zimmermann, “On the formulation of quantized field theories,” *Nuovo Cim.* **1** (1955) 205.
- [53] K. G. Wilson, “Quantum field theory models in less than four-dimensions,” *Phys. Rev. D* **7** (1973) 2911.
- [54] J. C. Collins, *Renormalization. An Introduction To Renormalization, The Renormalization Group, And The Operator Product Expansion*, CAMBRIDGE UNIVERSITY PRESS, UK (1984),
G. P. Lepage, “What is renormalization?,” [arXiv:hep-ph/0506330](#).

- [55] W. Beenakker, S. Dittmaier, M. Kramer, B. Plumper, M. Spira and P. M. Zerwas, “NLO-QCD corrections to t anti- t H production in hadron collisions,” Nucl. Phys. B **653** (2003) 151 [[arXiv:hep-ph/0211352](#)].
- [56] A. Grozin, “Lectures on QED and QCD,” [arXiv:hep-ph/0508242](#).
- [57] D. J. Gross and F. Wilczek, “Ultraviolet behavior of non-abelian gauge theories,” Phys. Rev. Lett. **30** (1973) 1343,
H. D. Politzer, “Reliable Perturbative Results For Strong Interactions?,” Phys. Rev. Lett. **30** (1973) 1346.
- [58] W. E. Caswell, “Asymptotic behavior of nonabelian gauge theories to two loop order,” Phys. Rev. Lett. **33** (1974) 244,
D. R. T. Jones, “Two loop diagrams in Yang-Mills theory,” Nucl. Phys. B **75** (1974) 531.
- [59] C. G. Callan, “Broken scale invariance in scalar field theory,” Phys. Rev. D **2** (1970) 1541,
K. Symanzik, “Small distance behavior in field theory and power counting,” Commun. Math. Phys. **18** (1970) 22,
K. Symanzik, “Small distance behavior analysis and Wilson expansion,” Commun. Math. Phys. **23** (1971) 49.
- [60] N. Metropolis and S. Ulam, “The Monte Carlo method”, J. Am. Statist. Assoc. **44** (1949) 335.
- [61] G. P. Lepage, “A new algorithm for adaptive multidimensional integration,” J. Comput. Phys. **27** (1978) 192,
G. P. Lepage, “Vegas: An adaptive multidimensional integration program,” CLNS-80/447.
- [62] R. K. Ellis, W. J. Stirling, B. R. Webber, *QCD And Collider Physics*, CAMBRIDGE UNIVERSITY PRESS, CAMBRIDGE, UK (2003)
- [63] M. Bähr, “Erzeugung einzelner Top-Quarks als Hintergrund bei der Higgs-Suche,” Diploma Thesis, Institut für Theoretische Physik, Universität Karlsruhe.
- [64] R. H. Dalitz, “On the analysis of τ -meson data and the nature of the τ -meson,” Philosophical Magazine **44** (1953) 1068
- [65] R. D. Field, *Applications Of Perturbative QCD*, ADDISON-WESLEY , READING, USA (1989)
- [66] M. Werner, “Hadronische W Zerfälle in Vektorbosonfusionsprozessen,” Diploma Thesis, Institut für Theoretische Physik, Universität Karlsruhe,
S. Prestel, “QCD-Korrekturen zu WW -Produktion am LHC”, Diploma Thesis, Institut für Theoretische Physik, Universität Karlsruhe.

- [67] H. Murayama, I. Watanabe and K. Hagiwara, “HELAS: HELicity Amplitude subroutines for Feynman diagram evaluations,” KEK-Report 91-11, 1992.
- [68] J. Alwall *et al.*, “MadGraph/MadEvent v4: The new web generation,” JHEP **0709** (2007) 028 [arXiv:0706.2334].
- [69] T. Gleisberg, S. Höche, F. Krauss, M. Schönherr, S. Schumann, F. Siegert and J. Winter, “Event generation with SHERPA 1.1,” JHEP **0902** (2009) 007 [arXiv:0811.4622].
- [70] A. Denner, S. Dittmaier, M. Roth, and D. Wackerroth, “Predictions for all processes $e^+e^- \rightarrow 4$ fermions + γ ,” Nucl. Phys. B **560** (1999), 33 [arXiv:hep-ph/9904472].
- [71] C. Oleari and D. Zeppenfeld, “Next-to-leading order QCD corrections to W and Z production via vector-boson fusion,” Phys. Rev. D **69** (2004), 093004 [arXiv:hep-ph/0310156].
- [72] K. Hagiwara, R. D. Peccei, D. Zeppenfeld and K. Hikasa, “Probing the weak boson sector in $e^+e^- \rightarrow W^+W^-$,” Nucl. Phys. B **282** (1987) 253.
- [73] N. D. Christensen and C. Duhr, “FEYNRULES - Feynman rules made easy,” Comput. Phys. Commun. **180** (2009) 1614 [arXiv:0806.4194].
- [74] R. Mertig, M. Böhm and A. Denner, “FEYN CALC: Computer algebraic calculation of Feynman amplitudes,” Comput. Phys. Commun. **64** (1991) 345.
- [75] R. Frederix, T. Gehrmann and N. Greiner, “Automation of the dipole subtraction method in MadGraph/MadEvent,” JHEP **0809** (2008) 122 [arXiv:0808.2128].
- [76] M. S. Chanowitz, M. Furman and I. Hinchliffe, “The axial current in dimensional regularization,” Nucl. Phys. B **159** (1979) 225.
- [77] B. Jäger, C. Oleari and D. Zeppenfeld, “Next-to-leading order QCD corrections to W^+W^- production via vector-boson fusion,” JHEP **0607** (2006) 015 [arXiv:hep-ph/0603177],
B. Jäger, C. Oleari and D. Zeppenfeld, “Next-to-leading order QCD corrections to Z boson pair production via vector-boson fusion,” Phys. Rev. D **73** (2006) 113006 [arXiv:hep-ph/0604200],
G. Bozzi, B. Jäger, C. Oleari and D. Zeppenfeld, “Next-to-leading order QCD corrections to W^+Z and W^-Z production via vector-boson fusion,” Phys. Rev. D **75** (2007) 073004 [arXiv:hep-ph/0701105],
C. Englert, B. Jäger and D. Zeppenfeld, “QCD corrections to vector-boson fusion processes in warped higgsless models,” JHEP **0903** (2009) 060 [arXiv:0812.2564].
- [78] T. Figy, C. Oleari and D. Zeppenfeld, “Next-to-leading order jet distributions for Higgs boson production via weak-boson fusion,” Phys. Rev. D **68** (2003) 073005 [arXiv:hep-ph/0306109].

- [79] W. Siegel, “Supersymmetric dimensional regularization via dimensional reduction,” *Phys. Lett. B* **84** (1979) 193,
W. Siegel, “Inconsistency of supersymmetric dimensional regularization,” *Phys. Lett. B* **94** (1980) 37.
- [80] P. Breitenlohner and D. Maison, “Dimensional renormalization and the action principle,” *Commun. Math. Phys.* **52** (1977) 11.
- [81] T. Hahn, “Generating Feynman diagrams and amplitudes with FeynArts 3,” *Comput. Phys. Commun.* **140** (2001) 418 [[arXiv:hep-ph/0012260](#)].
- [82] T. Hahn and M. Perez-Victoria, “Automatized one-loop calculations in four and D dimensions,” *Comput. Phys. Commun.* **118** (1999) 153 [[arXiv:hep-ph/9807565](#)].
- [83] S. Kallweit, “Precision calculations for gauge boson pair production with a hadronic jet at hadron colliders,” PhD Thesis, Ludwig-Maximilians-Universität, München.
- [84] T. Figy, V. Hankele and D. Zeppenfeld, “Next-to-leading order QCD corrections to Higgs plus three jet production in vector-boson fusion,” *JHEP* **0802** (2008) 076 [[arXiv:0710.5621](#)].
- [85] W. H. Furry, “A symmetry theorem in the positron theory,” *Phys. Rev.*, **51**, 125 (1937).
- [86] S. Catani, Y. L. Dokshitzer, M. H. Seymour, and B. R. Webber, “Longitudinally invariant $K(T)$ clustering algorithms for hadron hadron collisions,” *Nucl. Phys. B* **406** (1993), 187.
- [87] L. J. Dixon, Z. Kunszt and A. Signer, “Vector boson pair production in hadronic collisions at order α_s : Lepton correlations and anomalous couplings,” *Phys. Rev. D* **60** (1999) 114037 [[arXiv:hep-ph/9907305](#)].
- [88] F. K. Diakonov, O. Korakianitis, C. G. Papadopoulos, C. Philippides and W. J. Stirling, “ $W + \text{gamma} + \text{jet}$ production as a test of the electromagnetic couplings of W at LHC and SSC,” *Phys. Lett. B* **303** (1993) 177 [[arXiv:hep-ph/9301238](#)].
- [89] D. Levin [ATLAS Collaboration], “Diboson physics in ATLAS,” ATL-COM-PHYS-2008-179.
- [90] T. Müller, D. Neuberger, and W. Thümmel, “Sensitivities for anomalous $WW\gamma$ and $ZZ\gamma$ couplings at CMS,” CERN-CMS-NOTE-2000-017 (2000)
- [91] M. Dobbs, “Prospects for probing triple gauge-boson couplings at the LHC,” *AIP Conf. Proc.* **753**, 181 (2005) [[arXiv:hep-ph/0506174](#)].

-
- [92] V. M. Abazov *et al.* [DØ Collaboration], V. M. Abazov *et al.* [DØ Collaboration], “Combined measurements of anomalous charged trilinear gauge-boson couplings from diboson production in p-pbar collisions at $\sqrt{s} = 1.96$ TeV,” [arXiv:0907.4952].
- [93] J. Alcaraz *et al.* [ALEPH Collaboration and DELPHI Collaboration and L3 Collaboration], “A combination of preliminary electroweak measurements and constraints on the Standard Model,” arXiv:hep-ex/0612034.
- [94] R. W. Brown, K. L. Kowalski and S. J. Brodsky, “Classical radiation zeros in gauge theory amplitudes,” Phys. Rev. D **28** (1983) 624.
- [95] P. Fisher, U. Becker and J. Kirkby, “Very high precision tests of the electroweak theory,” Phys. Lett. B **356** (1995) 404,
U. Baur, S. Keller and W. K. Sakumoto, “QED radiative corrections to Z boson production and the forward backward asymmetry at hadron colliders,” Phys. Rev. D **57** (1998) 199 [arXiv:hep-ph/9707301].
- [96] J. M. Campbell and R. K. Ellis, “An update on vector boson pair production at hadron colliders,” Phys. Rev. D **60** (1999) 113006 [arXiv:hep-ph/9905386].

List of Figures

2.1	Parton distribution functions CTEQ6L1 [39] used for leading order cross section calculations in this thesis. Shown are distributions with factorization scale $Q = 241$ GeV. The anti-quark and quark distributions of the non-valence flavors of the proton lie on top of each other. At the Tevatron, quark- and anti-quark distribution get interchanged for the anti-proton beam.	12
2.2	Generic one-loop Feynman diagram. The external lines are on-shell, i.e. $(k_{j+1} - k_j)^2 = m_j^2 \equiv 0$	14
2.3	Feynman graph topologies that give rise to soft singularities (a), and collinear divergencies (b) at the one loop level.	14
2.4	A naive photon isolation criterion limits the phase space of the soft gluon and hence spoils the KLN-cancellation.	16
2.5	Quark self-energy correction at $\mathcal{O}(\alpha_s)$ contributing to the quark renormalization.	18
2.6	Gluon self-energy at $\mathcal{O}(\alpha_s)$ contributing to the gluon renormalization. k denotes the generation index, e.g. $d_k = (d, s, b)$	19
2.7	Vertex correction at $\mathcal{O}(\alpha_s)$, giving rise to the renormalization constant δ_1	19
2.8	Schematic representation of the used phase space set-up, which is used for the purpose of this thesis. The intermediate massive pseudo-particle of the factorization (2.81) is denoted by “im”.	25
3.1	Feynman diagrams of the partonic subprocess $q\bar{Q} \rightarrow \tilde{W}^-g$. \tilde{W} denotes the effective polarization vector of the three-body decay current $\tilde{W} \rightarrow \ell^- \bar{\nu}_\ell \gamma$, and the four-body decay current $\tilde{W} \rightarrow \ell^- \bar{\nu}_\ell \ell'^+ \ell'^-$ of fig. 3.2.	29
3.2	Feynman graphs of the decay currents $\tilde{W} \rightarrow \ell^- \bar{\nu}_\ell \gamma$, and $\tilde{W} \rightarrow \ell^- \bar{\nu}_\ell \ell'^+ \ell'^-$ via the off-shell decay $\gamma^*, Z^* \rightarrow \ell'^+ \ell'^-$ that follows from the vertex of eq. (2.26).	30
3.3	Feynman diagrams of the partonic subprocess $q\bar{Q} \rightarrow W^*g\gamma$, and $q\bar{Q} \rightarrow W^*(\gamma, Z)^*g$. W^* and $(\gamma, Z)^*$ denote the effective polarization vectors of the decay currents $W^* \rightarrow \ell^- \bar{\nu}_\ell$, $\gamma^* \rightarrow \ell'^+ \ell'^-$, and $Z^* \rightarrow \ell'^+ \ell'^-$, respectively.	30
3.4	Sample Feynman graphs contributing to the partonic real emission subprocess $q\bar{Q} \rightarrow \tilde{W}gg$ at $\mathcal{O}(\alpha^3\alpha_s^2)$. The \tilde{W} denotes the effective decay current of fig. 3.2. Comparing to fig. 3.1, the additional gluon is attached to the quark and gluon lines in all possible places. Not shown are real emission topologies that follow from fig. 3.3.	36

3.5	Representative topology leading to IR singularities of the final-initial dipoles. The shaded vertex denotes the Born-level insertions of figs. 3.1 and 3.3.	38
3.6	Representative topologies of real emission subprocesses with initial state soft and collinear divergencies, which are cancelled by subtracting initial-initial and initial-final dipoles. The shaded vertex denotes the corresponding tree-level matrix element of the subprocess $q\bar{Q} \rightarrow \ell^- \bar{\nu}_\ell \gamma g$, or $q\bar{Q} \rightarrow \ell^- \bar{\nu}_\ell \ell'^+ \ell'^- g$, i.e. the sum of figs. 3.1 and 3.3.	39
3.7	Ratio of the real emission matrix element for the process $pp \rightarrow W\gamma j(j) + X$ at $\mathcal{O}(\alpha_s^2 \alpha^3)$ and the subtraction dipoles, Tab. 3.3, in the limits $p_a \cdot p_4 \rightarrow 0$ (left panel) and $p_3 \cdot p_4 \rightarrow 0$ (right panel) for 10^5 randomly chosen phase space points.	44
3.8	Flow chart of the Monte Carlo integration of the IR-subtracted real emission differential cross section.	45
3.9	Self-energy corrections contained in the boxline building block, i.e. the self-energy contribution to $q\bar{Q} \rightarrow \tilde{W}g$ at $\mathcal{O}(g_s^3)$. The \tilde{W} decay current follows from fig. 3.2.	46
3.10	Abelian (left column) and mixed abelian – non-abelian triangle- and box corrections of the boxline building block, i.e. the triangle and box contribution to $q\bar{Q}\tilde{W}g$ at $\mathcal{O}(g_s^3)$. The decay current \tilde{W} can be found in fig. 3.2.	47
3.11	Non-abelian triangle- and box contributions to the non-abelian boxline building block, e.g. to $q\bar{Q} \rightarrow \tilde{W}g$ at $\mathcal{O}(g_s^3)$. The decay currents can be found in fig. 3.2.	48
3.12	Counter term diagrams contributing to $q\bar{Q} \rightarrow \tilde{W}g$ at $\mathcal{O}(g_s^3)$	48
3.13	Feynman graph topologies contributing to the abelian boxline building block. Not shown are the counter term graphs of fig. 3.12 that renormalize the corresponding graphs.	50
3.14	Mixed abelian–non-abelian and purely non-abelian pentagon contributions to $\bar{u}d \rightarrow g\ell^- \bar{\nu}_\ell \gamma$ via the off-shell decay of W^* at $\mathcal{O}(g_s^3)$. In $q\bar{Q} \rightarrow g\ell^- \bar{\nu}_\ell \ell'^+ \ell'^-$	52
3.15	Non-vanishing virtual corrections to $q\bar{Q} \rightarrow W^*Z^*g$ from closed loops of the third generation’s quarks (b, t).	53
4.1	Scale dependence of the leading order, next-to-leading order inclusive, and next-to-leading order exclusive $W^\pm \gamma j$ cross sections at the LHC for $\delta_0 = 1.0$	62
4.2	Scale dependence of the leading order and next-to-leading order inclusive $W^\pm \gamma j$ cross sections at the Tevatron for $\delta_0 = 1.0$. The cross sections correspond to either $W^- \gamma j$ or $W^+ \gamma j$ production, i.e. we do not sum over the two W^\pm bosons.	63
4.3	Individual renormalization and factorization scale dependencies of the leading order and next-to-leading order inclusive $W^\pm \gamma j$ cross sections at the LHC for $\delta_0 = 1.0$	64

4.4	Scale dependence of the leading order and next-to-leading order inclusive $W^- \gamma j$ cross sections ($\delta_0 = 1.0$) at the LHC for identified scales $\mu_R = \mu_F = \mu$ and different cuts on the transverse momentum of the jet. . . .	64
4.5	Scale dependence of the leading order and next-to-leading order $W^- \gamma j$ cross sections at the LHC for different dynamical scales and $\delta_0 = 1.0$. .	65
4.6	Minimal photon-jet separation in the azimuthal angle – pseudorapidity plane at leading order and next-to-leading order for different isolation scales, $\mathcal{E} = p_T^\gamma, p_T^{W,\gamma}, \max(p_T^\ell, p_t^\gamma, \not{p}_T)$ in (2.42). The isolation parameter is $\delta_0 = 0.6$ (denoted by the vertical line), and $\mu_F = \mu_R = 100$ GeV. . .	66
4.7	Separation of the photon from the jet with highest p_T in the azimuthal angle – pseudorapidity plane at leading order and next-to-leading order for different isolation scales with isolation parameter $\delta_0 = 0.6$ (denoted by the vertical line), and $\mu_F = \mu_R = 100$ GeV.	67
4.8	LO and NLO separation of the photon from a) the closest jet, and b) from the jet with largest p_T in the azimuthal angle – pseudorapidity plane. The isolation parameter $\delta_0 = 0.6$ is denoted by the vertical line. The isolation scale choice is $\mathcal{E} = p_T^\gamma$ in (2.42), and the differential k factor with k^{tot} plotted as horizontal line is depicted in the lower panels. . . .	68
4.9	Comparison of the parton momentum fractions of the incoming partons of the leading order and the pure di-jet part at NLO for $W^\pm \gamma j$ production. We choose $\delta_0 = 0.6$. The lower panel shows the ratio of the two distributions.	69
4.10	Leading order and next-to-leading order distributions of the minimum jet-lepton separation (left panel) and the lepton-photon separation (right panel) in the azimuthal angle – pseudorapidity plane, including the respective differential k factors. The horizontal dashed lines display the corresponding k^{tot}	70
4.11	Leading order and next-to-leading order distributions of (pseudo)rapidity differences $ y_W - \eta_\gamma $ (left panel) and $ \eta_\ell - \eta_\gamma $ (right panel), including the respective differential k factors. The horizontal dashed lines display the corresponding k^{tot}	71
4.12	Leading order and next-to-leading order distributions of the maximum transverse jet momentum (left panel) and the photon transverse momentum (right panel), including the respective differential k factors. The horizontal dashed lines display the corresponding k^{tot}	72
4.13	Leading order and next-to-leading order distributions of the W transverse momentum (left panel) and the lepton rapidity (right panel), including the respective differential k factors. The horizontal dashed lines display the corresponding k^{tot}	73
4.14	Leading order and next-to-leading order distributions of the ratios $\max(p_T^j)/p_T^\gamma$ (left panel) and $\max(p_T^j)/p_T^W$ (right panel), including the respective differential k factors.	74
4.15	Leading order and next-to-leading order distributions of the ratio p_T^W/p_T^γ , including the respective differential k factor.	74

4.16	Leading order and next-to-leading order distributions of the azimuthal angle between photon and lepton, and photon and W	76
4.17	Leading order and next-to-leading order uncertainty bands for the p_T^γ distribution, for exclusive and inclusive $W\gamma$ production. The band widths are determined from varying the factorization and renormalization scales by a factor two around $\mu_R = \mu_F = 100$ GeV only in the NLO distributions, while keeping the scale fixed for the LO distribution.	77
4.18	Leading order and next-to-leading order distributions of $\max p_T^j$, p_T^γ , $\min R_{j\ell}$, and $\min R_{j\gamma}$ at the Tevatron, including the respective differential k factors. The total k factor is plotted as horizontal line.	79
4.19	Total leading order cross section contours at the LHC (in fb) for anomalous input parameters $ \Delta\kappa_0 , \lambda_0 \leq 0.5$ with dipole form factor $n = 2$ and cutoff scale $\Lambda = 1$ TeV. The selection cuts are adopted from typical experimental studies [89–93], extended by inclusive criteria for the jets. They are quoted in (4.10). All other input parameters are chosen as described in sec. 4.1.	81
4.20	Total next-to-leading order cross section contours at the LHC (in fb) for anomalous input parameters $ \Delta\kappa_0 , \lambda_0 \leq 0.5$ with dipole form factor $n = 2$ and cutoff scale $\Lambda = 1$ TeV. Cuts and parameters are chosen as described in fig. 4.20.	82
4.21	Total k factor contours at the LHC for anomalous input parameters $ \Delta\kappa_0 , \lambda_0 \leq 0.5$ with dipole form factor $n = 2$ and cutoff scale $\Lambda = 1$ TeV. Cuts and parameters are chosen as described in fig. 4.20	82
4.22	Scale dependence of the leading order, next-to-leading order inclusive $W^- \gamma j$ in the SM $\Delta\kappa = \lambda = 0$ for the cut choice (4.10), (4.11), which we use to study the impact of anomalous couplings (4.9) on the cross sections in fig. 4.23. Varying around $\mu = 100$ GeV by a factor two yields a NLO scale uncertainty of 6.5% with an upper bound of 60.6 fb.	83
4.23	Leading order (top right) next-to-leading order (middle) cross sections in fb, and total k factor (bottom) for the anomalous couplings parameters (4.9) with dipole form factor $n = 2$ and cutoff scale $\Lambda = 2$ TeV [91,92] at the LHC. The cuts are chosen as described in the text, eqs. (4.10) and (4.11).	84
4.24	NLO- p_T^γ distributions for different anomalous couplings and $\Lambda = 2$ TeV and cuts (4.10), (4.11). The shaded band depicts the SM uncertainty, derived from varying the $\mu_R = \mu_F = 100$ GeV by a factor two around the central value. Note that the uncertainty band is covered by the green and red curve.	85
4.25	NLO- p_T^γ distributions for $W^- \gamma$ and $W^- \gamma + \text{jet}$ production the selection cuts of (4.13), combined to estimate the veto-performance at NLO in the large p_T^γ region.	86
4.26	NLO- p_T^γ distributions for $W^- \gamma$ production modified with NLO- $W^- \gamma j$ contributions to yield an approximation to the NNLO distribution. Details are described in the text.	86

5.1	Scale dependence of the leading order, next-to-leading order inclusive, and next-to-leading order exclusive $W^\pm Zj$ cross sections at the LHC.	90
5.2	Scale dependence of the leading order and next-to-leading order inclusive $W^\pm Zj$ cross sections at the Tevatron. The cross sections correspond to either $W^- Zj$ or $W^+ Zj$ production, i.e. we do not sum over the two W^\pm bosons.	91
5.3	Scale dependence of the leading order and next-to-leading order $W^- Zj$ cross sections at the LHC for different dynamical scales.	91
5.4	Individual renormalization and factorization scale dependencies of the leading order and next-to-leading order $W^\pm Zj$ cross sections at the LHC.	92
5.5	Minimum jet-lepton separation and missing transverse momentum at leading and next-to-leading in $W^- Zj$ production including the differential k factors. The horizontal dashed line displays the corresponding k^{tot}	93
5.6	Maximum jet p_T , invariant charged lepton mass, and transverse cluster mass at leading and next-to-leading order in WZj production including the differential k factors. The horizontal dashed line displays the corresponding k^{tot}	94
5.7	Maximum jet and lepton p_T at leading and next-to-leading in WZj production including the differential k factors. The horizontal dashed line displays the corresponding k^{tot}	95
5.8	Maximum p_T^j , minimum jet-lepton separation at leading and next-to-leading in WZj production including the differential k factor at the Tevatron.	96
A.1	Feynman graph topologies contributing to the abelian pentline building block. Not shown are the counter term graphs that renormalize the corresponding graphs.	101
A.2	Feynman graph topologies contributing to the non-abelian pentline building block. Not shown are the counter term contributions that renormalize the corresponding graphs.	102

List of Tables

2.1	Particle content of the minimal Standard Model. i denotes the generation index, i.e. $u^i = (u, c, t)$ and $d^i = (d, s, b)$. The table lists eigenstates of the Lagrangian, and the mass eigenstates after symmetry breaking. The bar denotes the complex conjugate module on which the complex conjugate representation operates.	5
3.1	Comparison of integrated $pp \rightarrow e^- \bar{\nu}_e \gamma j + X$ tree-level cross sections at the LHC. The cross sections were calculated with a modified version of VBFNLO, MADEVENT, and SHERPA, using CTEQ6L1 parton distributions and $\mu_F = \mu_R = 100$ GeV. The separation of the photon and the jet in the azimuthal-angle – pseudo rapidity plane is required to be $R_{j\gamma} \geq 1$. We also demand $R_{\ell\gamma} \geq 0.4$, and $p_T^j \geq 50$ GeV, $p_T^\gamma \geq 50$ GeV, $p_T^\ell \geq 30$ GeV, $ y_j \leq 4.5$, $ \eta_\ell \leq 2.5$, and $ \eta_\gamma \leq 4.5$	31
3.2	Comparison of integrated $W^- \gamma j j$ production cross sections at the LHC for selection cuts of Tab. 3.1.	37
3.3	List of the partonic subprocess of the real emission contribution $W^- \gamma j(j)$ and $W^- Z j(j)$ production at $\mathcal{O}(\alpha_s^2 \alpha^3)$, described in sec. 3.2.1. The dashed arrow stands for the suppressed electroweak part of the amplitude, i.e. $\bar{Q}q \rightarrow gg$ should be understood as $\bar{Q}q \rightarrow \ell^- \bar{\nu}_\ell \gamma gg$ or $\bar{Q}q \rightarrow \ell^- \bar{\nu}_\ell \ell'^+ \ell'^- gg$. The right column displays the needed dipoles for the IR-subtracted real emission cross section. Flavor-blindness of the dipoles in the chiral limit guarantees that the dipoles, for the subprocesses that are separated by a comma in the first column, are identical. Not shown are subprocesses and corresponding dipoles that follow from initial-state momenta-interchange. We also do not quote multiple dipoles for subprocesses with identical quark flavors or two gluons, i.e. for $\bar{u}(p_a)\bar{u}(p_b) \rightarrow \bar{u}d$, both $\bar{u}(p_a)$ and $\bar{u}(p_b)$ may act as emitter and spectator. This leads to a doubling of dipoles for the considered subprocess, which amounts computing algebraically identical dipoles with, however, different kinematics ($p_a \leftrightarrow p_b$).	43
4.1	Inclusive next-to-leading order cross sections and k^{tot} -factors for the processes $pp \rightarrow e^+ \nu_e \gamma j + X$ and $pp \rightarrow e^- \bar{\nu}_e \gamma j + X$ at the LHC for identified renormalization and factorization scales, $\mu_R = \mu_F = 100$ GeV. The cuts are chosen as described in the text.	63

5.1	Next-to-leading order inclusive cross sections and k^{tot} -factors for the processes $pp \rightarrow e^+ \nu_e \mu^+ \mu^- j + X$ and $pp \rightarrow e^- \bar{\nu}_e \mu^+ \mu^- j + X$ at the LHC for identified renormalization and factorization scales, $\mu_R = \mu_F = 100$ GeV. The cuts are chosen as described in the text.	89
5.2	Exclusive next-to-leading order cross sections and total correction factors for the processes $pp \rightarrow \ell^+ \nu_\ell \ell'^+ \ell'^- + X$ and $pp \rightarrow \ell^- \bar{\nu}_\ell \ell'^+ \ell'^- j + X$ at the LHC for identified renormalization and factorization scales, $\mu_R = \mu_F = 100$ GeV. The cuts are chosen as described in the text.	93
B.1	Cross-references of the modified pdfs' coefficient functions (B.29)-(B.34) to the results of Secs. B.2.1, B.2.2, and B.2.3.	113

Acknowledgements

First of all, I would like to thank Prof. Dr. Dieter Zeppenfeld for accepting me as a Ph.D. student, his indispensable advice, and his patience with me over the past years. I am grateful for the opportunity to learn and benefit from his amazing knowledge of particle physics and collider phenomenology. His valuable comments to the draft of this thesis are also gratefully acknowledged.

I thank Prof. Dr. Ulrich Nierste for agreeing to be the second referee of my dissertation.

I am highly indebted to my fellow collaborators Dr. Francisco Campanario, Dr. Stefan Kallweit, and Dr. Michael Spannowsky for contributing to the projects, which have been presented here. In particular, I am grateful to Michael for keeping me on track during times when my motivation was fading, by constantly reminding me of the reasons why I am a particle physicist. Also I want to thank Michael for proof-reading this thesis.

I cordially thank the members of the Institute for Theoretical Physics for the relaxed and enjoyable atmosphere on the 12th floor of the physics building.

My research was supported in parts by the *Graduiertenkolleg Hochenergiephysik und Teilchenastrophysik*, and by the *Strukturiertes Promotionskolleg des Landes Baden-Württemberg: Promotionskolleg am Centrum für Elementarteilchenphysik und Astroteilchenphysik CETA and KCETA*.

I wish to thank my parents for their never-ending support and their faith in me.

Finally, I want to thank Alice for picking up the challenge of sharing her life with a theoretical particle physicist, and for all her love and support.